ABSTRACT

Title of dissertation: A Multi-Wavelength Study of Spiral Arm
Substructure

Misty Ann La Vigne, Doctor of Philosophy, 2010

Dissertation directed by: Professor Stuart Vogel
Department of Astronomy

Spiral arms are the hallmark of spiral galaxies. Spiral density waves gather gas, dust, and stars in the disks of spiral galaxies, forming the arms. Observations show that these large-scale features are often composed of smaller scale substructures, commonly referred to as feathers and spurs, which give the arm a patchy and segmented appearance. Within these select galaxies, the substructure appears associated with much of the star formation in the arm. In this thesis, we study the frequency and characteristics of spiral arm substructure in a sample of 233 spiral galaxies; using newly acquired high-resolution ($\sim 4''$) CARMA CO(1-0) velocity-integrated intensity maps of five target spiral galaxies, we compare the distribution of star formation tracers along spiral arms and test formation theories for spiral arm substructure.

We use a multi-wavelength data set to study the frequency and characteristics of spiral arm feathers and test the predictions for their formation. Using broadband HST images, we study how common feathers are in our sample of 233 spiral galaxies. With high-resolution CARMA CO(1-0) observations of five target galaxies previously known to have feathers, we study the distribution of the molecular gas relative to the location of neutral gas and star formation tracers. We measure the spacing between the feathers and use the CO(1-0) observations to estimate the molecular gaseous surface density along the spiral arms.

We find that feathering substructure is not limited to late type, grand design spiral galaxies and is detected in a range of galaxy types, from early to late type, and spiral arm environments, including barred, ringed, and flocculent. In our target sample, we find that feathers are more than mere extinction features and are associated with a significant amount of the star-forming gas. We further find a relationship between the spacing of feathers and the gaseous surface density along spiral arms, which suggests these features form via a gravitational instability.

A Multi-Wavelength Study of Spiral Arm Substructure

by

Misty Ann La Vigne

Dissertation submitted to the Faculty of the Graduate School of the
University of Maryland, College Park in partial fulfillment
of the requirements for the degree of
Doctor of Philosophy
2010

Advisory Committee:
Professor Stuart N. Vogel, Chair/Advisor
Professor Eve C. Ostriker
Professor Alberto D. Bolatto
Professor Robert D. Hudson, Dean's Representative
Professor Michele D. Thornley

Preface

Portions of the research described in this work have been published elsewhere. Chapter 2 previously appeared in La Vigne, Vogel, and Ostricker (2006). Preliminary versions of the material in Chapter 5 were presented at the 211th meeting of the AAS, January 2008 (La Vigne and Vogel 2007), and at the 213th meeting of the AAS, January 2009 (La Vigne and Vogel 2009).

To my parents, Howard and Nancy La Vigne, and my husband,

Hezekiah Carty.

Contents

List of Tables

List of Figures

Abbreviations

ACS	Advanced Camera for Surveys
BIMA	Berkeley, Illinois, Maryland Array
CARMA	Combined Array for Research in Millimeter-Wave Astronomy
CO(1-0)	Carbon monoxide ground-state transition
FWHM	Full width half maximum
FOV	Field of view
GALEX	Galaxy Evolution Explorer
GMA	Giant molecular association
GMC	Giant molecular cloud
H$\textsc{i}$	Neutral hydrogen
H$\textsc{ii}$	Singly ionized hydrogen
H$_2$	Molecular hydrogen
Hα	Balmer series transition
HST	Hubble Space Telescope
IRAC	Infrared Array Camera
ISM	Interstellar medium
MIPS	Multi-band Imaging Photometer for Spitzer
MHD	Magneto-hydro dynamics
MJI	Magneto-Jeans instability
N$\textsc{ii}$	Singly ionized nitrogen
NGC	New General Catalogue
NIR	Near infrared
NRAO	National Radio Astronomy Observatory
PAH	Polycyclic aromatic hydrocarbons
PDL	Primary Dust Lane

RC3   Third Reference Catalogue of Bright Galaxies

SED   Spectral energy distribution

SFR   Star formation rate

SINGS   Spitzer Infrared Nearby Galaxies Survey

SONG   Survey of Nearby Galaxies

THINGS   The HI Nearby Galaxy Survey

WFPC2   Wide Field Planetary Camera 2

Chapter 1

Introduction

Spirals are one of the three main types of galaxies first categorized by Hubble (1926). Characteristically, they are composed of an older, central stellar bulge bisected by a thinner, more extended rotating disk of younger stars, gas, and dust. The most distinguishing feature of spiral galaxies is their spiral arms, elongated "structural features" of enhanced luminosity that "emerge from the [bulge]" and wind around the disk (Hubble 1926). Spiral arms are observed to be sites of increased concentrations of stars and have a higher density of star formation (Kennicutt 1998a). Associated with spiral arms are dark lanes that line the inside edge of the arms and are associated with concentrated gas and dust (Sandage 1961; Elmegreen 1980a).

1.1   Morphological Characteristics of Spiral Galaxies

Hubble (1926) originally sub-divided spiral galaxies into a range of types: "early" (Sa), "intermediate" (Sb), and "late" (Sc) for both unbarred (S) and barred (SB) galaxies based on their structure and stellar content. Early type galaxies are distinguished by having a large, luminous bulge and very tightly wrapped spiral arms. As the sequence progresses to later type, the spiral arms "build up at the expense of

the [bulge], unwinding as they grow, until in the end they are widely open and the [bulge] inconspicuous" (Hubble 1926). Today, Hubble's original scheme has been extended to include transition classes, e.g., Sab; Sd galaxies, which almost completely lack a bulge; and the Magellanic, Sm, systems (de Vaucouleurs 1959). The symbol SA has also been introduced to designate an ordinary, unbarred spiral galaxy. Its combination with Hubble's symbol for a barred spiral, SB, has been used to make a new compound symbol, SAB, to represent objects of "mixed characteristics" (de Vaucouleurs 1959).

It has been observed that the majority of star formation in the local Universe occurs in ordinary disk or spiral galaxies (Helou 1999). However, the stellar content and star formation activity vary along the Hubble sequence (Kennicutt 1998a, 1998b). On average, the mean optical color for spirals, as measured by the color indices (U-B) and (B-V), trends from redder to bluer from early type spirals (Sa) to late type spirals (Sd) (Roberts & Haynes 1994). Similarly, the average star formation rate (SFR) per unit stellar mass increases from early to later types (Sa - Sc) (Kennicutt & Kent 1983; Young et al. 1996). Furthermore, the number, size, and luminosity of HII regions in late type spirals are more numerous, larger, and on average 50 times more luminous than the brightest HII regions in early type Sa galaxies (Roberts & Haynes 1994, and references within). There is also a trend in the total gaseous content with Hubble type; later type Sc and Sd galaxies have a higher proportion of total gas (atomic and molecular) than early type Sa and Sb systems (Kennicutt 1989, 1998b). These trends are derived from global averages of the entire galactic disk or at best, radial profiles derived from an azimuthal average

(Kennicutt & Kent 1983; Kennicutt 1989, 1998b; Roberts & Haynes 1994; Young et al. 1996). Averaging over the disk, whether globally or azimuthally, smooths out any non-axisymmetric variations. This includes emission from spiral arms, which are the prominent sites of star formation in spiral galaxies (Elmegreen 1980b; Elmegreen & Elmegreen 1983). These trends with Hubble type, particularly SFRs, are assumed to result from variations in the physical and dynamical properties within the disks of spiral galaxies (Kennicutt 1998a).

1.2   Spiral Arms

Dynamically, rotation curves of spiral galaxies show that outside of the central region, the rotational velocity, $V_{\rm R}$, of the stars and gas in the disk is nearly independent of radius R (Prendergast & Burbidge 1960; Rubin, Thonnard, & Ford 1978). Since $V_{\rm R}$ is constant, the angular velocity, $\Omega_{\rm R}$, varies with radius as $\Omega_{\rm R} \propto V_{\rm R}{\rm R}^{-1} \propto {\rm R}^{-1}$, resulting in differential rotation. Therefore, spiral structures cannot be "material arms", permanently made up of the same stars and gas. If they were, the differential rotation of the disk would wind the arms tightly over a few galactic rotation periods, in which case the loose spiral arms commonly seen would be rare (Lindblad 1964). Oort (1962) first suggested a solution to the "persistence problem" of spiral arms, proposing that "the arms could retain their present spiral shapes if matter were constantly being added to their inner edges, while the outer edges would constantly lose matter". Today, it is conventionally thought that spiral arms are formed from spiral density waves, which compress the stellar distribution and gas as they pass through.

Though the stars and gas do not permanently reside in the spiral arms, they do spend much of their time there (up to a third or half of an orbit), concentrating in the spiral arms (Binney & Tremaine 1987).

In the quasi-stationary spiral structure theory of Lin & Shu (1964), a steady spiral density wave rotates like a solid body with uniform angular velocity. At the corotation radius, both the disk and the spiral pattern rotate at the same linear speed. Inside the corotation radius, the gas and stars rotate faster than the spiral pattern, and therefore overtake the pattern; they pass through the arms from the inside or concave side. As the gas enters the spiral arms, it is shocked and compressed. On the inside edge of the arms, the site of compression is marked by dust lanes that screen optical emission and by gaseous molecular arms, which are observed at millimeter wavelengths (Vogel et al. 1988). Further downstream, Hα emission peaks on the outside of the spiral arm, typically offset by $5''$-$10''$ from the gaseous molecular arms, and marks the site of massive star formation along spiral arms (Vogel et al. 1988).

1.3 Spiral Arm Substructure

Spiral arms are not however smooth, continuous features. Typically an arm is composed of many substructures commonly referred to as feathers, spurs, and branches, which give the arm its patchy, divaricate appearance. This substructure appears associated with much of the star formation in the arm.

1.3.1 Previous Observations of Spiral Arm Substructure

Early reports of spiral arm substructure were based on examination of photographic plates such as those used for prints in *The Hubble Atlas of Galaxies* (Sandage 1961). Weaver (1970) noted that the spiral arms of nearby galaxies appear clumpy, irregular, and mottled on small scales. In particular, he noted the presence of "spurs" (also referred to as branches or twigs), which appear to originate on the *outside* of the arm, with larger pitch angles than the arm itself. Spurs extend from the outside of the arm into the interarm, and are seen in photographic plates as *stellar* features. Weaver also noted the presence of *dark* material concentrated along the *inner* edges of spiral arms. He remarked that the outside regions of arms appear to be made of material drawn out or "brushed" from the inner edges, and that this brushed-out structure has a pitch angle typically a factor of two larger than the arm itself.

At the same time, Lynds (1970) reported a detailed study of dark nebulae in 17 late-type spirals using photographic plates from Mt. Wilson and Palomar Observatories. She commented on the well-known strong dust lanes along the inner edge of the arms, which she termed "primary dust lanes" (hereafter abbreviated PDLs), and noted the presence of thin dust lanes with large pitch angles cutting *across* the luminous arms. She called these features "feathers", and pointed out that these extinction features become mostly undetectable outside the luminous arm presumably owing to the absence of a sufficiently bright background. She also emphasized that bright H II regions are typically near or embedded in dust lanes (Lynds 1972, 1974). Later, Piddington (1973) noted that interarm stellar features called spurs

by Weaver are often found associated with the extinction features cutting across luminous arms called feathers by Lynds, and suggested that the two are related.

Subsequently, Elmegreen (1980b) studied seven spiral galaxies to investigate the properties of spurs, which, as noted above, are observable as stellar features. Elmegreen was able to identify two to six well-delineated spurs in each of her galaxies, with lengths ranging from one to five kpc; her spurs are generally located in the outer parts of the luminous disk. She observed that spurs are always located on the outside of spiral arms, have pitch angles equal to or greater than that of the originating arm, and commonly occur in pairs or groups with the spurs oriented roughly parallel to one another. Elmegreen also determined that on average spurs have pitch angles of roughly 50° with respect to spiral arms, which is comparable to the average pitch angles of the feathers measured by Lynds (1970). Noting the similarity between the pitch angles of feathers and spurs, Elmegreen added further observational support to Piddington's (1973) suggestion that spurs and feathers have a common origin.

1.3.2   Theoretical Studies of Substructure

Motivated to explain the formation of observed spurs, branches, and feathers in spiral galaxies, Balbus (1988, hereafter B88) conducted a local gas dynamical stability analysis of a single-fluid polytropic flow through spiral arm potentials, following the linear evolution of self-gravitating perturbations. In his analysis, the background gaseous surface density profile representing the arm has an arbitrary spatial form,

and the differentially rotating, expanding background flow is consistent with this profile. B88 investigated all wavenumber directions in the plane of the disk and modeled the spiral arms as tightly wound, with no magnetic field. B88 found that there are two preferred directions of growth in spiral arm flow: initial wavefronts roughly along the spiral arm, or perpendicular to it. The rate of growth in both directions depends on the properties of the underlying flow. In certain regimes, growth of instabilities leads to fragmentation parallel to the arms, observed as a thickening of the arms. In other situations, growth of initially leading wavenumbers results in branches, feathers, or spurs. For wavefronts initially perpendicular to the arm, as the gas moves into the interarm region, the flow expansion and shear (which increases downstream from the arm) shapes and stretches small-scale structure into the familiar large scale trailing 'spur' shapes that are observed.

B88 also suggested that a two-dimensional lattice of small-scale structure can develop when the two dominant modes of growth intersect. In *The Hubble Atlas of Galaxies* (Sandage 1961), B88 found that some barred spiral galaxies, in particular the western arm of NGC 1300, seemed to exhibit a lattice structure of HII regions. However, he found no examples of such structure in unbarred galaxies.

Kim and Ostriker (2002, hereafter KO) extended the local models of B88 by including the effects of non-linearity and magnetic fields. KO conducted local, two-dimensional, time-dependent, magneto-hydrodynamic (MHD) simulations of self-gravitating, differentially rotating, razor thin disks of gas. Their models followed the formation and fragmentation of "gaseous spurs" as the flow passes through spiral arm potentials. They found that local substructures are created via the magneto-

Jeans instability (MJI); as the background flow passes through the spiral pattern it is shocked and compressed until it becomes Jeans unstable, at which point gravity, aided by magnetic forces, begins to create alternating compressed and rarefied regions along an arm. The magnetic effects aid the formation of compressed, self-gravitating complexes because magnetic tension forces oppose the Coriolis forces that would otherwise stabilize the flow, helping to transfer angular momentum out of growing condensations. KO found that the gaseous spurs fragment into clumps within which star formation could commence. They suggest that these clumps could be the precursors of bright H II regions that jut from the outside of spiral arms inside corotation.

From their simulations, KO put together observable statistics of their gaseous spurs. Most potentially comparable to observations is the spacing of these features along a spiral arm, which they find ranges from 2–5 times the local Jeans wavelength (at the spiral arm density peak) and corresponds to a spacing of approximately 750 pc on average. KO also proposed that the shape and location of gaseous spurs within a spiral arm may potentially be used observationally to determine the spiral pattern speed of the arm. Recently, Kim & Ostriker (2006) have extended their thin disk simulations to three dimensions, also making comparison to two-dimensional "thick disk" models. The results they find are overall consistent with the conclusions of KO, with the difference that spur spacings increase by a factor ~ 2 due to the dilution of self gravity when the disk thickness increases.

Chakrabarti, Laughlin, and Shu (2003, hereafter CLS) studied the response of a thin, self-gravitating, singular isothermal gaseous disk to rigidly rotating spiral po-

tentials, specifically focusing on the effects of ultraharmonic resonances by choosing parameters that minimize swing amplification. In simulations with a low Toomre Q_g parameter, CLS found growth of spiral arm "branches" (which they define as trailing bifurcations of the main spiral arms). Long-term simulations with high Q_g exhibited the growth of stubby leading structures (referred to as "spurs" by CLS; this is however inconsistent with terminology of other authors).

Wada and Koda (2004, hereafter WK) performed two-dimensional, time dependent, global hydrodynamical simulations of a thin, isothermal, non-self-gravitating disk of gas in tightly and loosely wound, rigidly rotating spiral potentials. WK's model rotation profiles included both differentially rotating and rigidly rotating cases. They found that the spiral shock front is stable when the gas is modeled with a flat rotation curve and unstable when modeled with a rising rotation curve. In their models, they found the stability of the shock front is also dependent upon the pitch angle of the spiral arms: stable if $i \leq 10°$, unstable if $i \geq 10°$. In the unstable models of WK, strong shocks with arm-interarm density ratio ~ 100 become unstable by rippling. WK attribute this "wiggle" instability to Kelvin-Helmholtz (K-H) modes involving the strong velocity shear behind the shock. Over time, the instabilities become non-linear forming what WK refer to as "spurs" in the interarm regions. The spurs are quasi-regularly spaced, approximately 100-200 pc apart; the authors do not state, however, how spacing depends on model parameters. Due to the shape of the rotation curve, the spurs formed in the WK simulations are curved near the arm in the opposite sense (i.e. trailing then leading) to the gaseous spurs produced in the KO simulations and the small-scale structure predicted in B88's

9

analysis.

Dobbs and Bonnell (2006, hereafter DB) used three-dimensional SPH simulations to study the response of isothermal, non-self-gravitating gaseous disk models with varying temperatures to a four armed rigidly-rotating spiral potential. DB find that the temperature of the disk has a crucial effect on the growth of spiral arm substructure. In the lower temperature ($T < 10^3$ K) models of DB, the initially smooth arms become clumpy, and then the clumps are sheared into trailing features as they return to interarm regions. The shapes of the interarm features found by DB are similar to those of KO, reflecting the flat rotation curve they adopt. DB use somewhat nonstandard terminology in describing their results; they refer to the portions of interarm extinction features adjoining arms as "spurs", and the portions further downstream as "feathers". In their $T = 50$ K model, which has arm-interarm contrast ~ 50, the spacing of DB's spurs are ≈ 700 pc; DB also do not state, however, how spacing depends on model parameters.

1.3.3   Discussion of Substructure Nomenclature

As is evident from the above summaries, the terms "spurs", "feathers", and "branches" have been used in many ways. In this thesis, we adopt the definitions from the initial, observational papers:

feathers – thin dust lanes or extinction features that extend outward at a large angle from the *primary dust lane* (PDL) which lines the inner side of the arm, cutting across the outer bright part of the spiral arm (Lynds 1970).

spurs – bright chains of OB associations and Hɪɪ regions that jut at a large angle from the spiral arm into the interarm (Weaver 1970, Elmegreen 1980b).

branches – divarications of a spiral arm that lend to the overall spiral structure (Elmegreen 1980b).

1.4   Motivation & Goals of Thesis

Feathers are of considerable interest because there are both observational (Lynds 1970, Piddington 1973, Elmegreen 1980b, Scoville et al. 2001) and theoretical (B88, KO) reasons to associate them with a significant portion of star formation in spiral galaxies. Also, they may provide information on basic physical conditions in spiral arms, such as the mean gaseous surface density and magnetic field strength (KO). At least in principle, they may also be used to deduce the spiral pattern speed and details of the gas flow through spiral arms (KO, CLS). Lastly, they are a striking characteristic of prototypical grand design spiral galaxies (e.g. M51, Beckwith 2005) and may therefore tell us something about the evolutionary and environmental aspects of spiral structure. A complete description of spiral arms should include a characterization of the frequency and properties of such feathers, and a complete model of spiral structure should explain their dynamical origins.

The goals of this thesis include: confirming that feathers are a common feature of spiral galaxies, evaluating their frequency and characteristics, and determining the types of spiral galaxies in which feathers occur (barred or unbarred, early or late-type, grand design or flocculent). We aim to identify where feathers are located,

in the inner or outer disk, on the inside of spiral arms or the outside. In addition, we investigate the relation of the spacing of feathers to the gas surface density of a galaxy to determine their formation mechanism.

In Chapter 2, we present results from our survey of spiral arm substructure in 233 bright, nearby, spiral galaxies. Using HST archival, broadband observations we evaluate these galaxies for the presence of extinction substructure identified as feathers. We then characterize the frequency of detecting feathers and their properties as a function of galaxy type. We also consider the appearance of feathers at 8 μm and in CO(1-0) for two grand design spiral galaxies. We measure the spacing between feathers in these two galaxies and estimate the molecular surface density, Σ_{H_2}, along the spiral arms to compare with predictions from feather formation theories.

In Chapter 3, we introduce a target sample of five spiral galaxies used for more detailed study. We discuss observations of these galaxies using the newly operational Combined Array for Millimeter-wave Astronomy (CARMA) interferometer. The sample galaxies contain feathers previously identified in Chapter 2 and were selected to cover a range of morphological types (Sab-Sc) and spiral arm environment. We discuss the sample and our observational techniques, such as mosaicing, when observing the sample with CARMA, and our data reduction methods.

In Chapter 4, we present the CARMA CO(1-0) channel and velocity-integrated maps of our target sample. We characterize the distribution of the molecular and atomic gas in each galaxy. We analyze these tracers along the spiral arms to determine if the arms are molecular dominant. We then further compare the distribution of CO(1-0) to other star formation tracers, including 8 μm and Hα to determine

the location of the neutral gas relative to newly formed stars.

In Chapter 5, we extend our analysis of feathers utilizing the new, high-resolution CARMA CO(1-0) velocity-integrated maps of our target sample galaxies. We first identify the location of the feathers within each galaxy, and describe the process by which they were identified, using CO(1-0), 8 μm, and optical broadband HST observations. We then evaluate whether the feathers are associated with a significant amount of gas. We further test the theories for the formation of feathers by comparing the spacing between feathers and the local molecular surface density with predictions from theory in a range of galaxy types using high resolution datasets. We also assess the role of spiral arm pitch angle in the formation of feathers and compare our analysis with the predictions from hydrodynamical theoretical models.

In Chapter 6, we summarize the conclusions from this thesis and discuss the prospects of future work.

Chapter 2

An HST Archival Survey of Spiral Arm

Substructure

Abstract

We present a survey of spiral arm extinction substructure referred to as feathers in
223 spiral galaxies using HST WFPC2 images. The sample includes all galaxies in
the RC3 catalog with $cz < 5000$ km s^{-1}, B$_T < 15$, $i < 60°$, and types Sa–Sd with
well-exposed broadband WFPC2 images. The detection frequency of delineated,
periodic feathers in this sample is 20% (45 of 223). This work is consistent with
Lynds (1970), who concluded that feathers are common in prototypical Sc galaxies;
we find that feathers are equally common in Sb galaxies. Sb–Sc galaxies without
clear evidence for feathers either had poorer quality images, or flocculent or complex
structure. We did not find clearly defined feathers in any Scd–Sd galaxy. The
probability of detecting feathers was highest (83%) for spirals with well-defined
primary dust lanes (the lanes which line the inner edge of an arm); well-defined
primary dust lanes were only noted in Sab–Sc galaxies. The detection frequency of
feathers was similar in barred and unbarred spirals. Consistent with earlier work, we

find that neighboring feathers tend to have similar shapes and pitch angles. Well-defined feathers often emerge from the primary dust lane as leading features before they curve to trailing; some are quite elongated, extending into the interarm and merging with other feathers. OB associations are often found lining feathers, and many feathers transition to the stellar substructures known as spurs (Elmegreen 1980b). We find that feathers are coincident with interarm filaments strikingly revealed in Spitzer 8 μm images. Comparison with CO(1-0) maps of NGC 0628 and NGC 5194 from BIMA SONG shows that feathers originate at the primary dust lane coincident with gas surface density peaks. Contrary to the appearance at 8 μm, the CO(1-0) maps show that gas surface density in feathers decreases rapidly with distance from the primary dust lane. Also, we find that the spacing between feathers decreases with increasing gas surface density; consistent with formation via a gravitational instability.

2.1   Sample Selection

Our study was motivated by the WFPC2 Hubble Heritage image of M51 (Scoville et al. 2001), which revealed remarkable feather structure particularly in the inner galaxy. Since similar structure is difficult to discern in a casual inspection of M51 and other galaxies in *The Hubble Atlas of Galaxies* (Sandage 1961), we concluded that high angular resolution is important and sought to explore the Hubble Space Telescope (HST) archives for additional examples of galaxies with clearly delineated feathers.

The HST archive contains thousands of galaxy images. To narrow the list, we initially used the Elmegreen & Elmegreen (1987; hereafter EE) sample of 762 spirals, each classified as one of nine arm types ranging from "chaotic, fragmented, unsymmetric" to "two long symmetric arms dominating the optical disk". The EE sample might appear ideal, since we expected galaxies with well-defined spiral arms to be the best targets. However, many galaxies classified as grand design by EE have poorly-defined arms in HST images. Conversely, many galaxies classified by EE as having poorly-defined arms have well-defined arms in HST images. The EE classifications appear to be determined primarily by the arm structure outside the inner $1'$ of galaxies, beyond the region typically imaged by HST. This may be because in the Palomar Sky Survey images used by EE the inner arms are often saturated and the outer arms dominate the spiral structure. We conclude that EE arm classes do not provide reliable descriptions of arm type in the inner $1'$ of many nearby galaxies.

We therefore expanded our search using the *Third Reference Catalogue of Bright Galaxies* (RC3). This increased the sample size by including galaxies at more southern declinations not available in the EE sample, and allowed us to specify criteria optimized for identification of substructures. Based on the absence of clear examples of feathers in the photographic reproductions of ground-based images in the Hubble Atlas, we decided that distance to a galaxy should be the primary criterion for inclusion in the sample.

2.1.1 A Distance-Limited Sample

Using Vizier, we selected all galaxies in the RC3 catalog with de Vaucouleurs type Sa–Sd, $cz < 5000$ km s^{-1}, $i < 60°$, and B$_T < 15$. Our sample excludes galaxies with type Sdm or later because these typically lack well-delineated spiral arms.

The recessional velocity was limited to < 5000 km s^{-1} to ensure adequate linear resolution to resolve typical dust lanes and any substructure that may be present. Assuming H$_o$ = 71 km s^{-1} Mpc^{-1}, this redshift corresponds to a linear resolution of 34 pc for the 0.1″ resolution of the three Wide Field Cameras. The limit for inclination was set to 60° because at higher inclinations a galaxy may be too inclined to clearly discern structure. The B$_T$ magnitude was limited to galaxies brighter than 15th magnitude to eliminate small galaxies or low surface brightness galaxies, neither of which would be well suited for examination of extinction substructure. (In fact, few galaxies in the RC3 catalog at $cz < 5000$ km s^{-1} have B$_T > 15$, so this criterion did not significantly affect the sample size.) The total number of galaxies that meet these criteria is 630.

Ideally, for detection of feathers (extinction substructure), we need images taken with high resolution, a large field of view (FOV), and good sensitivity. These criteria are best satisfied by the HST ACS (Advanced Camera for Surveys) instrument. However, many of the ACS images were still proprietary at the time of this study (2003). We therefore used images taken with WFPC2 (Wide Field/Planetary Camera 2), which also satisfies the above criteria.

Since good signal-to-noise ratios are essential, we restricted the sample to

images with exposure time > 60 seconds obtained with wideband (W) filters. All images taken with filters shorter than 4311 Å and longer than 8012 Å were excluded due to the poor sensitivity of WFPC2 at shorter wavelengths, and because extinction features are less prominent at longer optical wavelengths. Lastly, observations of galaxies where the FOV did not cover a spiral arm were excluded from the sample. We found that 223 of the 630 RC3 galaxies had WFPC2 images meeting our criteria.

2.2   Data Reduction

We obtained from the HST archive calibrated, full resolution FITS files for images of all 223 galaxies which met the selection criteria described above. We then mosaiced the images and removed cosmic rays using standard procedures outlined in the HST handbook.

We selected images of 21 of the galaxies with well-defined substructure to present as prototypes (see Figures 2.1–2.14). Typically the original images vary significantly in brightness between the nucleus and outer regions, making it difficult to see substructure in different parts of the galaxy in a single image stretch. Therefore, images shown in the figures were further processed by subtracting a radial profile derived from the median value in annuli deprojected assuming the RC3 inclination and using nuclear positions obtained from the NASA/IPAC Extragalactic Database (NED).

2.3   Results

2.3.1   General Characteristics of Feathers

We illustrate many of the general characteristics of classic feathers using HST observations of NGC 5194 and NGC 0628. Images are shown in Figures 2.1 and 2.2 with thin lines to mark identified feathers, and in Figures 2.3 and 2.4 without the lines. Each arm exhibits dark, delineated extinction features, which emerge from the primary dust lane (PDL) that runs along the inside part of the arm, traverse across the luminous arm, and often extend into the interarm.

Typically, close inspection shows that well-delineated feathers emerge from the PDL as leading features and then gradually curve to become trailing features further downstream, on the outer edges of the spiral arms. Feathers that are near each other generally have similar pitch angles and curvature, as noted by Lynds (1970). Many are dotted with bright knots of star formation or HII regions, especially near the PDLs and the beginning of the interarm regions.

Many of the feathers extend well into the interarm regions. Several coalesce and can be traced through more than $180°$. The farthest-reaching feathers appear to merge with the PDL of the next arm, as is seen in both arms of NGC 0628 and NGC 5194.

2.3.2   Frequency of Feather Detections

Motivated by the observational and theoretical studies reviewed in § 1.3.1 and § 1.3.2, we considered a galaxy to have well-defined, classic feathers if it exhibited extinction

19

substructure meeting the following criteria: multiple dust lanes with approximately regular spacing emerging from a PDL at roughly similar large angles, frequently associated with star formation regions.

Feathers were clearly detected in 45 of the 223 (20%) galaxies examined. To investigate which galaxies have feathers, we classified all 223 galaxies according to how well the spiral arm PDLs are delineated, using the HST images. PDL delineation was categorized from "poor" (see NGC 5055, Figure 2.12) to "fair" (see NGC 1300, Figure 2.6) to "good" (see NGC 4548, Figure 2.10). Table 2.1 lists the number and percentage of galaxies with clear detections of feathers for each of the three PDL classifications. We see that the presence of delineated PDLs and feathers are highly correlated: 83% of galaxies with good PDL delineation show feathers. However, not all galaxies with delineated PDLs have feathers. NGC 4450 is an example of a galaxy with delineated PDLs categorized as good which has no feathers. Interestingly, NGC 4450 is also classified as an anemic galaxy (Elmegreen et al. 2002).

The feathers detected in the 45 galaxies mentioned above originate at delineated PDLs. We also find features resembling feathers present in flocculent galaxies that do not satisfy our strict definition of feathers because they do not appear to originate at a PDL (as well as in four flocculent galaxies with feathers that clearly do originate at PDLs). We detected such "flocculent feathers" in 17 out of 24 flocculent galaxies. We do not include cases of flocculent feathers without PDLs in Table 2.

Also, within the central kiloparsec of some galaxies the images reveal fine, smaller scale extinction features. These interesting features, seen for example in

NGC 5194 (Figure 2.3), also do not appear to originate at a PDL and therefore we do not classify them as classic feathers. Occasionally, the extinction features present could be interpreted as lattice structure.

In general, from our sample of 223, those galaxies in which we did not definitively detect feathers fall into one or more of the following categories: a) the galaxy image is of lesser quality, typically due to exposure time or distance of the galaxy; b) PDLs are not clearly detected, which in some cases may be due to the quality of the observations; c) the galaxy is a flocculent with no clear PDLs; or d) the spiral arm structure is too complex or confusing, sometimes as the result of interaction.

2.3.3   Feather Frequency and Characteristics as a Function of Galaxy Type

Previous observational work emphasized that feathers and spurs are a characteristic of late-type spirals (e.g. Lynds 1970; Elmegreen 1980b). Figure 2.17 shows that the sample of 223 spirals is sufficiently large to investigate feather frequency for all types of spirals. We see that feathers are most common in Sb–Sc galaxies, with feathers clearly detected in 26–33%.

At earlier Hubble types, the detection frequency is lower: 4/24 or 17% for Sab and 1/28 for Sa. Clearly, feathers are quite common in somewhat earlier types (e.g. Sb) than previously thought. For example, NGC 4736 (Sab) shows particularly clear feathers, as seen in Figure 2.11. Still, feathers are definitely rarer at the earliest types. This may be in part because some early type galaxies are relatively

deficient in gas, or because the shallower pitch angle of the arms results in lower shock compression of the PDL. Both of these might result in weaker PDLs; indeed, well-defined PDLs are detected in none of the 28 Sa galaxies and only 4 of the 24 Sab galaxies, compared to 31 of 129 Sb–Sc galaxies.

At later Hubble types, there are no feathers detected (0/37 for Scd and 0/15 for Sd). Note that no well-defined PDLs are detected in the 47 Scd–Sd galaxies, presumably because the spiral density enhancement is relatively weak in these generally lower luminosity galaxies, and this likely accounts for the paucity of feathers.

We found little difference between barred and unbarred galaxies in the frequency of feather detection. In particular, the frequencies are 14/66 (21%) for SA, 17/78 (22%) for SAB, and 14/73 (19%) for SB. As will be discussed in § 2.3.4, parallel PDLs and "lattice" feather structure connecting the parallel PDLs are common in the arms of barred spirals.

We expected feathers to be associated with grand design spirals. We were surprised to find feathers and PDLs in some flocculent spirals as well, since flocculents appear "fleecy" at optical wavelengths and typically lack large-scale, continuous spiral structure. This absence of large-scale, continuous spiral structure is generally credited to an absence of spiral density waves within the galaxy. However, Thornley (1996) presented K' (2.1 μm) observations of four nearby flocculent spiral galaxies[1] that clearly show low-level spiral structure, which suggests that kiloparsec-scale spiral structure is more prevalent in flocculent galaxies than previously thought. Interestingly, a comparison of the two PDLs with feathers seen in the HST WFPC2

[1]NGC 2403, NGC 3521, NGC 4414, NGC 5055

image of NGC 5055 to the stellar spiral arm observed at 2.1 μm shows that the feather PDLs and stellar arms are related structures (see Figure 2.18). This correlation between PDLs and spiral density waves suggests that feathers originating at delineated PDLs in flocculent galaxies may indicate an underlying spiral density wave not dominant at visible wavelengths.

As described in § 2.3.2, flocculents also harbor extinction structures which appear morphologically nearly identical to classic feathers, which we called flocculent feathers; these differ in that they are *not* associated with PDLs and tend to be associated with less star formation per feature. They are nicely illustrated in NGC 7217 (Figure 2.14) as well as the parts of NGC 5055 (Figure 12) not associated with the PDLs. The number of flocculent feathers in a flocculent may greatly outnumber the classic feathers associated with PDLs. Flocculent feathers are likely due to gaseous/dusty condensations sheared by differential rotation. As mentioned previously, we detected flocculent feathers in 17 of 24 flocculent galaxies.

2.3.4 A Catalog of Feather Morphology

General properties of the 45 galaxies with clearly delineated feathers are listed in Table 2.2. See Figures 2.5–2.14 for images of 21 of the 45 galaxies with classic feathers. We subjected this "catalog" of 45 galaxies to more detailed examination of feather morphology and characteristics.

2.3.4.1 "Beads on a String"

As noted above, feathers are typically associated with star formation, particularly near where they emerge from the PDL and outer edge of a spiral arm. In 38 of the 45 galaxies with feathers, a series of bright OB associations and H II regions occur which fit the "beads on a string" description used by Piddington (1970) and Elmegreen (1980b). The 38 galaxies with this characteristic are noted in Table 2.3. Typically, the star formation that comprises the "beads" is associated with feathers: near the beginning of feathers, along the PDL; lining feathers, within the arm; and in the interarm, as components of spurs. Spurs themselves are observed as short chains of star formation jutting outward from spiral arms at large angles. For example, along the outer edge of the spiral arms in NGC 3631 (Figure 2.9) several regions of OB associations are aligned in chains that are the beginnings of interarm spurs Also present in the southern arm of NGC 3631 is a chain of OB associations along the PDL.

2.3.4.2 Evolution of Feathers to Spurs

In eleven galaxies, we observe spurs on the outside of spiral arms, in the interarm regions, in addition to the star formation seen along feathers within arms. Within these eleven galaxies (see Table 2.3) we find feathers that transition to spurs across the outer edge of the spiral arm (Figure 2.3), forming a composite feature. These feathers appear to evolve into spurs with star formation developing as gas flows downstream from the PDL. B88 and KO both predicted that spurs result from

feathers. KO's simulations follow the evolution of feathers through their fragmentation into self-gravitating clumps on the outer edge of a spiral arm. The observations are consistent with this picture.

2.3.4.3   Elongated Feathers

As mentioned in §2.3.1, we also observe many feathers which are not solely contained within the luminous part of the spiral arms. These extend into the interarm similar to spurs; presumably these elongated feathers are the gaseous counterpart to spurs. Twenty-nine galaxies listed in Table 2.3 have elongated feathers, which are sometimes dotted with H II regions. Typically, elongated feathers are swept back more sharply in the interarm regions than they are at the outer edge of the luminous arm. The decrease in pitch angle along elongated feathers is due to the large interarm shear referred to in §2.3.4.5.

In many cases, elongated feathers merge into a common interarm dust lane. In 15 galaxies, the farthest reaching feathers actually merge with the PDL of the next arm.

2.3.4.4   Lattice Structure

Another intriguing feather structure, present in 14 galaxies noted in Table 2.3, is a series of feathers that appear to link one or more pairs of PDLs, forming a lattice within a single spiral arm. An example of such a network of extinction features is in the northern arm of NGC 4579 (Figure 2.11) which includes several tiers of

dust lanes connected by feathers emerging from the previous row. These multiple tracks should not be confused with the cases of elongated feathers that span an entire interarm region and merge with the PDL of another arm. Lattices are most common in strongly barred galaxies, and absent in unbarred galaxies. In total there are nine SB galaxies and five SAB galaxies with lattices in one or more arms. B88 predicted that multiple tracks of feathers could form if the background flow was sufficiently unstable, allowing growth along both preferred directions, parallel and perpendicular to the spiral arm.

2.3.4.5 Shape of Feathers

The shape of a feather is a measure of the change in shear as gas passes through an arm. The pitch angles of feathers, as mentioned in § 2.3.1, vary with the phase of an arm. Near the outer edges of an arm, feathers are almost always predominately trailing features. Well-delineated cases show, however, that they originate as leading features from the PDL, which marks the inner edge of a spiral arm.

The feathers described by B88, as well as those evident in the KO local MHD and DB hydrodynamical simulations, have the same characteristic shape as observed feathers. In these cases, both observations and models, the feathers emerge at a large, leading angle with respect to a spiral arm, and the pitch angles decrease outward. The outer portions of feathers are curved back into trailing features presumably by strong interarm shearing.

Nearest to the spiral arm, the feathers produced in the WK hydrodynamic

simulations curve in the opposite sense to observed feathers (from trailing to lead-ing). Further downstream in the interarm region, however, their features become trailing. This curvature is likely due to the rising background rotation curve they adopt.[2] Further, although the arm-interarm density ratio is ~ 100, their models do not include self-gravity. The WK model assumes physical conditions rather different from those where feathers have been observed: the gaseous disks are differentially rotating, self-gravity is important, and the arm-interarm surface density ratios are ≈ 10. Thus the existing WK models are probably not relevant for observed feathers.

2.3.5 Feathers in the Spitzer 8 μm Band

We have discussed feathers as extinction features. Despite the identification of some elongated feathers and also the association with spurs discussed in § 2.3.4, extinction features can be difficult to trace where the background stellar density is low or where there is confusing foreground or embedded emission. Recently released Spitzer SINGS data (Kennicutt et al. 2005) enable us to examine nine galaxies[3] from our catalog in the IRAC 3.6–8 μm bands. These galaxies appear dramatically different

---

[2]If Ω is the local angular velocity, local wavevectors rotate counterclockwise wherever

$$\frac{\partial \ln \Omega}{\partial \ln R} > 0$$

and clockwise where it is less than zero. Since

$$\frac{\partial \ln \Omega}{\partial \ln R} = \left(1 + \frac{\partial \ln V_c}{\partial \ln R}\right)\frac{\Sigma}{\Sigma_o} - 2$$

where Σ is the local density and Σ_o is the mean density, a solid body rotation curve would imply trailing-to-leading curvature in any overdense ($\Sigma > \Sigma_o$) region.

[3]NGC 0628, 1566, 4254, 4321, 4579, 4725, 4736, 5055, and 5194

at 8 μm from their appearance at optical wavelengths. We observe that their 8 μm spiral arms have prominent, bright features that extend well into the interarm, referred to as "filaments" in NGC 5194 by Calzetti et al. (2005). Particularly striking are NGC 5194 and NGC 0628 (see Figure 2.15 and Figure 2.16 for IRAC 8 μm images).

The bright interarm features seen at 8 μm emerge from the spiral arms at large pitch angles. Downstream from the arms, their pitch angle decreases with distance from the spiral arm. Some of the 8 μm features span the entire interarm region and a few eventually merge with an outer arm, similarly to observed elongated feathers. The dark lines overlaid on the 8 μm images in Figure 2.15 and Figure 2.16 represent the location and length of feathers as measured in the HST image of the corresponding galaxy. There appears to be a correlation between the elongated feathers observed in the visible and the bright interarm regions seen at 8 μm.

The primary source of emission at 8 μm is thought to be polycyclic aromatic hydrocarbons (PAHs), which are excited nonthermally by single UV photons (Sellgren 1984). PAHs are found in diffuse atomic clouds and in photodissociation-regions (PDRs) surrounding molecular clouds, where they are excited or photodissociated by stellar UV radiation (e.g. van Dishoeck 2004). Since the extinction that makes feathers visible is due to dust associated with relatively dense interstellar gas, it is not surprising that feathers should be traced by PAH emission at 8 μm, as we observe.

2.3.6 Association of Feathers with Molecular Gas

As discussed in the previous section, 8 μm emission can be used to trace feathers into the interarms, where extinction features are more difficult to observe. However, it is difficult to extract reliable gas column density estimates from either dust extinction or 8 μm emission. Dust extinction depends on the unknown distribution of dust relative to illuminating stars. How are the stars distributed above and below the dust clouds? Is the dust layer homogeneous or clumped? What is the dust emissivity and the dust to gas ratio? Quantitative extraction of gas column density from 8 μm emission has some of the same limitations, and also requires understanding of heating, formation, and destruction of PAHs. By contrast, interpretation of CO(1-0) emission is perhaps more straightforward, although it too has limitations. In this section, we evaluate the association of feathers with molecular gas emission as traced by CO(1-0) emission. Good observations are available for several galaxies from the BIMA SONG catalogue (Regan et al. 2001; Helfer et al. 2003).

In Figures 2.15 and 2.16 we show the locations of feathers (traced by lines) overlaid on maps of velocity-integrated CO(1-0) emission in NGC 0628 and NGC 5194. The figures show remarkable agreement between the location of CO(1-0) peaks and the intersection of feathers with their PDL. Most feathers are very clearly associated with CO(1-0) peaks and nearly all other feathers are plausibly associated with CO(1-0) peaks. In fact, along the arms the correspondence is nearly one to one: nearly all CO(1-0) peaks are associated with feathers. It should be noted that initially we drew the feather lines without reference to the CO(1-0) maps and later

noted the close association. For a few feathers, the precise location of the feather becomes unclear near the PDL owing to confusion from emission from massive star-forming regions. In these cases, we found that a straight-line extrapolation of the feather inward intersected the PDL slightly inward from the nearest CO(1-0) peak; if instead we assumed a curvature similar to neighboring feathers, the line intersected the PDL close to the CO(1-0) peak. For this small subset of feathers, we drew the line to have similar curvature and to intersect the CO(1-0) peak.

The coincidence between CO(1-0) peaks and the "base" of feathers is interesting, because it associates feathers with the highest gas surface density concentrations in the galaxy disk. It therefore connects the feather phenomenon with much of the star formation in the galaxy disk.

For some of the CO(1-0) peaks, we see weak extensions in CO(1-0) emission toward the outside of the arm along the feather. The dynamic range of the CO(1-0) map is limited; nonetheless for the stronger CO(1-0) peaks it is clear that the gas column density of feathers rapidly decreases by at least a factor of 5–10 with distance from the PDL. Thus, contrary to the impression given by both the dust extinction maps and the 8 μm Spitzer maps, CO(1-0) maps show that the gas column density of feather features is by far the highest at the PDL. Although it is conceivable that the CO(1-0) emissivity is higher in the arm, it is unlikely to vary by a factor of ten. The large enhancement in feather column density near the arm clearly pinpoints the PDL as the point of origin of the feather. Shear and divergent flow stretch out the condensations as the gas flows out of the arm. While the molecular gas is strongly peaked at the PDL, star formation (as traced by Hα and 24 μm tends to be more

distributed along the feather *downstream* of the PDL.

2.3.7   Feather Spacing and Gas Surface Density

It is clear from inspection of the HST images that the spacing between feathers
tends to increase with galactocentric radius, as can be seen for example in Fig-
ures 2.15 and 2.16. This might be related to the gas surface density, which generally
decreases with distance from the nucleus, and so it is interesting to compare feather
spacings with gas column density. We made this comparison for two galaxies with
both extensive feathers and good CO(1-0) maps, NGC 0628 and NGC 5194. For
this comparison we used the BIMA SONG CO(1-0) velocity-integrated maps, and
sampled the CO(1-0) maps along the PDLs of each spiral arm at $3''$ spacings (half
beam width). We then estimated the H_2 column densities using the relation

$$N_{H_2} = 2.2 \times 10^{20} \left(\frac{I_{CO}}{K \text{ km s}^{-1}} \right) \text{ cm}^{-2},$$

(Strong et al. 1988). The corresponding molecular surface density at each point is
then

$$\Sigma_{H_2} = 2.17 \times 10^{-20} N_{H_2} \cos i \quad M_\odot \text{ pc}^{-2}.$$

Noting that the gas surface densities are significantly lower in NGC 0628 than NGC
5194, we included azimuthally averaged Hi data (Shostak & van der Kruit 1984)
to obtain a lower limit on the total gas surface density. The radial atomic surface
density is

$$\Sigma_{\mathrm{H_I}} = 1.08 \times 10^{-20} N_{\mathrm{H_I}} \cos i \quad M_\odot \ \mathrm{pc}^{-2}$$

and the *total* gas surface density is $\Sigma_{\mathrm{gas}} = \Sigma_{\mathrm{H_2}} + \Sigma_{\mathrm{H_I}} \quad M_\odot \ \mathrm{pc}^{-2}$.

We plot (see Figures 2.19 and 2.20) the gas surface density versus the *deprojected* distance along the arms in both galaxies using the HST ACS image of NGC 5194 (larger FOV than WFPC2) and the HST WFPC2 image of NGC 0628. Also shown at the bottom of each figure are ticks marking the location of feathers along the arms.

In NGC 5194, the surface density rises from the beginning of both arms, peaking near a galactocentric radius of 1 kpc. Thereafter, the surface density generally declines, although there are significant fluctuations. Note that in the inner 1–2 kpc the peaks in Arm 1 tend to be higher (sometimes by a factor of two), but at larger radii Arm 2 peaks sometimes have higher surface density. Overall, it can be seen that the spacing between feathers increases as the surface density decreases along each arm, and that the feathers generally coincide with the gas column density peaks.

NGC 0628 also exhibits a general decline in surface density with radius although there are significant peaks at larger radii. As in NGC 5194, generally feather spacing increases and gas column density decreases as one moves out along the arm. However, the gas surface densities are lower by at least a factor of three compared to NGC 5194; the peak surface density in NGC 5194 is at least an order of magnitude higher.

The increase in feather spacing with decreasing gas surface density along a spiral arm and the association of feathers and gas surface density peaks evident in Figures 2.19 and 2.20 suggest a gravitational instability, such as the Jeans instability. To investigate this further, we estimated the Jeans length as

$$\lambda_{Jeans} = c_s^2/(G\Sigma),$$

where c_s is the effective sound speed. We adopt $c_s = 7$ km s^{-1} for both NGC 0628 and NGC 5194.

Figure 2.21 shows the feather separations and Jeans lengths, along with their ratio as a function of distance along each arm in NGC 5194. Figure 2.22 shows the same quantities for NGC 0628. Noticing that feathers tend to "clump" together in groups, with larger distances separating the groups than the average distance between the feathers within a group, we averaged the separations, Jeans length, and ratios separately for each group. For NGC 5194, it can be seen that the feather spacing increases from ∼200 pc in the inner galaxy to 500–1000 pc in the outer galaxy. Since the Jeans length increases by a similar factor, the ratio of separation to Jeans length does not exhibit a radial trend. NGC 0628 also shows evidence for some increase in feather spacing with galactocentric radius, while the ratio of separation to Jeans length is relatively flat.

While the feather spacings in NGC 0628 and NGC 5194 are roughly similar, the measured ratio of feather spacing to Jeans length is a factor of 4–6 higher in NGC 5194 and differs between its arms. The lower ratios in NGC 0628 are probably

due in part to the greater fraction of gas in NGC 0628 likely being in atomic form. Although we have included azimuthally averaged H I (Shostak & van der Kruit 1984) to calculate the total gas surface density, the H I data are at low resolution ($13.8''$x $48.5''$), and therefore the column densities are lower limits. In NGC 5194, the addition of H I is not a problem since the gas is overwhelmingly molecular, but in NGC 0628 the unresolved H I column density could be substantial. Another factor lowering the measured ratio is that a significant fraction of the CO(1-0) flux is likely undetected in NGC 0628, owing to low signal to noise (Helfer et al. 2002, 2003). Thus, while the peaks and radial trends observed for NGC 0628 are credible, the magnitudes of the Jeans length and ratio are probably only useful for NGC 5194.

We also measured the separation of feathers in NGC 3433 and NGC 5985, Figure 2.8 and Figure 2.12. As in NGC 0628 and NGC 5194, both galaxies display a trend of increasing separation along an arm. In NGC 3433, the average separation along Arm 1 is 310 pc between 0.9 kpc and 2.9 kpc galactocentric radius. For Arm 2, the average is 380 pc between 1.5 kpc and 1.6 kpc and 430 pc between 2.7 kpc and 7.1 kpc. In NGC 5985, the average separation along Arm 1 is 445 pc between 3.7 kpc and 5.1 kpc. For Arm 2, the average is 770 pc between 3.0 kpc and 3.1 kpc.

It would of course be interesting to measure and characterize the typical feather spacing in more galaxies. However, either due to the quality of observations, the complexity of extinction substructure, or the contamination due to star formation, most of the images did not lend themselves to reliable estimates of feather spacings. As we have shown, molecular gas offers a non-extincted, less-confused tracer of feathers. Therefore, separation measurements using CO(1-0) observations with

CARMA and ALMA may yield better estimates in more galaxies.

Feather spacings found in NGC 0628 and NGC 5194 are typically larger than the 100–200 pc range predicted by WK. DB predicted feather spacings of 700 pc; such large spacings are only seen in the outer part of Arm 2 in NGC 5194. We note that DB and WK did not include self-gravity in their calculation; particularly in NGC 5194, the observed gas densities are comparable or larger the stellar surface densities, indicating that self-gravity is likely important.

KO and Kim & Ostriker 2006 predicted the characteristic spacing of feathers to be up to 7–10 times the local Jeans length for their magnetized models, which are stable to quasi-axisymmetric modes. For models which are unstable to quasi-axisymmetric modes, the arms do not have a well-defined "pre-fragmentation" surface density, but the feather spacings are in general smaller. The range in ratios of feather spacing to Jeans length observed in NGC 5194 centers on the values of 7–10 predicted by KO. This, along with the increase in feather spacing with decreasing gas surface density and the correlation between the location of feathers and gas surface density peaks, is consistent with the view that feathers form via a gravitational instability.

2.4   Conclusions

We find extinction feathers in nearly 20% of 233 spiral galaxies. We show that feathers are most common in Sb–Sc galaxies; Sb–Sc galaxies in which we did not detect feathers either had poor quality images, or flocculent or complex structure. Feathers

are rare in Sa galaxies and undetected in Scd–Sd galaxies. The presence of feathers is closely tied to the existence of a primary dust lane (PDL). The probability of detecting feathers increases with PDL delineation; the highest being 83% for spirals with well-delineated PDLs, within which feathers are ubiquitous. Characteristically, feathers: (1) are associated with bright star forming regions within spiral arms and interarm regions; (2) extend beyond the outer edge of spiral arms, sometimes far into interarm regions, and merging with the PDL of another arm; (3) transition or evolve into stellar spurs; and (4) often form lattice structures or multiple rows of feathers within a single spiral arm in barred galaxies. Furthermore, we find that the spacing of feathers is related to the molecular surface density along spiral arms; (1) typically, the distance between feathers increases as the molecular surface density decreases and (2) the majority of feathers originate in regions of higher gas surface density. The mean separation of feathers is $1.7\lambda_{Jeans}$ and $10.4\lambda_{Jeans}$ in NGC 0628 and NGC 5194; the value for NGC 0628 is likely an underestimate due to poor signal to noise and a lower limit of H I data. The above observable characteristics are consistent with models in which feathers are produced by local gravitational instabilities (i.e. Jeans or magneto-Jeans instability) in the gas.

Table 2.1.   Delineation of Primary Dust Lanes and Frequency of Feather Detection

Primary Dust Lane Delineation	# of Galaxies	# of Galaxies with Feathers	% with Feathers
Poor	142	4	3%
Fair	46	12	26%
Good	35	29	83%
Total	223	45	20%

Table 2.2.   Properties of the 45 Galaxies with Clearly Delineated Feathers

Galaxy	Figure Number	Type	Incl. (deg)	PA (deg)	B_T (mag)	CZ (km s^{-1})	Arm Class (EE)
IC 2056		RSABRbc*	34	8	12.48	1099	
NGC 0214	2.5	SABRbc	42	35	12.86	4495	9
NGC 0289		SBTbc	45	130	11.72	1690	12
NGC 0488		SARb	42	15	11.15	2233	3
NGC 0613		SBTbc	41	120	10.73	1510	9
NGC 0628	2.2, 2.4	SASc	24	25	10.01	632	9
NGC 0986		SBTab	41	150	11.64	1994	
NGC 1241	2.5	SBTb	53	140	12.64	3939	4
NGC 1300	2.6	SBTbc	49	106	11.11	1592	12
NGC 1365	2.5	SBSb	57	32	10.23	1675	12
NGC 1512		SBRa	51	90	11.13	735	6
NGC 1566	2.7	SABSbc	37	60	10.13	1449	12
NGC 1667		SABRc	39		12.77	4587	
NGC 2207		SABTbcP	50	141		2728	5
NGC 2336	2.7	SABRbc	57	178	11.26	2205	9
NGC 2339	2.8	SABTbc	41	175	11.98	2361	5
NGC 2997		SABTc	41	110	10.06	1090	9
NGC 3177	2.8	SATb	36	135	12.9	1220	6
NGC 3433	2.8	SASc	27	50	12.29	2591	9
NGC 3631	2.9	SASc	17		11.05	1143	9
NGC 3783		PSBRab	27			2926	9
NGC 4030		SASbc	44	27		1449	9
NGC 4254	2.9	SASc	29		10.17	2453	9
NGC 4303		SABTbc	27		10.18	1607	9
NGC 4321	2.10	SABSbc	32	30	10.26	1579	12
NGC 4394		RSBRb	27		11.73	772	6
NGC 4548	2.10	SBTb	37	150	11.04	498	5
NGC 4579	2.11	SABTb	37	95	10.68	1627	9
NGC 4593		RSBTb	42			2662	5
NGC 4647		SABTc	37	125	11.94	1421	3
NGC 4725		SABRabP	45	35	10.11	1180	6
NGC 4736	2.11	RSARab	36	105	8.99	297	3
NGC 5055	2.12	SATbc	55	105	9.57	516	3
NGC 5194	2.1, 2.3	SASbcP	24	170	9.08	463	12
NGC 5236	2.13	SABSc	27		8.31	503	9
NGC 5248		SABTbc	44	110	10.97	1189	12
NGC 5383		PSBTb*P	32	85	12.05	2226	12
NGC 5427		SAScP	32		11.93	2645	9
NGC 5643		SABTc	29		10.74	1163	
NGC 5970		SBRc	48	88	12.24	2063	9
NGC 5985	2.12	SABRb	58	13	11.67	2467	9
NGC 6753		RSARb	29	30	11.97	3142	8
NGC 6814		SABTbc	21		12.06	1509	9
NGC 6890	2.14	SATb	37	152	13.05	2471	

Table 2.2 (cont'd)

Galaxy	Figure Number	Type	Incl. (deg)	PA (deg)	B_T (mag)	CZ (km s^{-1})	Arm Class (EE)
NGC 7392		SASbc	54	123	12.62	2908	5

Table 2.3.   Feather Characteristics

Galaxy	Figure Number	Feather[a] ⇒ Spur	"Beads on a String"	Elongated Feathers	Lattice of Feathers
IC 2056			x		x
NGC 0214	2.5		x	x	
NGC 0289				x	x
NGC 0488				x	
NGC 0613			x		
NGC 0628	2.2, 2.4		x	x	
NGC 0986		x	x	x	x
NGC 1241	2.5		x		
NGC 1300	2.6	x	x	x	x
NGC 1365	2.5		x		x
NGC 1512			x	x	x
NGC 1566	2.7	x	x	x	
NGC 1667			x	x	
NGC 2207			x		
NGC 2336	2.7		x	x	
NGC 2339	2.8				
NGC 2997			x		
NGC 3177	2.8		x	x	
NGC 3433	2.8	x	x	x	
NGC 3631	2.9	x	x	x	
NGC 3783			x	x	
NGC 4030			x		
NGC 4254	2.9	x	x	x	
NGC 4303			x		
NGC 4321	2.10		x		
NGC 4394				x	x
NGC 4548	2.10		x	x	x
NGC 4579	2.11			x	x
NGC 4593			x		x
NGC 4647			x	x	
NGC 4725		x	x	x	
NGC 4736	2.11		x	x	
NGC 5055	2.12				
NGC 5194	2.1, 2.3	x	x	x	
NGC 5236	2.13	x	x	x	x
NGC 5248			x		
NGC 5383			x		x
NGC 5427		x	x	x	
NGC 5643			x		x
NGC 5970			x	x	
NGC 5985	2.12	x	x	x	x
NGC 6753			x	x	
NGC 6814				x	
NGC 6890	2.14		x		

Table 2.3 (cont'd)

Galaxy	Figure Number	Feather[a] ⇒ Spur	"Beads on a String"	Elongated Feathers	Lattice of Feathers
NGC 7392			x	x	

[a]Galaxies within which we identified feathers transitioning into spurs.
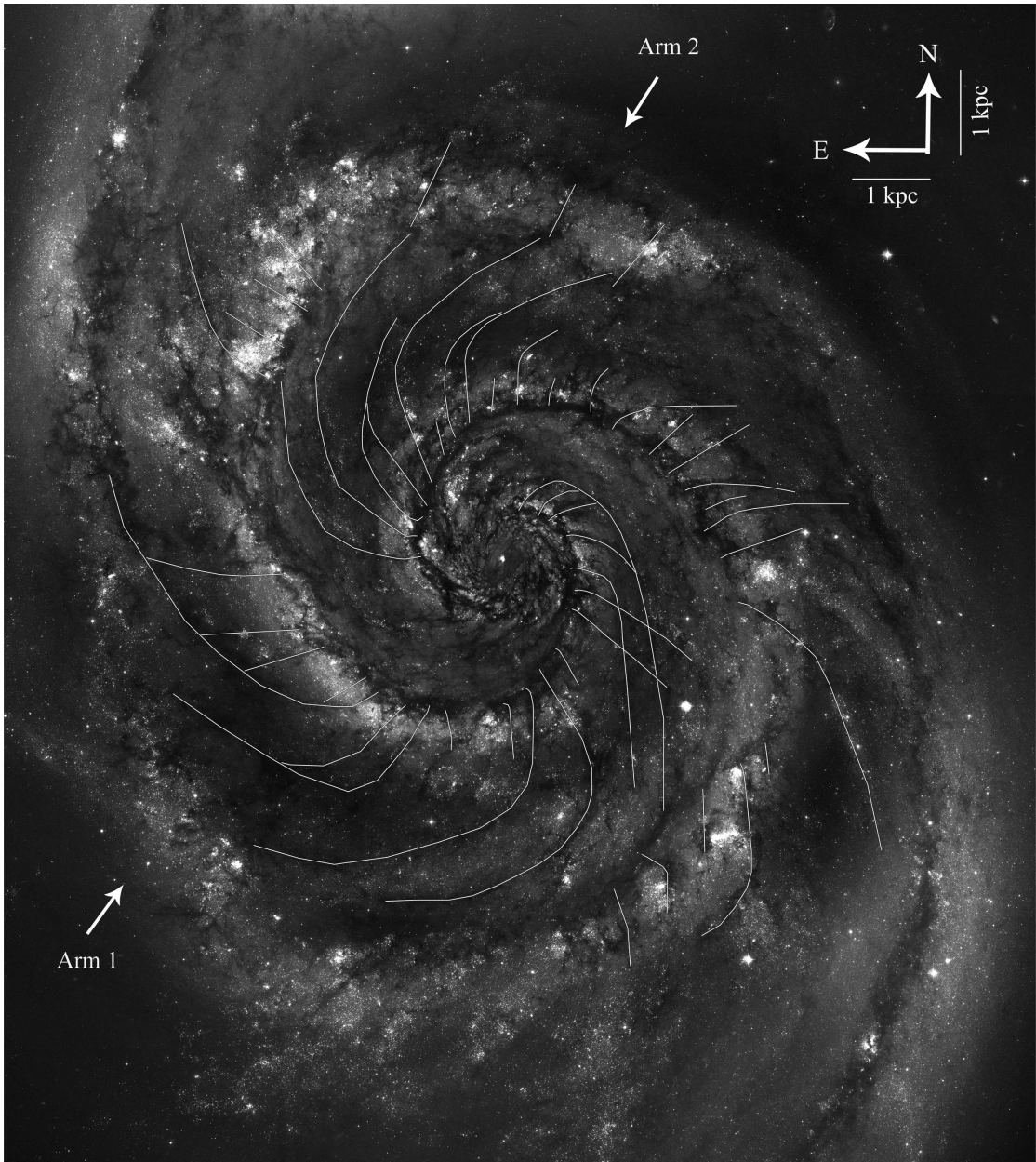
Figure 2.1 A prototypical galaxy with feathers, NGC 5194. Feathers are marked by white lines.
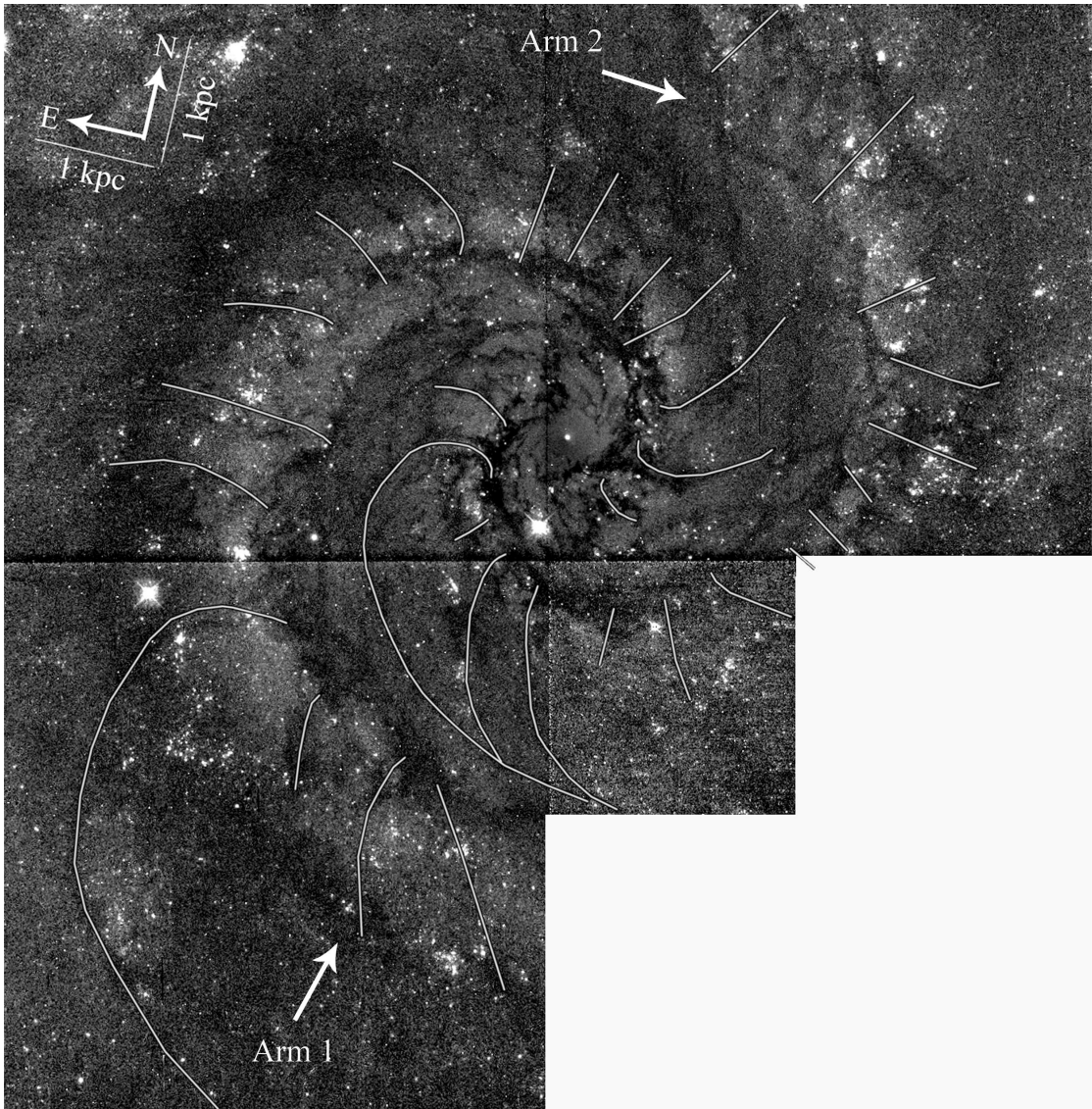
Figure 2.2 A prototypical galaxy with feathers, NGC 0628. Feathers are marked by white lines.
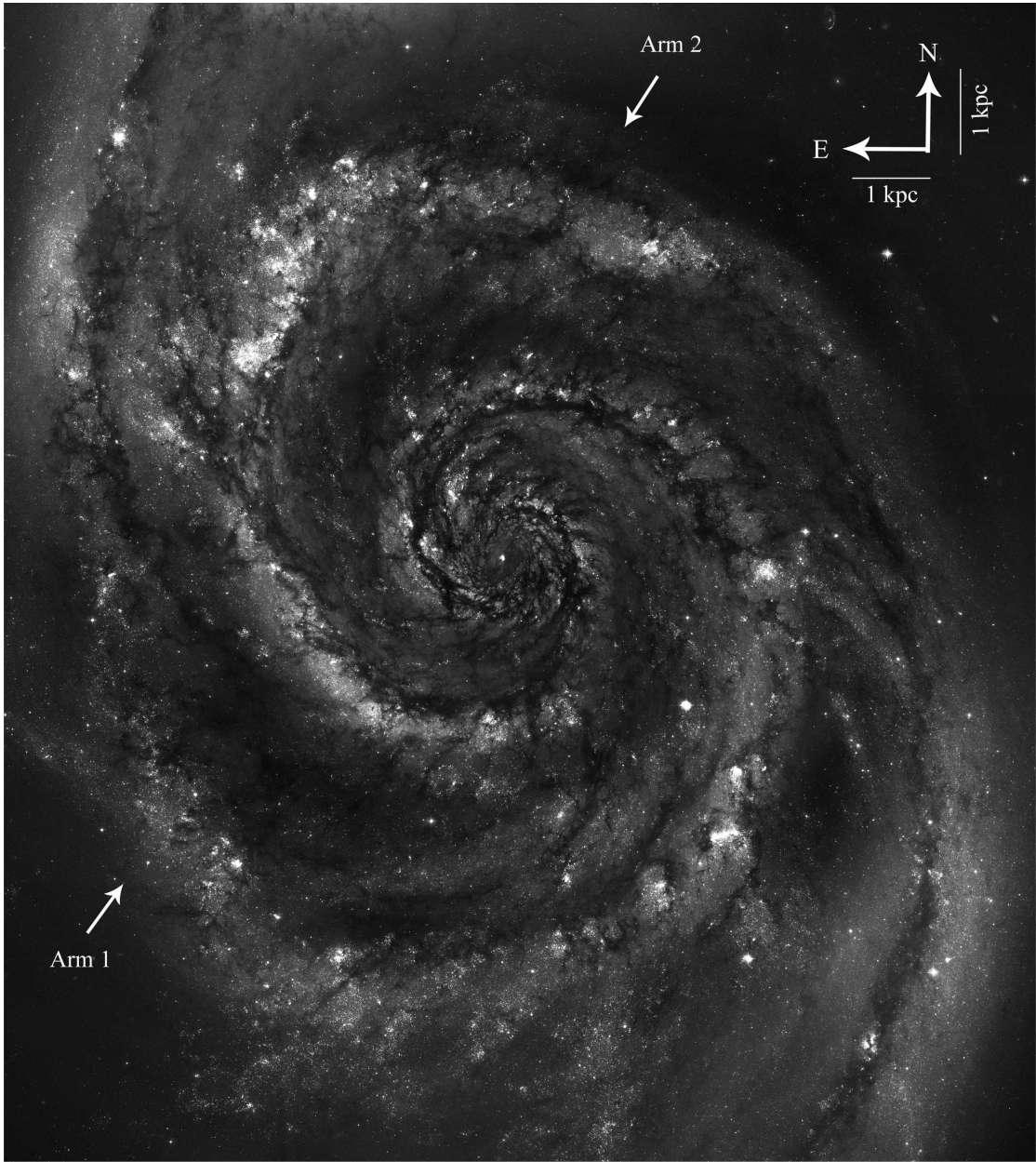
Figure 2.3 NGC 5194, with the feather overlay omitted.
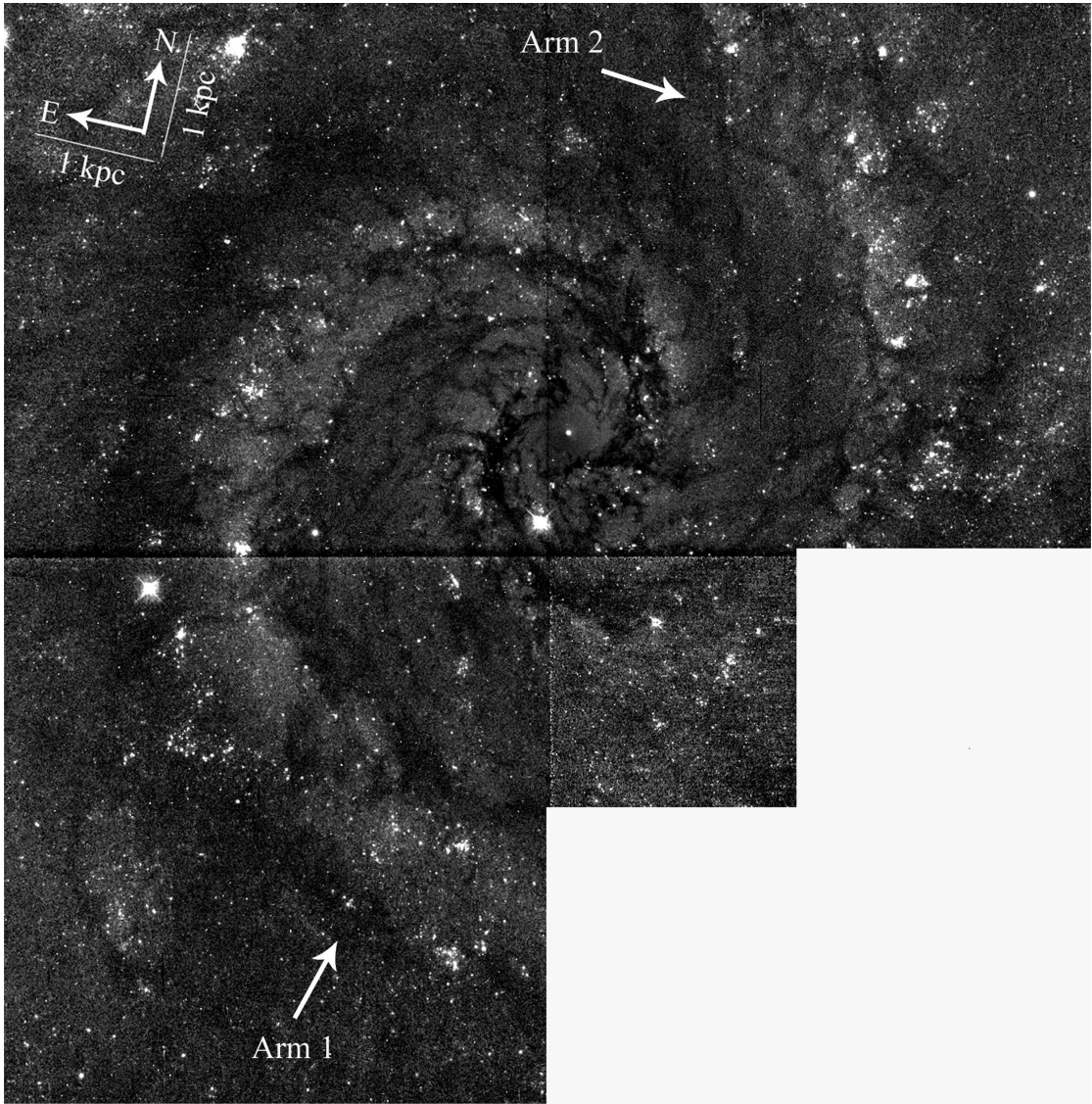
Figure 2.4 NGC 0628, with the feather overlay omitted.
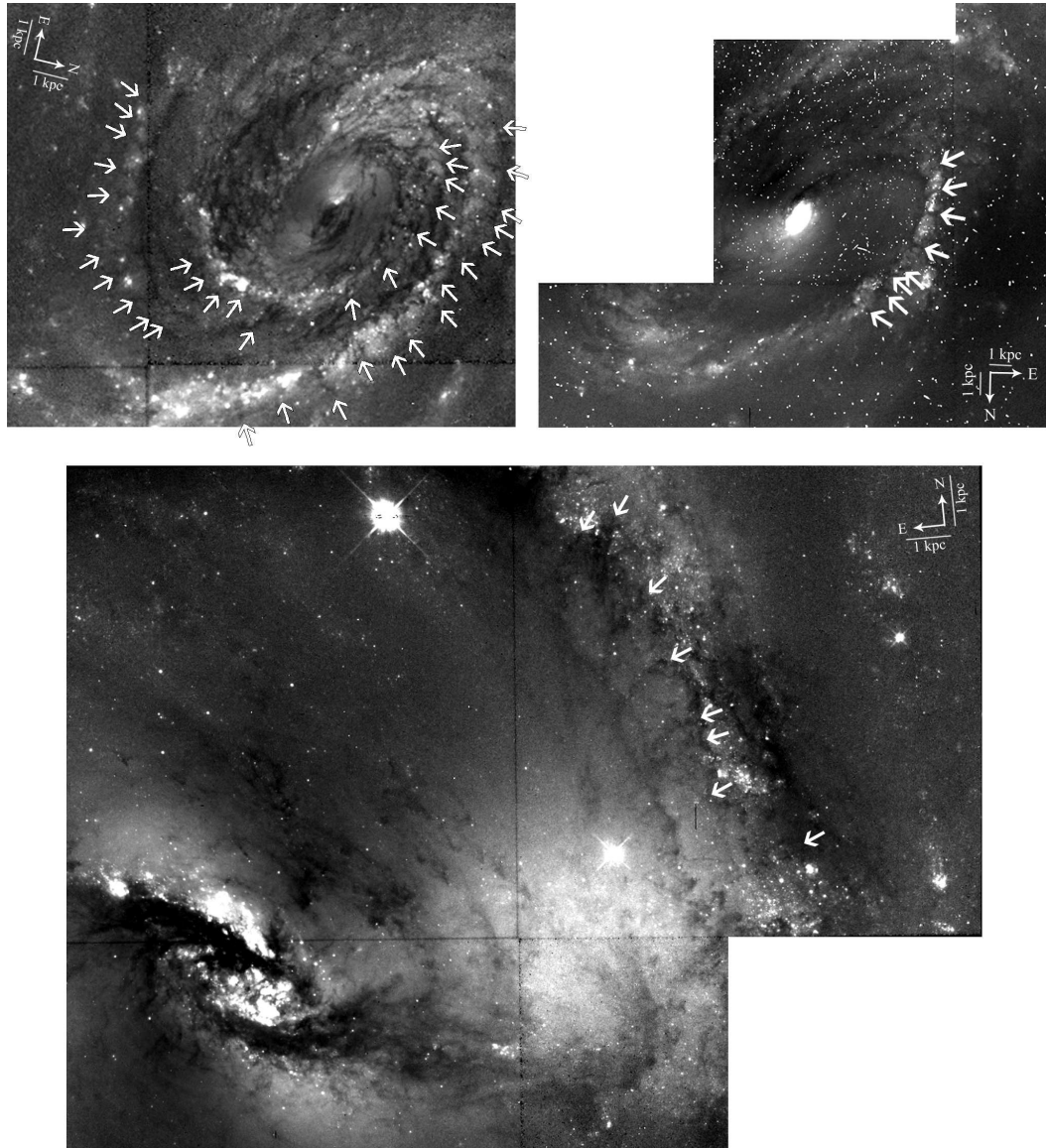
Figure 2.5 *Top left*: NGC 0214, *Top right*: NGC 1241, *Bottom*: NGC 1365. The white arrows mark identified feathers.
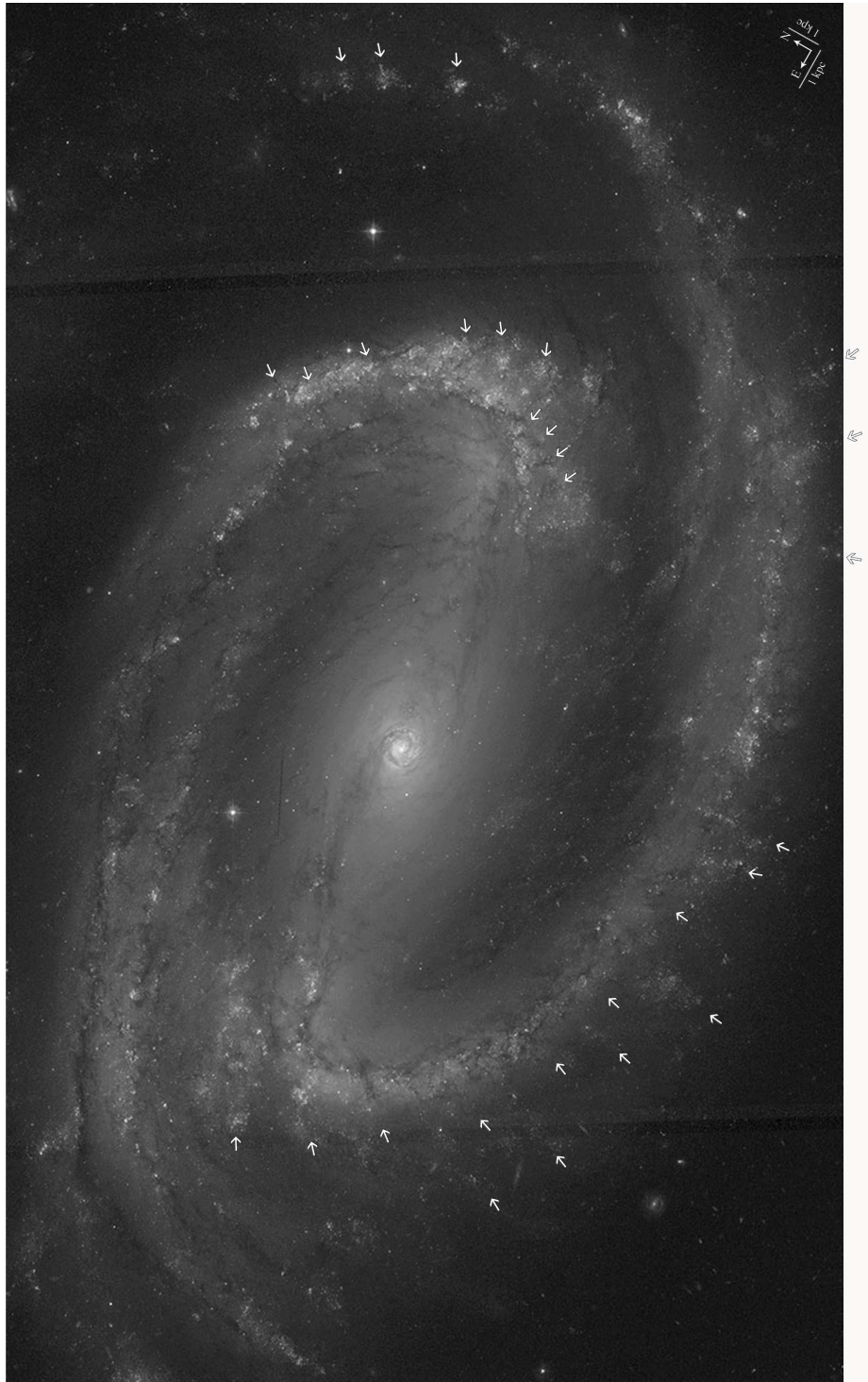
Figure 2.6 Image: NGC 1300. The white arrows mark identified feathers.
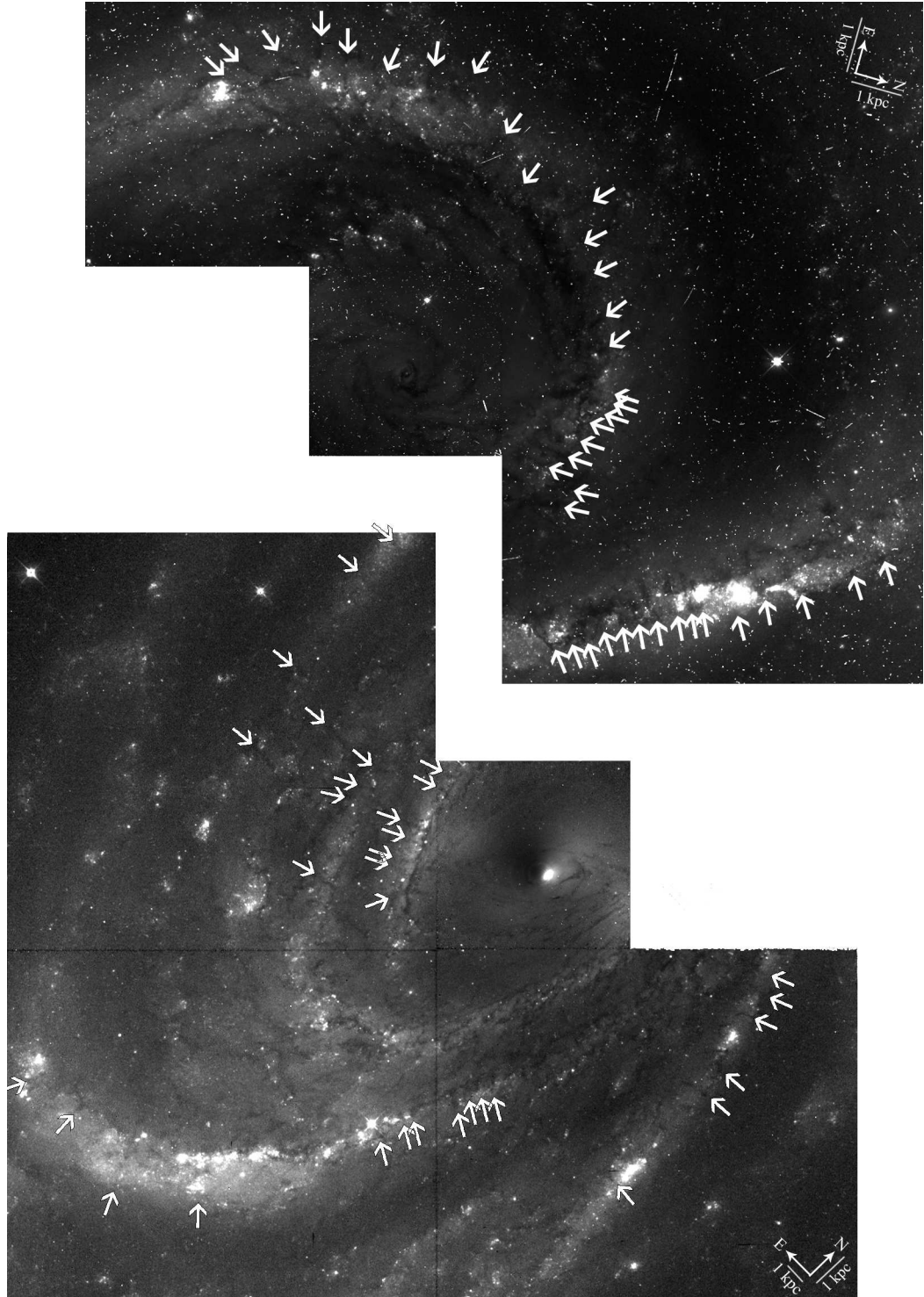
Figure 2.7 *Top*: NGC 1566, *Bottom*: NGC 2336. The white arrows mark identified feathers.
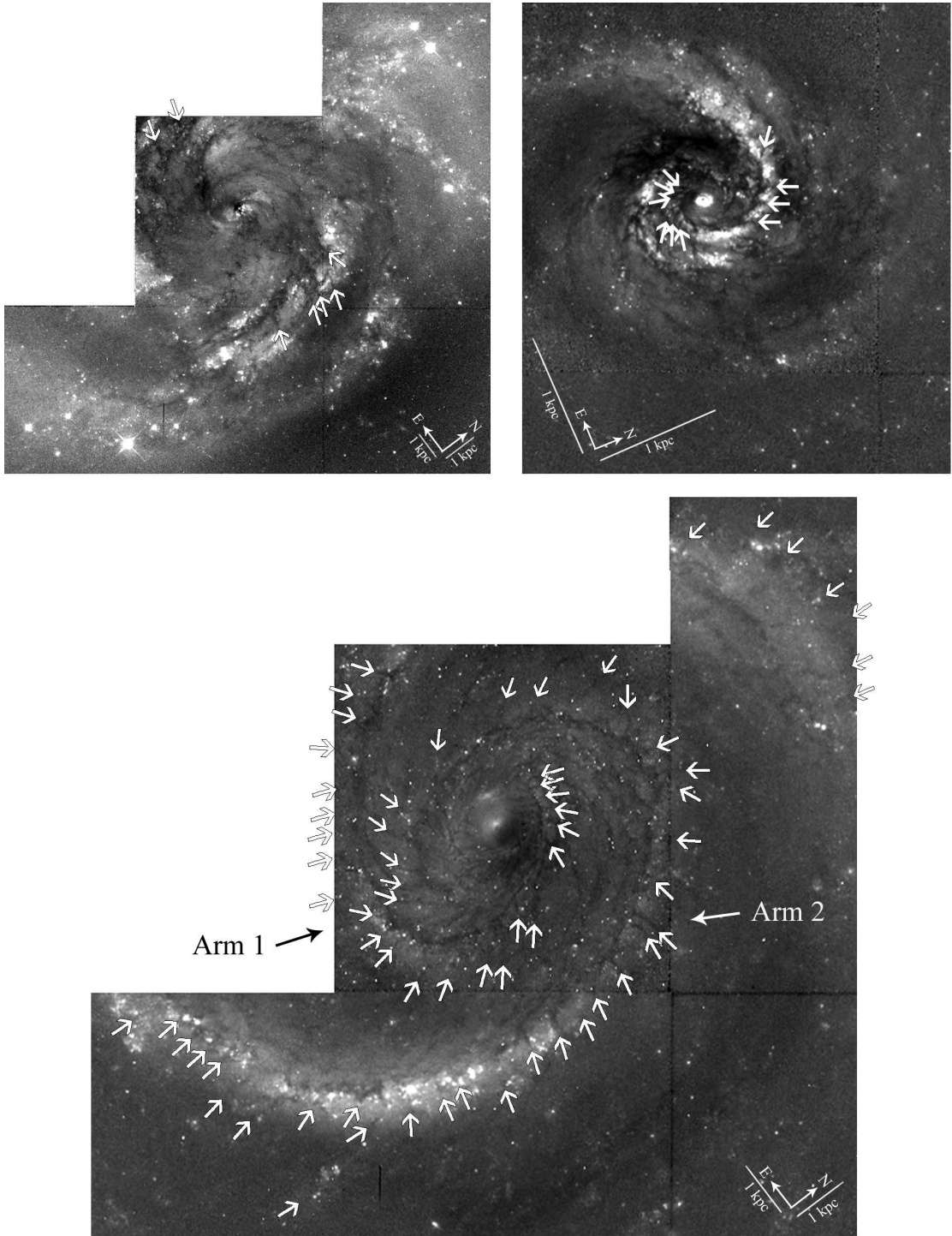
Figure 2.8 *Top left*: NGC 2339, *Top right*: NGC 3177, *Bottom*: NGC 3433. The white arrows mark identified feathers.
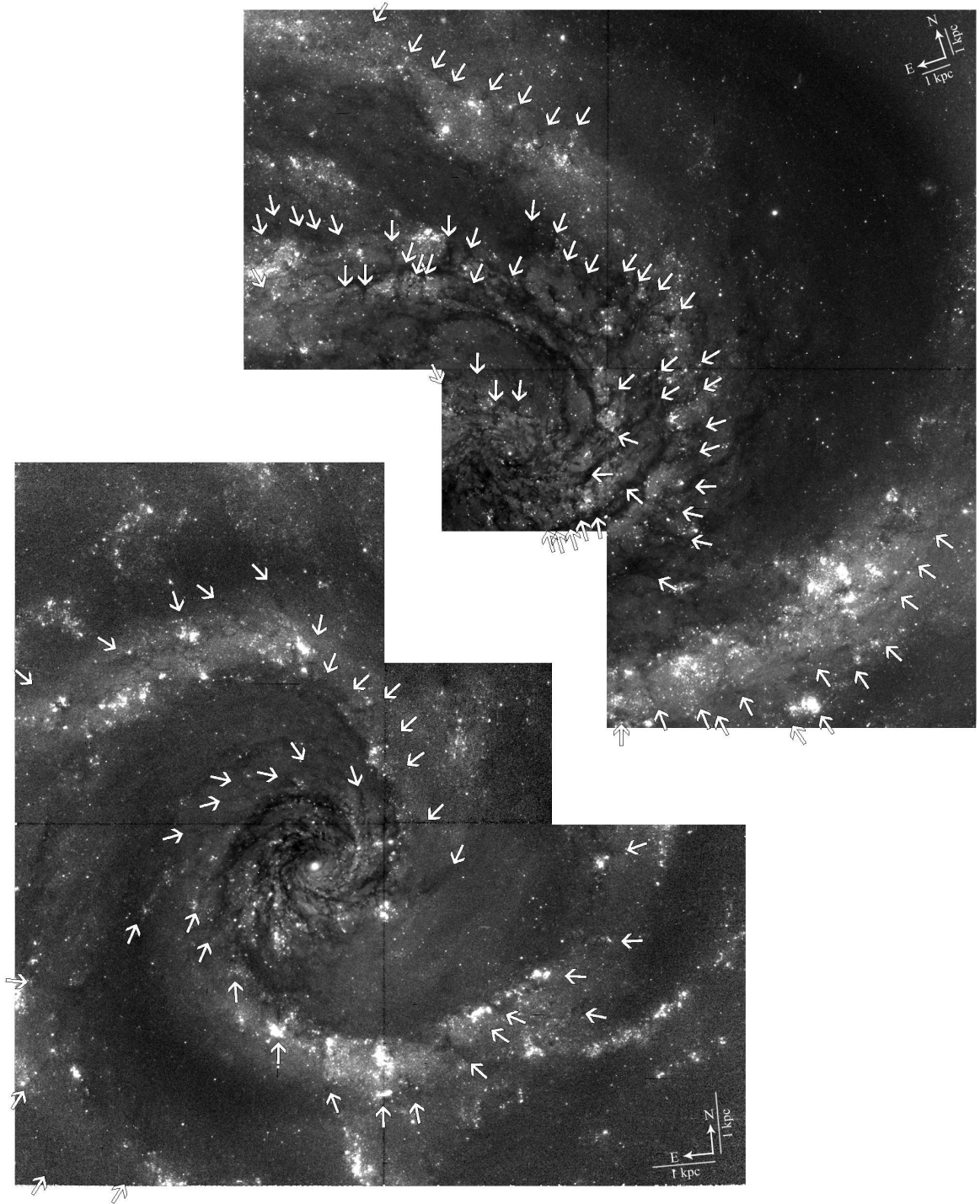
Figure 2.9 *Top*: NGC 4254, *Bottom*: NGC 3631. The white arrows mark identified feathers.
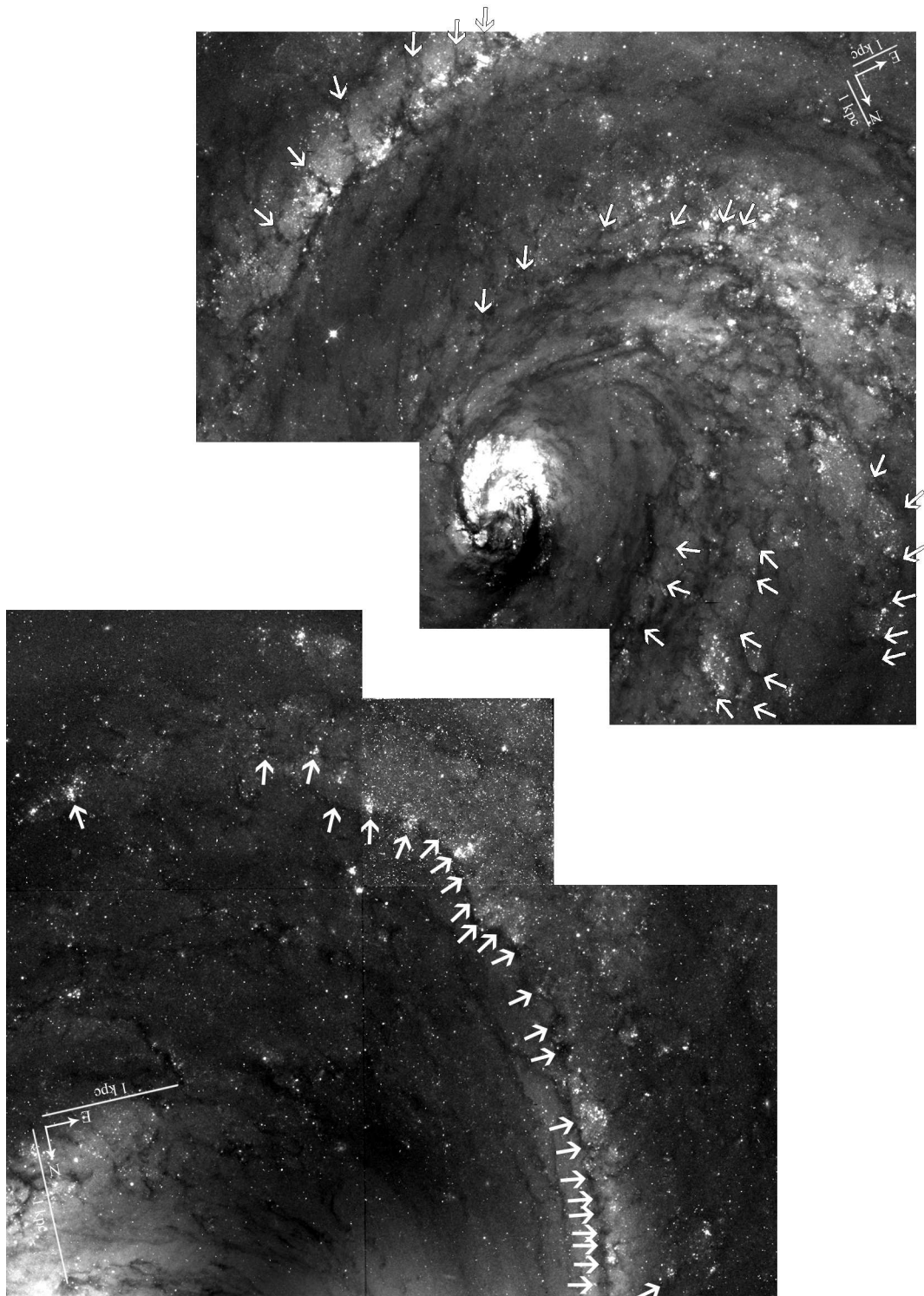
Figure 2.10 *Top*: NGC 4321, *Bottom*: NGC 4548. The white arrows mark identified feathers.
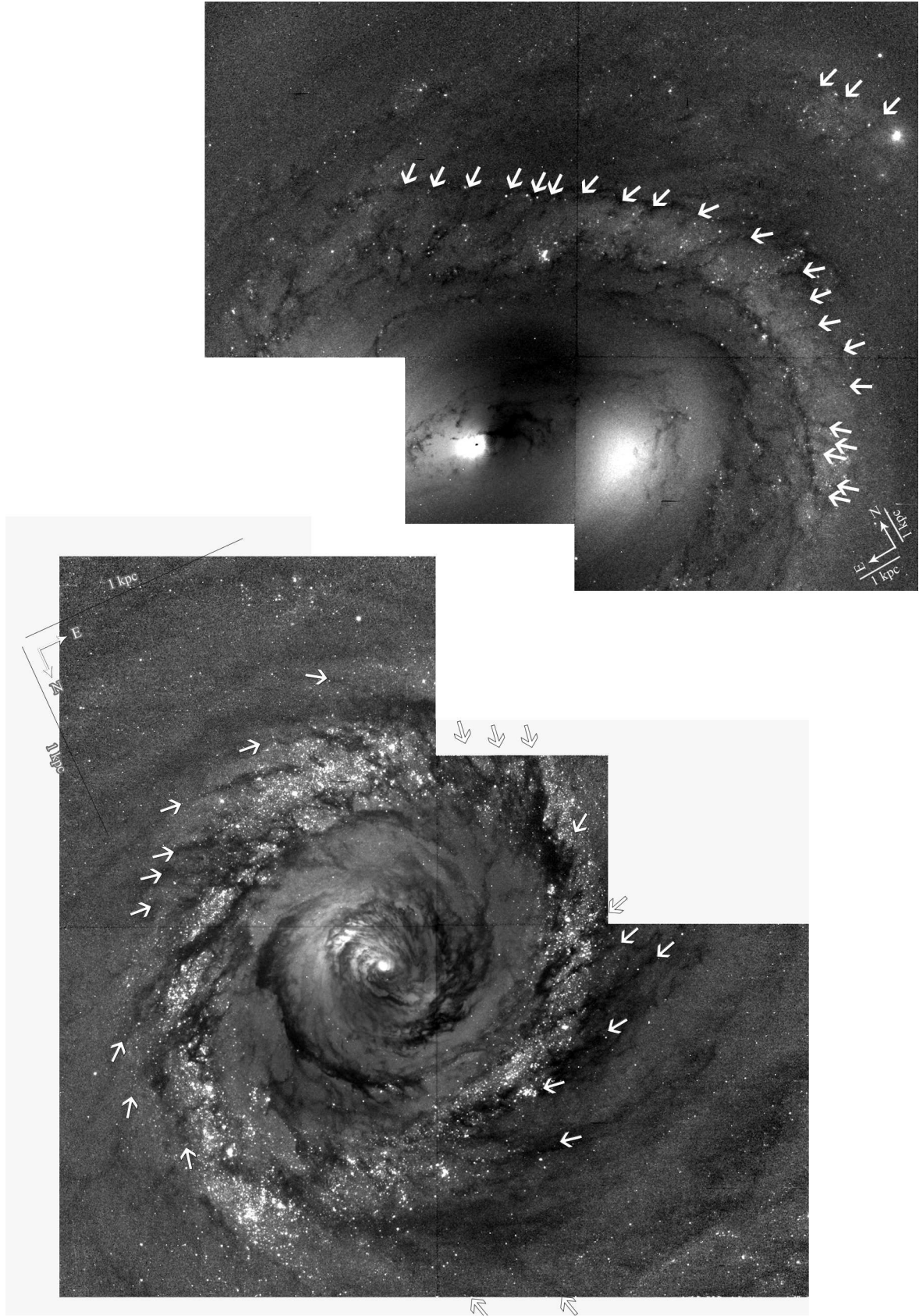
Figure 2.11 *Top*: NGC 4579, *Bottom*: NGC 4736. The white arrows mark identified feathers.
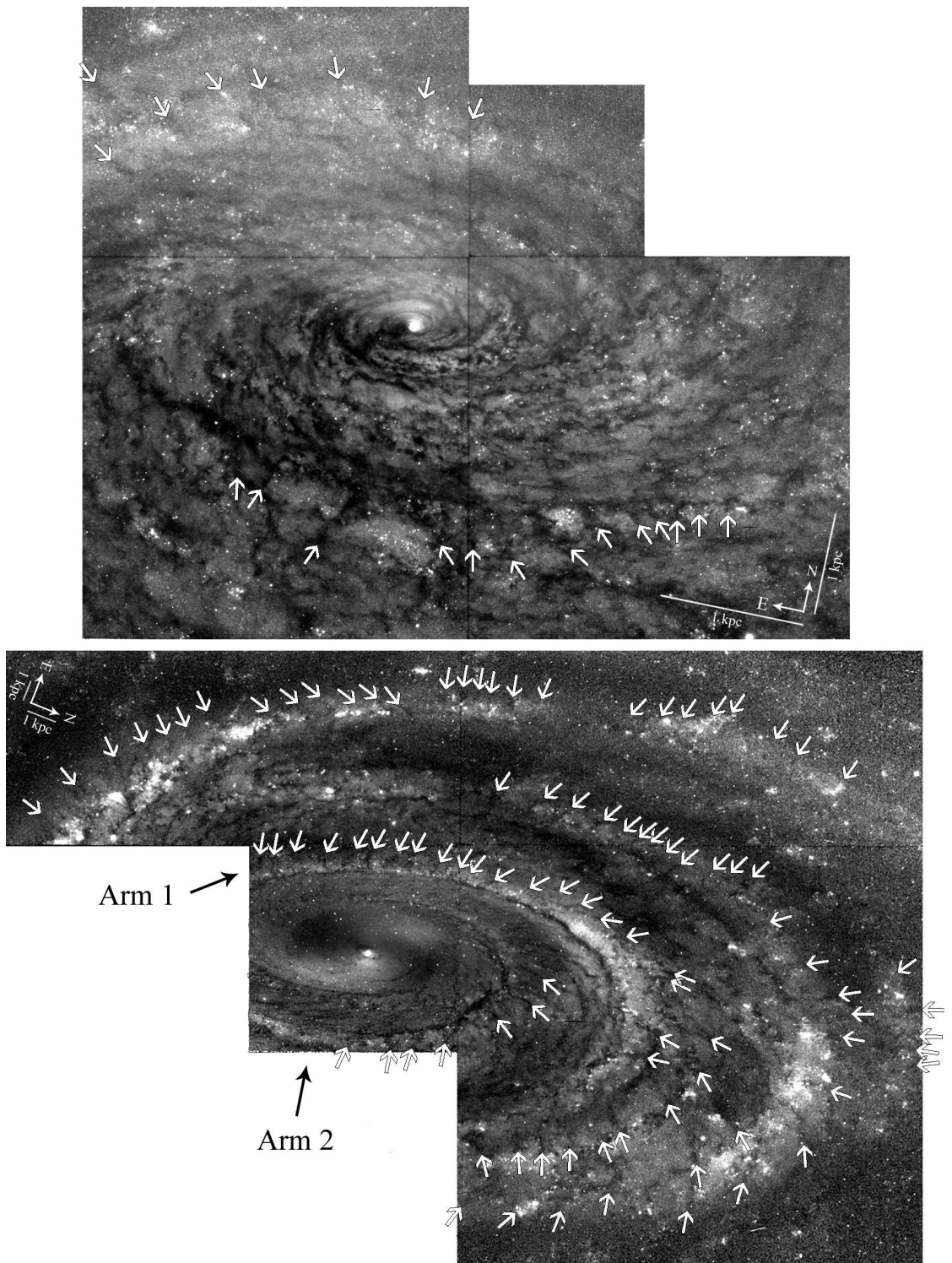
Figure 2.12 *Top*: NGC 5055, *Bottom*: NGC 5985. The white arrows mark identified feathers.

Figure 2.13 Image: NGC 5236 (Larsen and Richtler 1999). The white arrows mark identified feathers.
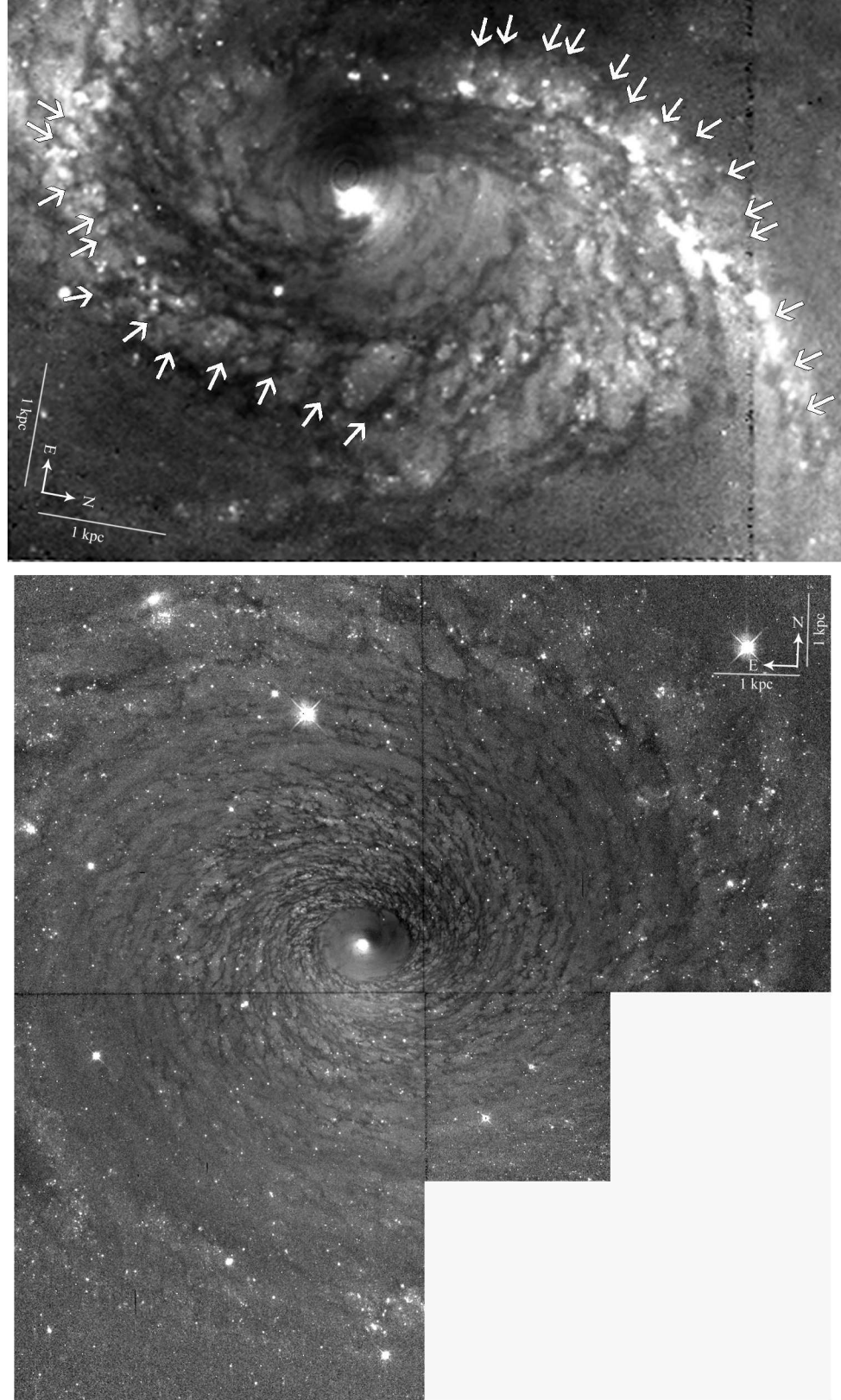
Figure 2.14 *Top*: NGC 6890, the white arrows mark identified feathers. *Bottom*: NGC 7217, an example of a galaxy with flocculent feathers.
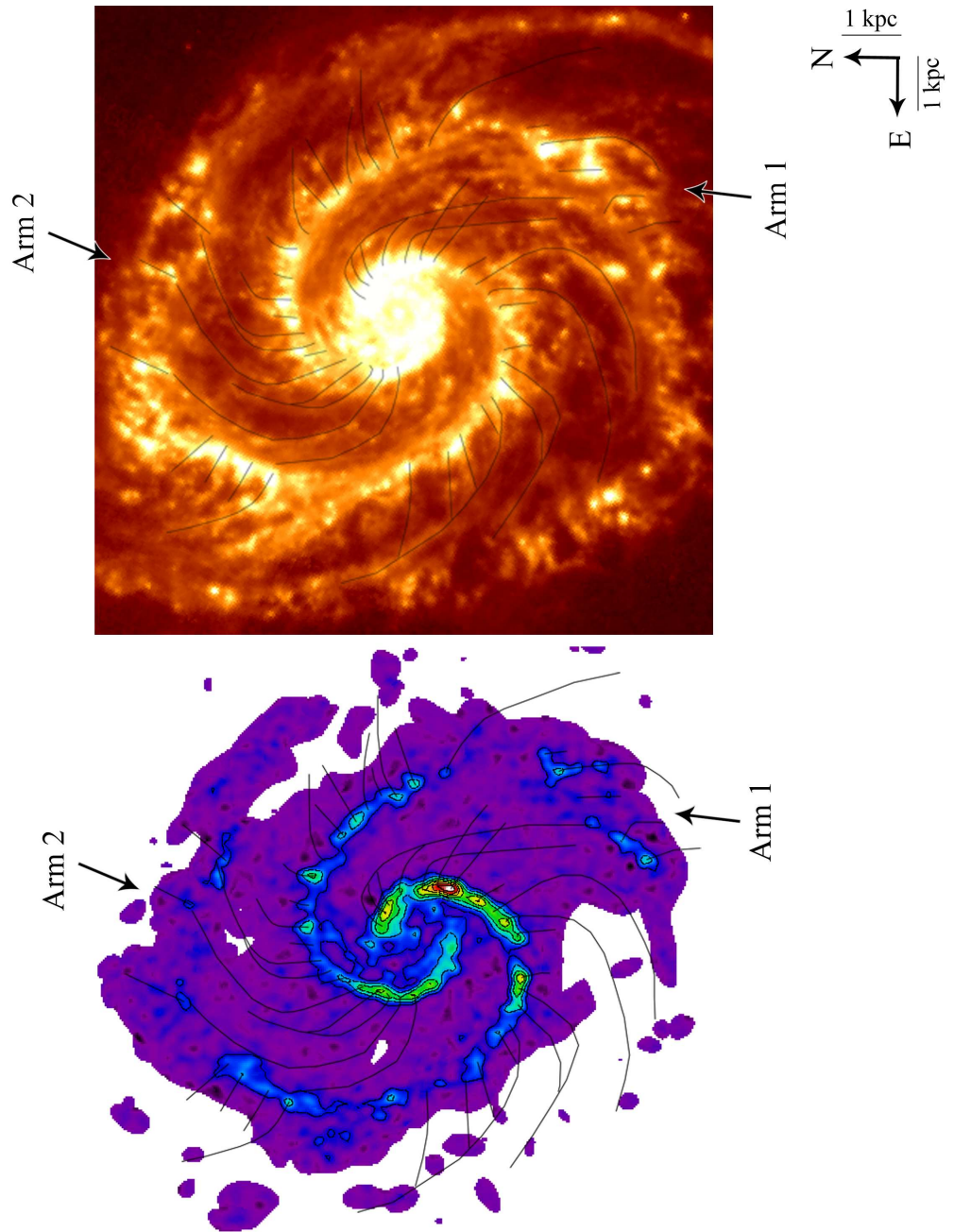
Figure 2.15 Two views of NGC 5194, with lines marking the feathers from HST image shown in Fig. 2.1 – *Top*: Spitzer 8 μm image. *Bottom*: BIMA SONG CO(J=1-0) image.
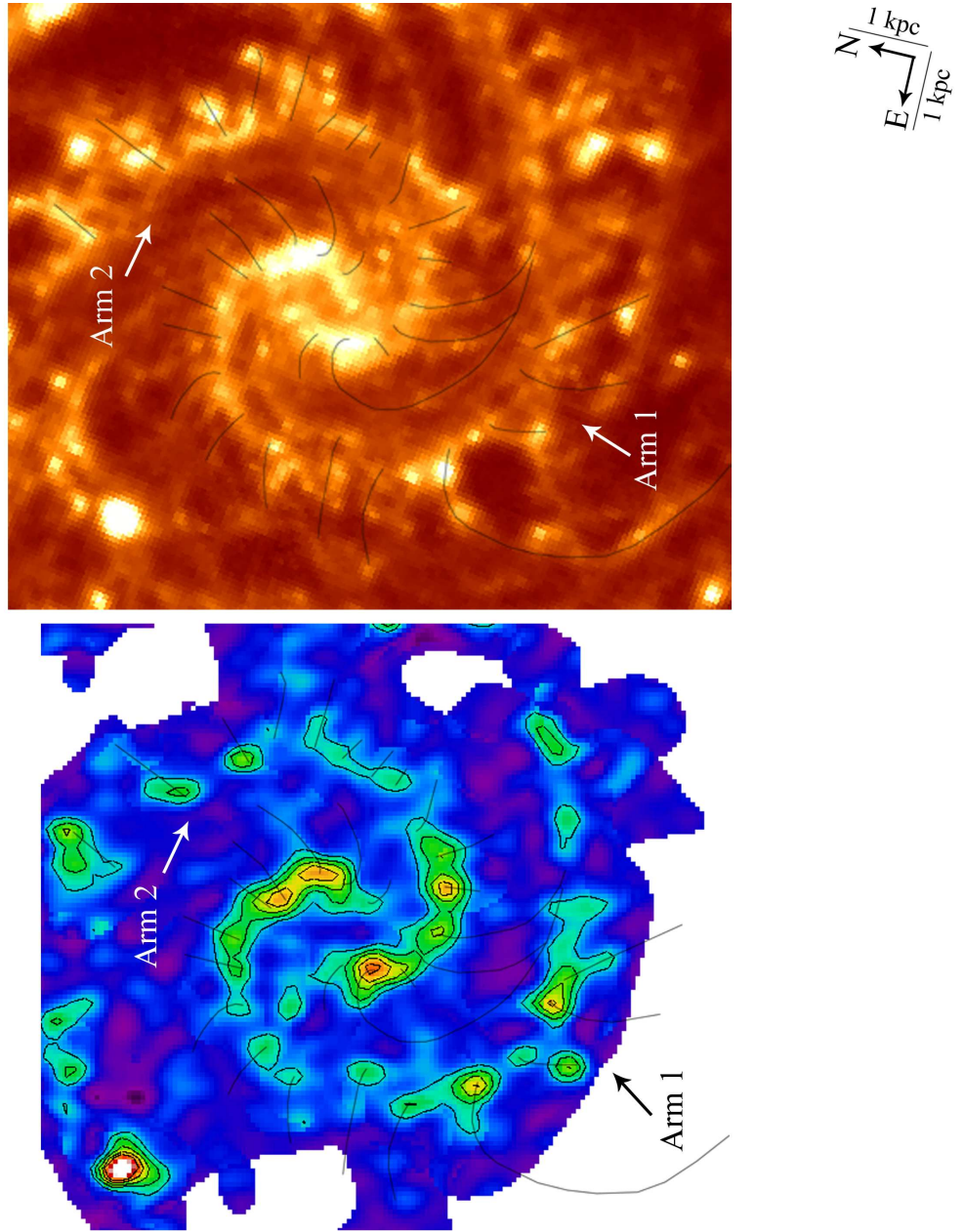
Figure 2.16 Two views of NGC 0628, with lines marking the feathers from HST image shown in Fig. 2.2 – *Top*: Spitzer 8 μm image. *Bottom*: BIMA SONG CO(J=1-0).
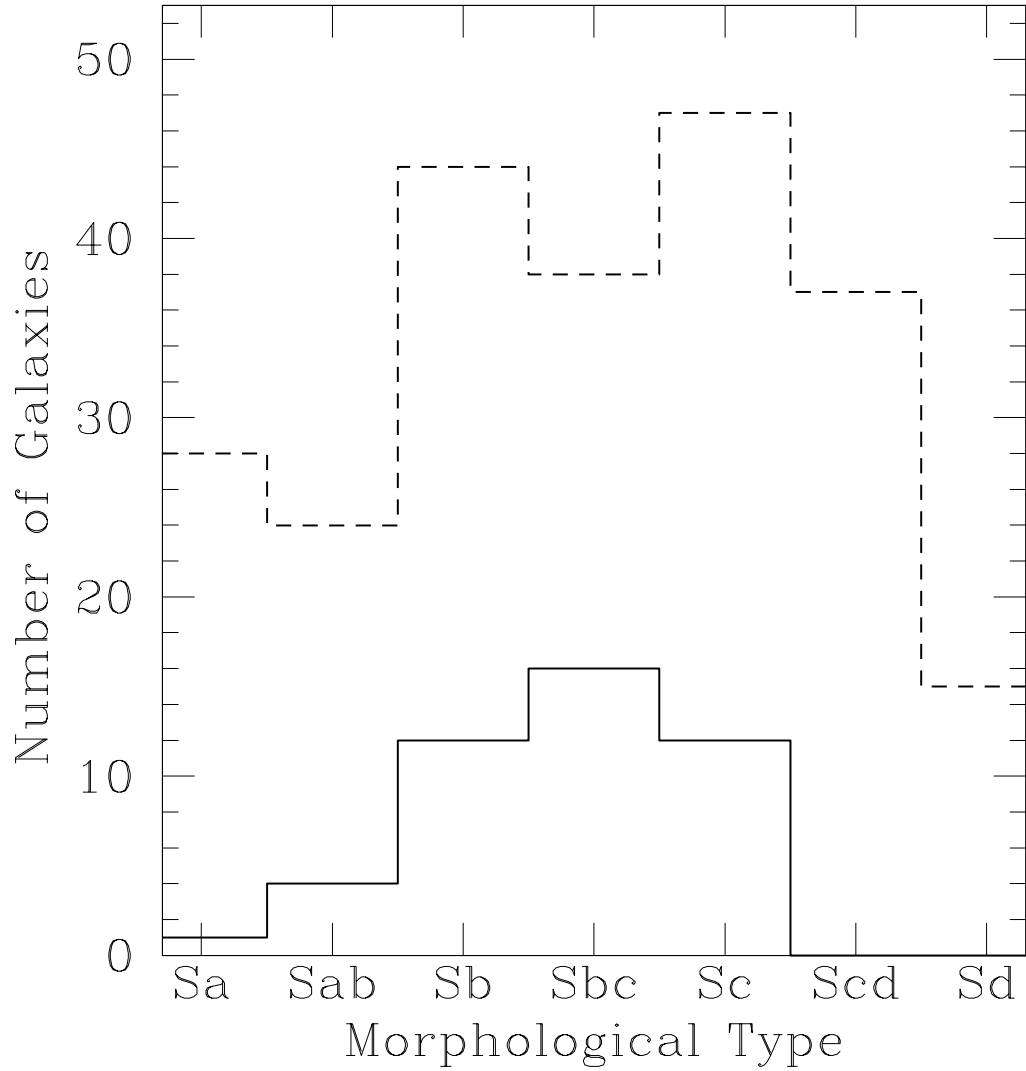
Figure 2.17 Distribution of galactic morphological types included in sample. The dashed line represents the distribution of morphological types of all the galaxies in the sample. The solid line shows the distribution for galaxies with feathers.
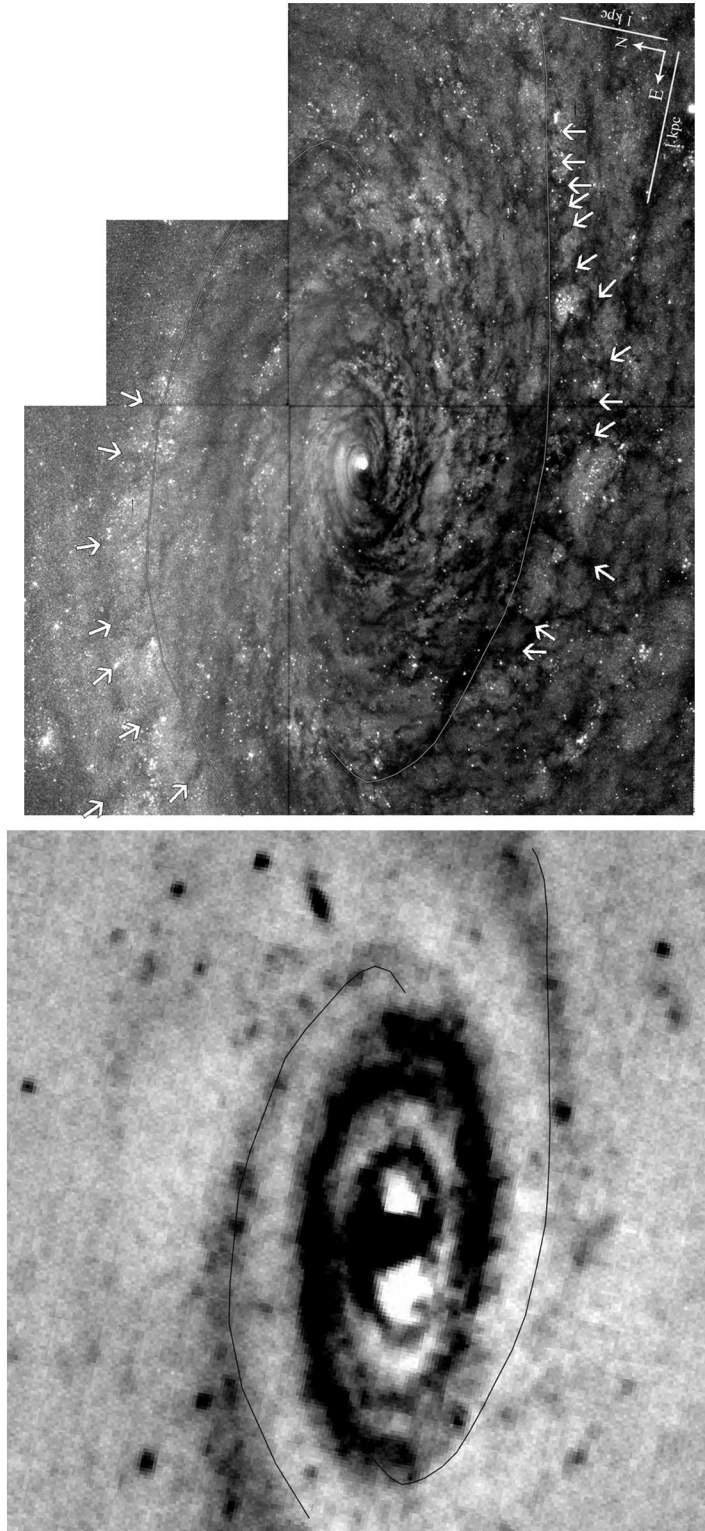
Figure 2.18 *Top*: WFPC2 HST F814W band image of NGC 5055. *Bottom*: 2.1μm image. The thin grey lines in the HST image indicate observed PDLs within the galaxy. The same lines are overlaid on the 2.1 μm image, which show there is a clear association between PDLs observed in the visible and observed infrared emission marking the peak of the stellar arms.
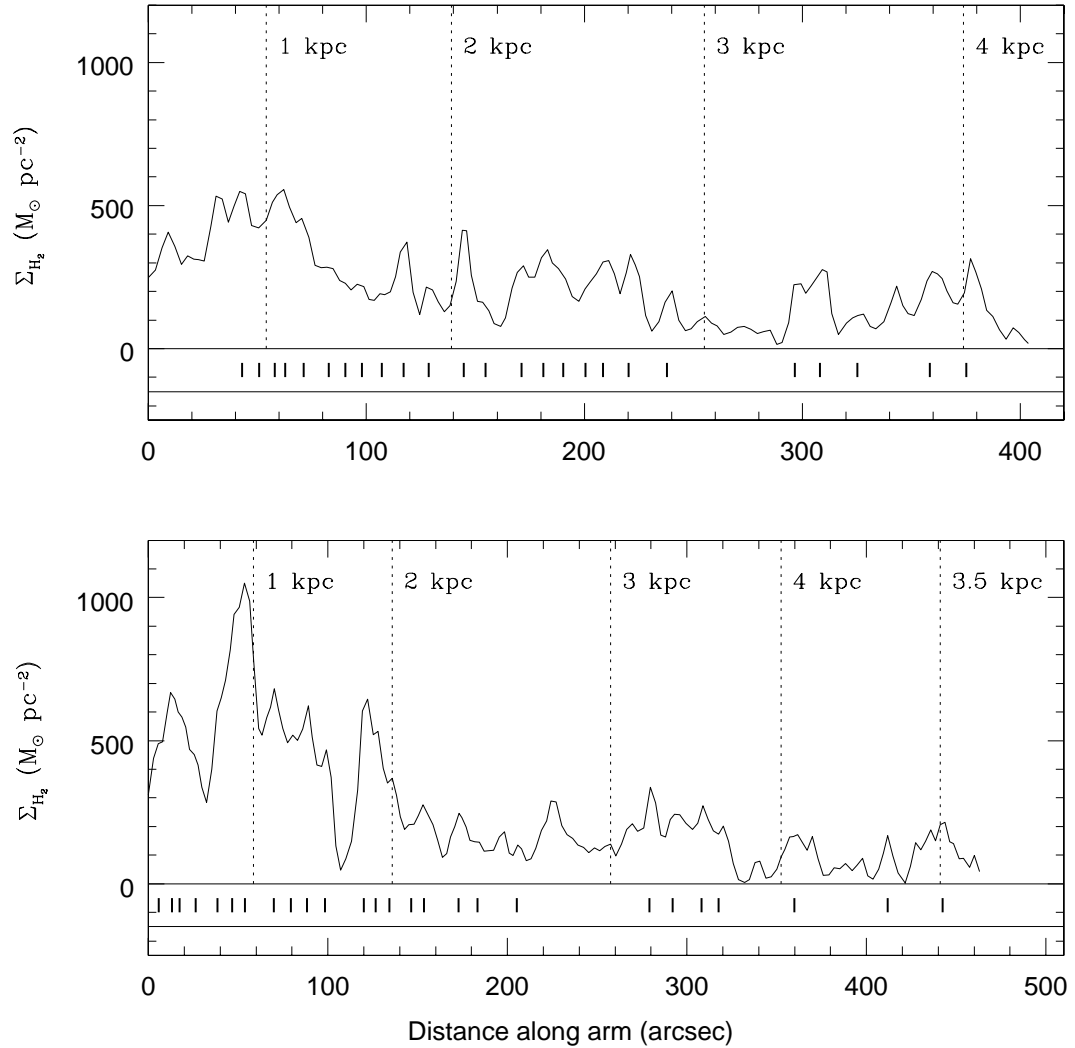
Figure 2.19 Variation in gas surface density along Arm 1 (top) and Arm 2 (bottom) in NGC 5194. The short vertical lines indicate the location of a feather along an arm. The dotted vertical lines indicate galactocentric radius. Note that Arm 2 bends inward near ~4 kpc.
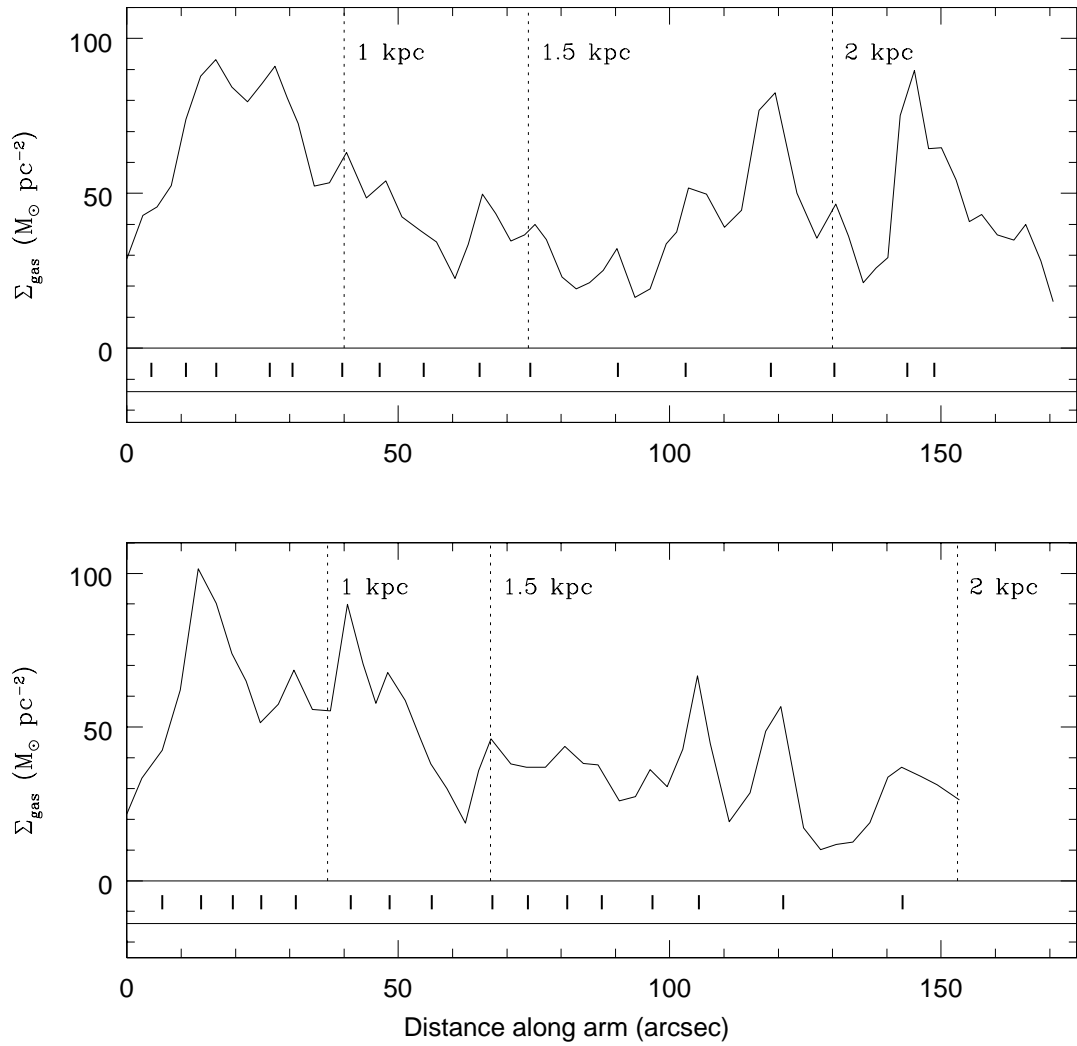
Figure 2.20 Variation of gas surface density along the arms of NGC 0628. See Figure 2.19 for details.
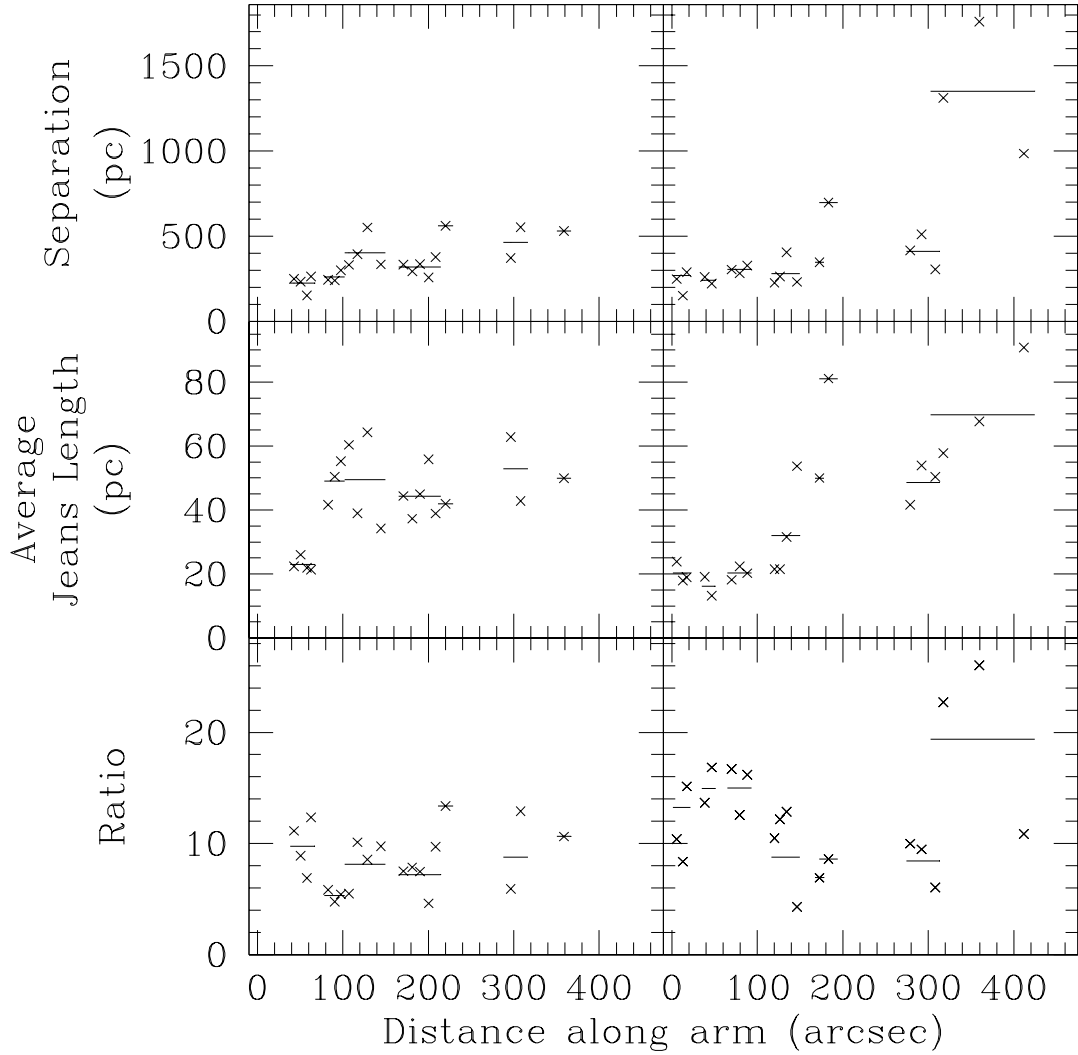
Figure 2.21 Comparison of feather separation to the local Jeans length averaged over 6″ in NGC 5194, as a function of distance along an arm; the left and right columns show data for Arms 1 and 2, respectively. (*Top*) Deprojected feather separation. (*Middle*) Average Jeans length at each feather. (*Bottom*) Ratio of deprojected feather spacing to the local Jeans length. The lines indicate the mean value for each group of feathers along an arm; the length of a line indicates the width of a group.
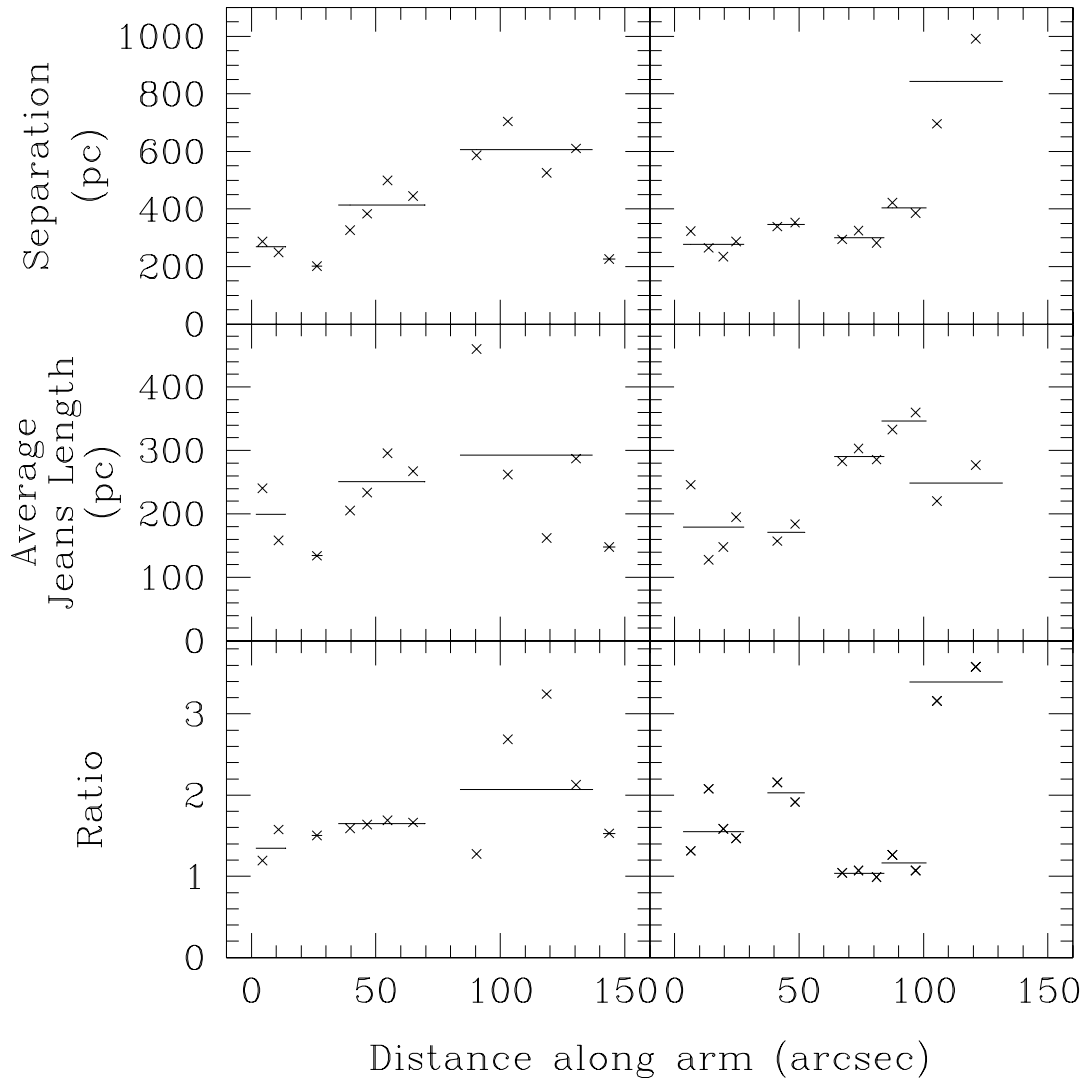
Figure 2.22 Comparison of feather separation to the local Jeans length averaged over 6″ in NGC 0628. See Figure 2.21 for details.

Chapter 3

Sample, Observations, and Data Reduction

3.1 Introduction

3.1.1 Association of Feathers with Star Formation

Perhaps the most striking features of the spectacular HST image of the grand-design spiral M51 (Fig 3.1a; Scoville et al. 2001) are the extinction "feathers" (Lynds 1970) that arch from the arm dust lanes into the interarms. More than simply structural, these feathers are associated with much of the star formation in the disk of the galaxy. This is particularly evident in the recent high resolution, multi-wavelength, ACS HST observations of M51, which include Hα. The Hα emission traces bright OB associations and H II regions, which line the feathers. Similar filamentary features, seen as emission "spurs" (Weaver 1970; Elmegreen 1980b), are one of the most remarkably noted (Calzetti et al. 2005) aspects of the Spitzer 8 μm image of M51 (Fig. 3.1b; Kennicutt 2004). La Vigne et al. (2006; hereafter LV) find a spatial coincidence in M51 between the extinction feathers and the emission spurs seen in 8 μm emission, which traces polycyclic aromatic hydrocarbons (PAHs) that are heated by UV photons from young massive stars. This alignment of extinction

feathers and emission spurs further associates feathers with recent star formation in the galaxy. Furthermore, analysis of BIMA SONG CO(1-0) observations of M51 also links feathers to star formation (LV). In M51, the feathers appear to originate in the massive concentrations of molecular gas termed giant molecular associations (GMAs) by Vogel, Kulkarni, & Scoville (1988) (see Fig 3.1c), which are sites of massive star formation in spiral arms (Young & Scoville 1991). However, feathers are not limited to M51: in a recent study of spiral galaxies in the HST archive, LV find that feathers are common in the arms of spirals, with detection frequency ranging up to 83% in galaxies with well–defined spiral arm primary dust lanes (PDLs).

3.1.2   Association of Feathers with Molecular Gas

While feathers in M51 have been associated with GMAs along the spiral arms, it is not yet clear whether extinction feathers in other galaxies trace significant gas mass concentrations, though they are associated with widespread star formation as seen in M51 (LV). As discussed in Chapter 2.3.5, 8 μm emission traces feathers well into the interarm region, where extinction features become more difficult to observe. Unfortunately, it is difficult to determine from either optical extinction or 8 μm emission alone whether there is significant gas column density in feathers.

Over the last four decades, CO(1-0) observations have been used to probe the molecular gas in galaxies (Rickard et al. 1975; the first observations of CO(1-0) in external galaxies). CO(1-0) observations are used to deduce both the mass and distribution of molecular gas in galaxies. In particular, it is believed that CO(1-0) emission traces the mass of giant molecular clouds (GMCs) in luminous galaxies
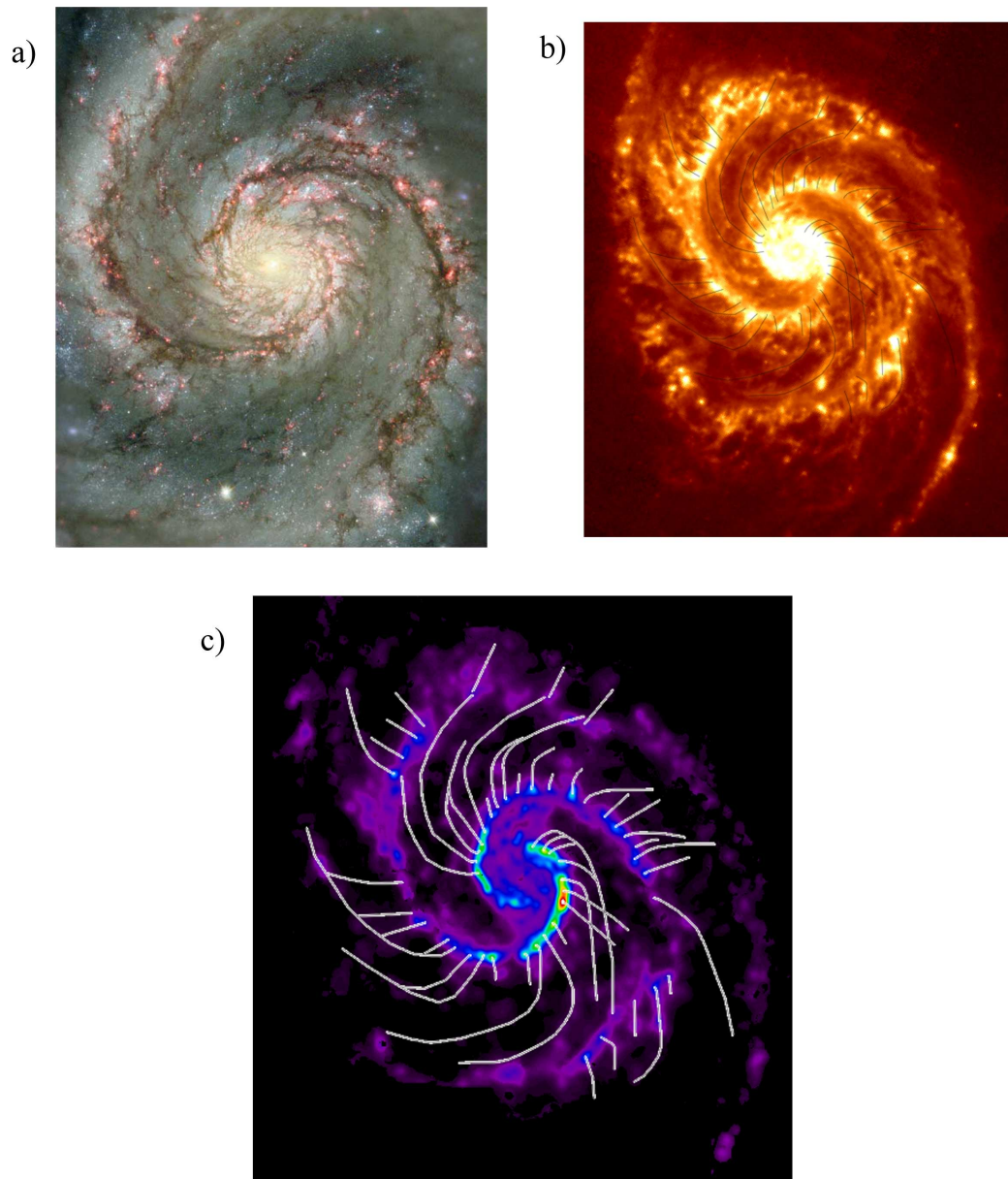
Figure 3.1 M51 – a) HST high resolution image (Scoville et al. 2001). b) Spitzer 8 μm image (Kennicutt 2004); feathers appear as emission features. c) BIMA variable 2-8″ resolution CO(1-0) image; feathers along the PDL can be distinguished at this resolution. – Lines marking feathers in the 8 μm and CO(1-0) images represent the location and length of feathers as measured in the HST ACS image of M51 (Beckwith 2005).

(Young & Scoville 1991). Interpretation of CO(1-0) observations is not without its limitations. However, determining the gas column density is more straight–forward from CO(1-0) than from extinction or 8 μm observations.

In Chapter 2, we compared extinction feathers with BIMA SONG CO(1-0) observations of two grand design spiral, NGC 0628 and NGC 5194. It is important to compare extinction feathers with CO(1-0)in other types of spirals, since feathers are **not** limited to grand-design spirals. LV find feathers in the spiral arms of flocculent, barred, and ringed galaxies as well. It is important to study this range of galaxy types in order to (1) fully characterize the molecular content of feathers within and (2) understand the formation mechanism of *all* types of feathers. The 'classic' feather is characterized by emerging from the PDL as a leading feature and then gradually curving to become trailing farther downstream, on the outer edges of the spiral arms. However, feathers are not limited to a single type of morphology – common types of feathers include (1) 'elongated', not solely contained within the luminous part of the spiral arms; (2) 'lattice structure', a series of feathers linking one or more pairs of PDLs in barred galaxies; and (3) 'transitioning', feathers observed to evolve into spurs.

3.1.3 Motivation for CARMA Observations

Despite their importance as a structural element and as the sites of considerable star formation, the origin of feathers remains controversial. Kim & Ostriker (2002; hereafter KO) found that feathers form via a gravitational instability (including the magneto-Jeans Instability, MJI), while in other models feathers form via non-

gravitational instabilities, such as the Kelvin-Helmholtz (KH) instability in the model of Wada & Koda (2004; hereafter WK). The survey previously conducted by LV hinted that feathers are formed by local gravitational instabilities; however the resolution of the BIMA SONG data was 6″. At this resolution, many feathers are not well separated, making it difficult to distinguish among different theoretical predictions. Typical extinction features identified in the HST images can be distinguished at 2″ resolution (e.g. Fig. 3.1c). The analyses of the limited 6″ SONG molecular data performed by LV were only for M51 and NGC 0628, two well known grand-design spiral galaxies. By contrast, the 2″ BIMA data available for the brighter regions of M51 show that the gas column density of feathers is highest at the PDL and rapidly decreases downstream from the PDL, well before much of the star formation occurs (LV). This rapid decrease in column density has been used in various analyses (e.g. Mouschovias et al. 2006, Ballesteros-Paredes & Hartmann 2006) to draw conclusions regarding the mechanisms that trigger star formation. Similar investigations in other galaxies will help understand factors that trigger star formation and determine the overall efficiency and star formation rate.

The newly operational Combined Array for Research in Millimeter-wave Astronomy (CARMA) provides both the resolution and the sensitivity needed to separate feathers along the spiral arm, and detect molecular gas if it exists along the feathers in the interarm region. With 2-4″ resolution CARMA observations of five carefully selected spiral galaxies covering a range of morphologies (grand-design, flocculent, barred, and ringed; early to late type), we hope to confirm that feathers observed in this range of galaxy types are associated with significant gas concentra-

tions and are not simply low column density extinction features. Furthermore, with these observations we will test the theories of feather formation by yielding accurate estimates of feather spacing, spiral arm width and pitch angle, as well as arm and feather gas column density. The KO model forms feathers via a gravitational instability; therefore feather spacing is expected to scale with the Jeans length. In particular, the feather spacing is expected to be 3-5 times the Jeans length and several times the width of the PDL. By contrast, KH models expect feather spacing to be approximately equal to the PDL width, and to not be closely related to the Jeans length (WK, Dobbs & Bonnell 2006). Moreover, KH models depend primarily on velocity flow and pitch angle of the spiral arms to form feathers. WK note that the KH instability is actually stable to collapse in tightly wound or early type spirals. We will evaluate the success of the various models in each of the different types of galaxies studied, as well as determine whether the theories apply for all morphologies of feathers.

3.1.4 Multi-wavelength Observations

Our targets are considered classic galaxies, selected for inclusion in the Spitzer SINGS Legacy sample (Kennicutt et al. 2003) and therefore have a wide range of excellent multi-wavelength data. The Spitzer 8 μm images clearly highlight the extension of feathers into the interarm region (§2.3.5) and will be utilized in the process of identifying the feathers in our sample in Chapter 5. Additionally, the combination of the Spitzer Ancillary Hα observations plus the 24 μm observations is an excellent extinction-corrected tracer of the recent star formation in galaxies and

can be used to calculate the SFR (Calzetti et al. 2007). Complementing the data from the SINGS survey, our sample galaxies were also included in the NRAO VLA THINGS Hɪ survey (Walter et al. 2008), which provides high-resolution ($\sim 6''$) observations of the distribution of Hɪ in nearby galaxies. Furthermore, the five proto-typical spiral galaxies we selected already have BIMA SONG lower resolution ($\sim 6''$) CO(1-0) maps that can combined with the new high resolution CARMA data to obtain greater signal-to-noise in the final maps for each galaxy. With this unique high-resolution molecular data added to the plethora of multi-wavelength observations, we are well-positioned for an in-depth study of the mechanisms that lead to molecular clouds and star formation in the disks of spiral galaxies.

3.2 Sample

Our sample is composed of a distinct group of nearby, relatively face-on spiral galaxies, whose distances range from ~ 5 Mpc to ~ 11 Mpc and in inclination from $\sim 7°$ to $\sim 60°$. This set of target galaxies was selected from the group of 43 galaxies previously identified as having feathers (§2.3.2) and to cover a range of morphological types, from early to late type (Sab–Sc), and spiral arm types. Observing galaxies with different spiral density wave strength (i.e. grand design vs. flocculent), pitch angle (i.e. early vs. late type), and non-circular motion (i.e. barred vs. unbarred) will help determine the kinematic and spiral arm features that produce different feather types. For example, the KH instability is not likely to occur in tightly wound spirals (with flat rotation curves) (Wada & Koda 2004). Therefore,

Table 3.1.   Sample of Target Galaxies

Galaxy	type	inc (deg)	PA (deg)	Distance (Mpc)
NGC 0628	Sc - grand design	7	20[*]	10[a]
NGC 3627	Sb - strong bar	62	173[1]	11.1[b]
NGC 4736	Sab - ring	41	296[1]	5.1[c]
NGC 5055	Sbc - flocculent	63	93[*]	7.2[d]
NGC 5194[1]	Sbc - grand design	24	170[2]	8.4[e]

[*]fit with the NEMO program *rotcurshape*; [1]de Blok et al. 2008; [2]Shetty et al. 2007;

[a]Elmegreen 2006; [b]Saha et al. 1999; [c]Jalocha et al. 2008; [d]Shetty et al. 2007; [e]Tully 1988

[1]CARMA CO(1-0) data provided by Koda et al. 2009

if the CO(1-0) maps demonstrate that the feathers noted in the tightly-wrapped spiral NGC 4736 consist of significant gas mass concentrations, spaced at regular intervals, this would tend to contradict the WK model.

We now discuss each sample galaxy individually.

3.2.1   NGC 0628 (M74)

NGC 0628 is an isolated (Briggs 1982, Smith et al. 2007), nearby ($\sim$10 Mpc), later type (SA(s)c) galaxy with an enormous HI disk that extends out to $\sim 4R_{25}$ (Briggs 1982). A proto-typical grand design spiral galaxy, its spiral arms are very symmetrical in the ultraviolet (UV) (Marcum et al. 2001), and are highlighted by bright knots of star formation that appear like "beads on a string" (Elmegreen 1980b, Chen et al 1992, Cornett et al 1994, LV), similar to M51. This similarity in arm type between NGC 0628 and M51 allows us to study the effect of spiral density

wave strength on the characteristics and formation of feathers. In particular, both galaxies also have the same types of feathers: classical, elongated, and transitioning. The questions we ask are: do NGC 5194 and NGC 0628 differ in spacing between feathers, in their molecular content, or in how far the feathers can be traced in CO(1-0)?

3.2.2   NGC 3627 (M66)

NGC 3627 is a member of the Leo Triplet with NGC 3628 and NGC 3623. HI observations indicate a tidal encounter with NGC 3628 (Zwicky 1956, Afanasiev & Sil'chenko 2005; references within), which has also been modeled by Toomre (1978) and Rots (1978). The southern arm of NGC 3627 is extended pointing towards NGC 3628 and does not lie in the same plane as the rest of the galaxy; the inclination changes from, $i = 62°$, and position angle, P.A. $= 173°$ interior to radius, R$= 90''$ to $i \sim 50°$ and P.A.$\sim 155°$ beyond (Chemin et al. 2003). It is classified as a barred galaxy, SAB(s)b, in the RC3. CO(1-0) and IR observations show NGC 3627 is very strongly barred; the bar is 2.6 kpc in radius (Jarrett et al. 2003, Rand & Wallin 2004). In the northern arm of the galaxy, a particular type of feather, called "lattice structure", has been previously identified in 8 μm (LV). This special type of feather was first predicted by Balbus (1988) to occur only in barred galaxies. High resolution, CARMA observations of NGC 3627 allow us to (1) characterize the molecular content of this unique feather structure and (2) test if lattice feathers form via the same mechanism as other types.

3.2.3 NGC 4736 (M94)

NGC 4736 is an isolated (Smith et al. 2007), early type galaxy, (R)SA(r)ab (RC3). Though it is not classified as a barred in the RC3, a weak bar is seen in the near-IR (Mollenhoff et al. 1995) and in CO(1-0) (Wong & Blitz 2000). It features a ring of star formation at a radius of $\sim45''$ visible in Hα. This corresponding structure in CO(1-0) is a pair of tightly wrapped spiral arms (Wong & Blitz 2000). Rand & Wallin (2004) find that corotation is just outside the Hα ring, at about $R = 40'' - 70''$. NGC 4736 has also been classified as having classical feathers. Since the CO(1-0) arms are very tightly wrapped, this galaxy is an excellent arm environment to test the WK criteria which requires large pitch angle for the arm in order for the spiral density wave to be unstable to the K-H instability.

3.2.4 NGC 5055 (M63)

NGC 5055, classified as SA(rs)bc in the RC3, is a flocculent galaxy at visible wavelengths with short patchy spiral arms. It has a large, warped HI disk that extends out to about $3.5R_{25}$; the warp begins at the end of the bright stellar disk (Battaglia et al. 2006). A companion, UGC 8313, is detected in HI at the projected distance of 50 kpc to the North-West of NGC 5055, but it is not clear if the companion has any significant role in causing the warp (Battaglia et al. 2006). Though optically it is flocculent, near-IR and CO(1-0) observations (Thornley 1996) reveal symmetric, two arm spiral structure that extend over 150° in azimuth and out to a radius of $2'$ (Sakamoto et al. 1999). NGC 5055 has also been classified as having classical

feathers, connected to PDLs that are aligned with the near-IR and CO(1-0) spiral arms (LV). NGC 5055's unique disk environment allows us to further understand the mechanism(s) by which stars form in spiral galaxies that appear optically flocculent, but have weak underlying spiral density waves.

3.2.5 NGC 5194 (M51)

NGC 5194 is classified as SA(s)bc in the RC3 and is often considered *the* prototypical grand design spiral galaxy, with intense star formation along its two well defined spiral arms. The numerous OB associations and HII regions that line the arms, which can be traced for more than a whole revolution, have been well studied in the optical and IR (Calzetti et al. 2005; references within). NGC 5194 is also known as Arp 85 due to its interaction with the early type galaxy NGC 5195. It is thought that the inner arms of NGC 5194, out to R$\sim$4′, are produced by spiral density waves while the outer arms are tidally induced (Shetty et al. 2007). Both arms of NGC 5194 have also been previously classified as having feathers (LV). High resolution, CO(1-0) observations of the entire disk of NGC 5194 allow us to test the effect of interactions on the formation of feathers: is there a difference between the feathers formed at R$<$4′ and those along the tidal arms? These observations also allow us to compare the characteristics of feathers formed in galaxies with different spiral arm density wave strength by comparing the properties of feathers in NGC 5194 to those in NGC 0628.

3.3 Observations & Data Reduction

3.3.1 Combined Array for Research in Millimeter-wave Astronomy (CARMA)

3.3.1.1 Antennas

CARMA is a university-based millimeter array combining the six 10.4 m antennas of Caltech's Owens Valley Radio Observatory (OVRO) and the nine 6.1 m antennas of the Berkeley-Illinois-Maryland Association (BIMA). The antennas have been relocated to the new CARMA site, Cedar Flat, CA, which is in the Inyo Mountains at an elevation of 2200 m (Bock 2006). The 15 antennas are used in combination producing 105 ($n_{baselines} = (n_{antennas}^2 - n_{antennas})/2$) baselines and operate at 3 mm (85–116 GHz) and 1 mm (215–270 GHz). The antennas are also configurable. There are various stations distributed over an area 2 km in diameter at the site at which antennas may be located. This provides antenna spacing ranging from 8 m up to 2 km, yielding both resolution and wide-field imaging that are unprecedented at millimeter wavelengths (Bock 2006). Typically, the antennas are deployed in one of the five standard configurations (A, B, C, D, E), providing angular resolutions of roughly 0.3″, 0,8″, 2″, 5″, or 10″ at 100 GHz[1].

3.3.1.2 Receivers

Both the 10.4 m and 6.1 m antennas are outfitted with SIS receivers and currently receive one linear polarization (Bock 2006). Both sidebands of the first local oscil-

---

[1]http://www.mmarray.org

lator are also received and the sidebands are separated in the correlator by phase-switching the local oscillators. Currently, the intermediate frequency (IF) band is 1–5 GHz at 3 mm and 1–4.5 GHz at 1 mm[2].

3.3.1.3 Correlator

The digital correlator currently used for both the 10.4 m and 6.1 m antennas uses field programmable gate array (FPGA) technology (Bock 2006). It provides up to 366 complex channels per sideband for each of the 105 interferometric baselines, within a maximum of bandwidth of 1.5 GHz per baseline per sideband[3]. Signals entering the correlator are split into three separate bands. Crosscorrelation of the signal places the upper side band in the upper half of the channels and the lower side band in the lower half of the channels. By setting the frequencies of the second local oscillators, these bands may be positioned independently within the IF bandwidth. The three bands may be placed in any order, overlapped, or used with different velocity resolutions. This flexibility is particularly important since an analog filter attenuates the edge channels of the 62 MHz band. An overlap of about 6 channels is recommended if multiple 62 MHz bands are used to cover a single line. Additionally, weighting, such as hanning smoothing, is not automatically applied to the data.

---

[2]http://www.mmarray.org
[3]http://www.mmarray.org

3.3.1.4 Mosaicing

The half-power beamwidths of the 10.4 m and 6.1 m antennas are $60''$ and $100''$, respectively, at 115 GHz, and the typical radio pointing accuracy is $5''$ rms[4]. Sources anywhere within the primary beam can be imaged, but the sensitivity and pointing errors become more critical beyond the half-power points. To image objects larger than $\sim 1'$ in size, it is necessary to mosaic or make observations at multiple pointing centers with the interferometer. The total number of mosaic pointings should cover the object being imaged (typically in an hexagonal pattern), and be spaced by no more than $\lambda/(2 \times D_{10m})$ or $\sim 26''$, in order to sample the short u-v spacings[5].

3.3.1.5 CARMA Observations

Using the newly operationally CARMA interferometer, we observed the inner $\sim 3'$ diameter of our morphologically distinct sample, between January 2007 and July 2008, in CO(1-0). We used a 19 point, hexagonal mosaic (Fig 3.2) grid, observing each field for 1 min before the telescope slewed to the next pointing. After a cycle of 19 fields, a phase calibrator was observed. Observations were taken in the C array configuration to acquire the resolution needed to separate the feathers along the arms (Table 3.3) and in the D & E array configurations to recover extended emission in the galaxies; antenna spacing ranged from 8 m–350 m. The final uv coverage was rather uniform for all of the galaxies (see Figure 3.3 for the total coverage of NGC 0628), the longest spacing being $\sim 140\ k\lambda$. The number of "on source" hours per galaxy is listed

---

[4]http://www.mmarray.org

[5]http://www.mmarray.org
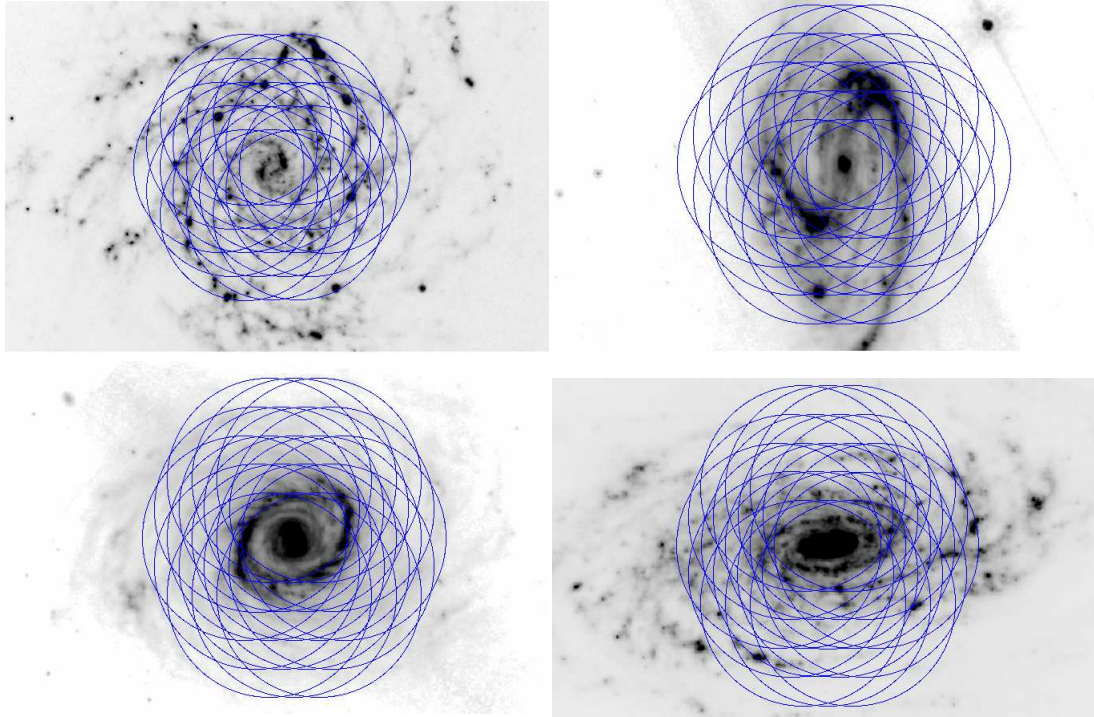
Figure 3.2 Interferometric mosaic fields superimposed on 8μm images of four of the sample galaxies; clockwise from top left: NGC 0628, NGC 3627, NGC 5055, NGC 4736. The circles are $80''$ in diameter, corresponding to the FWHM of an 8 m dish.

for each configuration in Table 3.2. The system temperatures varied from track to track, but typically ranged between 200 K–1000 K. The galaxies were observed with either a single 32 MHz filter or overlapping 62 MHz filters (depending on the required velocity resolution and coverage) as listed in Table 3.3. The phase, bandpass, and flux calibrators were all observed with the 500 MHz band of the correlator. The bandpass sources typically included 3C273, 0927+390, and 1058+105 and the flux calibrators were Mars & Uranus, when available.
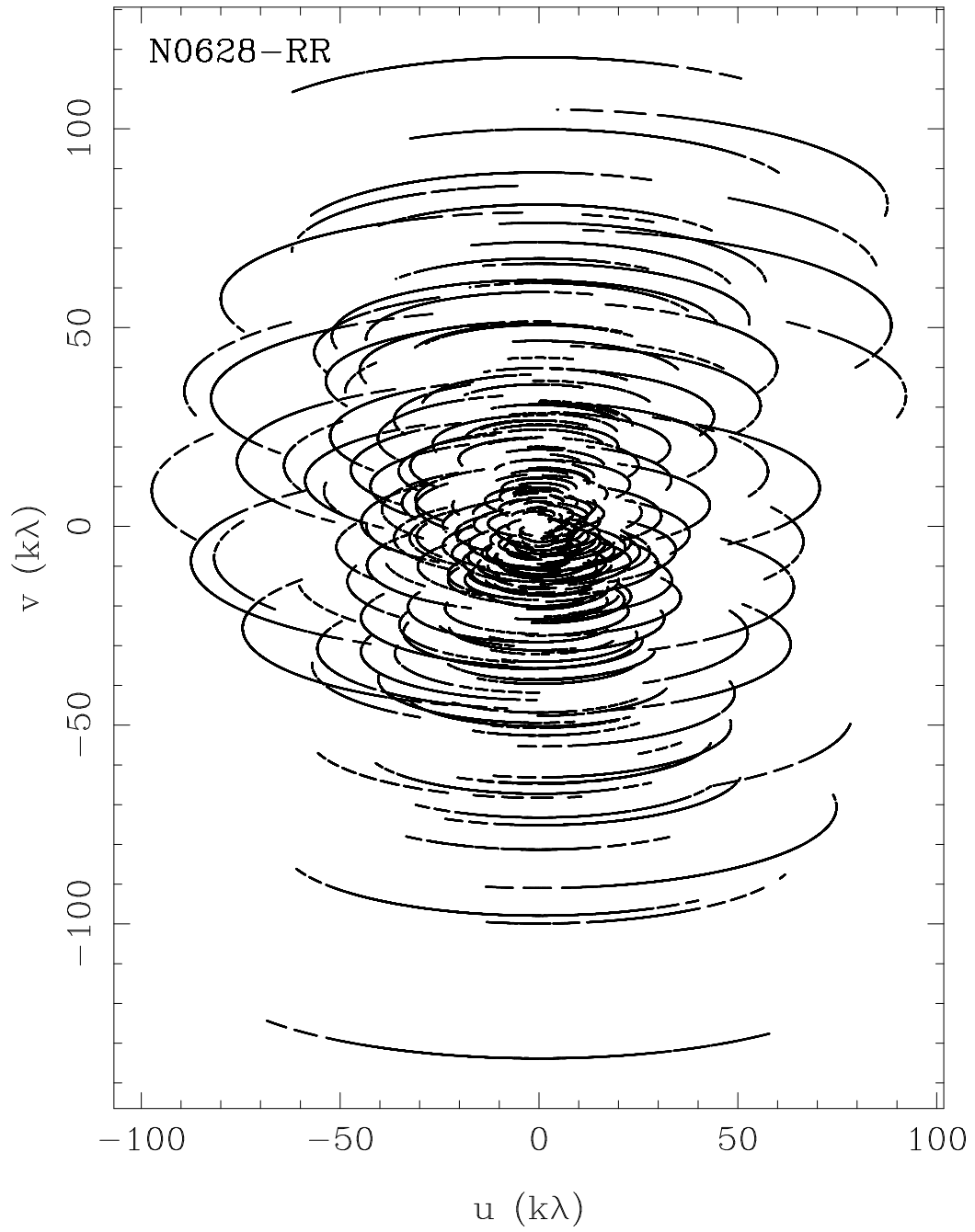
Figure 3.3 *uv* coverage for NGC 0628.

Table 3.2.   Observations per Configuration

Galaxy	C hrs	D hrs	E hrs	Total hrs
NGC 0628	16.6	12.6	8.2	37.4
NGC 3627	7.5	−	3.1	10.6
NGC 4736	7.8	3.8	1.9	13.5
NGC 5055	16.3	7.6	5.0	28.9

Table 3.3.   Observational Parameters

Galaxy	Correlator Setup	$\theta_{maj} \times \theta_{min}^a$ (arcsec × arcsec)	bpa^b (deg)	Δv^c (km s^{-1})	σ^d (mJy beam^{-1})
NGC 0628	1 32 MHz band	4.0 × 3.25	42	2.54	32
NGC 3627	3 62 MHz bands	3.84 × 3.24	24	5.08	85
NGC 4736	2 62 MHz bands	3.84 × 3.27	73	5.08	38
NGC 5055	3 62 MHz bands	3.33 × 2.88	72	5.08	27
NGC 5194[1]	3 62 MHz bands	4.1 × 3.28	77	5.08	40

[a]FWHM of major and minor axes of synthesized beam.

[b]Beam position angle.

[c]Velocity width of channels after hanning smoothing.

[d]RMS noise in the inner quarter of the channel map, measured within emission free channels.

[1]Koda et al. 2009

3.3.2   BIMA SONG Observations

The galaxies in our sample were previously imaged as part of the BIMA Survey of Nearby Galaxies (BIMA SONG), which was the first systematic imaging survey of CO(1-0) emission in the centers and disks of 44 nearby galaxies (Helfer et al. 2003). Observations occurred between November 1997 through December 1999 using the

then 10-element BIMA array (Welch et al. 1996), which was located at Hat Creek, CA. The observations were taken in the BIMA C & D array configurations, with antenna spacings ranging from 7.7 m to 87 m. The inner $3'$ diameter of the galaxies were imaged using a 7 point, hexagonal mosaic grid with a spacing of $\lambda/(2 \times D_{6m})$ or $44''$. The resolution of the final BIMA SONG maps was $\sim6''$ and the velocity resolution was 5 km s^{-1}.

3.3.3 THINGS Observations

Our sample of galaxies is a subset in "The HI Nearby Galaxy Survey" (THINGS; Walter et al. 2008), which imaged the HI (21 cm) line in 34 nearby galaxies using the National Radio Astronomy Observatory (NRAO) Very Large Array (VLA). The VLA consists of 27, 25 m diameter antennas in a Y-shaped configuration, located fifty miles west of Socorro, New Mexico[6]. The THINGS observations were taken in the VLA B, C, & D array configurations, with antenna spacings ranging from 35 m to 11.4 km. The acquired angular resolution was $\sim 6''$, in order to resolve atomic gas complexes, and the velocity resolution was 5 km s^{-1}, in order to Nyquist sample the HI line (Walter et al. 2008).

3.3.4 Spitzer Observations

The members of our sample were also imaged as part of the *Spitzer* Infrared Nearby Galaxies Survey (SINGS; Kennicutt et al. 2003), a coordinated multi-wavelength campaign to study the process of star formation in nearby galaxies. With a diameter

---

[6]http://www.vla.nrao.edu/

of).85 m, the *Spitzer* Space Telescope is the largest infrared telescope launched into space and has three cryo-genically cooled instruments on board: the Infrared Array Camera (IRAC), which images at 3.6, 4.5, 5.8, and 8 μm; the Infrared Spectrograph (IRS); and the Multiband Imaging Photometer for Spitzer (MIPS), which images at 24, 70, and 160 μm[7]. The SINGS galaxies were imaged in the IRAC and MIPS bands to at least the full optical radii (R_{25}) of the galaxies (Kennicutt et al. 2003). The IRAC observations were performed in two sets of dithered exposures separated by 1–24 hr in order to recover more spatial information and to detect and remove asteroids (Kennicutt et al. 2003). For the IRAC bands, the final point-spread-function (PSF) FWHM is $\sim 1.7''$ except for the 8 μm band, which has a PSF FWHM of $\sim 2''$. For the 24, 70, and 160 μm MIPS bands, the PSF FWHM is $\sim 5.7''$, $\sim 17''$, and $\sim 38''$, respectively (Calzetti et al. 2005).

3.3.5 GALEX Observations

Our sample galaxies were also imaged by the Galaxy Evolution Explorer (GALEX; Martin et al. 2005) for the Nearby Galaxy Survey (NGS; Bianchi et al. 2003) in the far-ultraviolet (FUV; $\lambda_{eff} = 1516\mathring{A}$) and near-ultraviolet (NUV; $\lambda_{eff} = 2267\mathring{A}$). GALEX is a space borne, 50 cm aperture Ritchey-Chretien telescope that has a dichrioc beam splitter allowing simultaneous FUV and NUV observations (Martin et al. 2005). The NGS observations occurred between June 2003 and April 2005; all observations occurred at night. The PSF FWHM for the FUV and NUV ranges from 4.0-4.5$''$ and 5.0-5.5$''$, respectively.

---

[7]http://www.spitzer.caltech.edu/about/index.shtml

3.4 Data Reduction

3.4.1 CARMA Data

The CARMA data were calibrated using the MIRIAD (Sault, Teuben, & Wright 1995) data reduction package. After flagging bad channels, time periods, antennas, pointing, and shadowed data (baselines down to 8 m along OVRO-OVRO baselines and 5 m along BIMA-BIMA baselines were included) the narrow-band data (the source data along with any narrow-band bandpass data) were hanning smoothed. The narrow-band source data were bandpass calibrated and phase calibrated. The data were then flux calibrated using planets when available.

The calibrated CARMA visibility data, excluding M51, were combined with the calibrated BIMA SONG interferometric visibility data using INVERT to acquire more signal-to-noise in our maps. We weighted the combined visibility data sets by the noise variance and applied robust weighting (Briggs 1995) producing datacubes in right ascension, declination, and LSR velocity. The combined datacubes were then deconvolved and restored in an iterative process. For a first pass, the datacubes were deconvolved using MOSSDI2, which performs a steer CLEAN on a mosaiced image (Steer, Dewdney, & Ito 1984), not including the attenuated edges of the mosaic and then restored using the task RESTOR. RESTOR convolves the CLEAN solution with the major and minor axes, which were fit to the central lobe of one plane of the synthesized beam (Helfer et al. 2003), then adds the residuals from the CLEAN solution to the result. From this first pass of cleaning and restoring, integrated intensity, velocity, and velocity dispersion maps were made (moment 0, 1, & 2).

We then fit the rotation curve and kinematic parameters of the galaxies using the first moment map and the parameters listed in Table 3.1. By determining the rotation curve for each galaxy, we were able to create a mask, using the MIRAD program ROTCURMASK, to limit the contribution of noise in the datacubes produced by INVERT. We then deconvolved these "rotation curve masked" datacubes, cleaning deeply to a cutoff of 1.5 times the theoretical rms in each pixel, using MOSSDI2. The data were then restored using the CLEAN solution from the first iteration as a model.

We then combined the CARMA+BIMA SONG maps with single dish observations from the 12 m NRAO telescope to recover the total power and short spacing visibilities for each galaxy. The data were combined using the Stanimirovic et al. (1999) linear combination method (Regan et al. 2001, Helfer et al. 2003). To combine the single dish data with the interferometric data (CARMA+BIMA SONG), a new dirty map is made through a linear combination of the interferometric map and the single dish map. The single dish map is scaled by the ratio of the area of the interferometric beam to the area of the single dish beam. A new dirty beam is also created by linearly combining the synthesized interferometric beam and the single dish beam. The single dish beam is assumed to be a truncated Gaussian using the same relative weighting. After the single dish and interferometric data were linearly combined, they were then deconvolved using MOSSDI2, performing a Steer CLEAN for mosaiced data. The data were then restored.

For M51, the total power and short spacing data were obtained with the 25-Beam Array Receiver System (BEARS) on the Nobeyama Radio Observatory 45 m

telescope (NRO45; Koda et al. 2009). The M51 CARMA and NRO45 data were combined in Fourier space and then inverted, using theoretical noise and uniform weighting. Deconvolved channel maps used in this thesis were provided by Jin Koda and are published in Koda et al. (2009).

3.4.2   Spitzer Data

Due to the bandwidth of the Spitzer IRAC 8 μm filter and the spectral energy distribution (SED) of late type or evolved stars, emission from stars as well as warm dust contributes to emission at 8 μm with Spitzer (Pahre et al. 2004). Therefore, for the purpose of tracing extinction features, we removed the unwanted stellar emission from the Spitzer 8 μm images by creating 'dust only' 8 μm images. To produce a 'dust only' image for each galaxy in the sample, first the 3.6, 4.5, and 8 μm images were scaled to match the theoretical colors of M0 III stars (Pahre et al. 2004). Then, using the average of the stellar dominated (Pahre et al. 2004) 3.6 and 4.5 μm images, 'stellar only' images were made and then subtracted from the 8 μm images, producing 'dust only' images for each galaxy in the sample.

Chapter 4

Tracing the Neutral Gas Distribution in Spiral Galaxies

4.1 Introduction

One of the major goals of extragalactic surveys is to understand the process by which the interstellar medium (ISM) in spiral galaxies evolves. A key requirement for understanding the ISM is to obtain the distributions of the various components of the ISM and their relationship to each other. The ISM is multi-phase, consisting of a very cold (T$\sim$10–20 K) and dense molecular component; a cold (T$\sim$100 K), less dense neutral atomic component; a warm (T$\sim$10^4 K) component, which is composed of an atomic and an ionized phase; and a hot (T$\sim$10^6 K) ionized component. The chemical composition of the ISM is $\sim$90% hydrogen by number, $\sim$9% helium, and $\sim$1% heavier elements (Ferriere 2001). Used loosely, the terms "H I content" and "H$_2$ content" are used as a gauge for the amount of neutral and molecular gas within galaxies, respectively (Haynes et al. 1984).

Both the molecular and the neutral atomic gas in the ISM are traced by radio emission lines. The CO(J=1-0) transition is used as a proxy to measure the molecular content in spiral galaxies due to the relative ease with which it can be

detected. The neutral atomic component is traced by the 21 cm line, which is primarily optically thin in the disks of face-on spiral galaxies (Giovanelli & Haynes 1988). Therefore, the 21 cm transition suffers little absorption. Typically, the average column density of H$\textsc{i}$ is similar ($10^{19} - 10^{20}$ cm^{-2}) in nearby, normal spiral galaxies (Irwin 1995). At higher column densities, hydrogen atoms become self–shielded and are able to combine to form H$_2$. At lower column densities, extragalactic radiation begins to ionize the neutral gas (Brinks 1994). As discussed previously, the distribution of atomic (H$\textsc{i}$) and molecular gas (H$_2$) varies with Hubble type. Studies have shown distinct radial and azimuthal differences between the location and abundance of H$\textsc{i}$ and H$_2$ among spiral galaxies.

4.1.1 Radial Distribution

Observations of the radial distribution of molecular and atomic gas have been measured and compiled by various authors for numerous galaxies, ranging in morphological type (Young & Scoville 1991; Roberts & Haynes 1994; Kennicutt 1998a; Sakamoto et al. 1999; Regan et al. 2001; Wong & Blitz 2002; Bigiel et al. 2008). These observations have been azimuthally averaged to minimize significant azimuthal variations, such as spiral arms, and the same CO(1-0) - H$_2$ conversion factor is used across morphological types in individual studies. Typically, the H$_2$ is found to be much more strongly concentrated towards the center of late–type spiral galaxies, while there is a slight depression of H$\textsc{i}$ in the center. At lower resolution ($\sim$45–60″), the molecular gas in luminous late type spirals is observed to fill this "central hole" of H$\textsc{i}$ (Young & Scoville 1991, references within). However, higher

resolution ($\sim$6$''$), BIMA SONG observations have shown that the H_2 emission does not always peak at the center of late type spirals, such as in NGC 0628 (Regan et al. 2001). For intermediate type galaxies, H_2 is again much more strongly concentrated in the center of galaxies than H I. However, nearly half of the intermediate type galaxies also show a central depression of both H_2 and H I rather than H I alone. The radial profiles of early type galaxies are very similar to those of late type galaxies; the H_2 is strongly centrally concentrated and peaks at the center while the H I is centrally depressed. However, the H I radial surface density in early type galaxies typically peaks around 1–4 $M_\odot pc^{-2}$ while in late type galaxies it peaks around 5–10 $M_\odot pc^{-2}$. Bigiel et al. (2008) find $\Sigma_{H I_{saturation}}$ $\sim$9 $M_\odot pc^{-2}$ for their sample of molecule-dominated galaxies. Finally, the H_2 distribution is less extended than the stellar distribution in the disks of spiral galaxies, typically $0.5R_{25}$ while the H I distribution is more extended, typically out to $\sim$2R_{25} but can be as large as $4R_{25}$ in some late–type galaxies (Briggs 1982).

4.1.2   Azimuthal Distribution

Just as there are differences in the radial distribution of H_2 and H I so too are there differences in the azimuthal distribution of both gases. Detailed two-dimensional, interferometric maps show that CO(1-0) emission, and thus the H_2 is concentrated along dust lanes along the inner edge of spiral arms (Lo et al 1987, Vogel et al. 1988, Rand & Kulkarni 1990). The largest concentrations of molecular gas are termed giant molecular associations (GMAs) (Vogel et al. 1988) and typically have masses $>10^7 M_\odot$. These maxima in CO(1-0) emission typically coincide with enhanced

regions of dust obscuration along the spiral arms and approximately 25% of the CO(1-0) emission is concentrated in the spiral arms (Vogel et al. 1988). Further downstream, the H I gas concentrates in regions of ongoing star formation, near the Hα emission in the arms (Rand & Tilanus 1990). This offset in H I emission from H$_2$ azimuthally along spiral arms is believed to arise from the photo-dissociation of H$_2$ gas by young, recently formed stars in the spiral arms (Allen et al. 1985; Kennicutt et al. 2007).

In this chapter we present the new CARMA CO(1-0) channel and velocity integrated maps for our sample of galaxies. Using the CO(1-0) emission to trace the distribution of H$_2$ in the galaxies, we compare the two-dimensional distribution of the molecular to atomic gas along the spiral arms. We also compare the azimuthal distribution of the neutral gas to both 8 μm and Hα emission within the galaxies, which trace the location of the primary dust lanes in the spiral galaxies, shown in §4.4, and star formation, respectively.

4.2   The Molecular ISM: CO(1-0)

4.2.1   Maps of CO(1-0) Emission

The new CARMA CO(1-0) data are presented in Figures 4.1- 4.15. Both channel maps and velocity-integrated intensity ("moment-0") emission maps are presented for each source. The channel maps for each galaxy are presented for the observed velocity range in Figures 4.1, 4.2, 4.4, 4.5, 4.6, 4.8, 4.9, 4.11, 4.12, & 4.13. The channel maps are shown in false-color and the stretch is shown to the right of the

last velocity panel, which ranges from $2\sigma_{rms}$ to 0.75 times the peak in the channel map. The gain=0.5 locus is represented by the blue solid contour displayed in the first velocity panel. In the upper left corner of the velocity panels is the V_{LSR}. The velocity width of each channel is 2.54 km s^{-1} for NGC 0628 and 5.08 km s^{-1} for the other galaxies.

The distribution of CO(1-0) velocity-integrated intensity emission is shown by the red contours in Figures 4.3, 4.7, 4.10, 4.14, & 4.15; the CO(1-0)contours are overlaid on a grey-scale image of R-band emission. The velocity-integrated emission maps were created using the BIMA SONG "smooth-and-mask" technique (Helfer et al. 2003). First, a mask was created by smoothing with a Gaussian of 8″ or 12″ depending on the amount of interarm emission in the galaxy; all pixels above $3\sigma_{rms}$ were included in the mas. Then the original resolution datacubes were summed over the velocity range of emission, accepting only those pixels in the mask, to create the masked velocity-integrated intensity maps.

For each galaxy, the CO(1-0) velocity-integrated intensity emission is displayed in a similar manner to the BIMA SONG catalog form (Helfer et al. 2003) for easy comparison with the previous CO(1-0) observations. The contours in the left panel of Figures 4.3, 4.7, 4.10, 4.14, & 4.15 are spaced logarithmically with levels at 2.51 times the previous level (i.e. comparable to the astronomical magnitude scale). As discussed in §3.3.1.5, each of the galaxies is mosaiced with a large number of pointings, in which the FWHM of the primary beam overlaps, and so the sensitivity and the primary beam response vary across the map. The dashed blue line indicates the region within which the primary beam gain was scaled so that the response (flux

scale) is uniform; the solid blue line indicates where the response and therefore the fluxes are attenuated by 50%.

The velocity-integrated CO(1-0) emission is also displayed in the right panel of Figures 4.3, 4.7, 4.10, 4.14, & 4.15 as black contours over a false color image. The contours are spaced 1.59 times the previous level. The false color images for each galaxy have the same minimum, -4 Jy beam^{-1} km s^{-1}, and the same maximum, 50 Jy beam^{-1} km s^{-1}. In the lower left hand corner, the FWHM and P.A. of the synthesized beam are shown. There is also a vertical line delineating the angular size of 1 kpc at the assumed distances to the galaxies.

4.2.2 Distribution of CO(1-0) Emission

As can be seen from Figures 4.1-4.15, the peak intensity in our sample of galaxies varies greatly. However, even in the galaxies with the lowest intensity, the CO(1-0) is primarily concentrated along spiral arms with semi-regular peaks in the emission. The emission peaks upstream from the stellar component of the spiral arms seen in the R-band images. Some CO(1-0) emission extends past the spiral arms into the interarm region, shearing out from CO(1-0) peaks. Now we discuss the CO(1-0) distribution in each galaxy.

4.2.2.1 NGC 0628

The CO(1-0) emission nicely delineates the grand design, two-arm spiral pattern of NGC 0628, with fainter interarm emission connecting the two arms. Inside of $\sim$0.5 kpc, there is an overall central depression of CO(1-0) emission that was noted by

Figure 4.1 Channel maps of CO(1-0) emission in NGC 0628. V_{LSR} is indicated in the upper left of each panel. The flux scale is shown in the color bar, with a maximum of 0.43 Jy km^{-1} and a minimum of 0.07 Jy km^{-1}.

Figure 4.2 NGC 0628. Continued from Fig.4.1.

Figure 4.3 Velocity–integrated CO(1-0) emission in NGC 0628. (Left) CO(1-0) contours overlaid on R–band DSS image.

Figure 4.4 Channel maps of CO(1-0) emission in NGC 3627. V_{LSR} is indicated in the upper left of each panel. The flux scale is shown in the color bar, with a maximum of 0.84 Jy km^{-1} and a minimum of 0.17 Jy km^{-1}.

Figure 4.5 NGC 3627. Continued from Fig.4.4.

Figure 4.6 NGC 3627. Continued from Fig.4.5.

Figure 4.7 Velocity–integrated CO(1-0) emission in NGC 3627. (Left) CO(1-0) contours overlaid on R–band DSS image.

Figure 4.8 Channel maps of CO(1-0) emission in NGC 4736. V_{LSR} is indicated in the upper left of each panel. The flux scale is shown in the color bar, with a maximum of 0.53 Jy km^{-1} and a minimum of 0.076 Jy km^{-1}.

Figure 4.9 NGC 4736. Continued from Fig.4.8

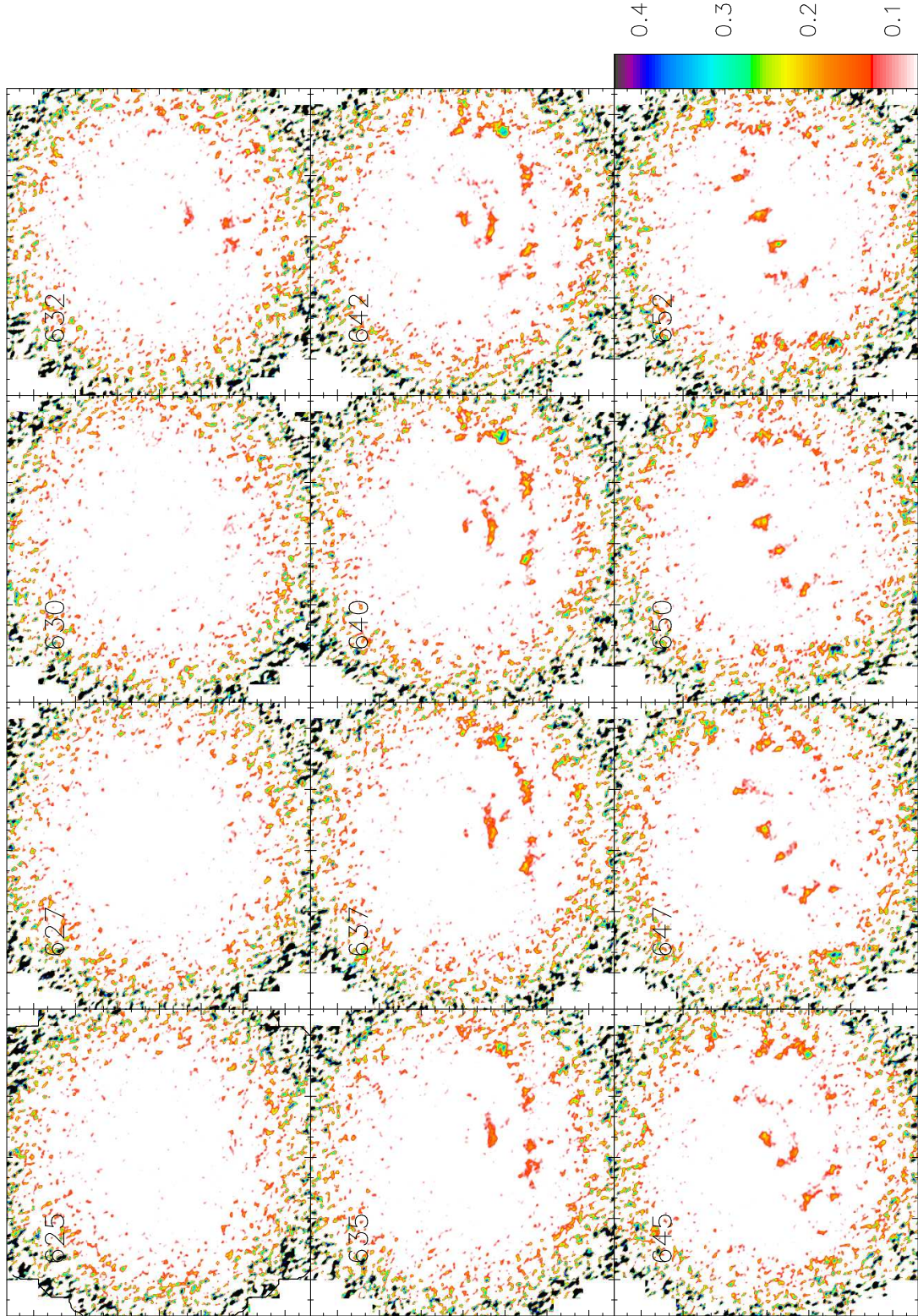Figure 4.10 Velocity–integrated CO(1-0) emission in NGC 4736. (Left) CO(1-0) contours overlaid on R–band DSS image.
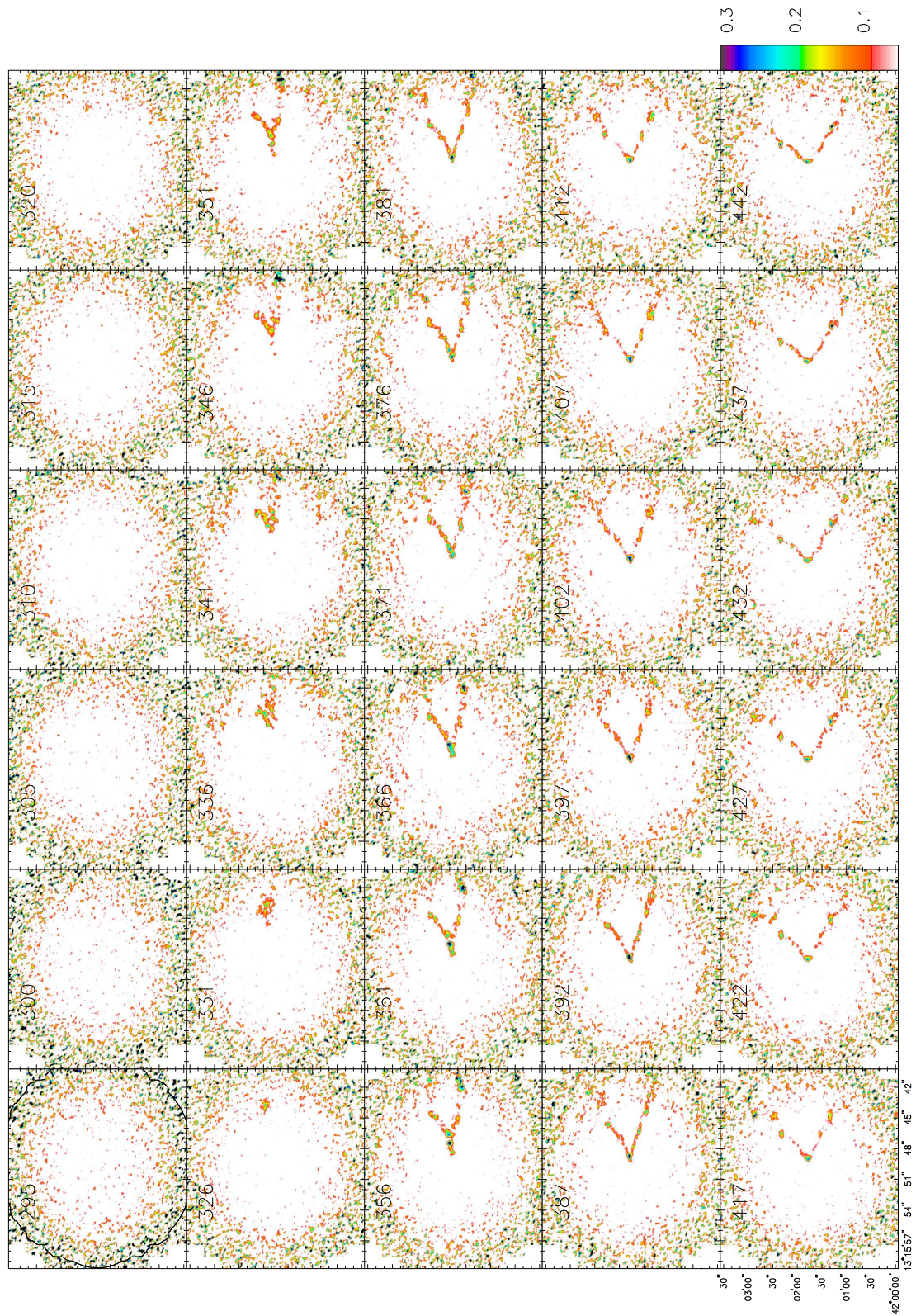
Figure 4.11 Channel maps of CO(1-0) emission in NGC 5055. V_{LSR} is indicated in the upper left of each panel. The flux scale is shown in the color bar, with a maximum of 0.31 Jy km^{-1} and a minimum of 0.05 Jy km^{-1}.
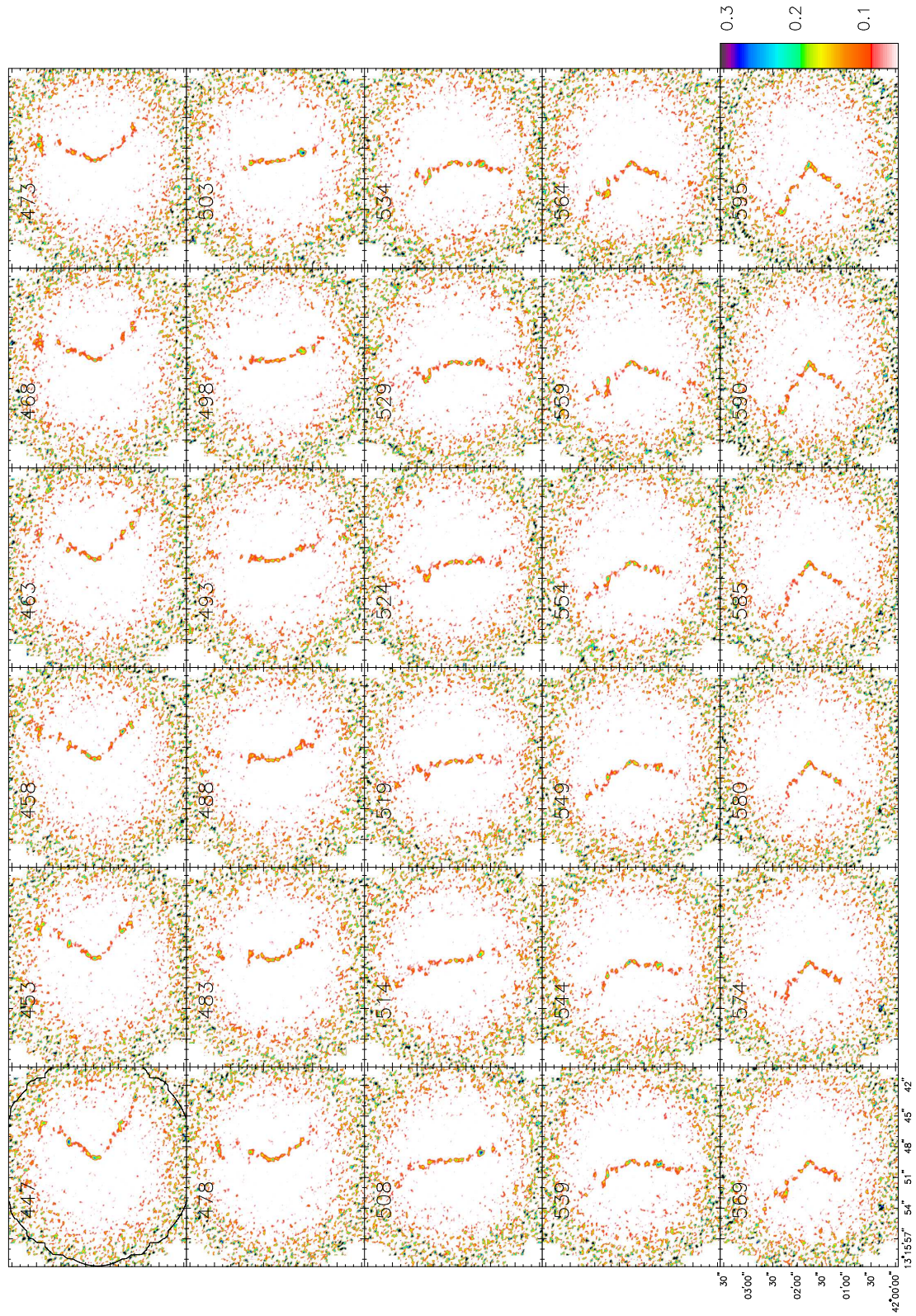
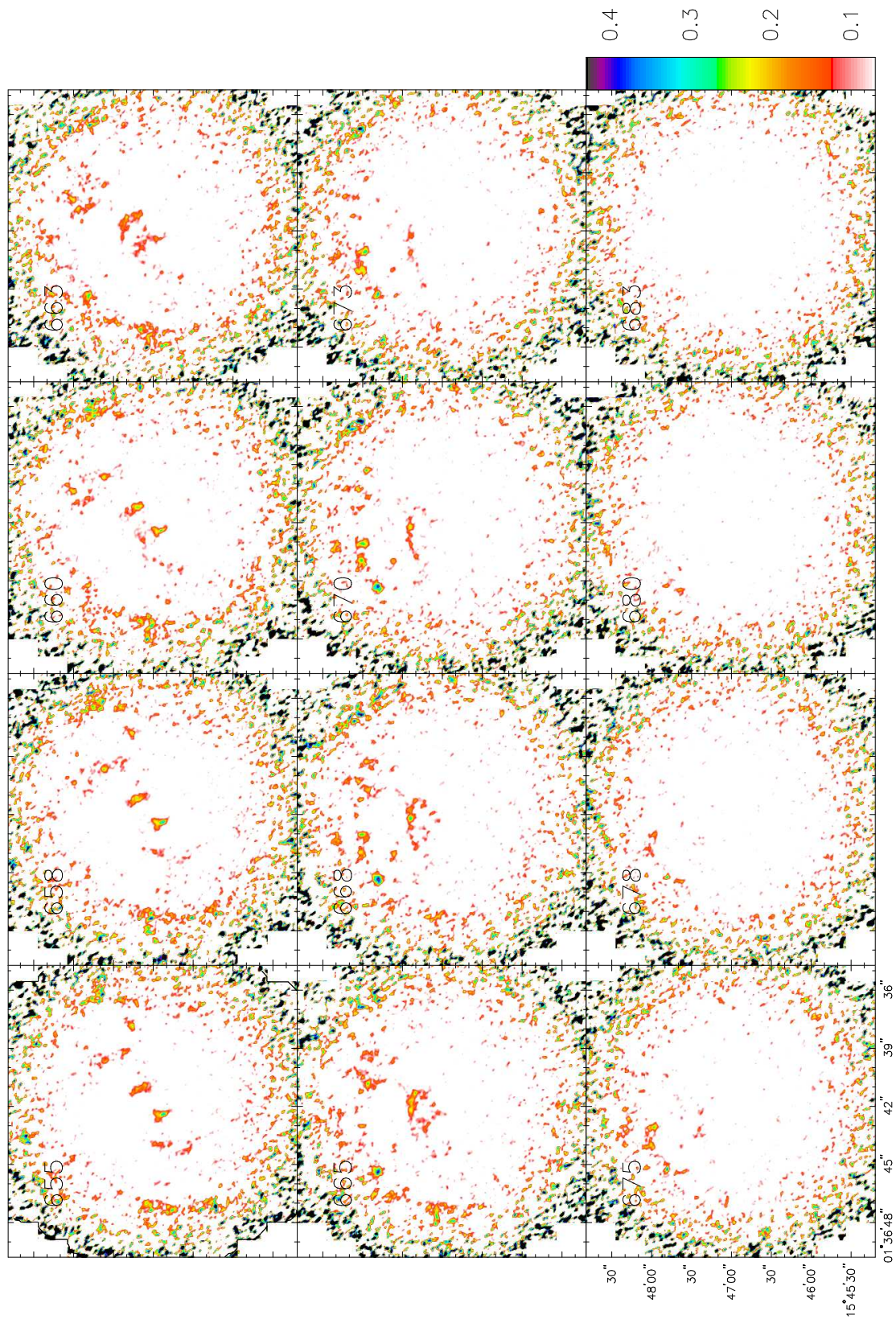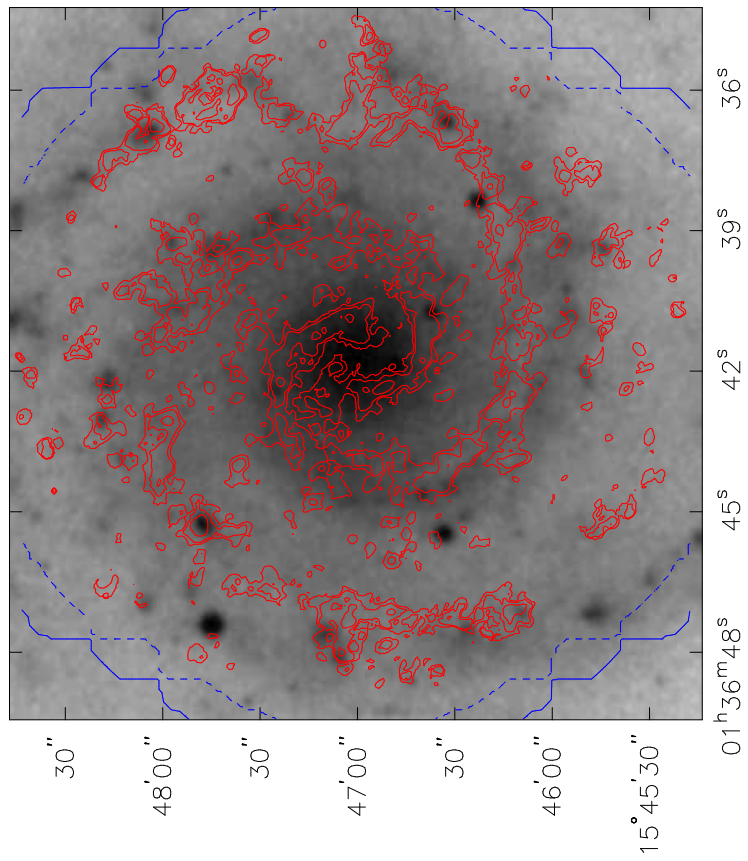Figure 4.12 NGC 5055. Continued from Fig.4.11.
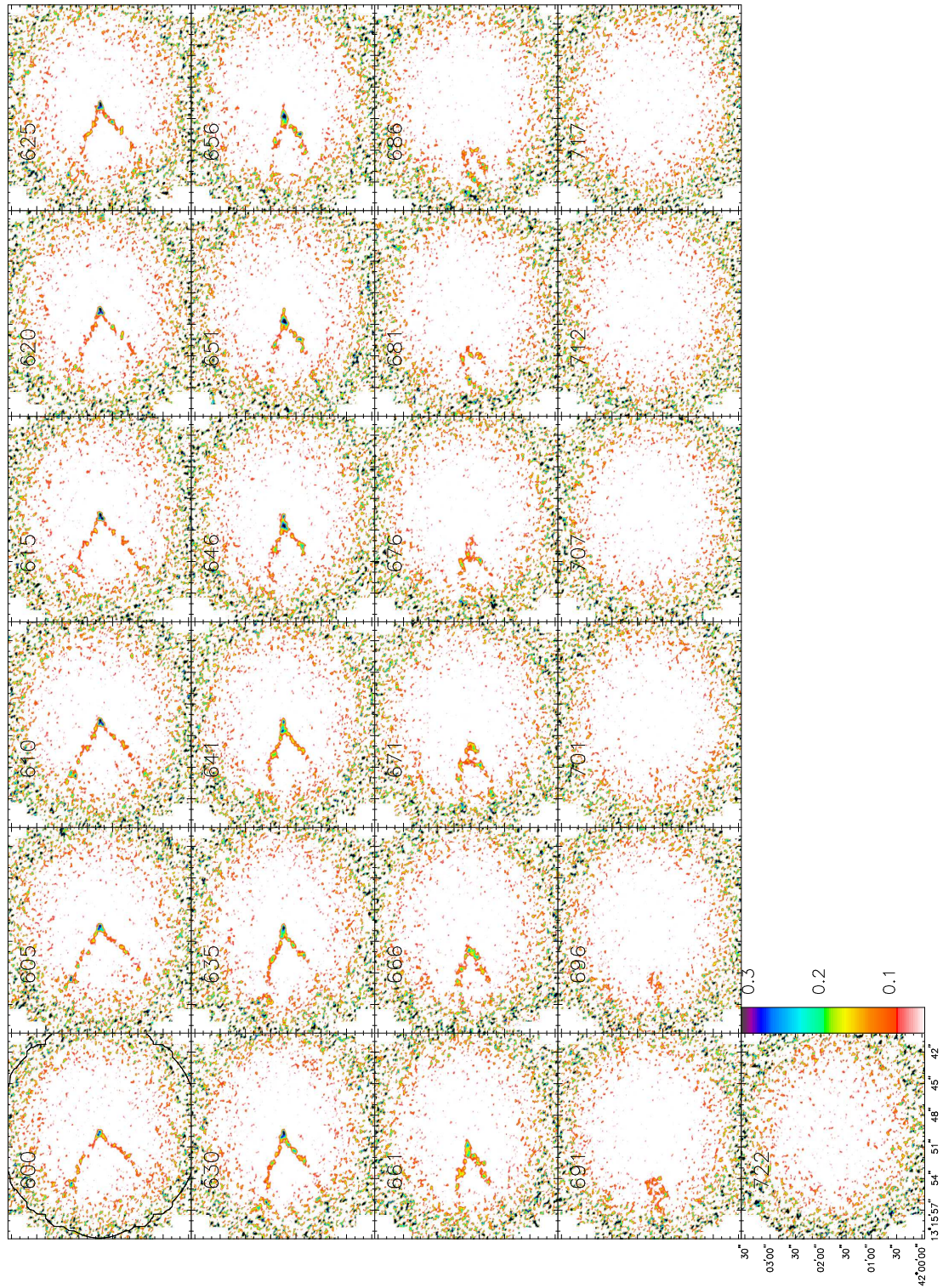
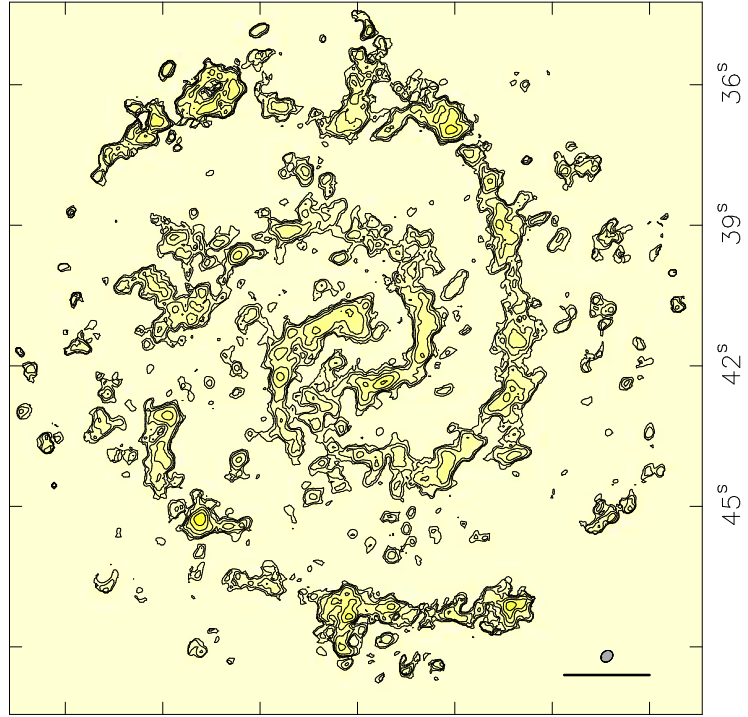Figure 4.13 NGC 5055. Continued from Fig.4.12.
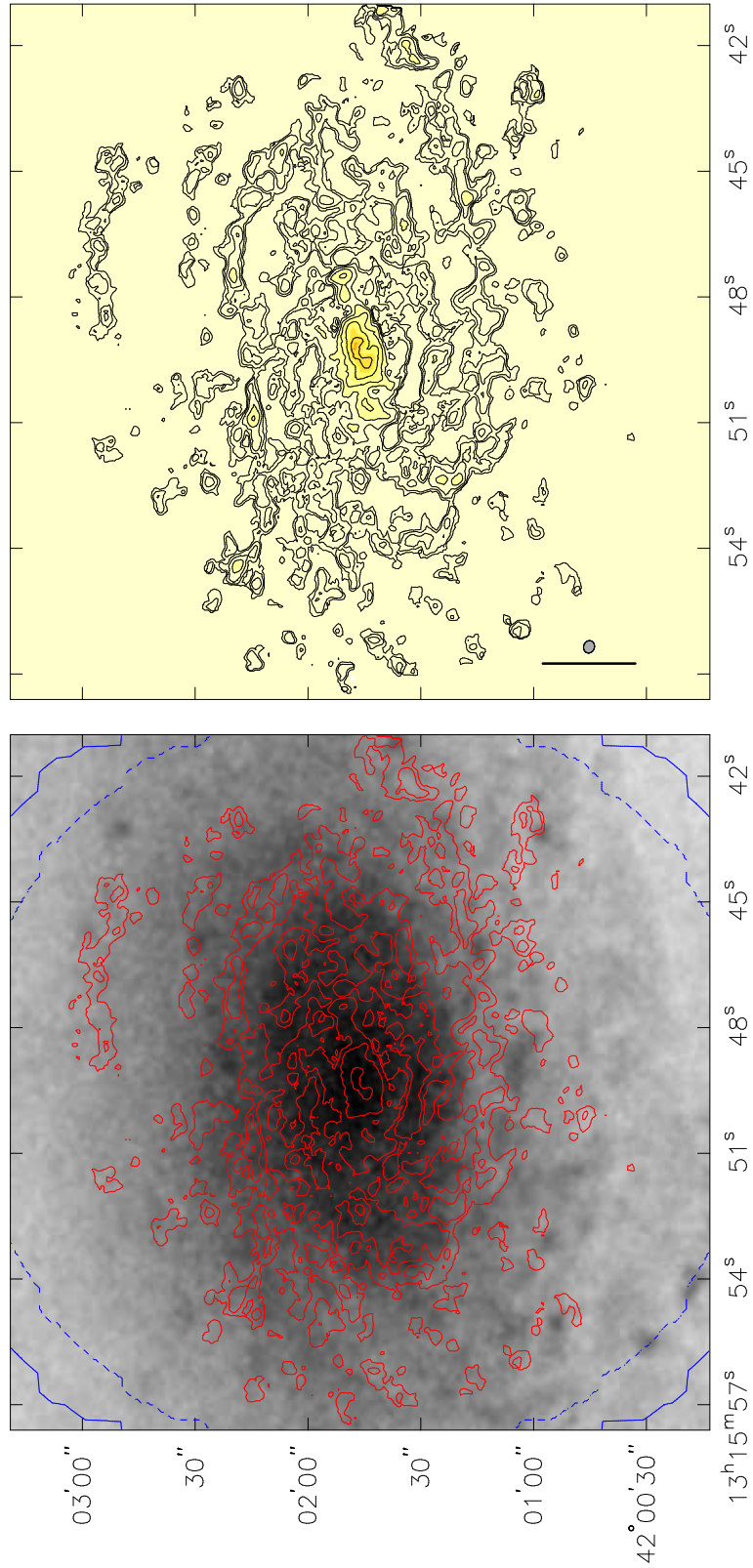
Figure 4.14 Velocity–integrated CO(1-0) emission in NGC 5055. (Left) CO(1-0)
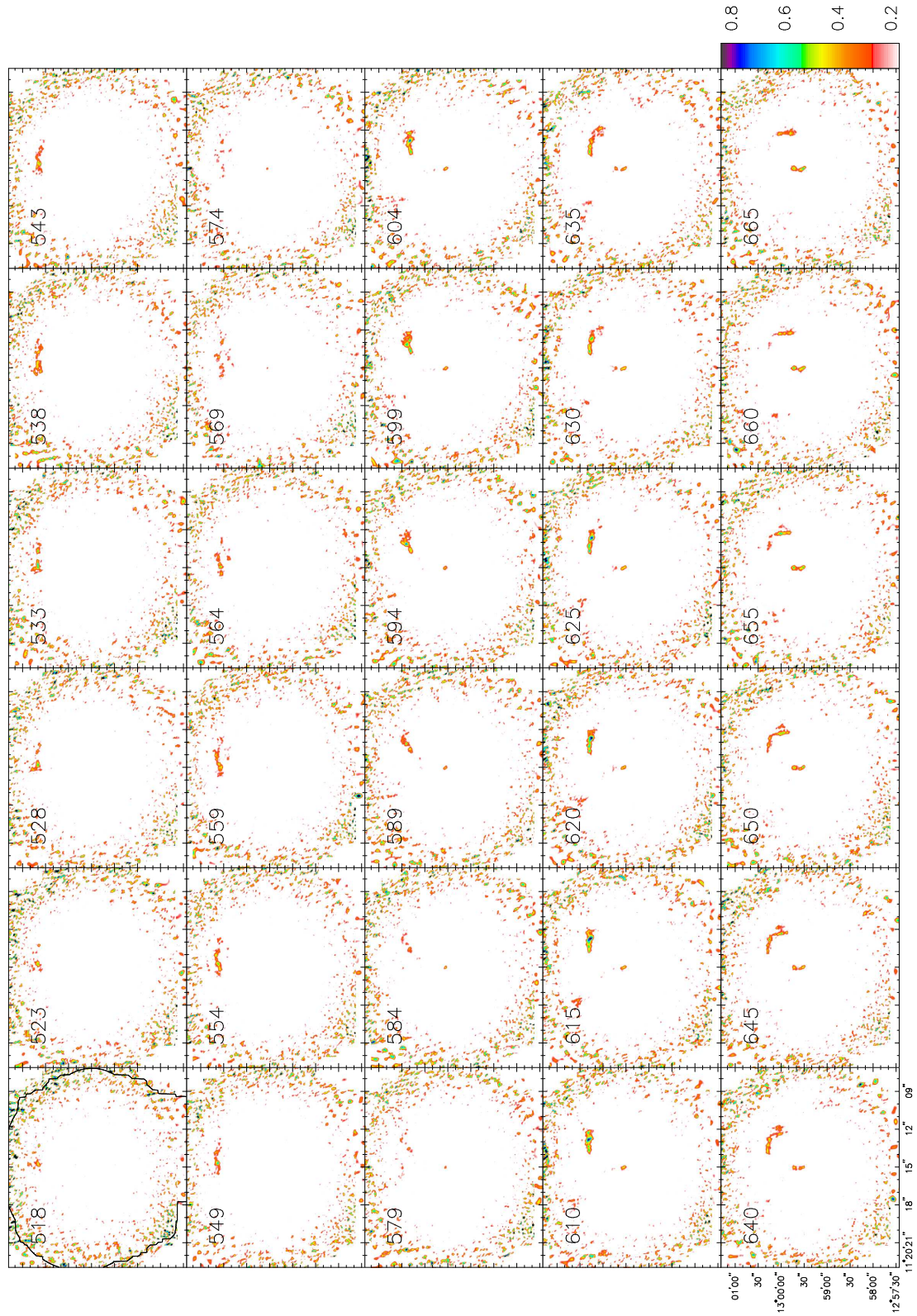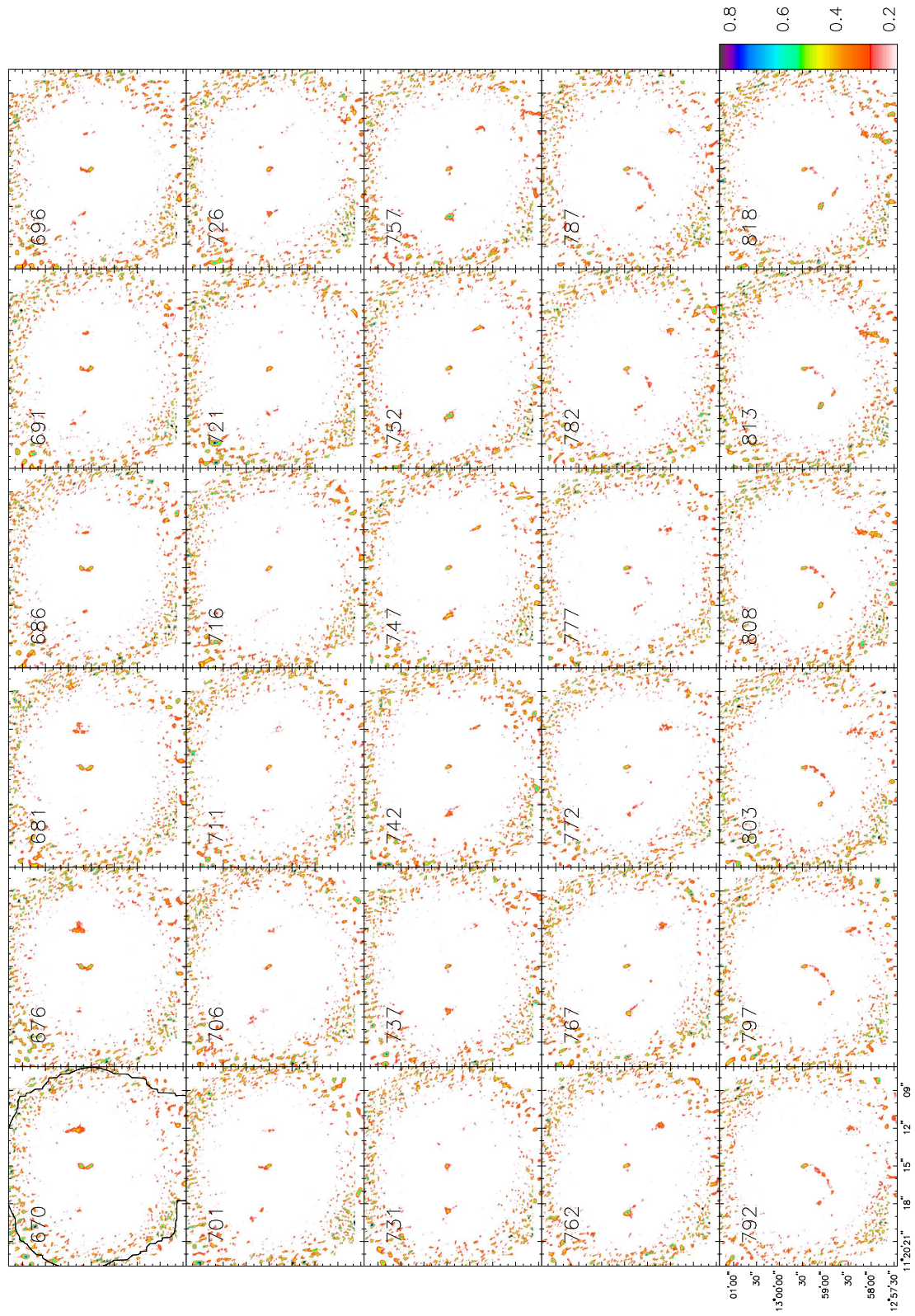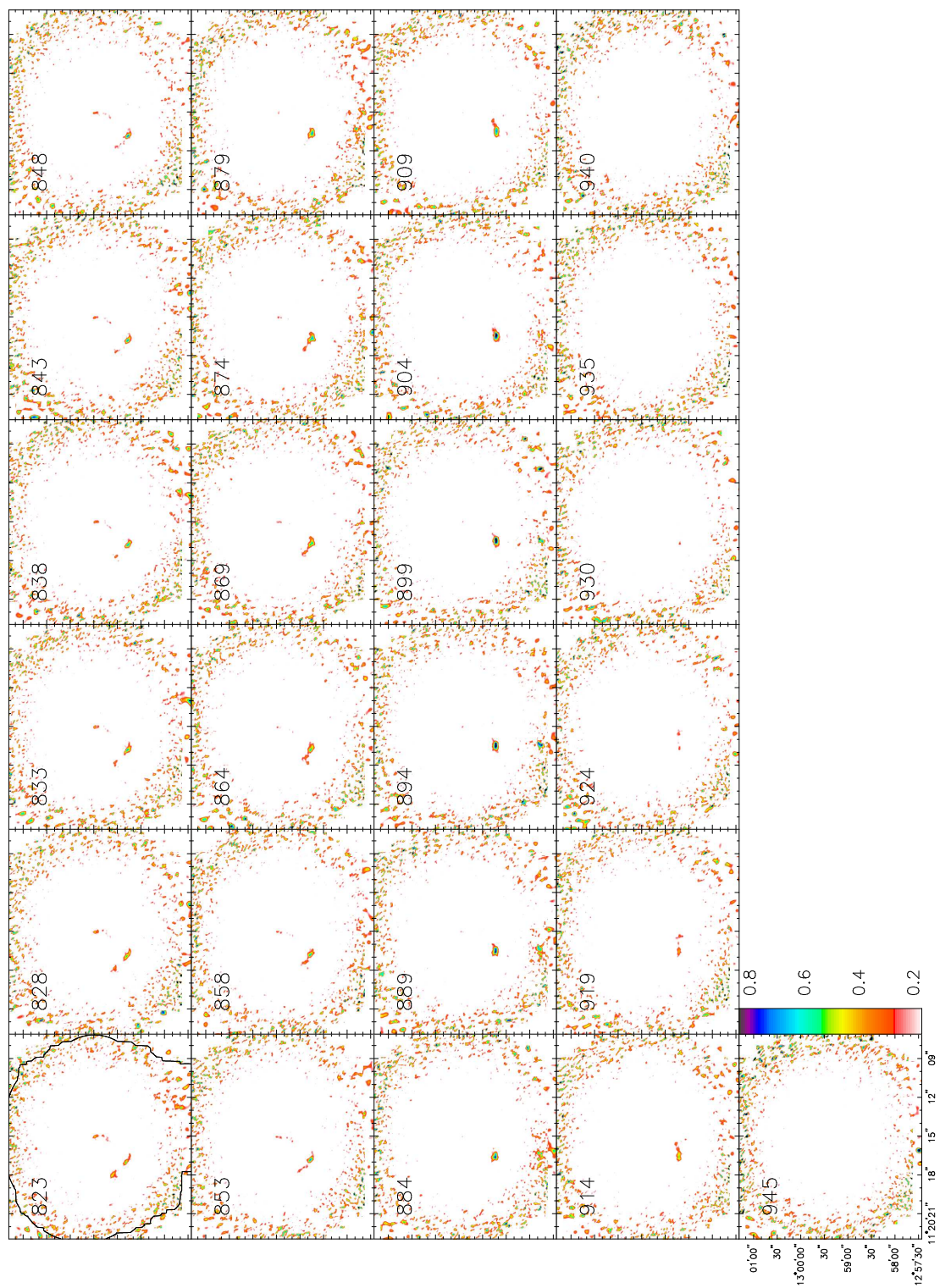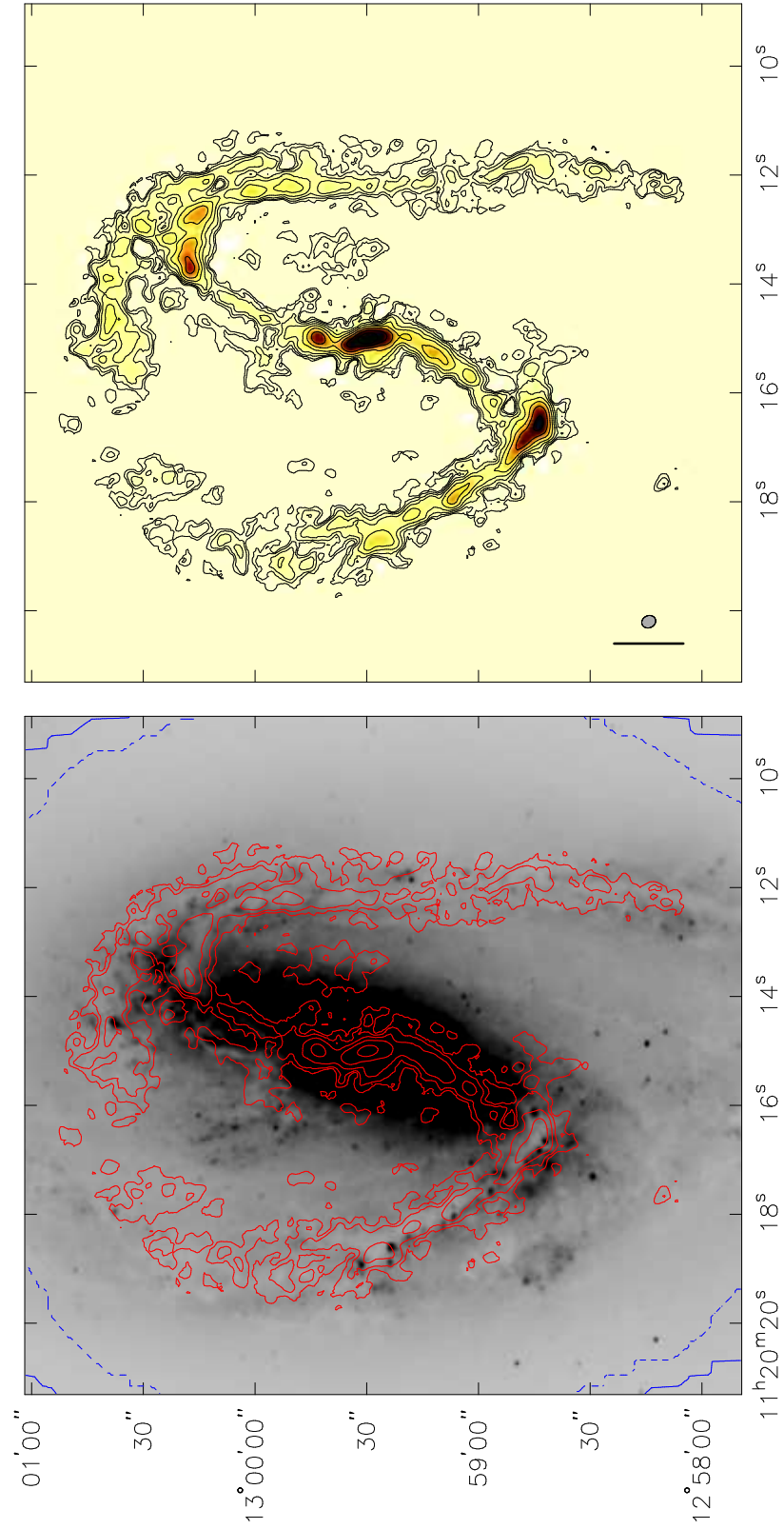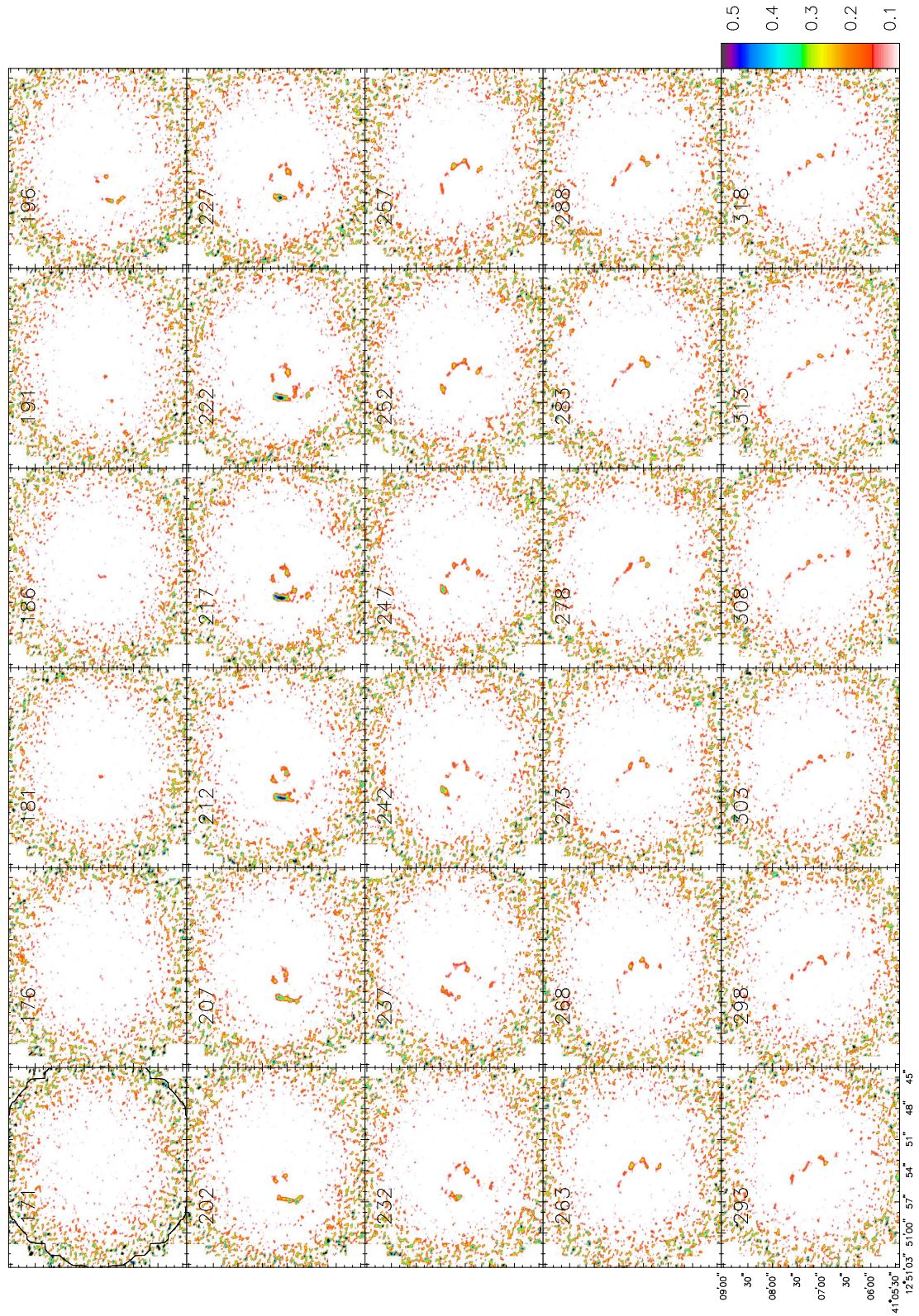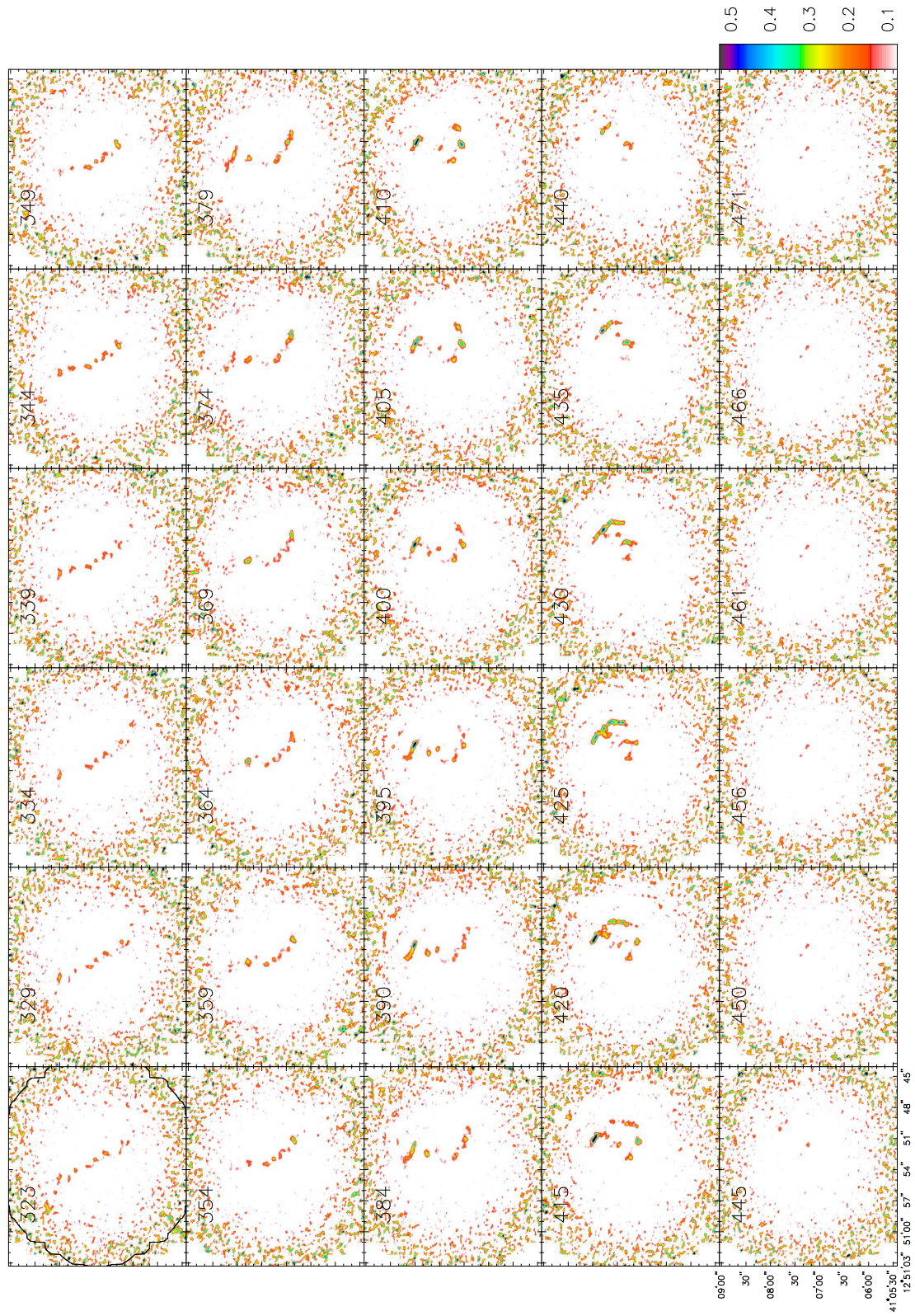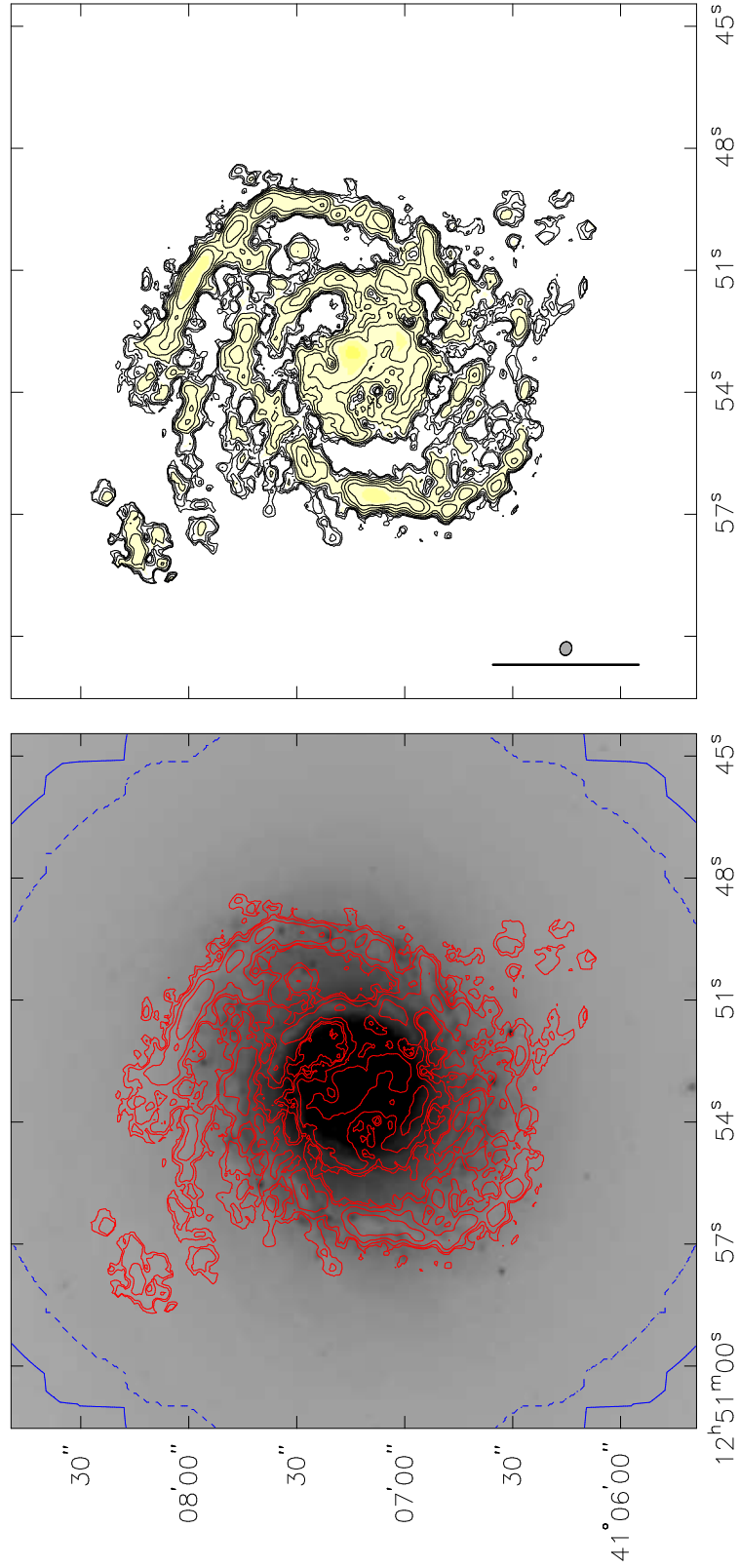contours overlaid on R–band DSS image.
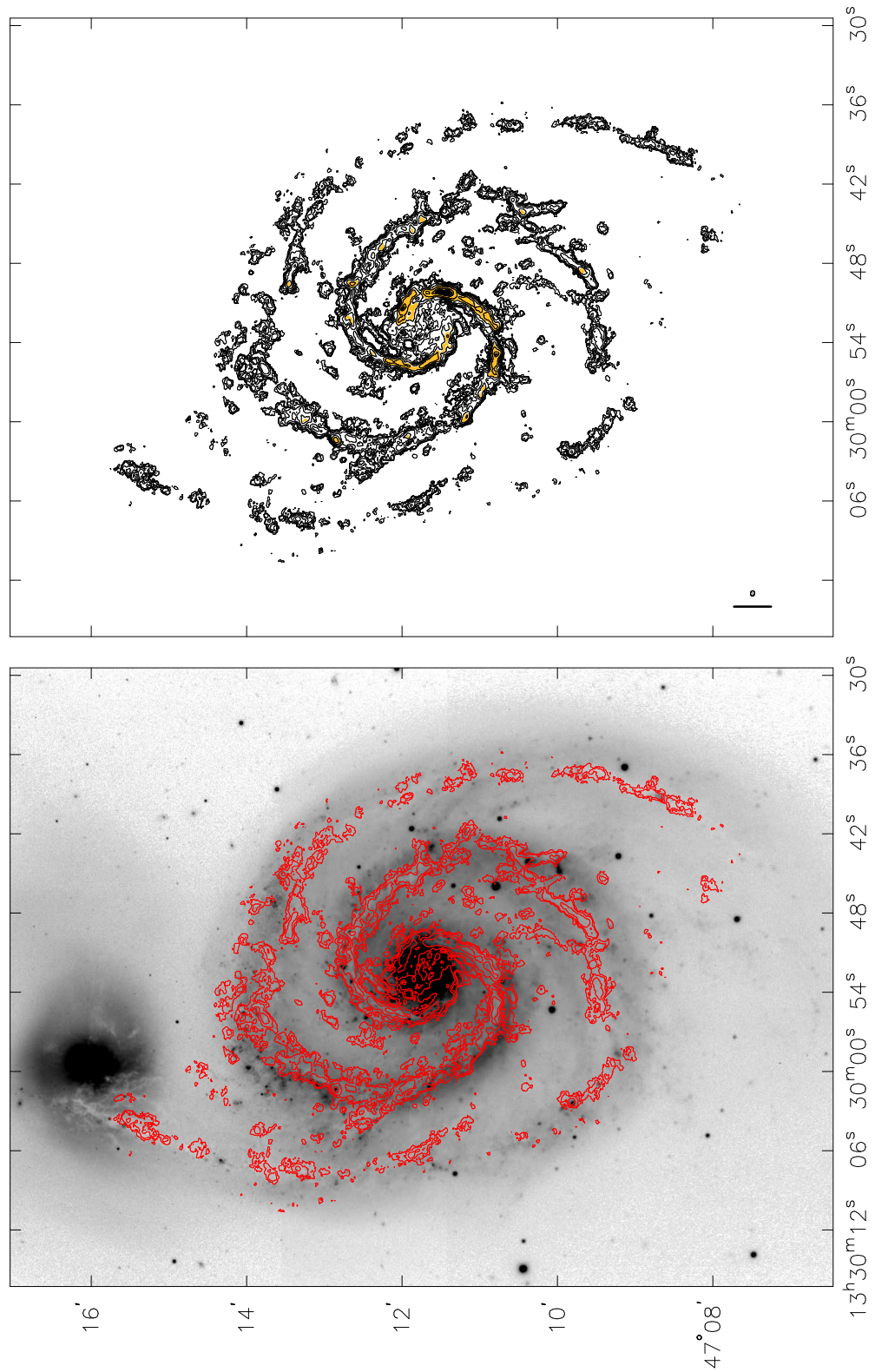
Figure 4.15 Velocity–integrated CO(1-0) emission in NGC 5194. (Left) CO(1-0) contours overlaid on R–band DSS image.

Regan et al. (2001). The arms are thin, coinciding with the narrow dust lanes on the inner edge of the spiral arms seen in Fig 4.3, upstream from the stellar component in the R-band image (it is difficult to see the dust lanes in the printed version). The CO(1-0) arms exhibit numerous emission peaks along the arms that are spaced at quasi-regular intervals. Inspection of the channel maps shows that most interarm emission extends from these peaks, and is concentrated in feathers (discussed in Chapter 5). Overall, the CO(1-0) emission in NGC 0628 is quite a bit weaker than in the rest of the sample.

4.2.2.2 NGC 3627

The distribution of CO(1-0) within NGC 3627 is dominated by the large central bar from which well-defined spiral arms emanate. Around the bar an inner ring of CO(1-0) is resolved, which was first detected by Regan et al. (2002). The brightest peaks of CO(1-0) emission in NGC 3627 occur at the nucleus and the two bar ends. The spiral arm emanating from the end of the northern bar exhibits two parallel structures, which we call 1a & 1b. One, 1a, emanates from the end of the bar; 1b occurs on the outside or downstream of 1a and begins further north. Fainter interarm CO(1-0) emission appears to link 1a and 1b. There are numerous, regularly spaced peaks of CO(1-0) emission along the spiral arms with fainter CO(1-0) emission observed to extend into the interarm region from these peaks, except where the faint emission connects structures 1a to 1b.

4.2.2.3   NGC 4736

In NGC 4736 the CO(1-0) emission clearly traces the nuclear bar and the two prominent spiral arms, which begin at a galactocentric radius of $\sim 30''$. The two spiral arms are very tightly wrapped and are displaced upstream from the stellar component in the R-band image (see Fig. 4.10). The CO(1-0) arms are quite thin and primarily composed of discrete, quasi-regularly spaced, peaks of emission. Unlike NGC 3627, the highest peaks of CO(1-0) emission do not occur at the beginning of the arms, near the bar ends. The peak of emission along the western arm occurs almost at the end of the observed CO(1-0) arm and stellar $H\alpha$ ring. Both arms have fainter CO(1-0) emission extending from the peaks. The eastern arm is observed to have longer and more obvious feathers in CO(1-0) than the western arm.

4.2.2.4   NGC 5055

The CO(1-0) emission is strongest at the center of the galaxy and appears elongated, $\sim 30''$ in radius, as noted by Thornley & Mundy (1997). A ring or tight spiral of CO(1-0) emission is detected at a radius of $\sim 40''$ which was previously identified by Thornley (1996) in the NIR. Outside this ring, the CO(1-0) emission forms a two-arm spiral pattern, which is not evident at optical wavelengths. The emission is clumpy along both the inner ring and the spiral arms, with numerous peaks spaced at somewhat regular intervals. The emission is not solely confined to the arms, as noted by Thornley & Mundy (1997) and Tosaki et al. (2002). Clumps of interarm emission are observed, many of which extend from peaks of emission along the arms

and ring into the interarm region.

4.2.2.5   NGC 5194

The grand design spiral arms of NGC 5194 are strong, prominent CO(1-0) emission features. Similar to NGC 0628, NGC 5194 has a central depression of CO(1-0) emission inside a radius of $\sim 8''$ (also noted by Helfer et al. 2003). The arms are thin, composed of discrete clumps of emission spaced at quasi-regular intervals and offset upstream from the stellar component observed in the R-band (see Fig. 4.15). There is interarm emission which appears to emerge from the sites of peak emission along the arms. A few of these feathers span the entire interarm region and connect the two spiral arms.

4.3   Comparison of CO to HI

To directly compare the molecular component of our sample of spiral galaxies to the atomic component, we used The HI Nearby Galaxy Survey (THINGS) newly released observations (Walter et al. 2008). The THINGS HI velocity-integrated intensity maps are presented in false-color in the left panels of Figures 4.16 - 4.20. The right panels show a zoomed in region of the HI marked by a rectangle in the left panels, in which contours of velocity-integrated CO(1-0) emission overlay the HI false color emission. In the right panels, the red contours represent the CO(1-0) velocity-integrated intensity emission; the contour levels are the same as in Figures 4.3, 4.7, 4.10, 4.14, & 4.15, spaced logarithmically at half magnitude intervals; the background false-color HI intensity map is displayed for the area imaged by

CARMA.

As can be seen in the left panels of Figures 4.16 - 4.20, a central depression of
H I is observed in each galaxy, which was also noted by Bigiel et al. (2008). Beyond
the central H I depression, the CO(1-0) and H I distributions can be compared. In
NGC 0628, NGC 3627, NGC 4736, and NGC 5194 the H I emission peaks along
the CO(1-0) arms, particularly in NGC 4736, though there is not a 1:1 correlation
between the location of CO(1-0) and H I peaks along the arms. The H I arms are
typically wider than the CO(1-0) arms, particularly in NGC 3627. For NGC 5055,
the H I appears more "fleece"-like than the CO(1-0) emission, similar to the light
at optical wavelengths, though there are indications that the H I traces the CO(1-0)
spiral arms. Finally, there is interarm H I emission in each of the galaxies, which
emanates from peaks of H I emission along the spiral arms. These feathers observed
in H I are typically wider than those seen in CO(1-0) and extend further into the
interarm region. Many of the H I feathers coincide with those observed in CO(1-0).

Previous studies have shown that for a wide range of spiral galaxy types it is
the *total* gaseous surface density, $\Sigma_{\mathrm{total}_{gas}} = \Sigma_{\mathrm{H_2}} + \Sigma_{\mathrm{H\,I}}$, which correlates most strongly
with the SFR per unit area (Kennicutt 1998b, 1989). However, Wong & Blitz
(2002) and Bigiel et al. (2008) showed that within "molecule-rich" spiral galaxies,
the azimuthally averaged SFR correlates best with $\Sigma_{\mathrm{H_2}}$. Their samples included
NGC 0628, NGC 4736, NGC 5055, and NGC 5194, suggesting that for our sample
of galaxies the molecular gas is the most influential component. However, these
studies performed azimuthal averages over the disk of the galaxies, which smooth
out variations in the amount of molecular and atomic gas within the spiral arms.
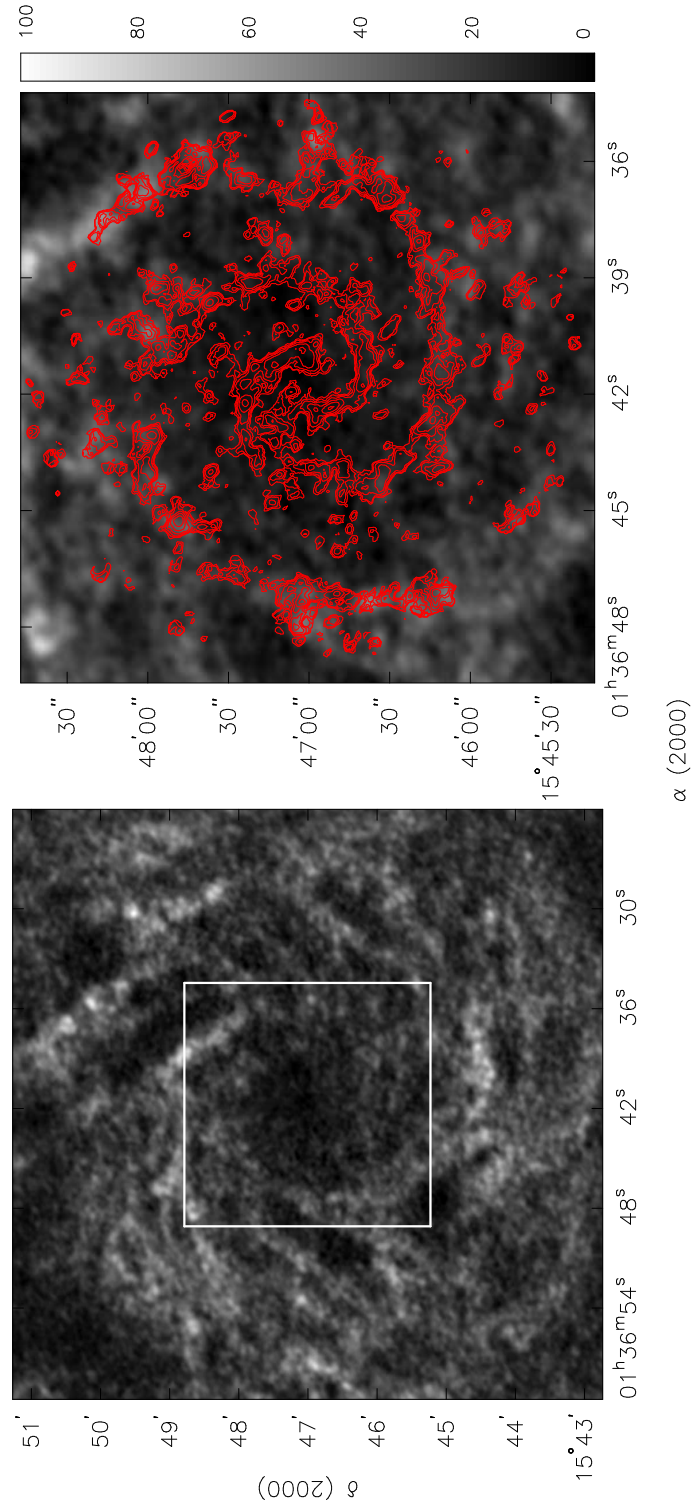
Figure 4.16 Comparison of H I and CO(1-0) in NGC 0628. (*Left*) THINGS velocity–integrated H I map. The grey–scale wedge on the right indicates the flux scale, in units of Jy beam^{-1} m s^{-1}. (*Right*) Zoomed in version of THINGS H I map, with zoomed area indicated by the rectangle in the left panel. Contours of CO(1-0) emission overlay the H I image, with contours spaced at 1.59 times the previous level.
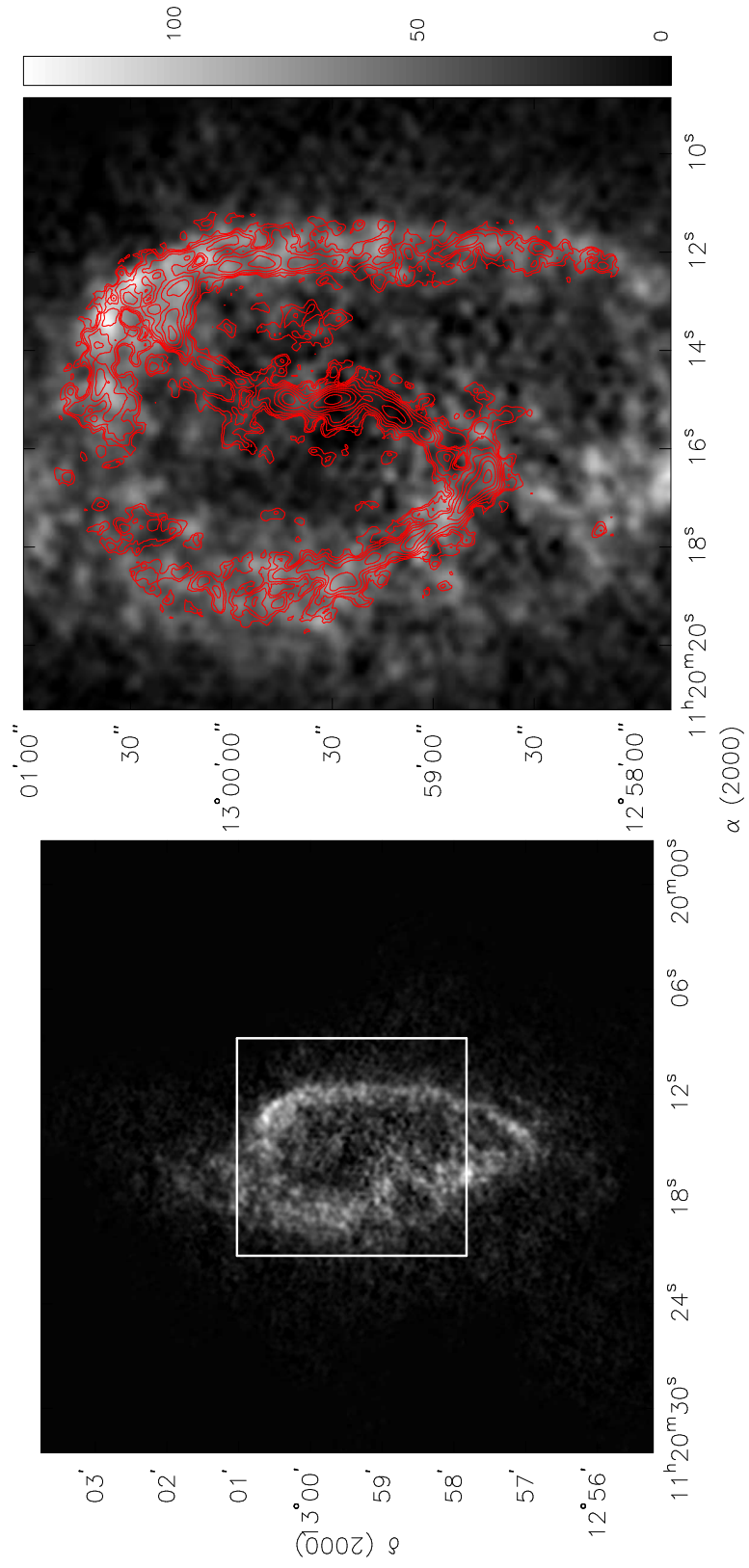
Figure 4.17 Comparison of H I and CO(1-0) in NGC 3627. See Fig. 4.16 for details.
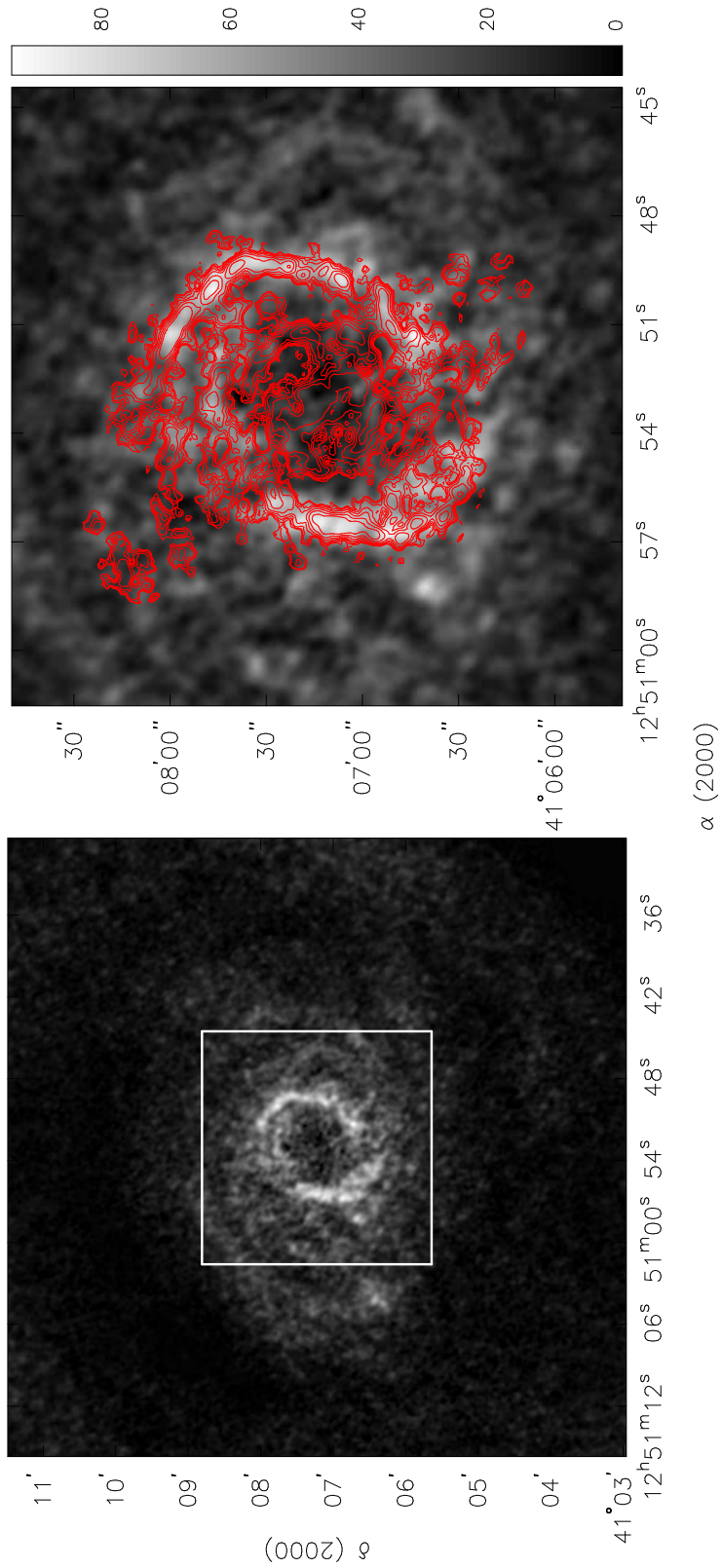
Figure 4.18 Comparison of H I and CO(1-0) in NGC 4736. See Fig. 4.16 for details.
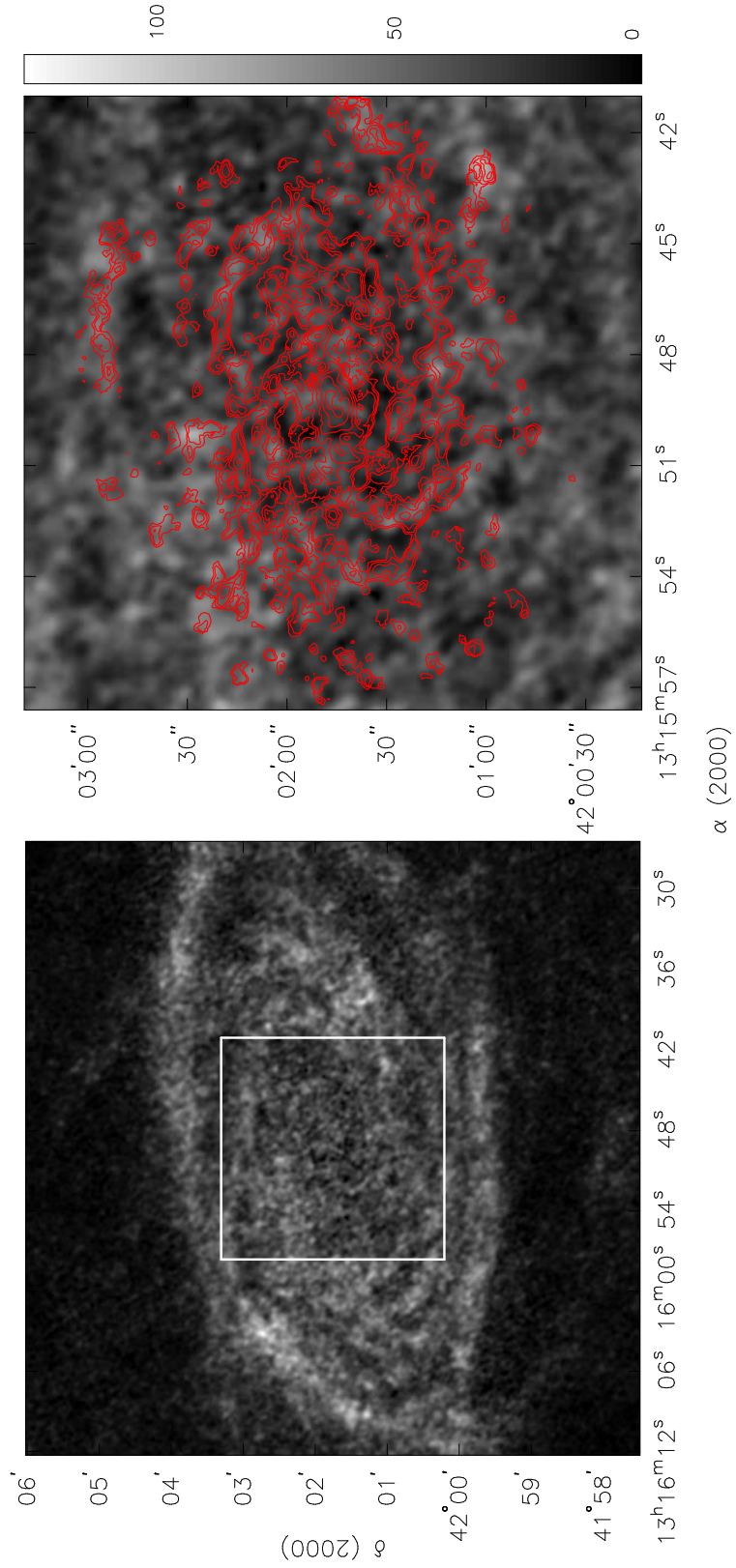
Figure 4.19 Comparison of Hi and CO(1-0) in NGC 5055. See Fig. 4.16 for details.
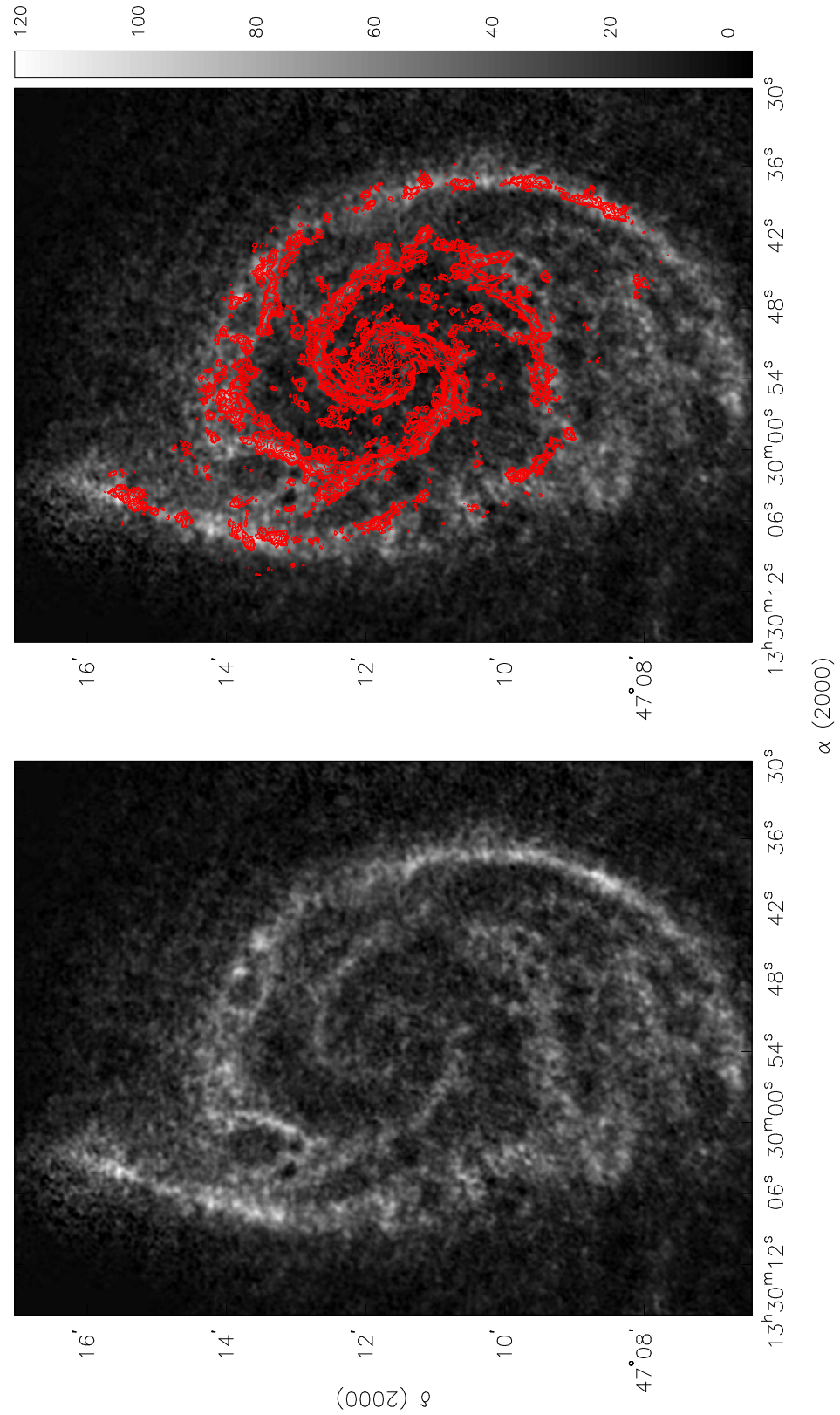
Figure 4.20 Comparison of H I and CO(1-0) in NGC 5194. See Fig. 4.16 for details.

Since, for the purposes of the this study, we are interested in the formation of substructure along spiral arms, it is important to consider these variations and measure the amount of atomic and molecular gas along the arms to determine if they are indeed molecule dominant.

After calibrating the CARMA and THINGS data sets, which were scaled and registered to the same astrometric grid size ($1.5''$) and beam size (6-$7''$), we calculated Σ_{H_2} and Σ_{HI} at each position in each galaxy and measured the contributions from each gaseous component as a function of position along the arms. The atomic and molecular surface densities are plotted as a function of position along the arm in Figures 4.21-4.23, along with the total surface density obtained by summing Σ_{HI} and Σ_{H_2}. It can be seen that in each of the galaxy spiral arms, the gas is mostly molecular along the entire length, often overwhelmingly so.

In Figures 4.24 & 4.25, we show the ratio of HI to total gas surface density for each galaxy for the regions imaged with CARMA, along with lines indicating the arm locus. Again it can be seen that the spiral arms are overwhelmingly molecular. For many of the galaxies, the molecule-dominated region extends well into the interarm. The Σ_{HI} is at most $\sim$20% of the total gaseous surface density within gaseous surface density peaks along the arm.

Since we find spiral arms are strongly molecule dominated, as are the structures extending off the arms (i.e. feathers), we will be justified later in ignoring the atomic contribution to the surface density. Note that this is true even at the relative coarse resolution of the HI observations, and will be even more true at the full resolution of the CO(1-0) observations, enabling us to draw conclusions about surface density
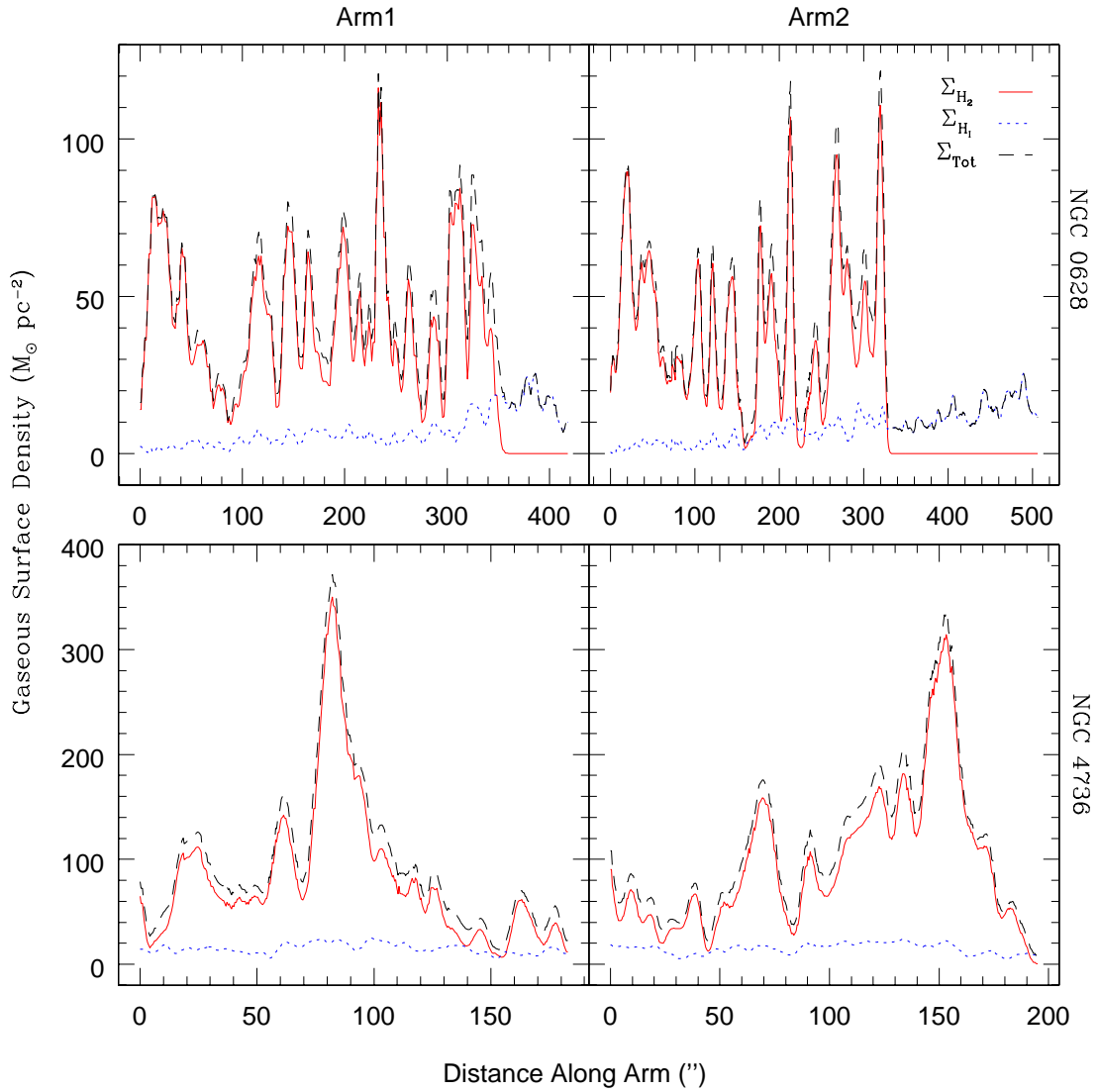
Figure 4.21 Gas surface density as a function of distance along the spiral arms of NGC 0628 (top) and NGC 4736 (bottom). The red solid line shows molecular gas, the blue line atomic gas, and the black line total gas.
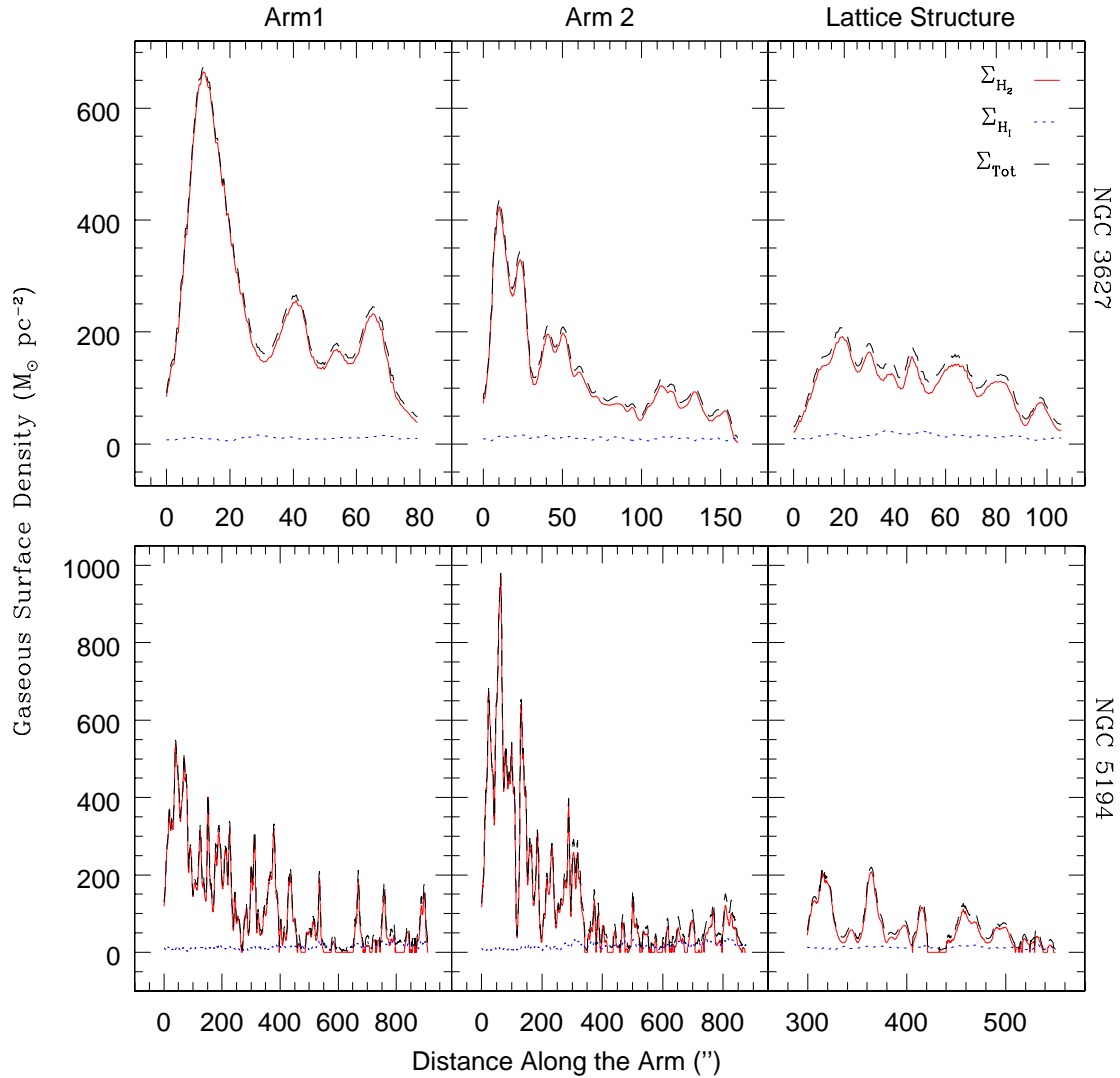
Figure 4.22 Gas surface density as a function of distance along the spiral arms of NGC 3627 (top) and NGC 5194 (bottom). The right panel shows the lattice structures present in both galaxies. The red solid line shows molecular gas, the blue line atomic gas, and the black line total gas.
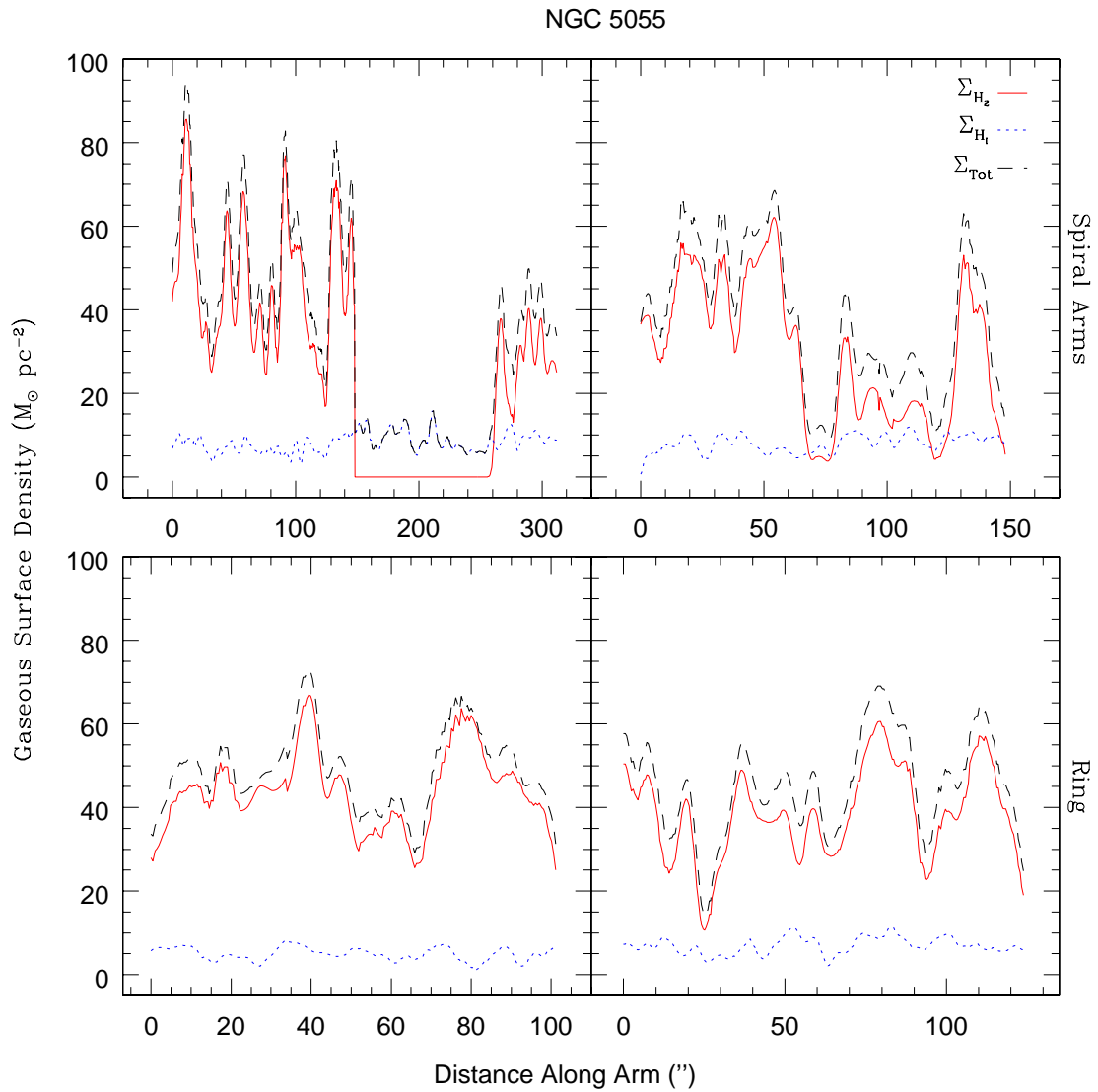
Figure 4.23 Gas surface density as a function of distance along the spiral arms of NGC 5055; Arm 1 top left panel, Arm 2 top right panel. The bottom panels show the ring structure present NGC 5055. The red solid line shows molecular gas, the blue line atomic gas, and the black line total gas.
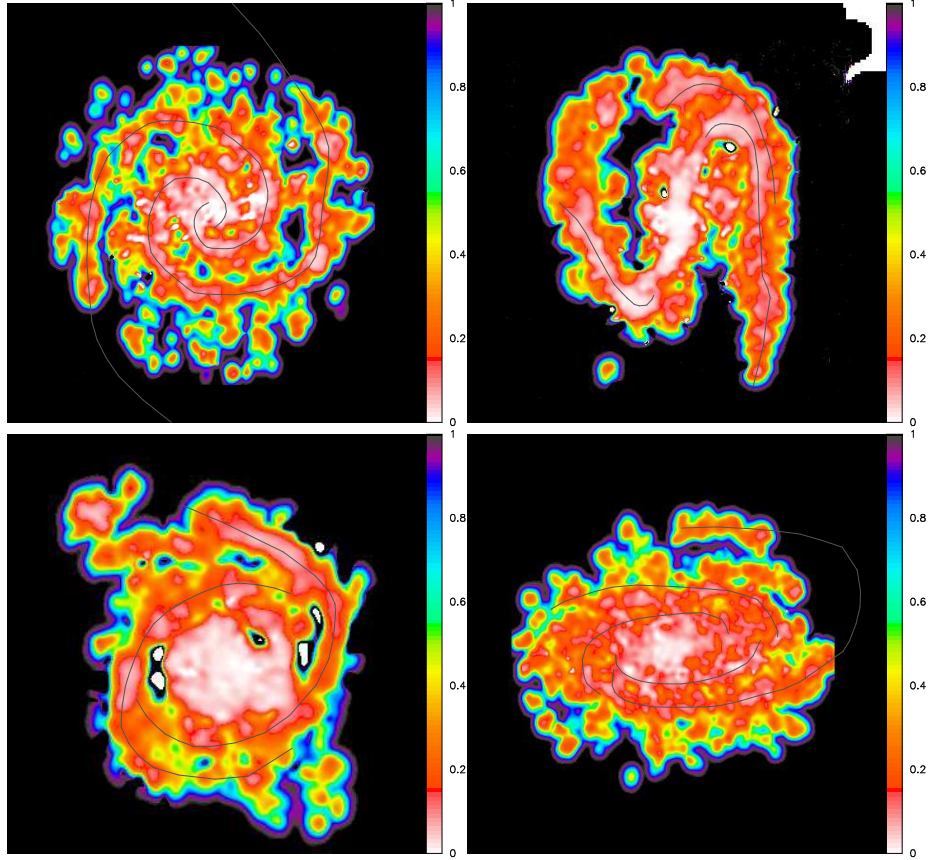
Figure 4.24 The ratio of $\Sigma_{\mathrm{H\,I}}$ to Σ_{tot} shown in false-color. The color bar on the right indicates the ratio. Clockwise from top left: NGC 0628, NGC 3627, NGC 5055, NGC 4736.

at the highest resolution.

4.4   Comparison with Other Tracers

It is also important to compare the neutral gas distribution to other tracers. Differences in the azimuthal distribution of the molecular, atomic, and ionized gas relative to the spiral arm dust lane are important for understanding the mechanisms of massive star formation. The dust lane on the inner edge of a spiral arm is assumed to be the interstellar material that is shocked and compressed by the spiral density wave
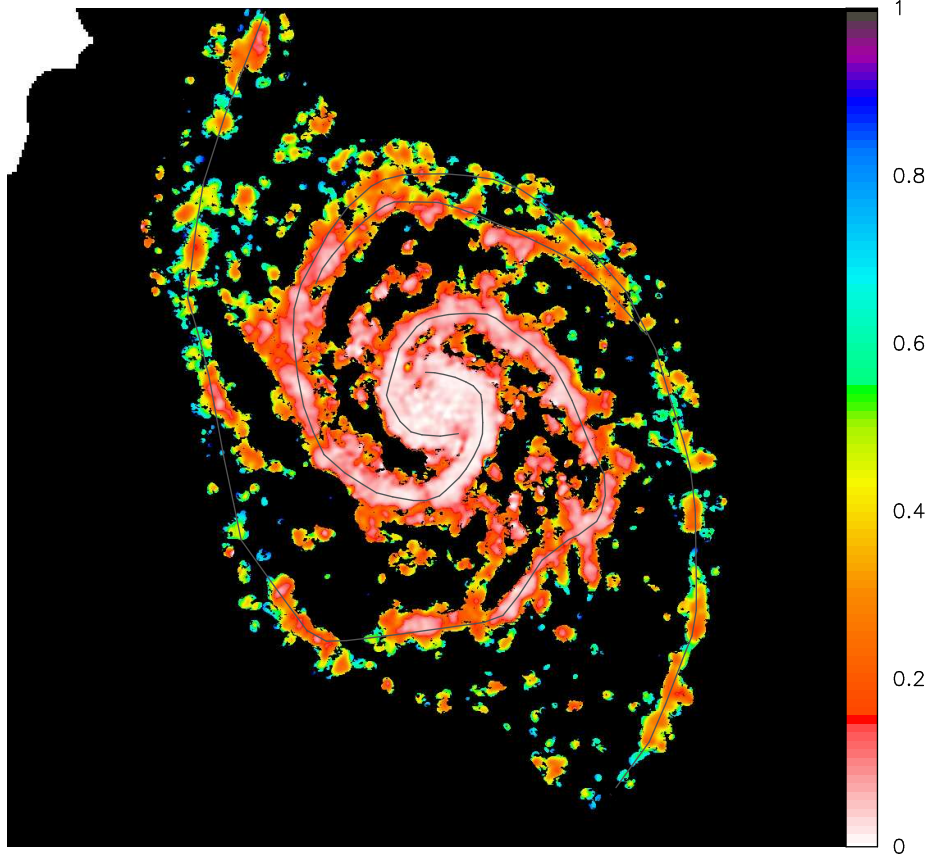
Figure 4.25 The ratio of $\Sigma_{\mathrm{H\,I}}$ to Σ_{tot} shown in false-color for NGC 5194. The color bar on the right indicates the ratio.

(Roberts 1969; Shu 1985; Allen et al. 1985). As discussed in §2.3.5, 8 μm emission is a good tracer of extinction features in the disks of spiral galaxies. Therefore, we used the continuum subtracted, "dust-only" 8 μm images, which are displayed in the left panel of Figures 4.26-4.30, to identify the locus of the primary dust lanes (PDLs) along the spiral arms in our sample of galaxies. To verify these tracings, we used the HST broadband images and the CO(1-0) arms, which are aligned with the dust lanes (see §4.2.2), to confirm the identified position of the PDLs. The right panels show the velocity-integrated H I emission (plotted as in Figures 4.16-4.20), with the addition of the white line showing the locus of the PDL. As can been seen in

Figures 4.26–4.30, the peak of H I emission is aligned with the PDLs in the majority of the galaxies. NGC 5055 is unique from the other galaxies. While there are clearly defined spiral arms in both 8 μm and CO(1-0) emission, the H I emission does not exhibit such features and appears more flocculent than at the other wavelengths.

We also compare the azimuthal location of ionized gas to the location of the PDL and atomic gas. By using Hα emission, we can trace the recent star formation ($\sim$10 million years), which ionizes the surrounding gas along the spiral arms. In Figures 4.31- 4.35 the Spitzer SINGS Ancillary Hα + N II images are presented with the H I emission contours in red, spaced 1.26 times the previous contour, along with the spiral arm PDLs indicated in white. As is illustrated in Figures 4.31- 4.35, the Hα emission peaks downstream from the PDL for the majority of the galaxies in the sample and in the interarm Hα emission appears concentrated along the feathers; this is particularly evident in NGC 0628 and NGC 5194. In both NGC 4736 and NGC 5055, the Hα emission peaks along the PDL, though it also extends well into the interarm region, along feathers. The location of the atomic gas appears related to the location of the ionized gas in NGC 5055. The distribution of Hα in NGC 5055 (Fig 4.34) appears less organized than in the other galaxies due to a large portion of the emission arising from the interarm region as well as from along the PDLs. However, the H I contours are located near the Hα emission, which results in atomic gas being spread out throughout the disk of the galaxy and appearing more flocculent at the resolution of the H I map.
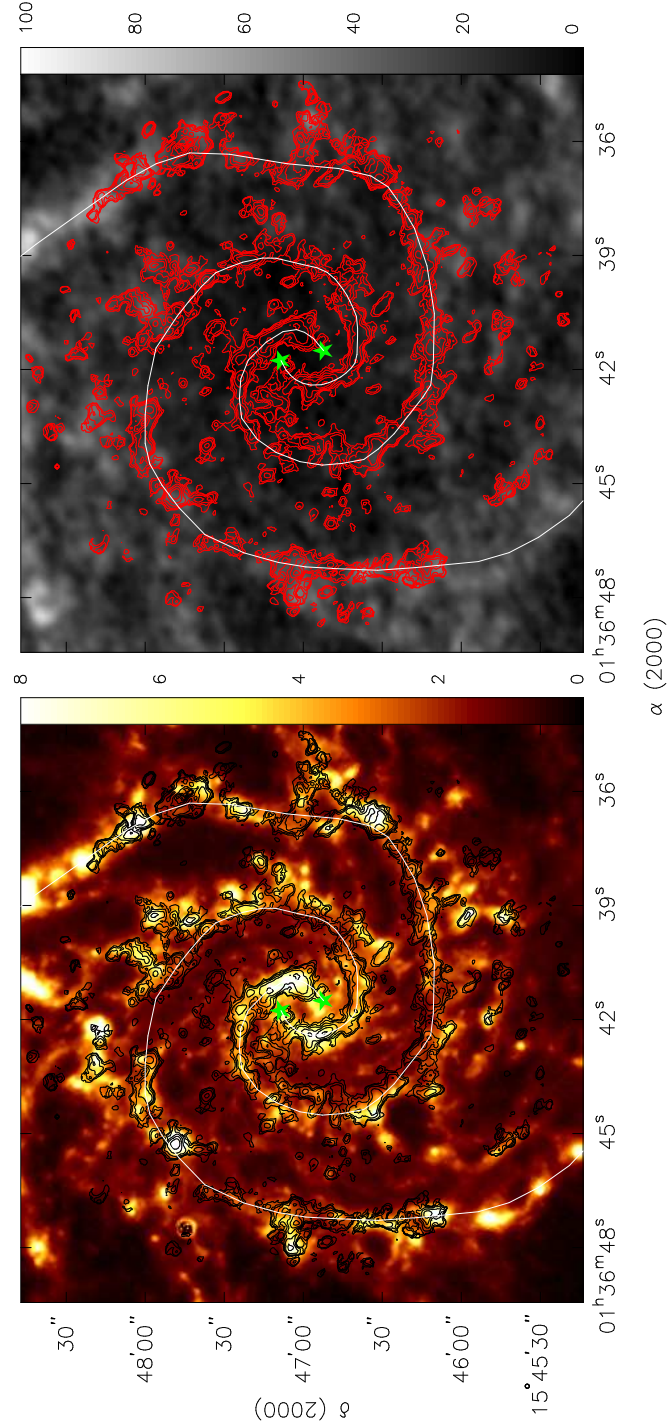
Figure 4.26 NGC 0628. (*Left*) Spitzer SINGS 8 μm "dust only" map. Contours of CO(1-0) emission overlay the image and are spaced at 1.59 times the previous level. The white lines indicate the position of the PDLs, and the green stars indicate where they begin. The false-color scale is shown on the right, in units of MJy sr^{-1}. (*Right*) Zoomed in version of THINGS HI map, in units of Jy beam^{-1} m s^{-1}. The same contours of CO(1-0) emission as in the left panel. The white lines indicate the position of the PDLs, and the green stars indicate where they begin.

123
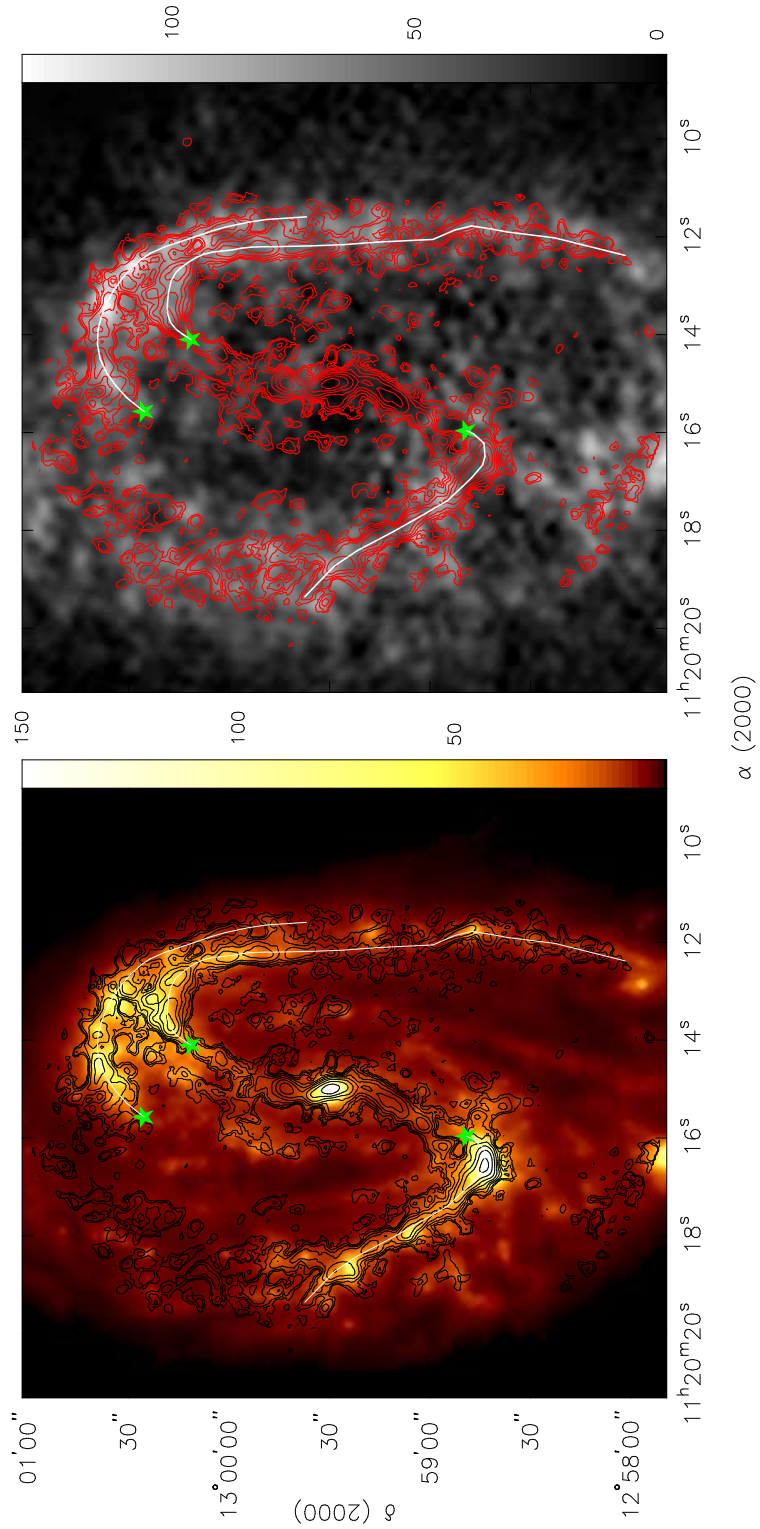
Figure 4.27 Comparison of CO(1-0) emission, Spitzer SINGS 8 μm "dust only" emission, and THINGS Hi emission for NGC 3627. See Fig. 4.26 for details.
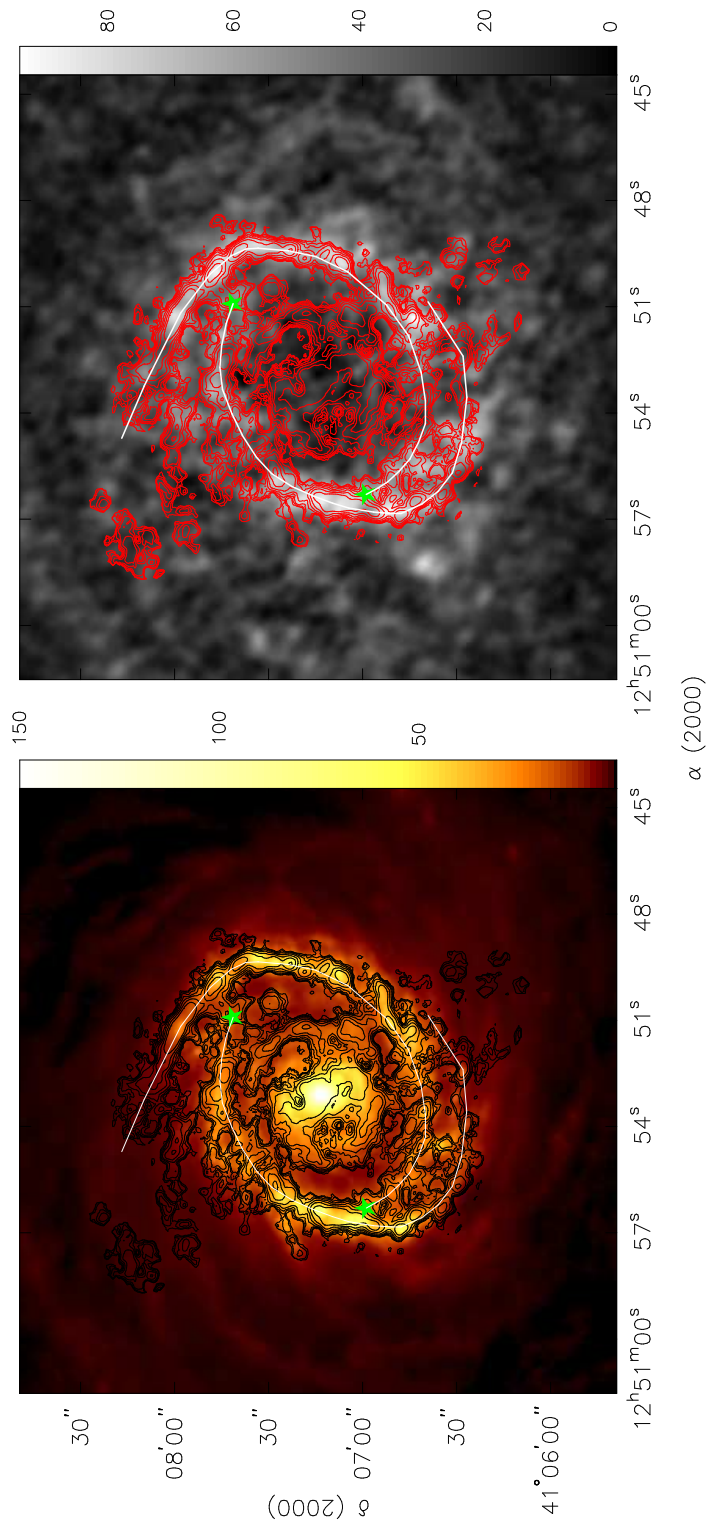
Figure 4.28 Comparison of CO(1-0) emission, Spitzer SINGS 8 μm "dust only" emission, and THINGS H I emission for NGC 4736. See Fig. 4.26 for details.
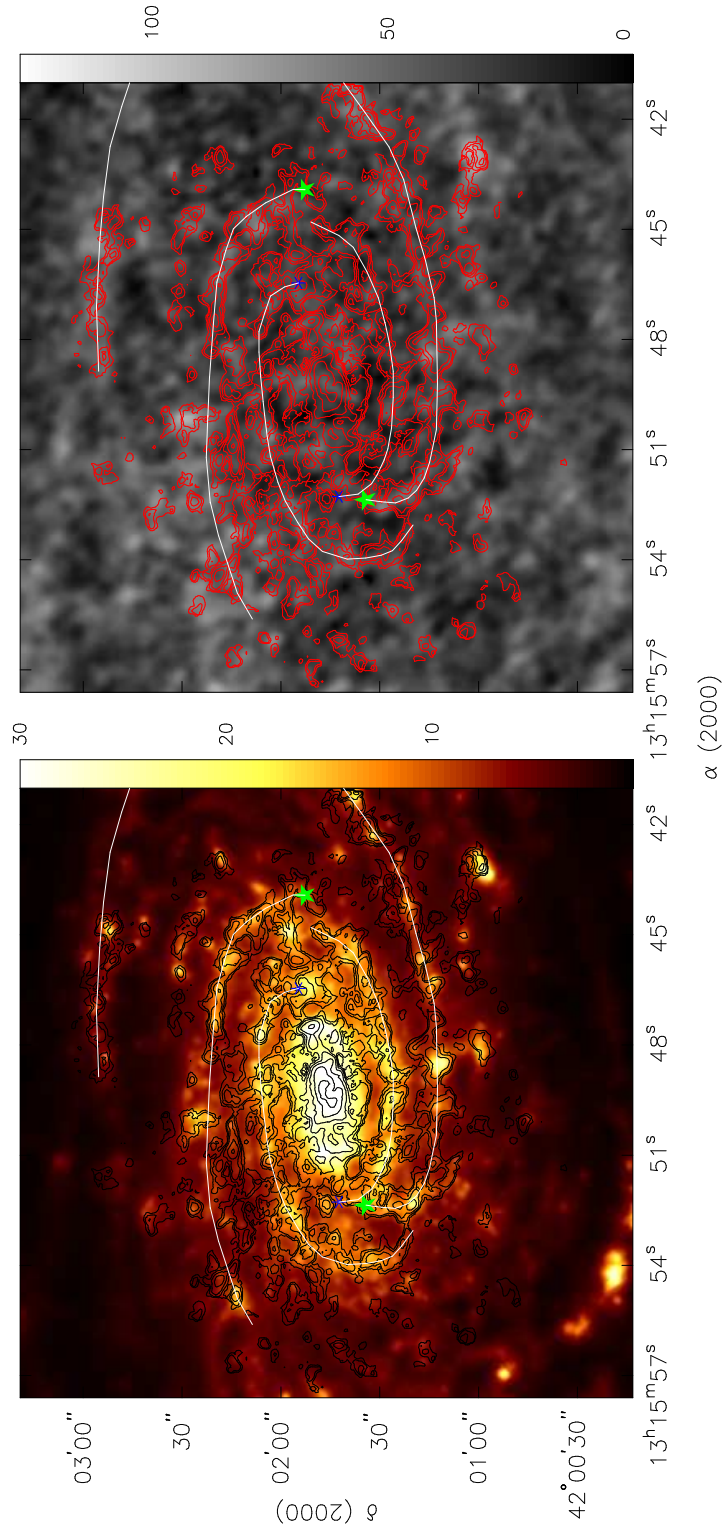
Figure 4.29 Comparison of CO(1-0) emission, Spitzer SINGS 8 μm "dust only" emission, and THINGS H I emission for NGC 5055. The blue stars indicate the beginning of the PDLs along the ring. See Fig. 4.26 for details.
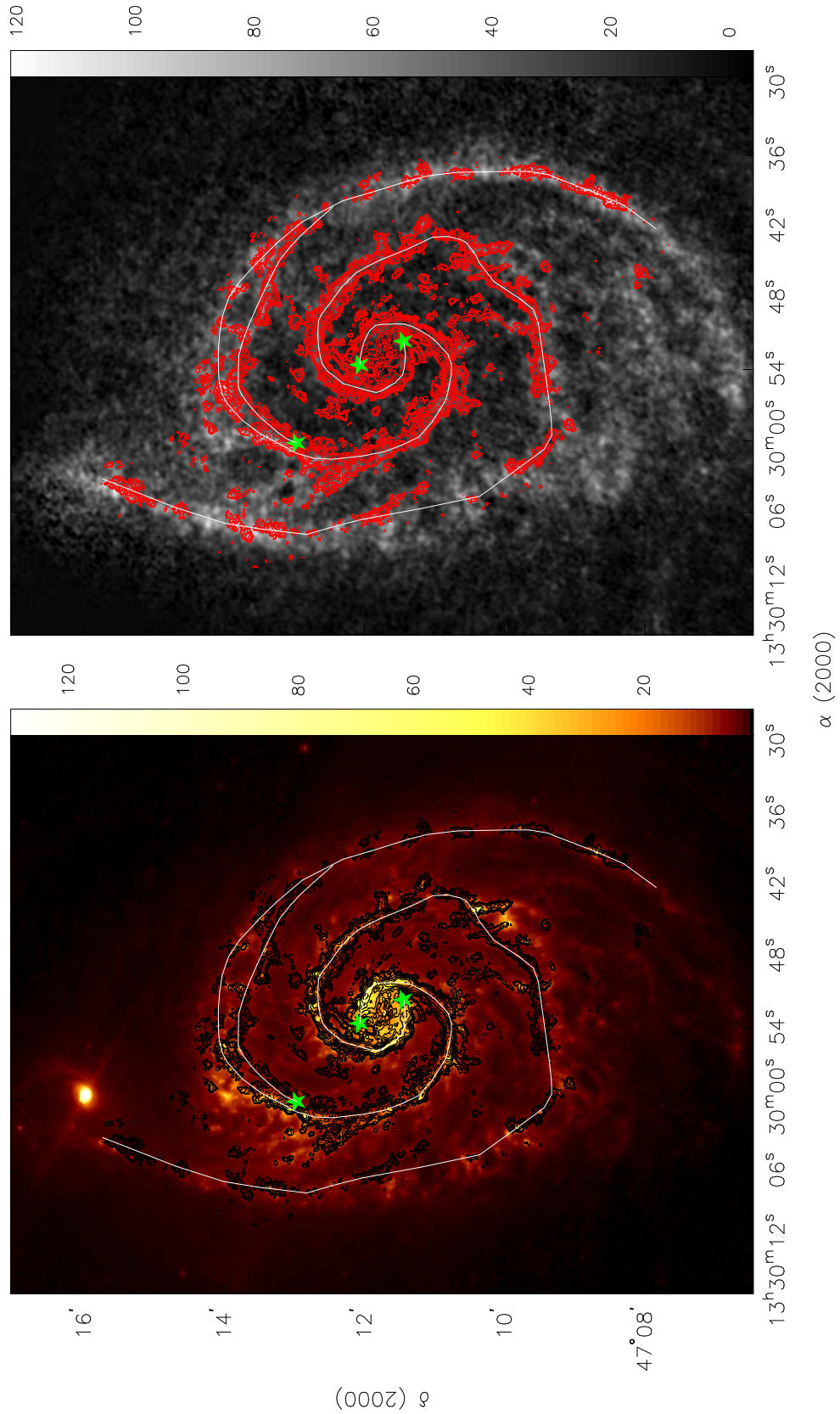
Figure 4.30 Comparison of CO(1-0) emission, Spitzer SINGS 8 μm "dust only" emission, and THINGS H I emission for NGC 5194. See Fig. 4.26 for details.

Figure 4.31 SINGS Ancillary Hα + NII map of NGC 0628. A relative flux scale is shown by the grey–scale wedge on the right, in units of DN pixel^{-1} sec^{-1}. Contours of HI emission overlay the Hα image, with contours spaced at 1.26 times the previous level. The white lines indicate the location of the PDLs along the spiral arms and the green stars indicate where the PDLs begin.

Figure 4.32 SINGS Ancillary Hα + N II map of NGC 3627. A relative flux scale is shown by the grey–scale wedge on the right, in units of DN pixel^{-1} sec^{-1}. Contours of H I emission overlay the Hα image, with contours spaced at 1.26 times the previous level. The white lines indicate the location of the PDLs along the spiral arms and the green stars indicate where the PDLs begin.

4.5   Conclusions

We present new high resolution, $\sim 4''$, CARMA CO(1-0) velocity-integrated maps of

five target spiral galaxies that range in type (Sab–Sc) and spiral arm morphology.

We find that the sample of galaxies is H I deficient in the center of the galaxies. We

find contrary to previous observations that the H I is not offset azimuthally along

Figure 4.33 SINGS Ancillary Hα + N$\textsc{ii}$ map of NGC 4736. A relative flux scale is shown by the grey–scale wedge on the right, in units of DN pixel^{-1} sec^{-1}. Contours of H$\textsc{i}$ emission overlay the Hα 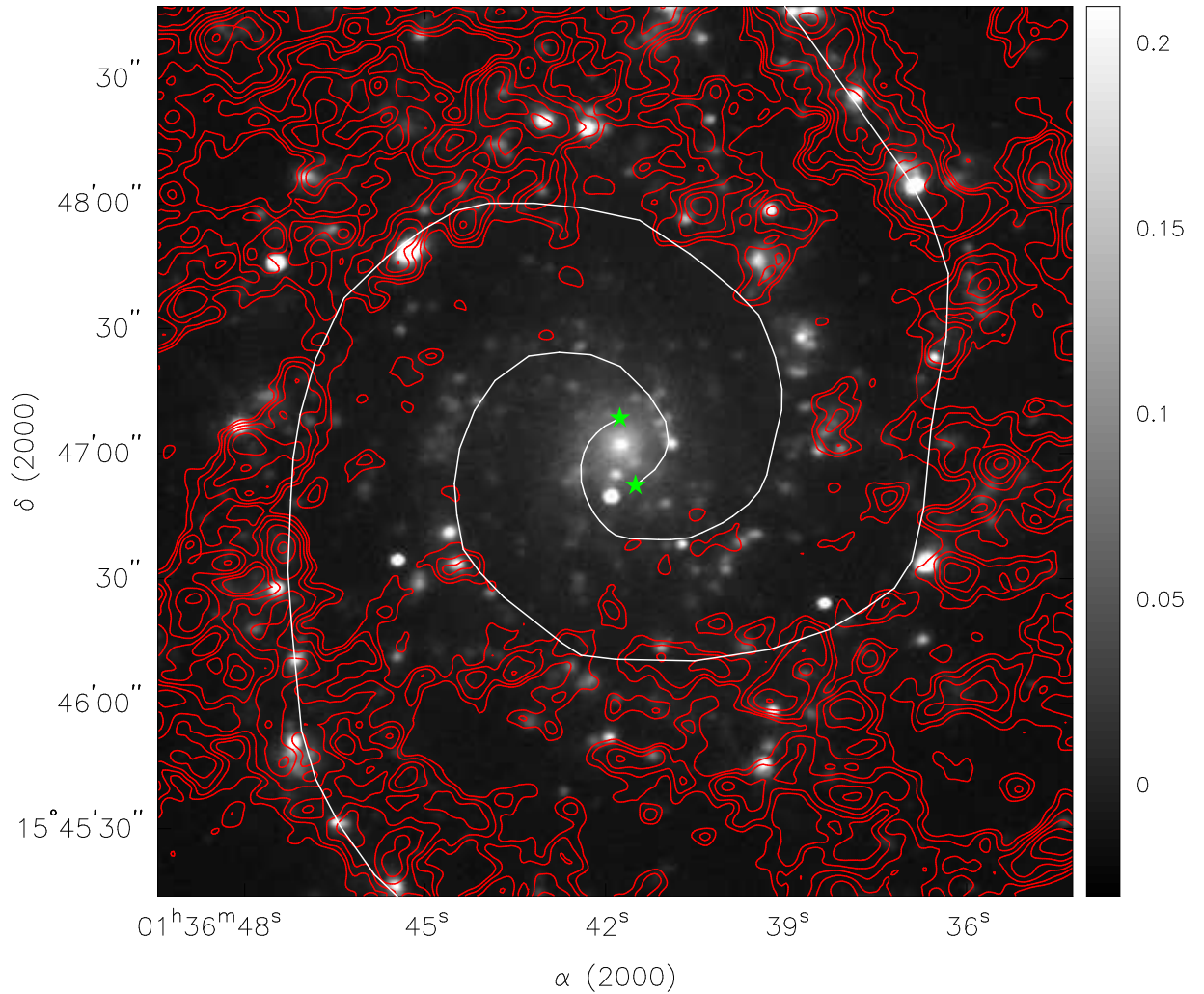image, with contours spaced at 1.26 times the previous level. The white lines indicate the location of the PDLs along the spiral arms and the green stars indicate where the PDLs begin.

the spiral arm from the CO(1-0). While we did not find a 1:1 correlation between

CO(1-0) and H$\textsc{i}$ peaks, the H$\textsc{i}$ peaks do lie along the location of the spiral arms as

traced by CO(1-0) and 8 μm emission. We further find that spiral arms of these

five targeted galaxies are molecular dominated; $\Sigma_{\text{H\textsc{i}}}$ is at most $\sim$20% of the total

gaseous surface density within surface density peaks along the arms. We find that

the CO(1-0) and 8 μm emission are well aligned, tracing the PDLs of the spiral

arms. Similar to previous studies, the Hα emission however, is offset from both the
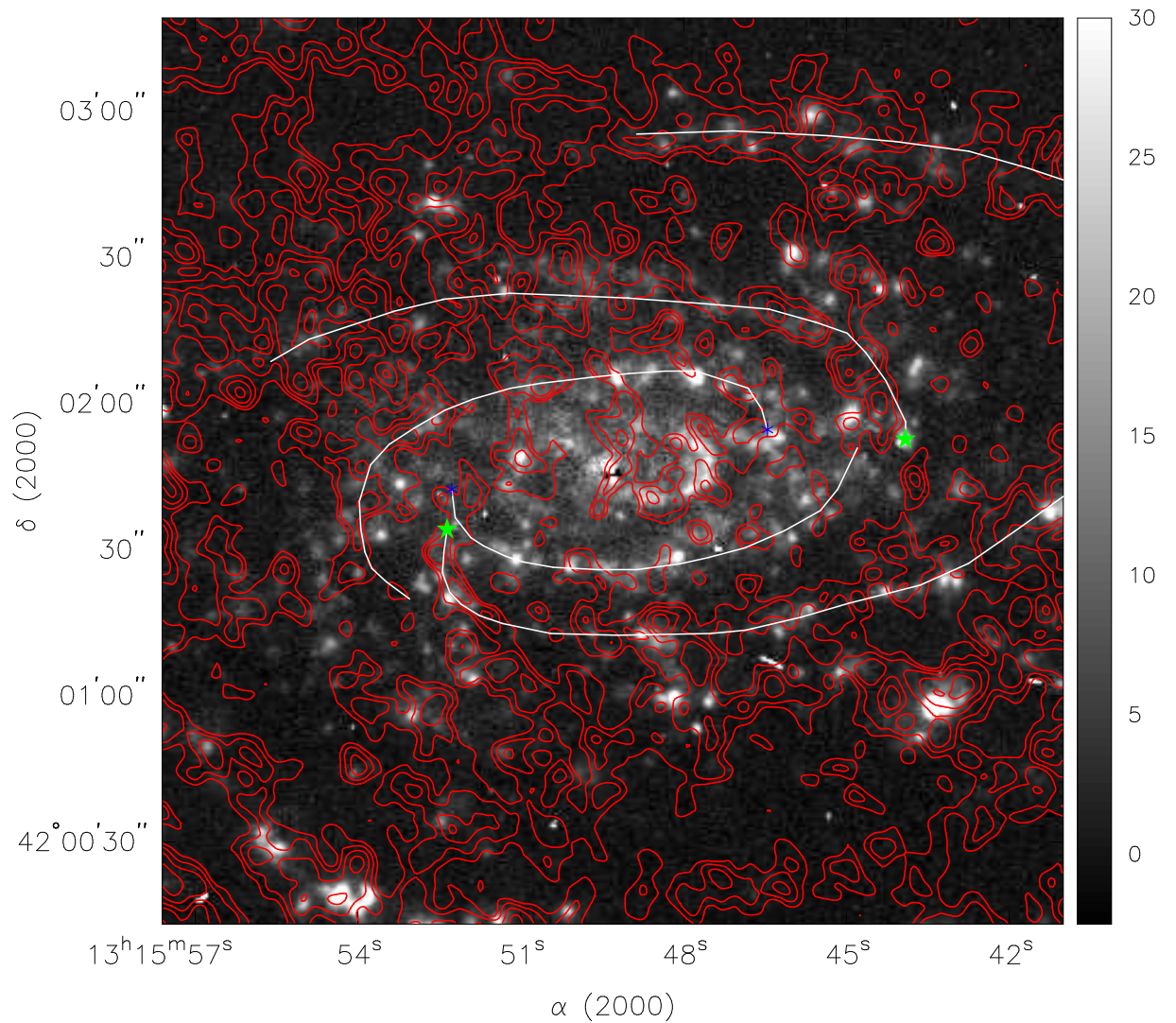
Figure 4.34 SINGS Ancillary Hα + N$_{\text{II}}$ map of NGC 5055. A relative flux scale is shown by the grey–scale wedge on the right, in units of DN pixel^{-1} sec^{-1}. Contours of H$_{\text{I}}$ emission overlay the Hα image, with contours spaced at 1.26 times the previous level. The white lines indicate the location of the PDLs along the spiral arms and the green stars indicate where the PDLs begin.
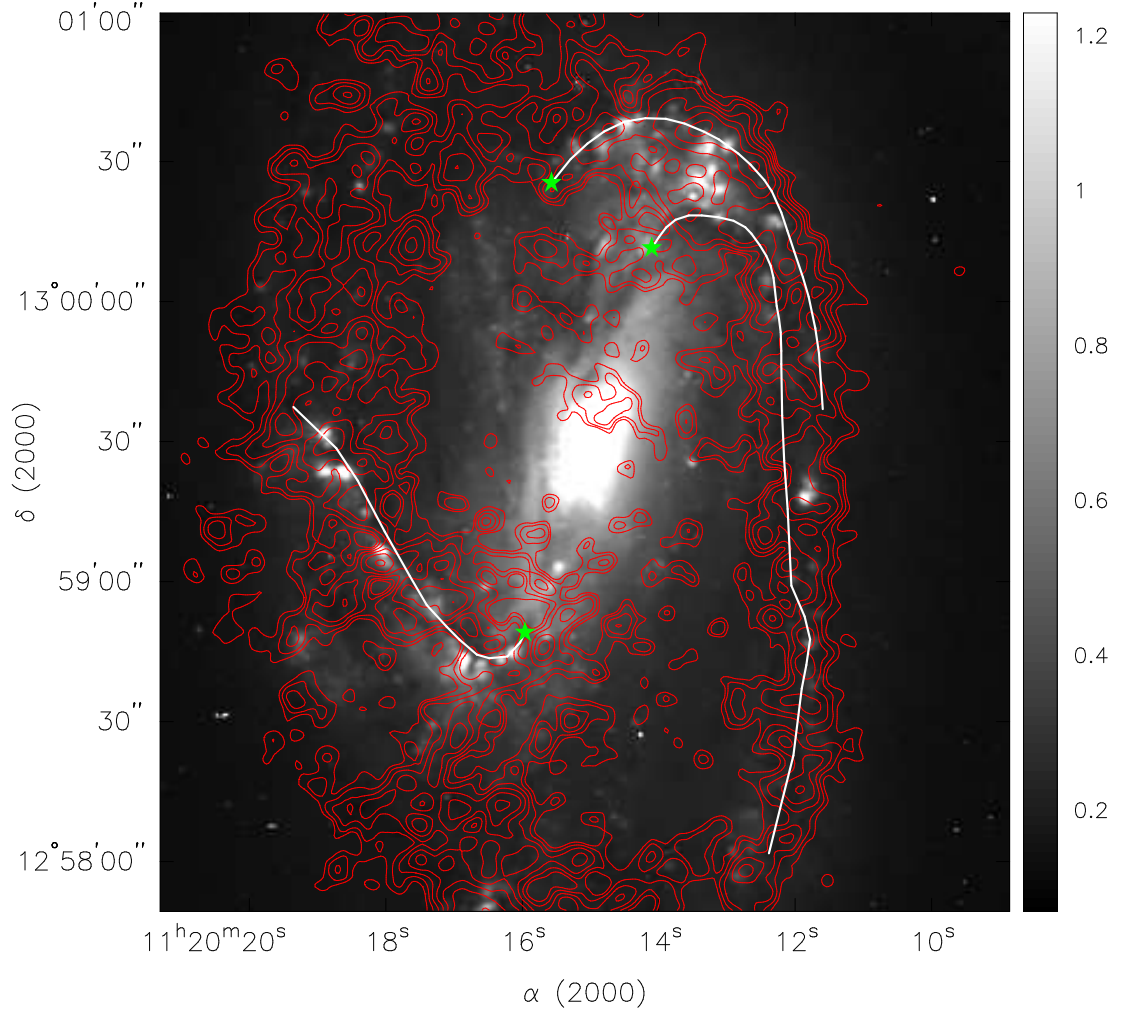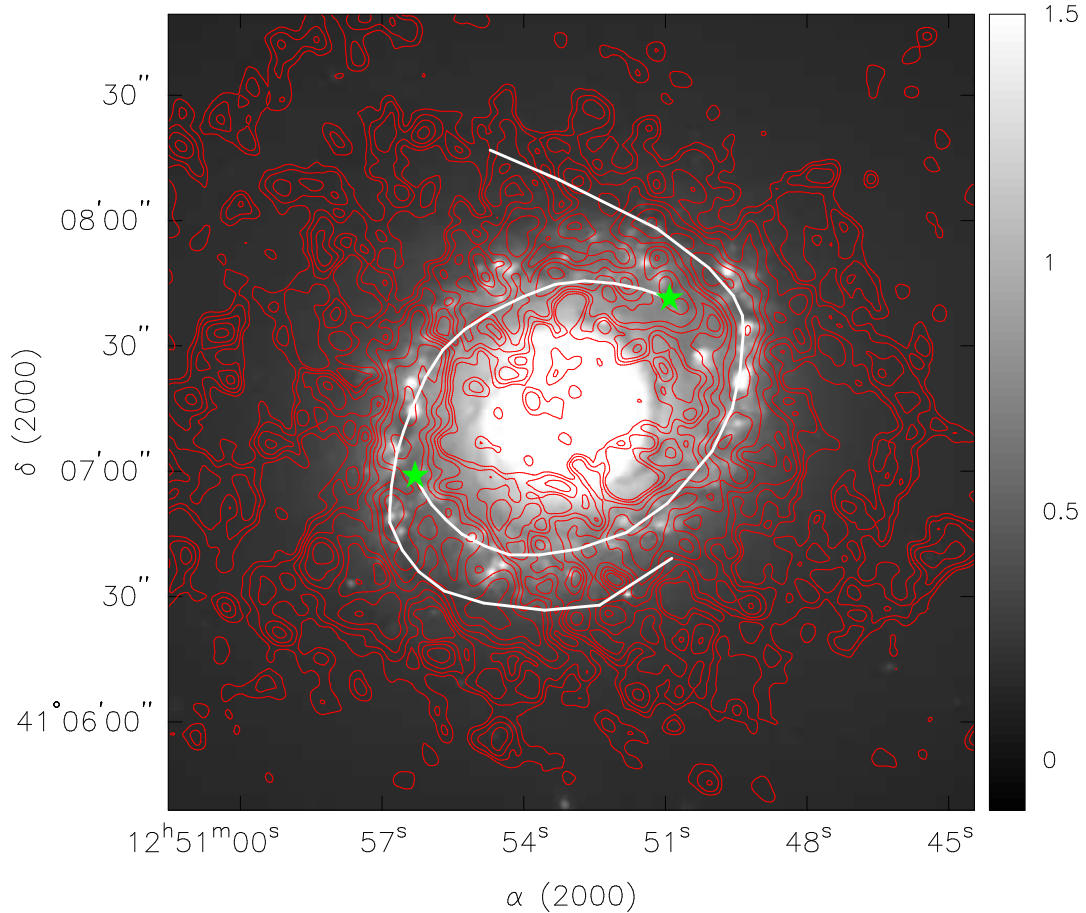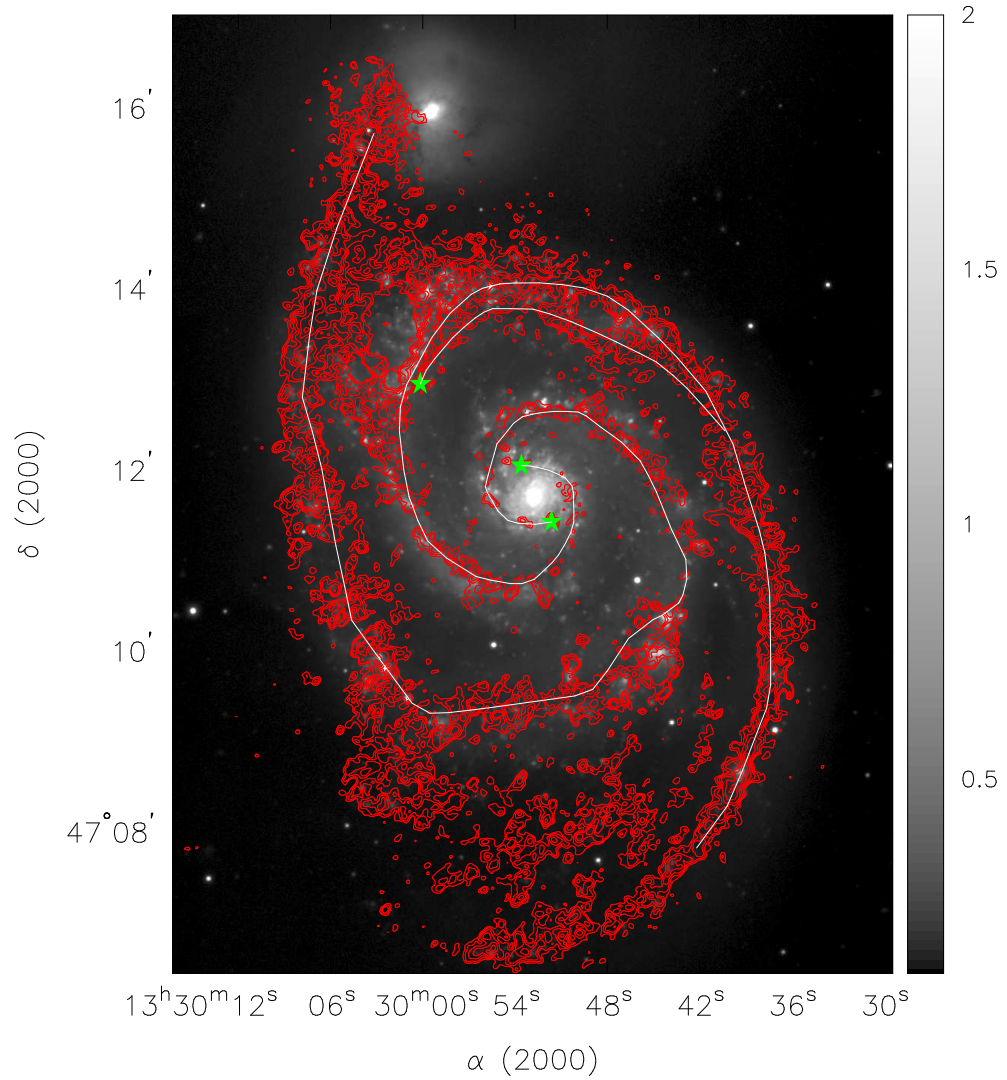
Figure 4.35 SINGS Ancillary Hα + N$\textsc{ii}$ map of NGC 5194. A relative flux scale is shown by the grey–scale wedge on the right, in units of DN pixel^{-1} sec^{-1}. Contours of H$\textsc{i}$ emission overlay the Hα image, with contours spaced at 1.26 times the previous level. The white lines indicate the location of the PDLs along the spiral arms and the green stars indicate where the PDLs begin.

CO(1-0) and 8 μm emission, further downstream in the spiral arms.

Chapter 5

Feather Substructure in Spiral Galaxies

5.1 Introduction

Previously, feathers have primarily been identified and analyzed as extinction features (Lynds 1970, La Vigne et al. 2006). In §2.3.5, we showed for two grand design spirals, NGC 0628 and NGC 5194, that 8 μm emission traced extinction feathers well into the interarm region. We also found that feathers appeared to originate from peaks in CO(1-0) emission along the spiral arms in both galaxies (see §2.3.6; associating the extinction features with dense star forming gas). However, as shown in §2.3.2, feathers do not occur only in late type, grand design spiral galaxies. Galaxies identified with feathers range from early to late type (Sa - Sc), and in spiral arm type, including flocculents. Therefore, it is important to characterize the molecular content of feathers in other galaxies in addition to grand design spirals. Using the high-resolution, CARMA CO(1-0) observations of our target sample (see §3.2), we will determine if extinction feathers are associated with significant gas mass, in galaxies spanning a range of types. We will also test models for the formation of feathers.

In this chapter we present the multi-wavelength process used to identify feathers in our target sample of galaxies (see §3.2). We then measure the gas mass

associated with feathers to determine if they are structures with significant mass or instead merely minor extinction features. Next we compare the molecular surface density profiles along the spiral arms with the location the feathers. We then test gravitational theories for feather formation by comparing the deprojected feather separation to the model predictions. Finally, we test hydrodynamical theories of feather formation by comparing the arm pitch angles to predictions.

5.2 Identifying Feathers

By comparing different high-resolution tracers, we can more accurately identify and determine the full extent of feathers. Through the comparison of optical, near-IR (8 μm), and CO(1-0) emission, we can identify (1) the location of the PDL (primary dust lane) on the inside edge of the spiral arm, (2) the origin of feathers along the PDL, and (3) their extension into the interarm region. Each wavelength has its advantages and disadvantages.

5.2.1 CO(1-0) Emission

The peaks of CO(1-0) emission along the arm are excellent indicators of the sites where feathers originate along the PDL. This is particularly true when the peaks are associated with emission trailing into the interarm region. The primary limitation of the CO(1-0) line is that the emission falls off radially from the PDLs much more rapidly than extinction or 8 μm emission.

5.2.2   8 μm PAH Emission

The 8 μm emission is an excellent tracer of the extended emission from feathers in the interarm region. As discussed in §2.3.5, the primary source of 8 μm emission is the vibrational excitation of polycyclic aromatic hydrocarbons (PAHs) by UV photons (Sellgren 1984). PAH emission typically originates from photodissociation regions (Peeters et al. 2004), which surround molecular clouds, thus tracing prominent extinction features.

5.2.3   Extinction

The highest resolution images can be obtained at visible wavelengths with the Hubble Space Telescope ACS camera, which has a resolution of $0.05''$. Extinction features are useful for 1) identifying the location of the PDL, 2) following the extension of the feathers into the interarm region, and 3) at $0.05''$ resolution, clearly separating the closest spaced feathers in the inner regions of galaxies. However, extinction features can be masked by the bright emission from stars lining the spiral arms. Furthermore, at $0.05''$ resolution the fragmentation of individual feathers is resolved in the larger structures in the outer regions of galaxies, which can lead to "over identifying" the number of feathers present if used as the sole identifier. Finally, we note that it is difficult if not impossible to extract column densities from the extinction observations owing to the uncertain geometry and contamination by emission.

5.2.4 General Procedure for Identifying Feathers

By combining the advantages of the three tracers above, as seen in Figures 5.1 –
5.30, we are able to better identify the full extent of a feather. First, we use all three
tracers to identify the location of the PDL. We next use the CO(1-0) peaks along
the PDL to locate the origin of each feather; these peaks in CO(1-0) emission are the
best tracer to determine the intersection of feathers with the PDL (see §2.3.6). Then
we compare the location of 8 μm emission extending into the interarm region to the
identified CO(1-0) peaks. Finally, we use the extinction images, which typically
encompass both the CO(1-0) and 8 μm emission, to confirm the identification of the
feathers. For cases like NGC 3627 where optical observations are only available for
part of the galaxy, we rely on the agreement of the CO(1-0) peaks and the extended
8 μm emission to confirm the identification of a feather.

Figure 5.1 Feather markings for NGC 0628 overlaid on the CARMA CO(1-0) velocity-integrated map.

Figure 5.2 Feather markings for NGC 0628 overlaid on the Spitzer 8 μm map.

Figure 5.3 Feather markings for NGC 0628 overlaid on the HST broadband image.

Figure 5.4 NGC 0628 CARMA CO(1-0) velocity-integrated map without feather markings.

Figure 5.5 NGC 0628 Spitzer 8 μm map without feather markings.

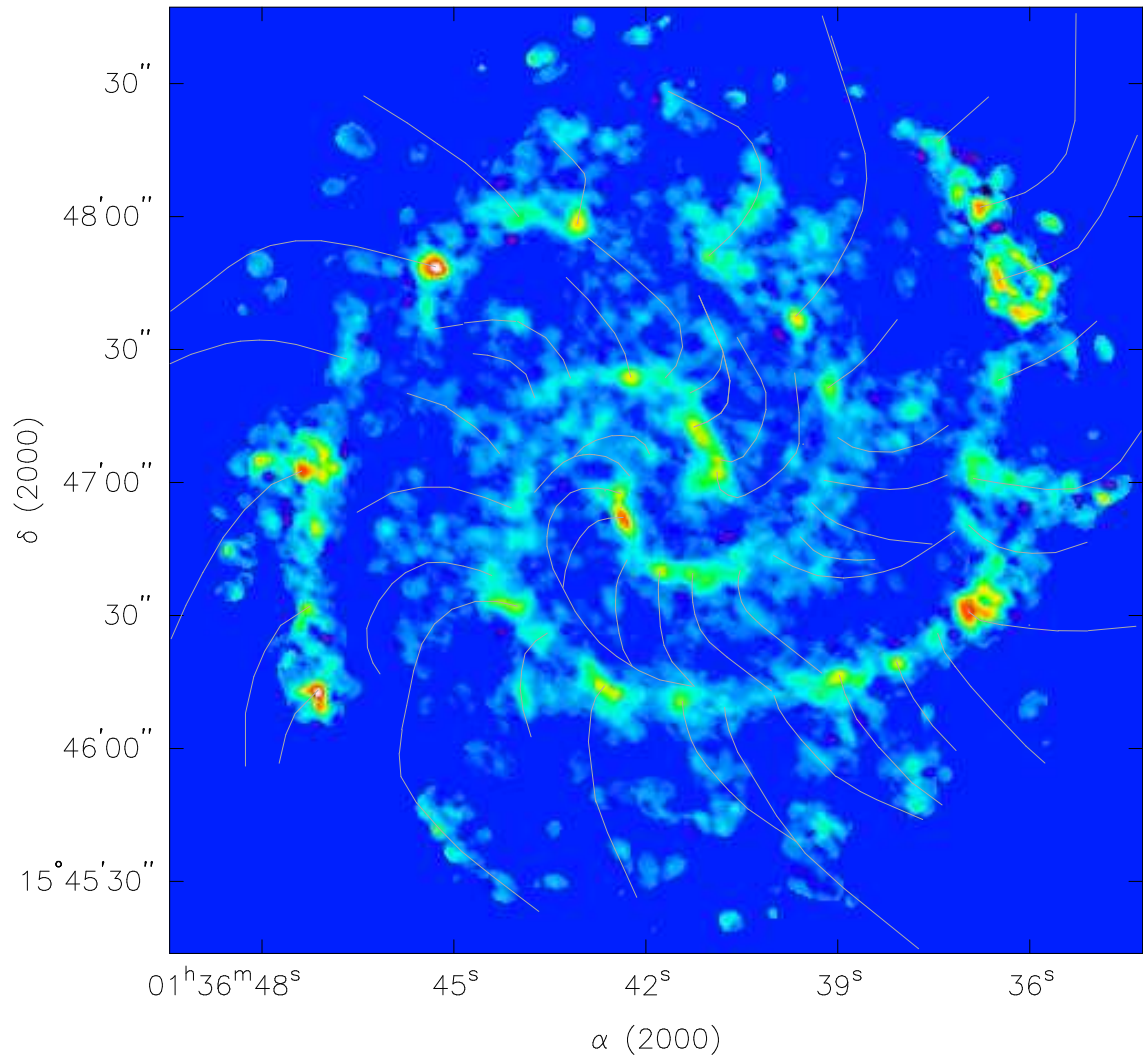Figure 5.6 NGC 0628 HST broadband image without feather markings.

Figure 5.7 Feather markings for NGC 3627 overlaid on the CARMA CO(1-0) velocity-integrated map.

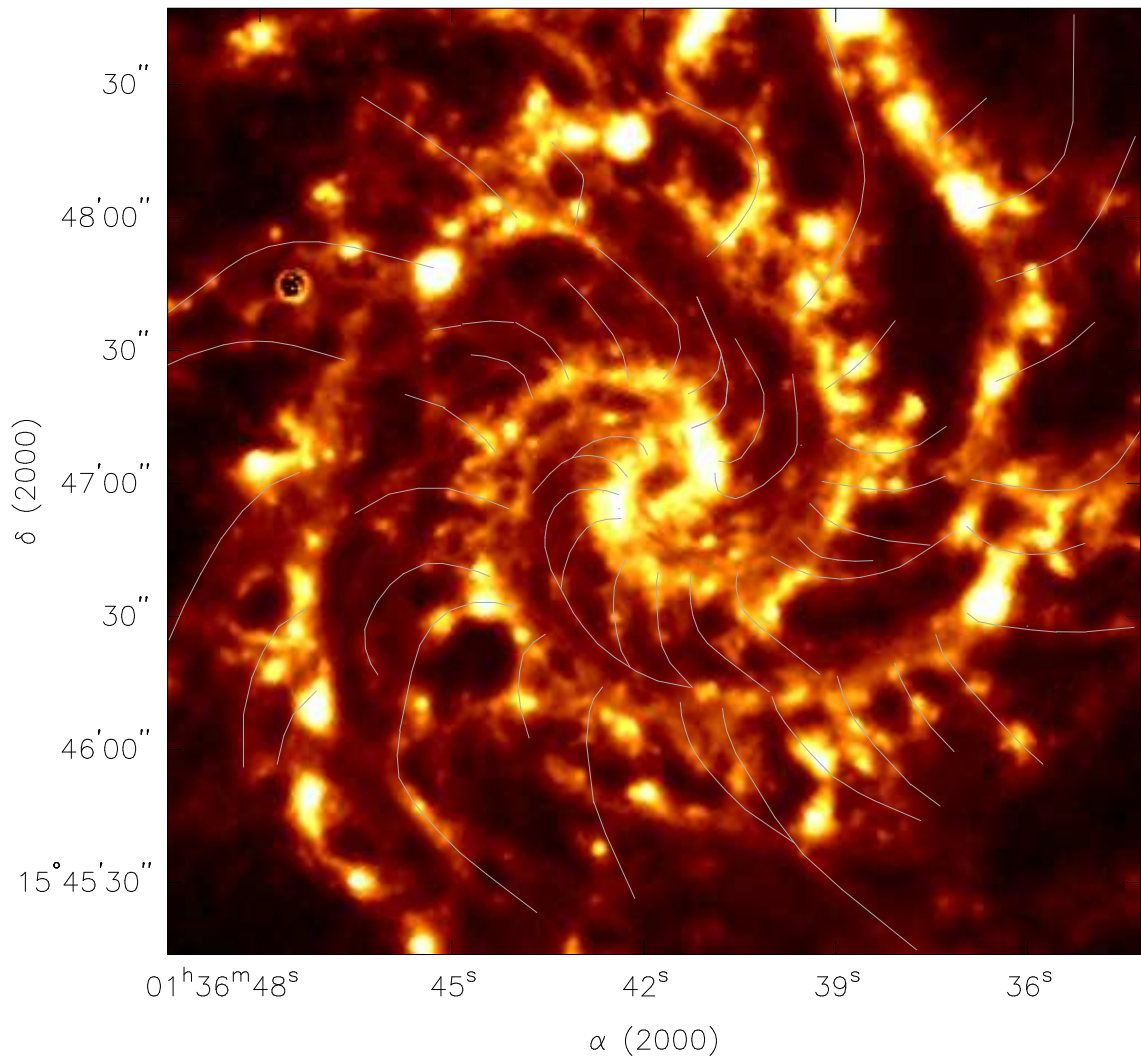Figure 5.8 Feather markings for NGC 3627 overlaid on the Spitzer 8 μm map.

Figure 5.9 Feather markings for NGC 3627 overlaid on the HST broadband image.

Figure 5.10 NGC 3627 CARMA CO(1-0) velocity-integrated map without feather markings.

Figure 5.11 NGC 3627 Spitzer 8 μm map without feather markings.
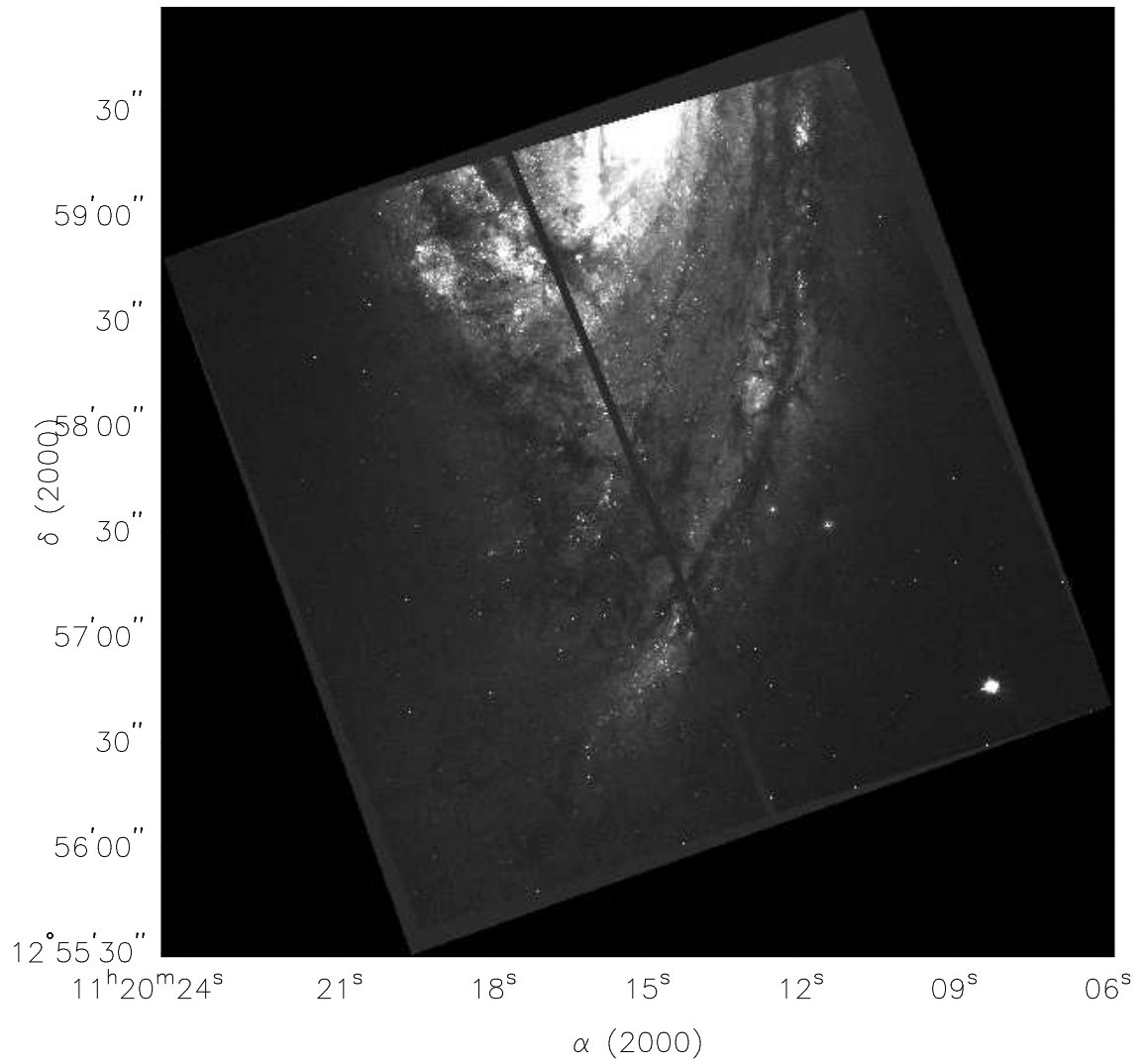
Figure 5.12 NGC 3627 HST broadband image without feather markings.
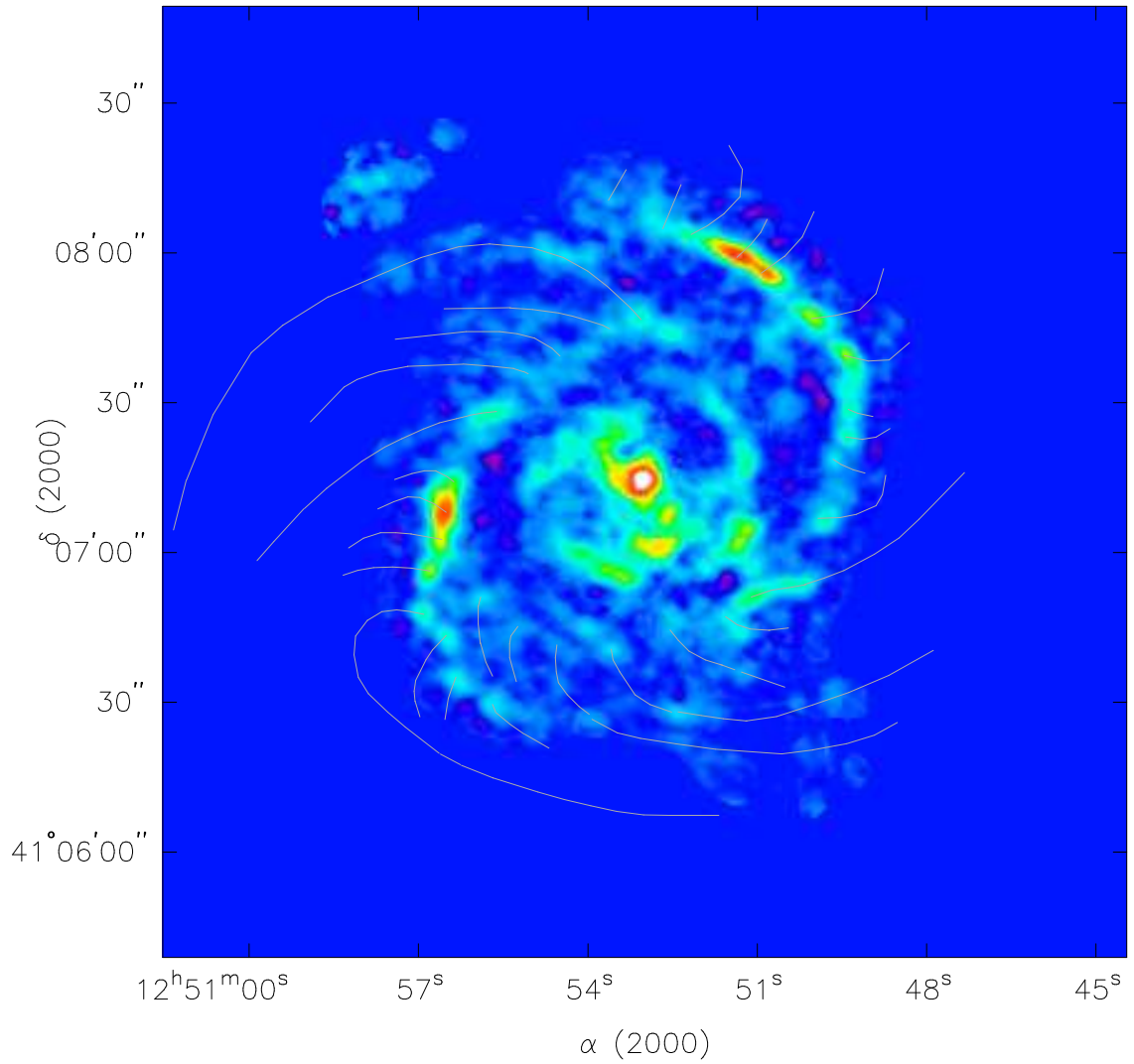
Figure 5.13 Feather markings for NGC 4736 overlaid on the CARMA CO(1-0) velocity-integrated map.
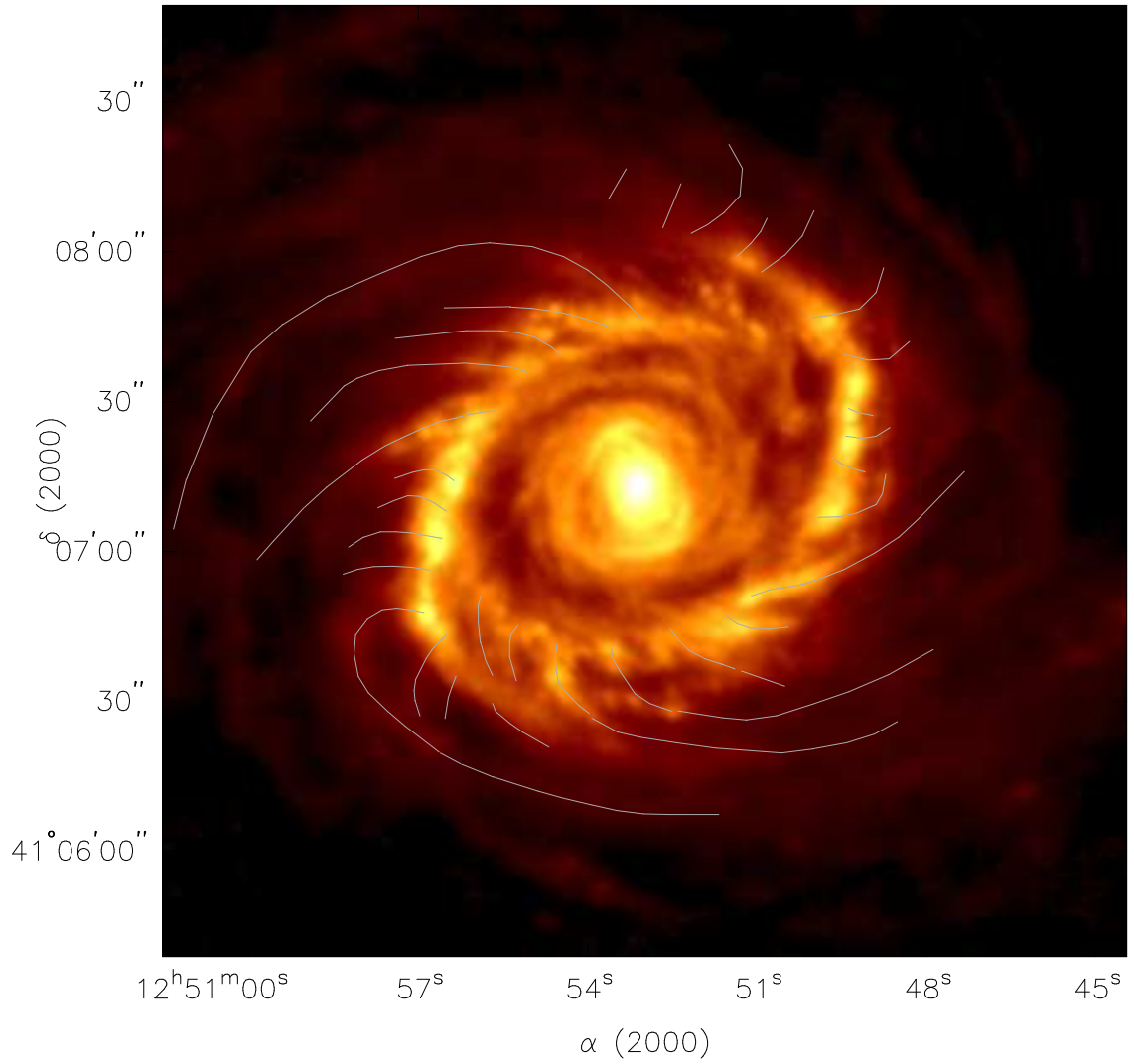
Figure 5.14 Feather markings for NGC 4736 overlaid on the Spitzer 8 μm map.
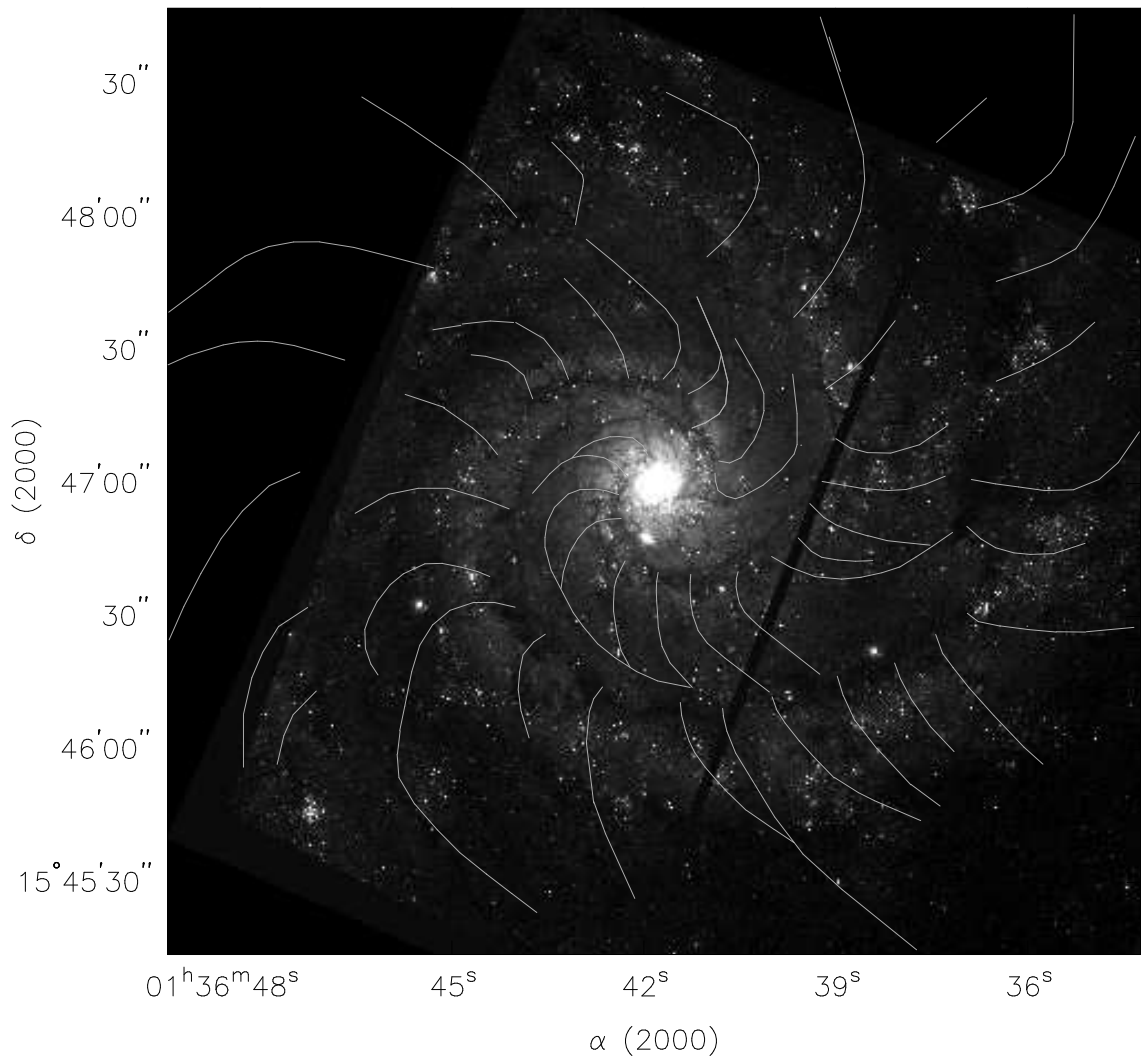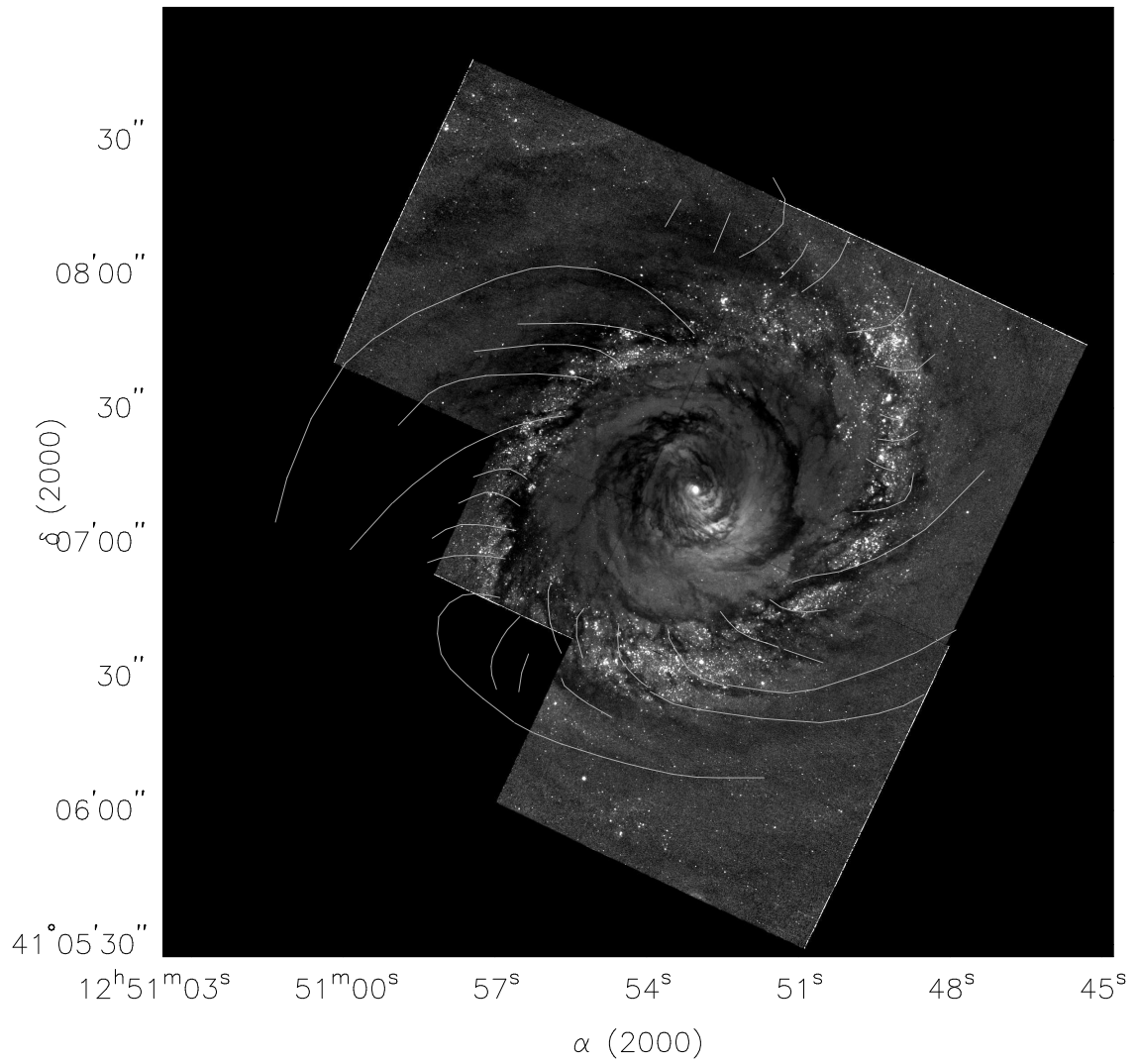
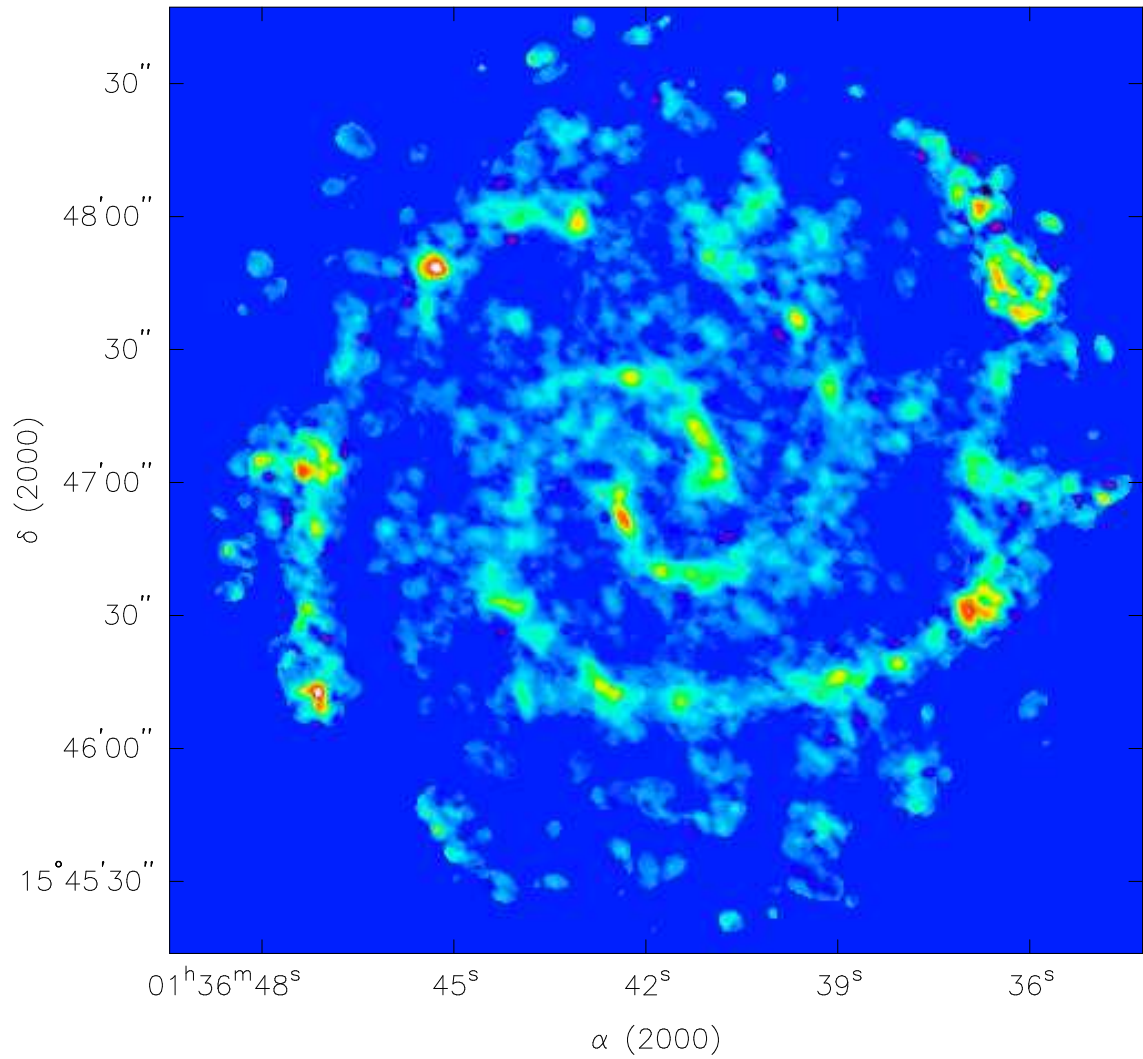Figure 5.15 Feather markings for NGC 4736 overlaid on the HST broadband image.

Figure 5.16 NGC 4736 CARMA CO(1-0) velocity-integrated map without feather markings.

Figure 5.17 NGC 4736 Spitzer 8 μm map without feather markings.

Figure 5.18 NGC 4736 HST broadband image without feather markings.
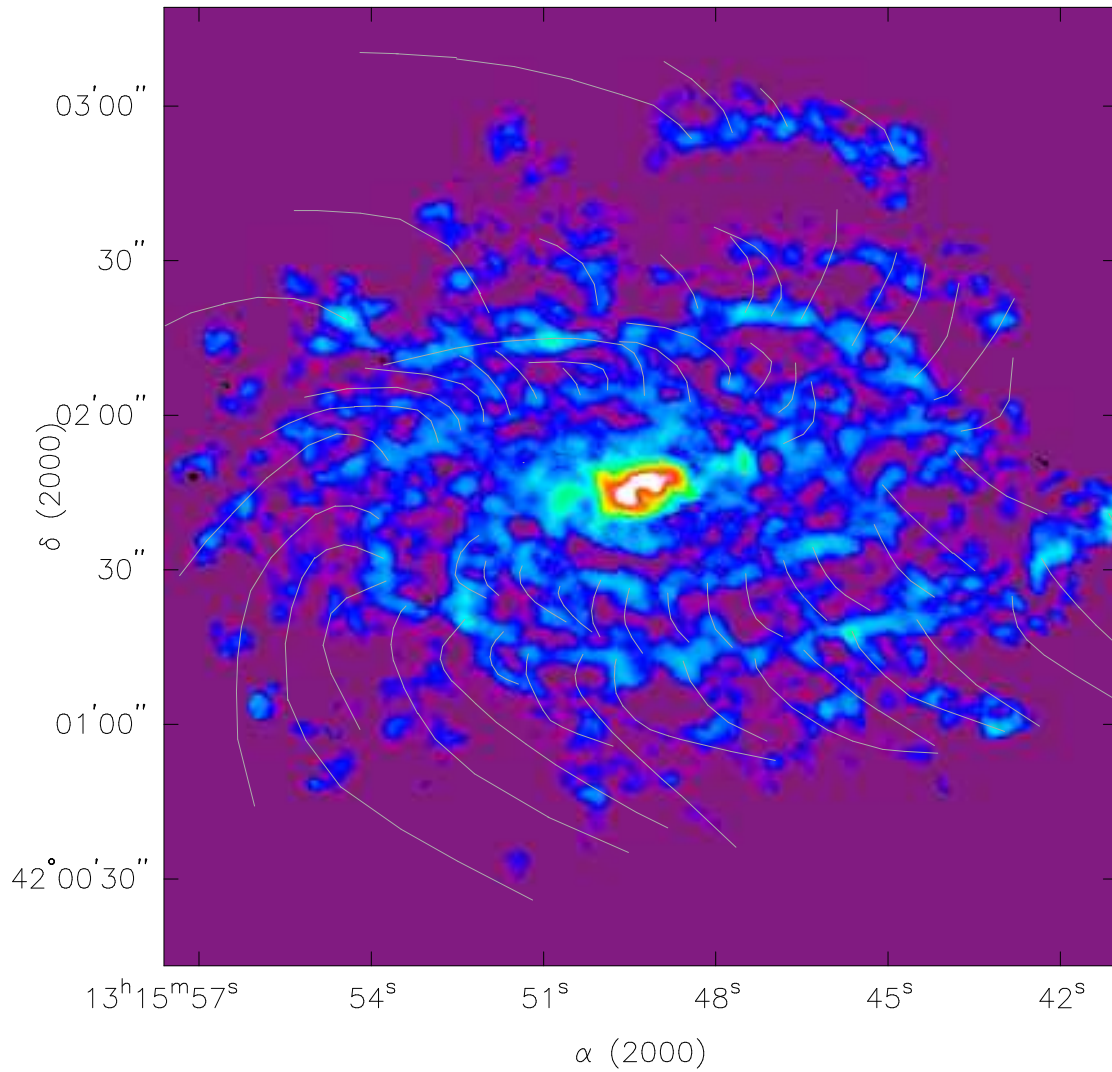
Figure 5.19 Feather markings for NGC 5055 overlaid on the CARMA CO(1-0) velocity-integrated map.
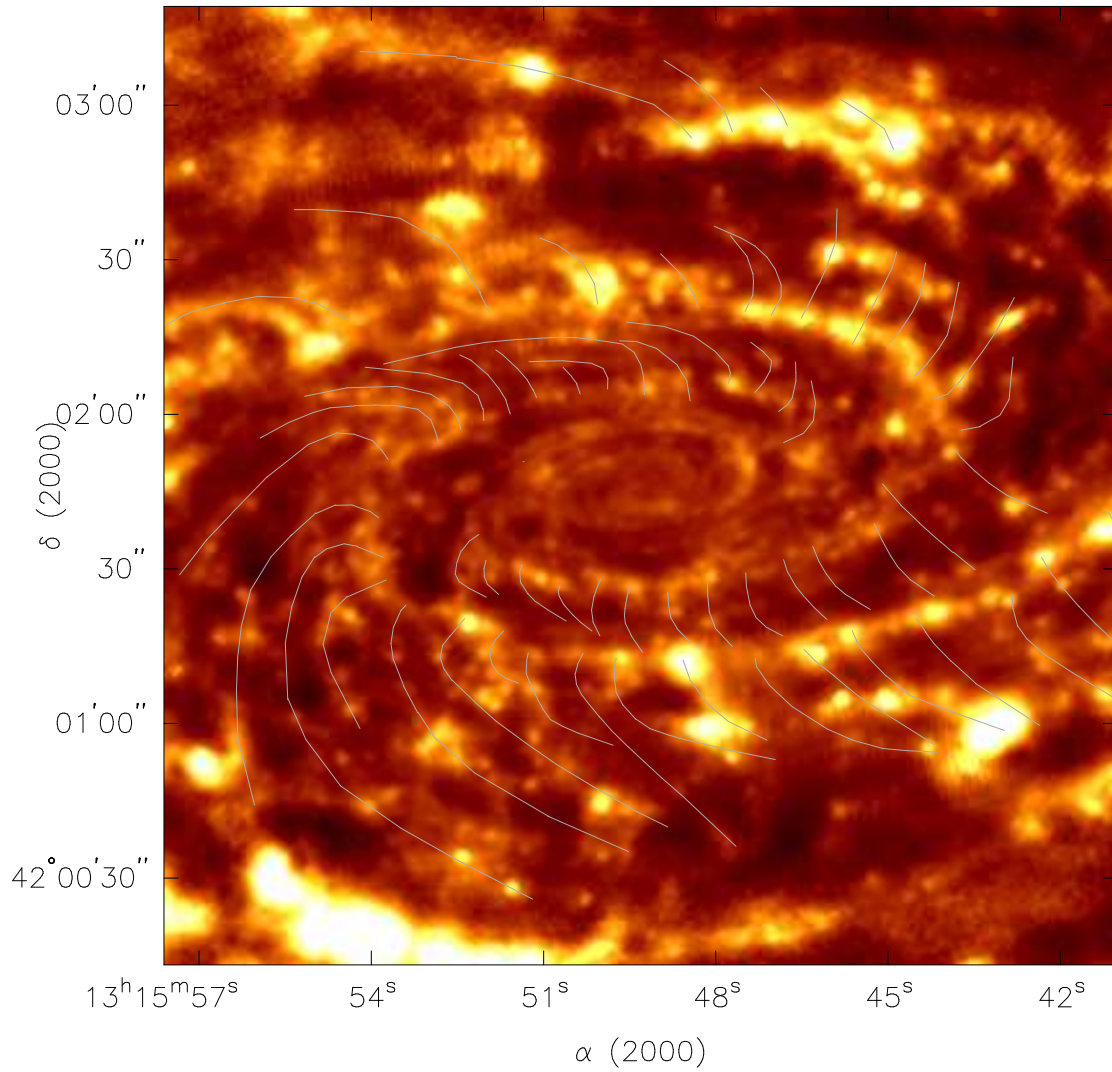
Figure 5.20 Feather markings for NGC 5055 overlaid on the Spitzer 8 μm map.
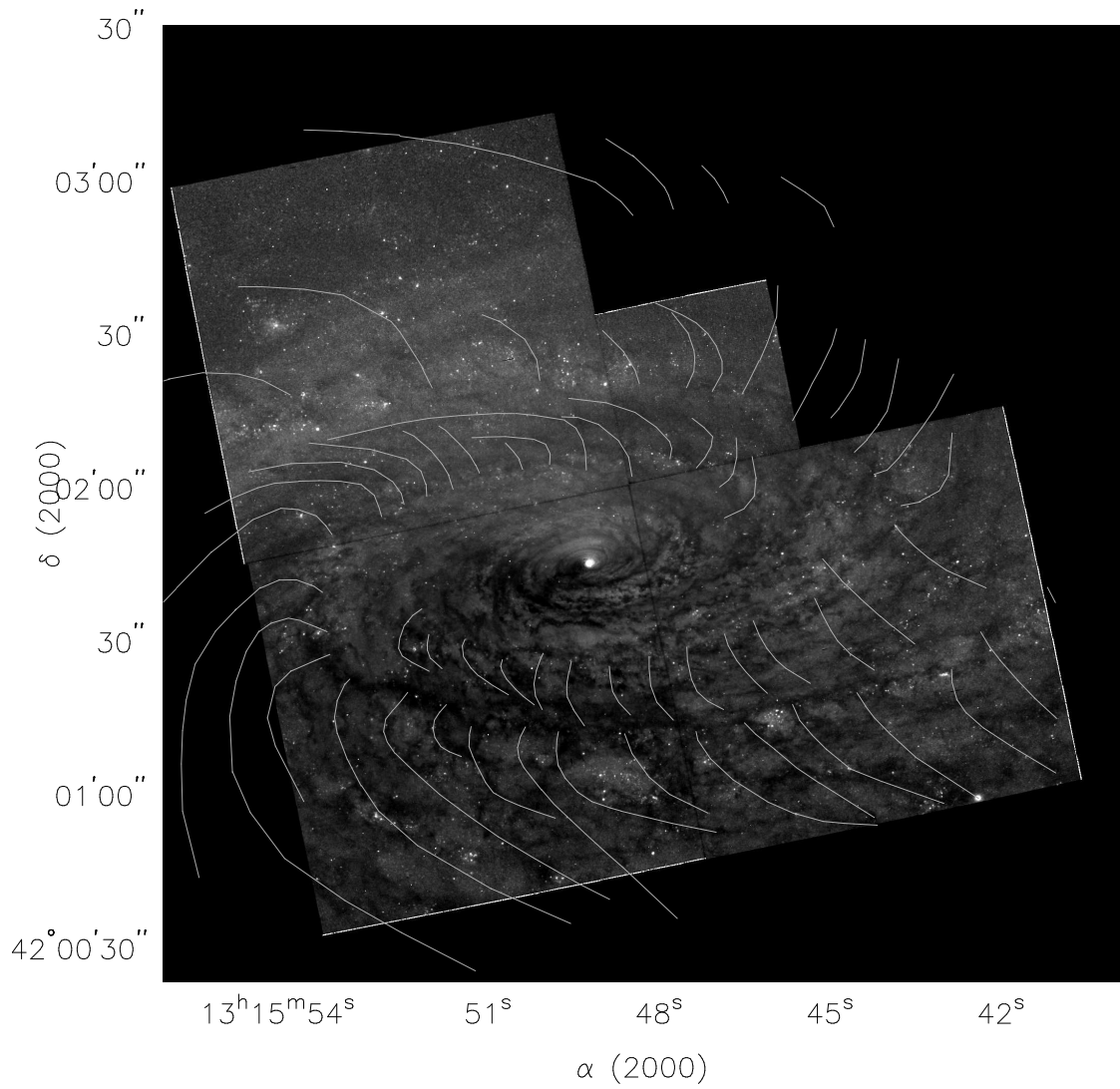
Figure 5.21 Feather markings for NGC 5055 overlaid on the HST broadband image.
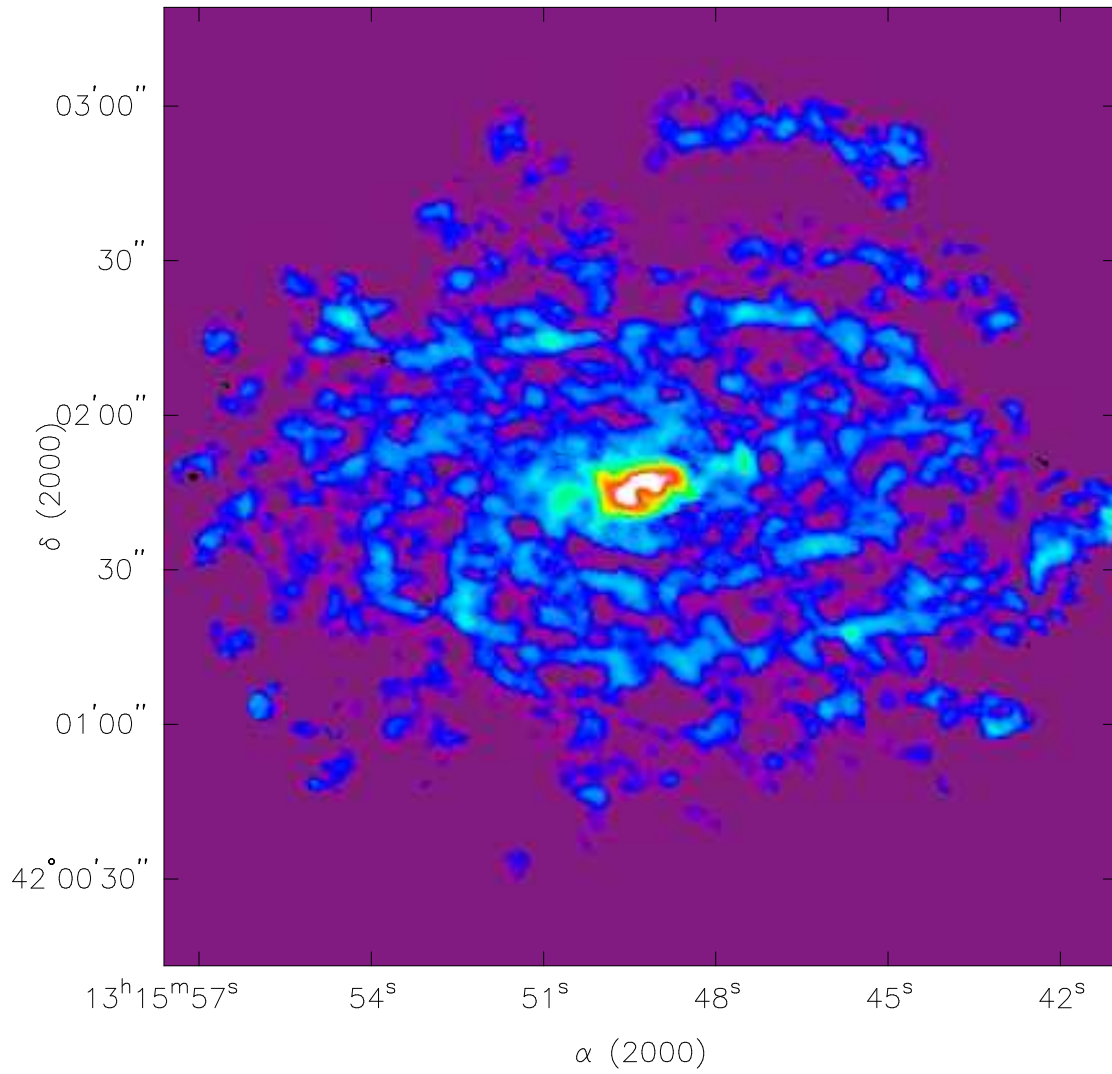
Figure 5.22 NGC 5055 CARMA CO(1-0) velocity-integrated map without feather markings.
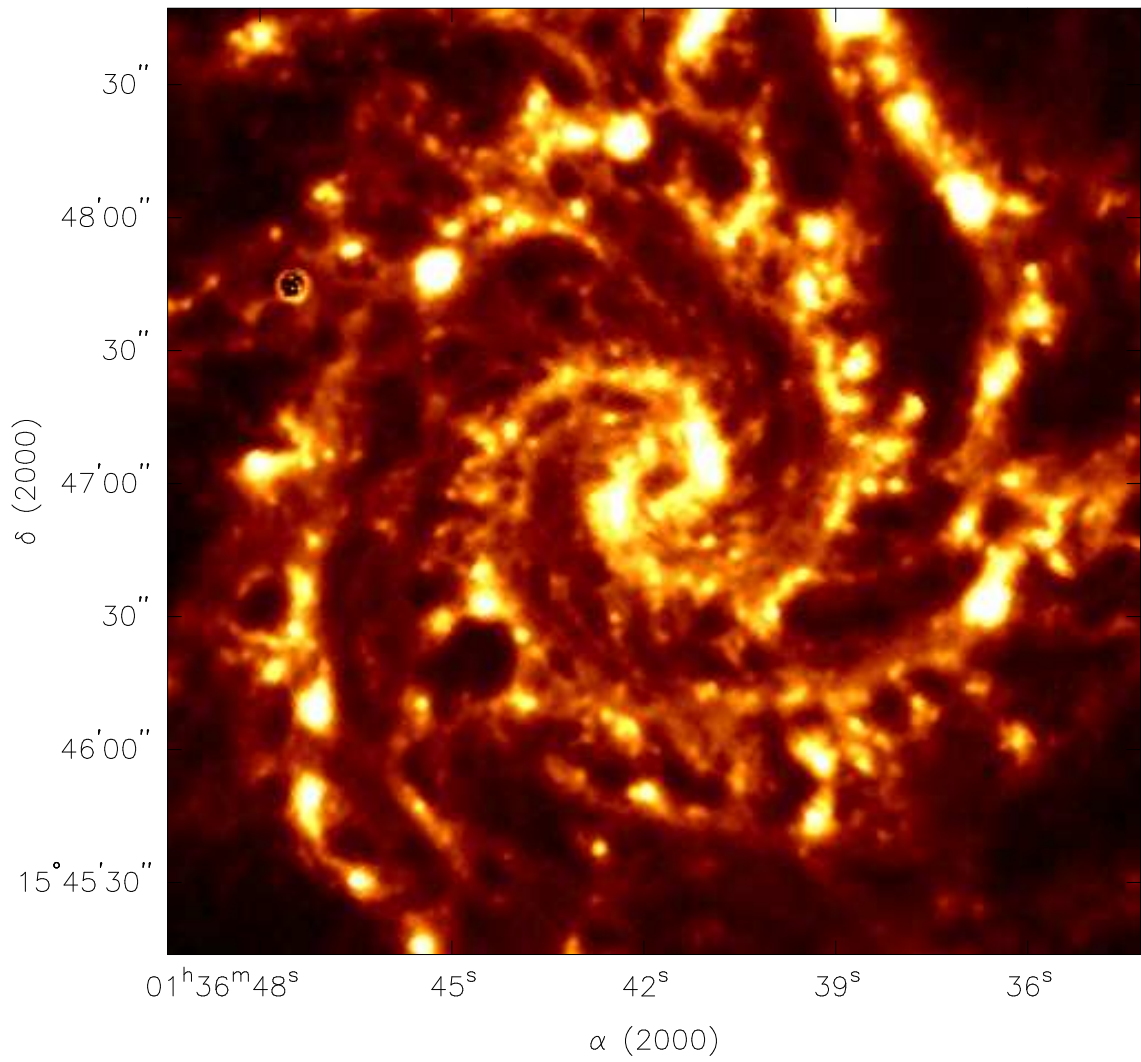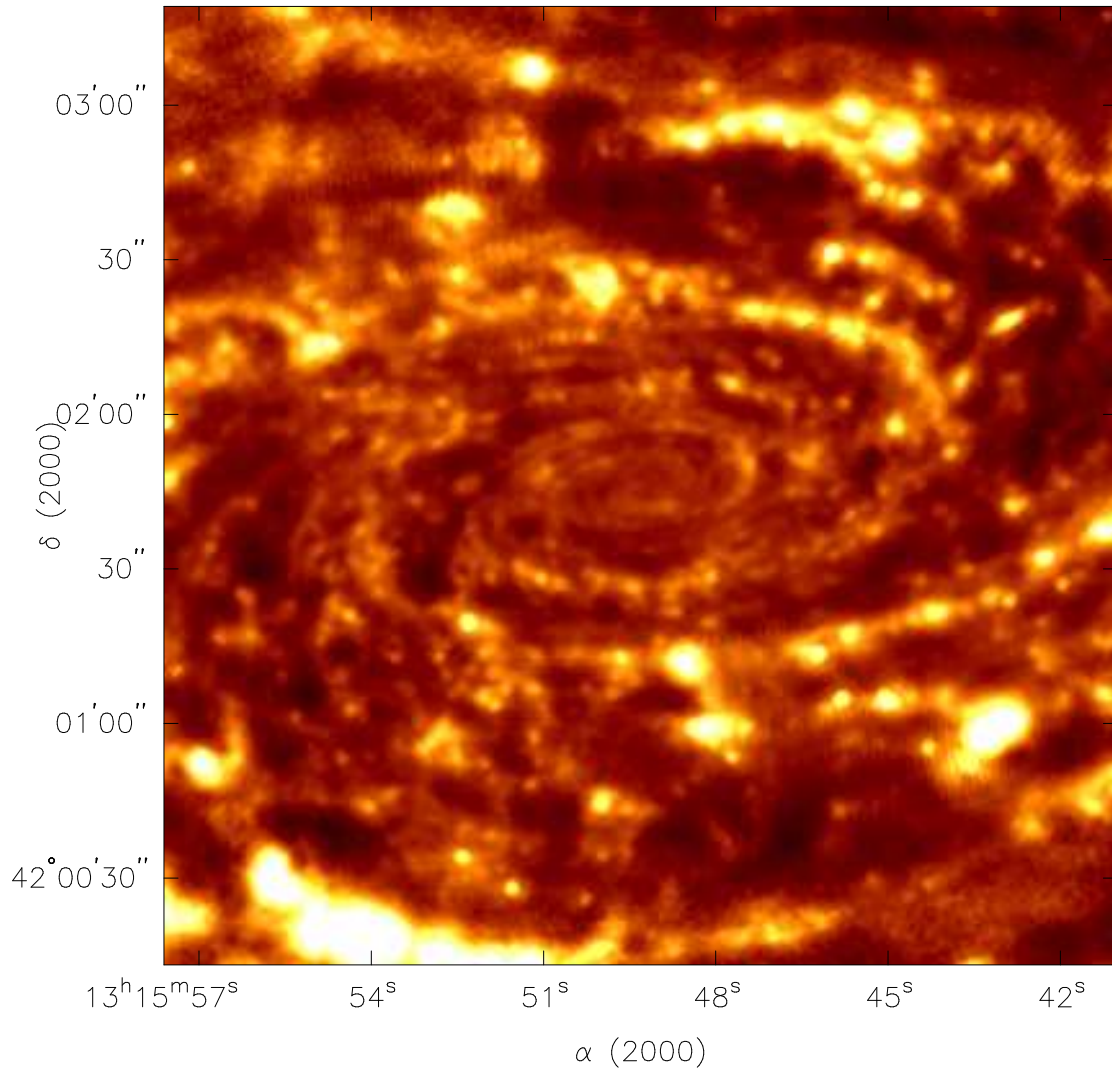
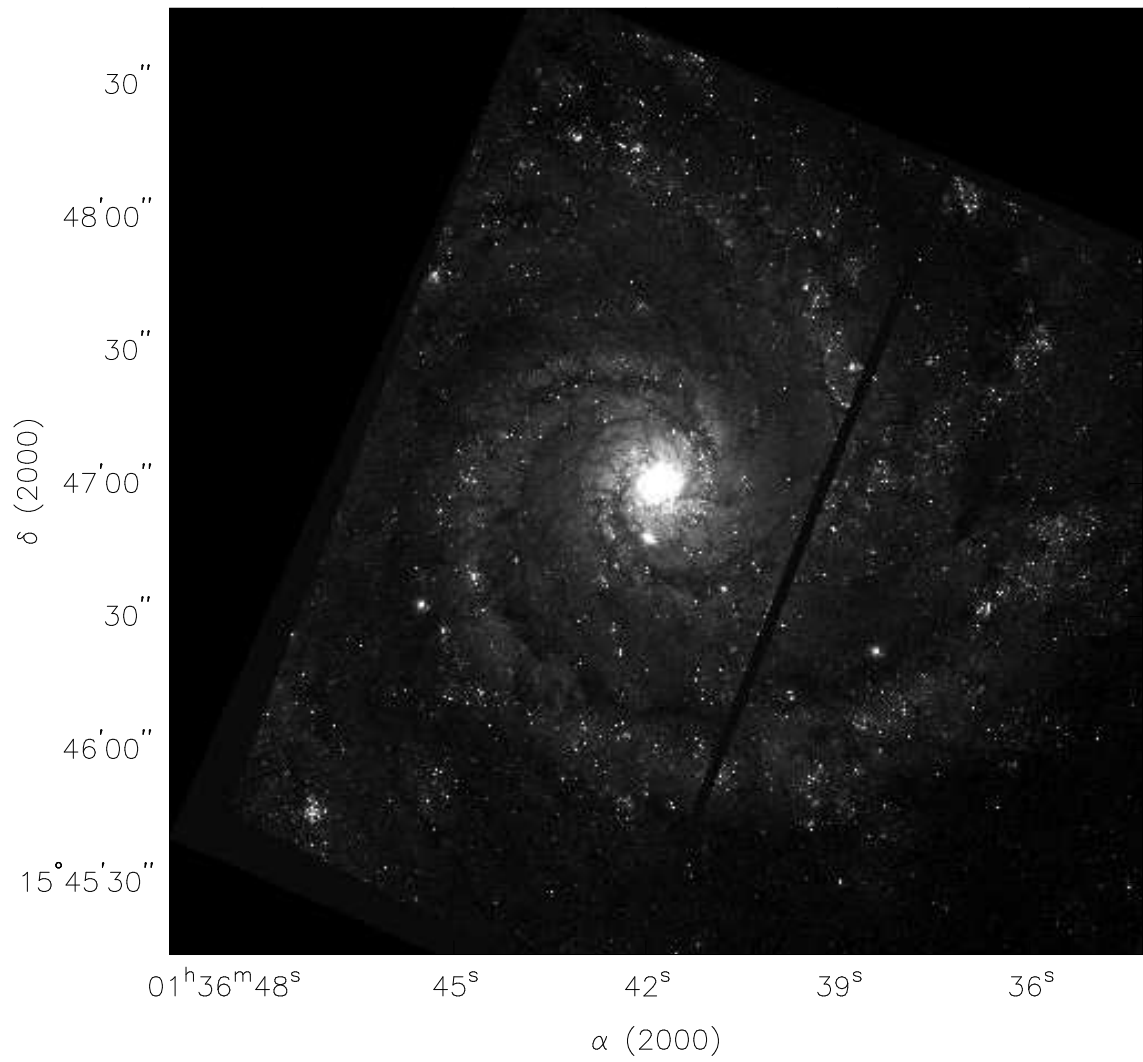Figure 5.23 NGC 5055 Spitzer 8 μm map without feather markings.
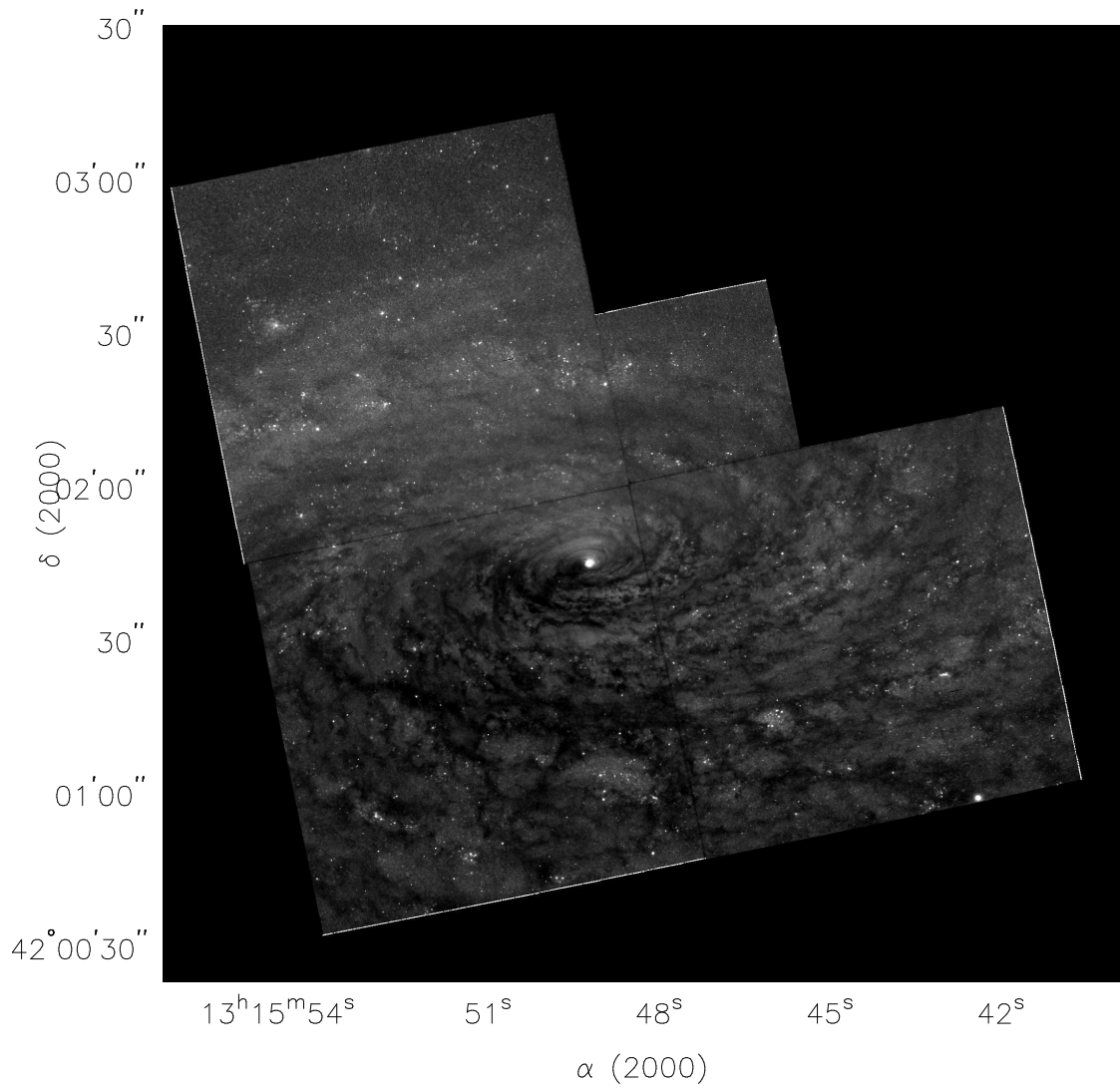
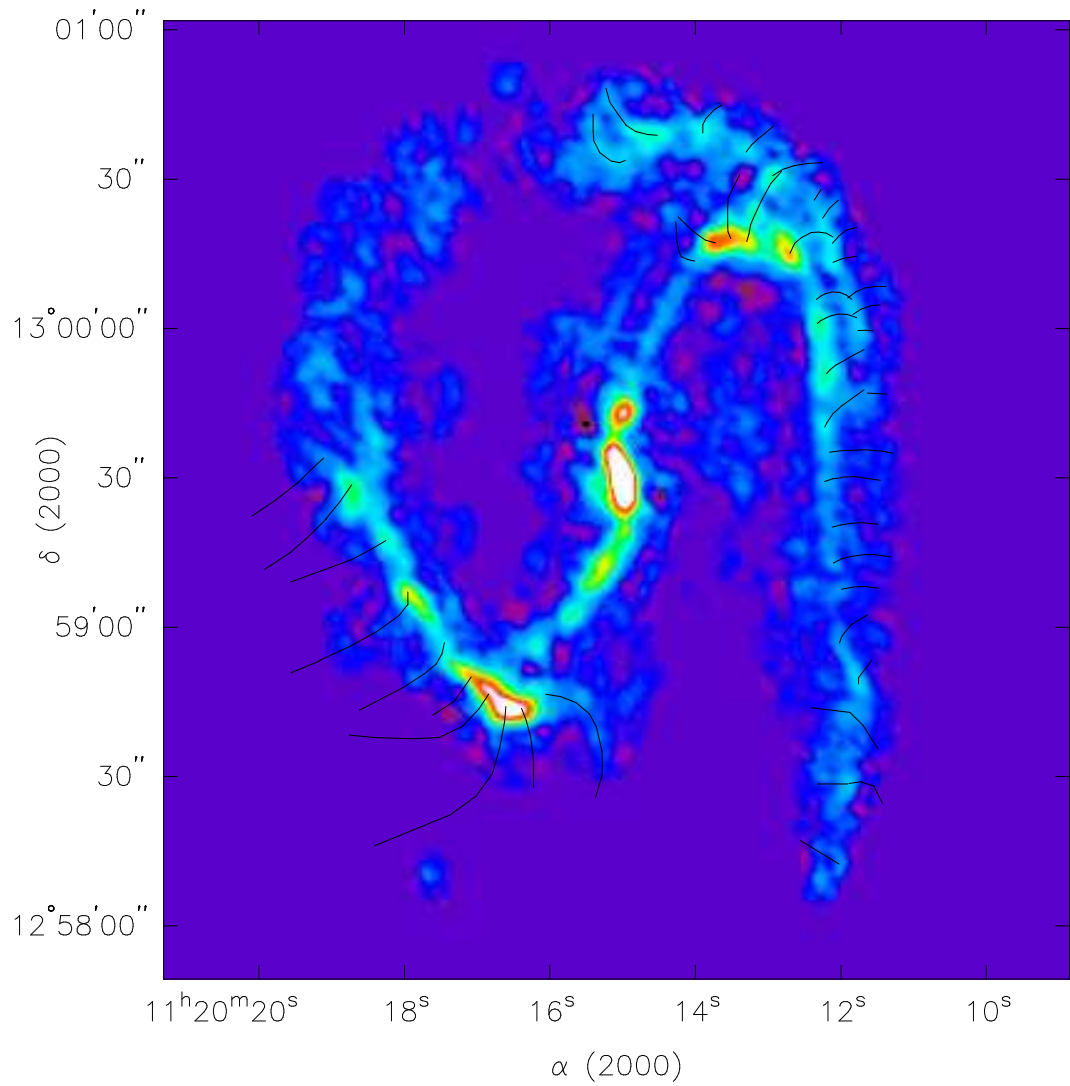Figure 5.24 NGC 5055 HST broadband image without feather markings.
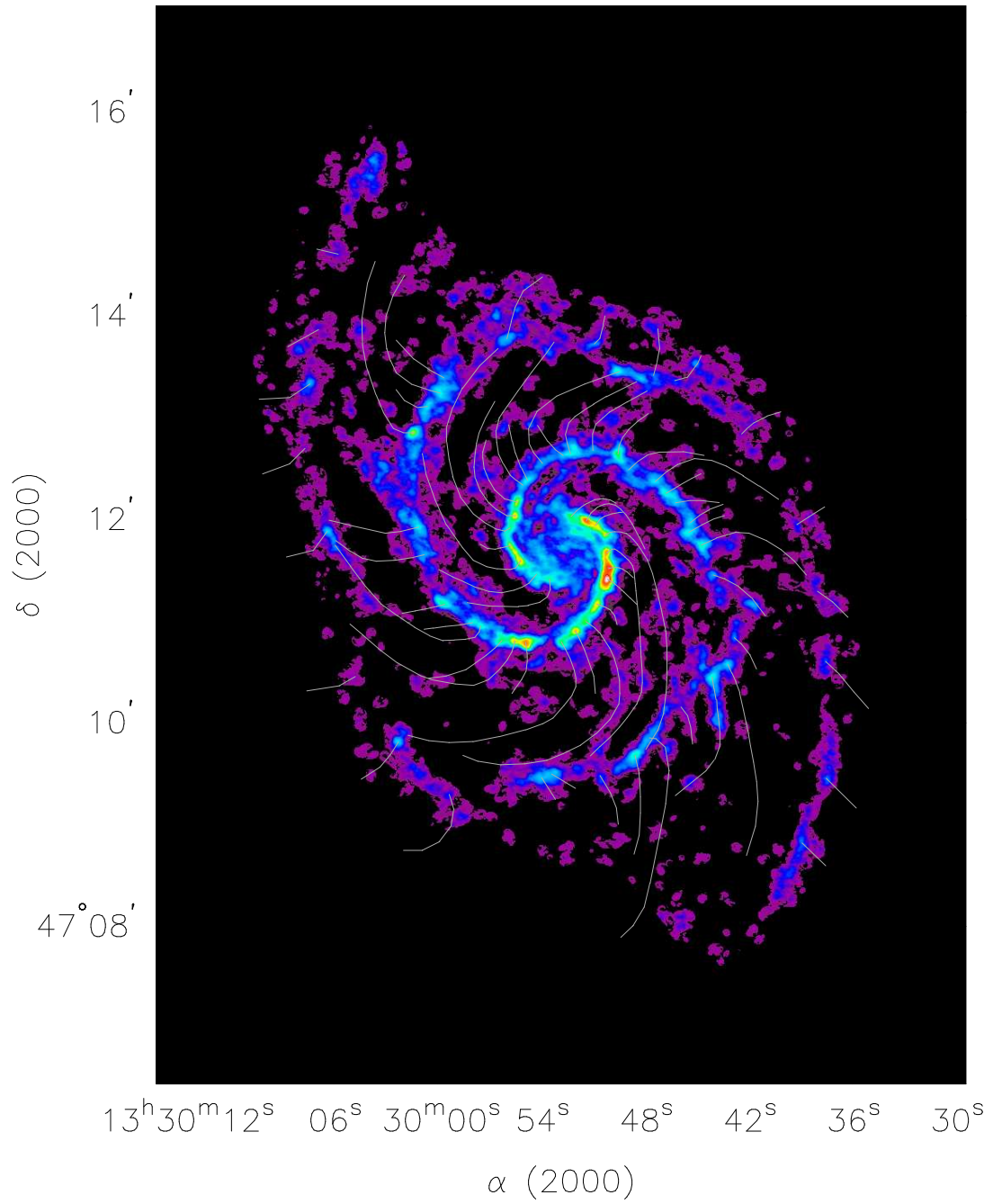
Figure 5.25 Feather markings for NGC 5194 overlaid on the CARMA CO(1-0) velocity-integrated map.
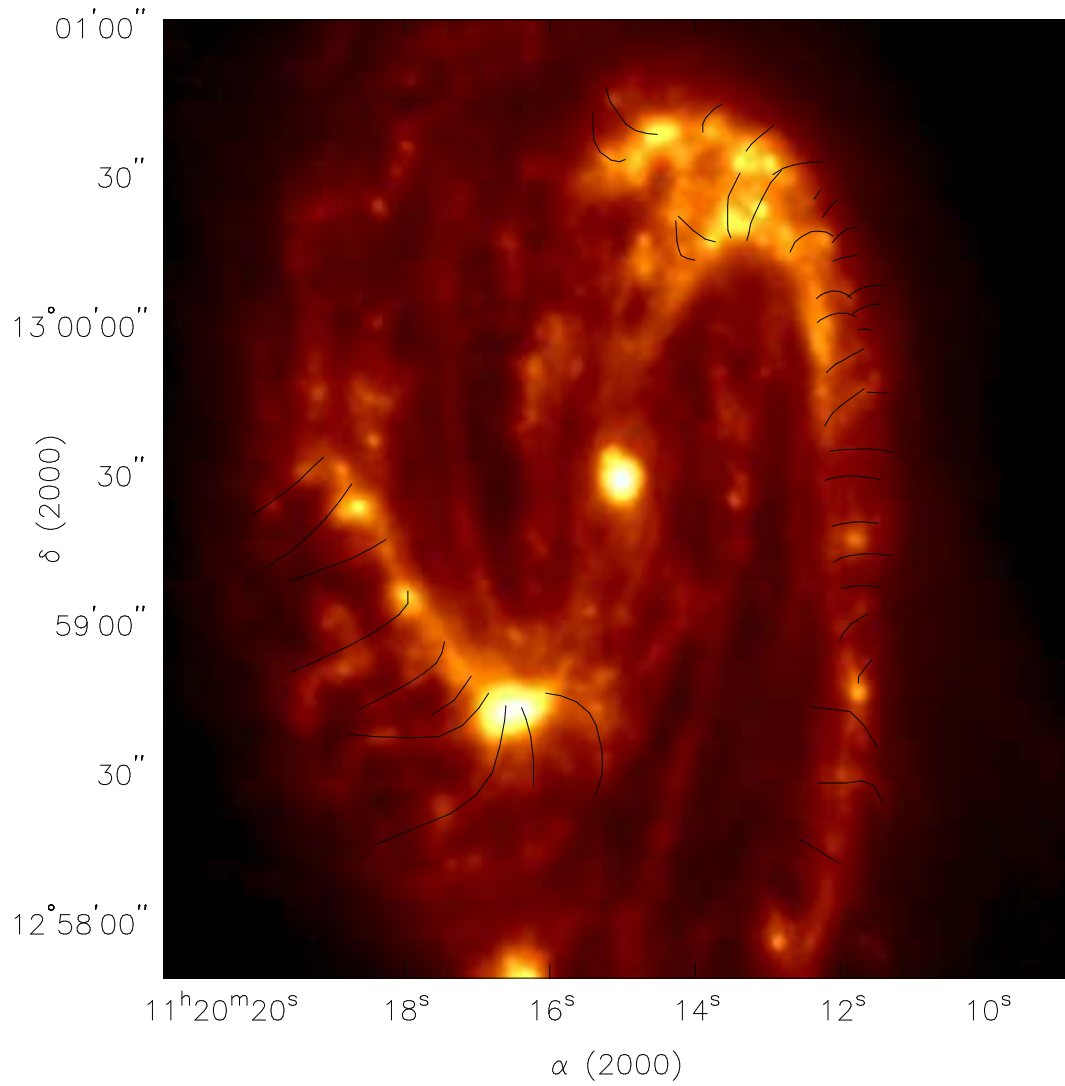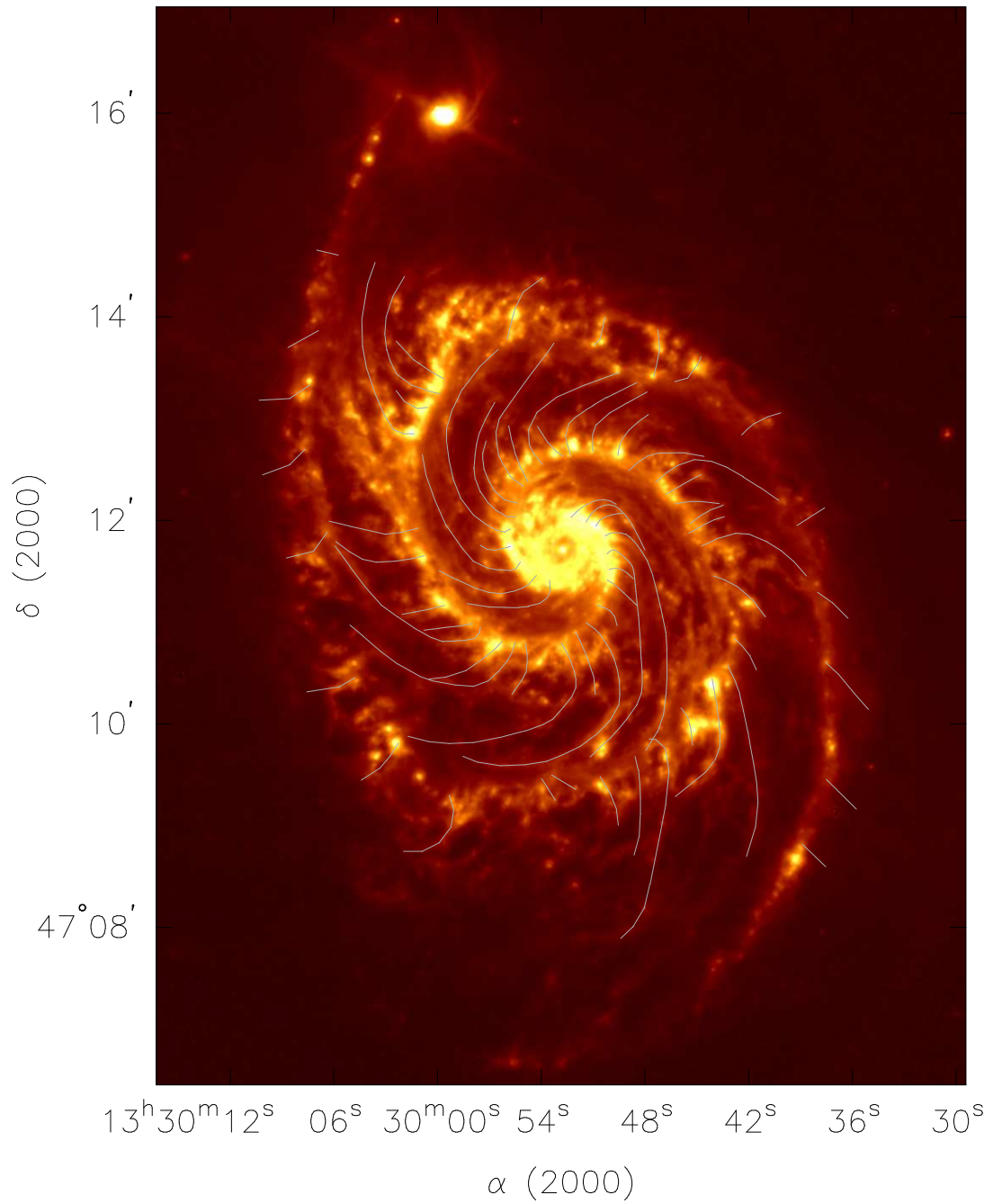
Figure 5.26 Feather markings for NGC 5194 overlaid on the Spitzer 8 μm map.
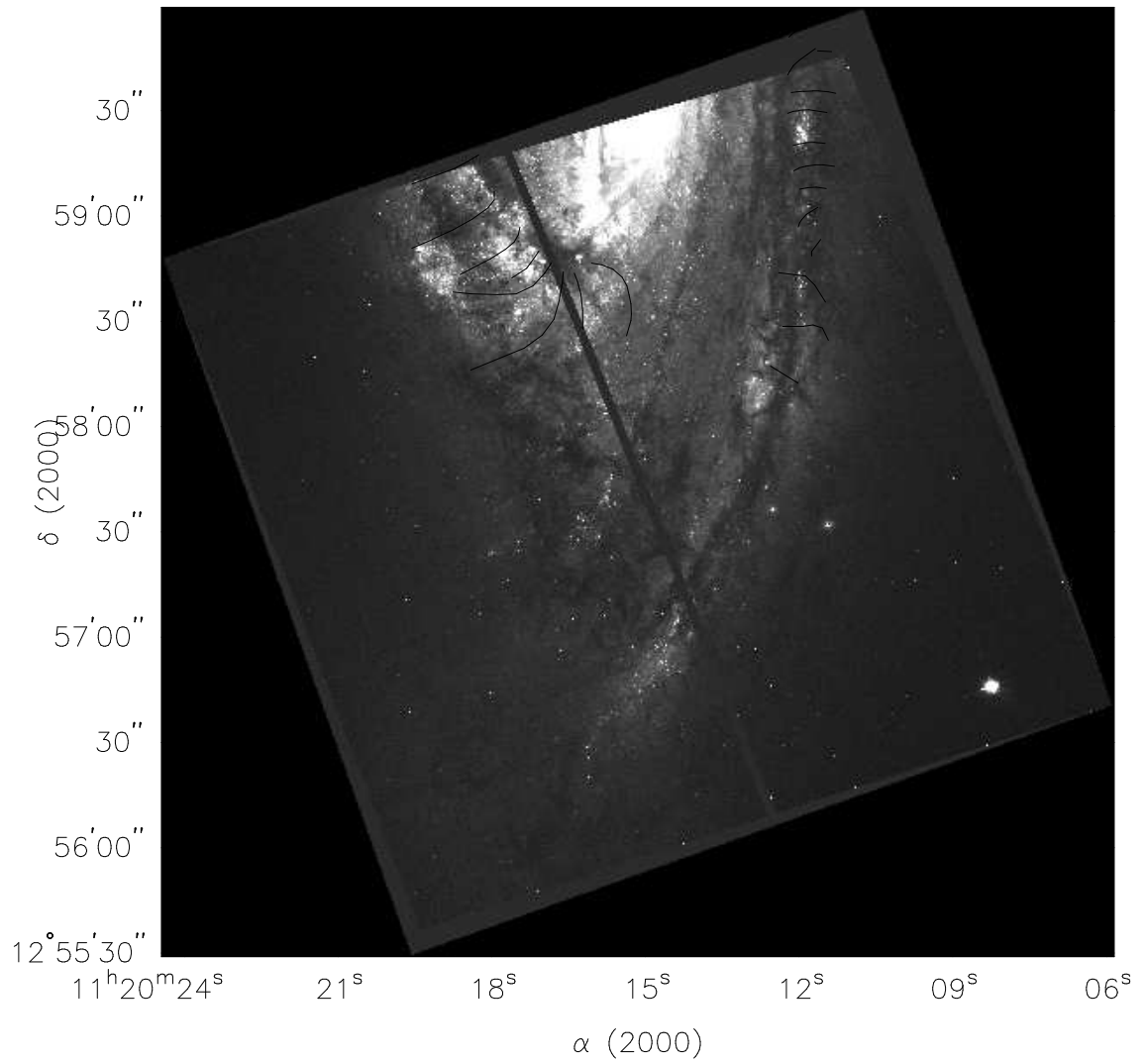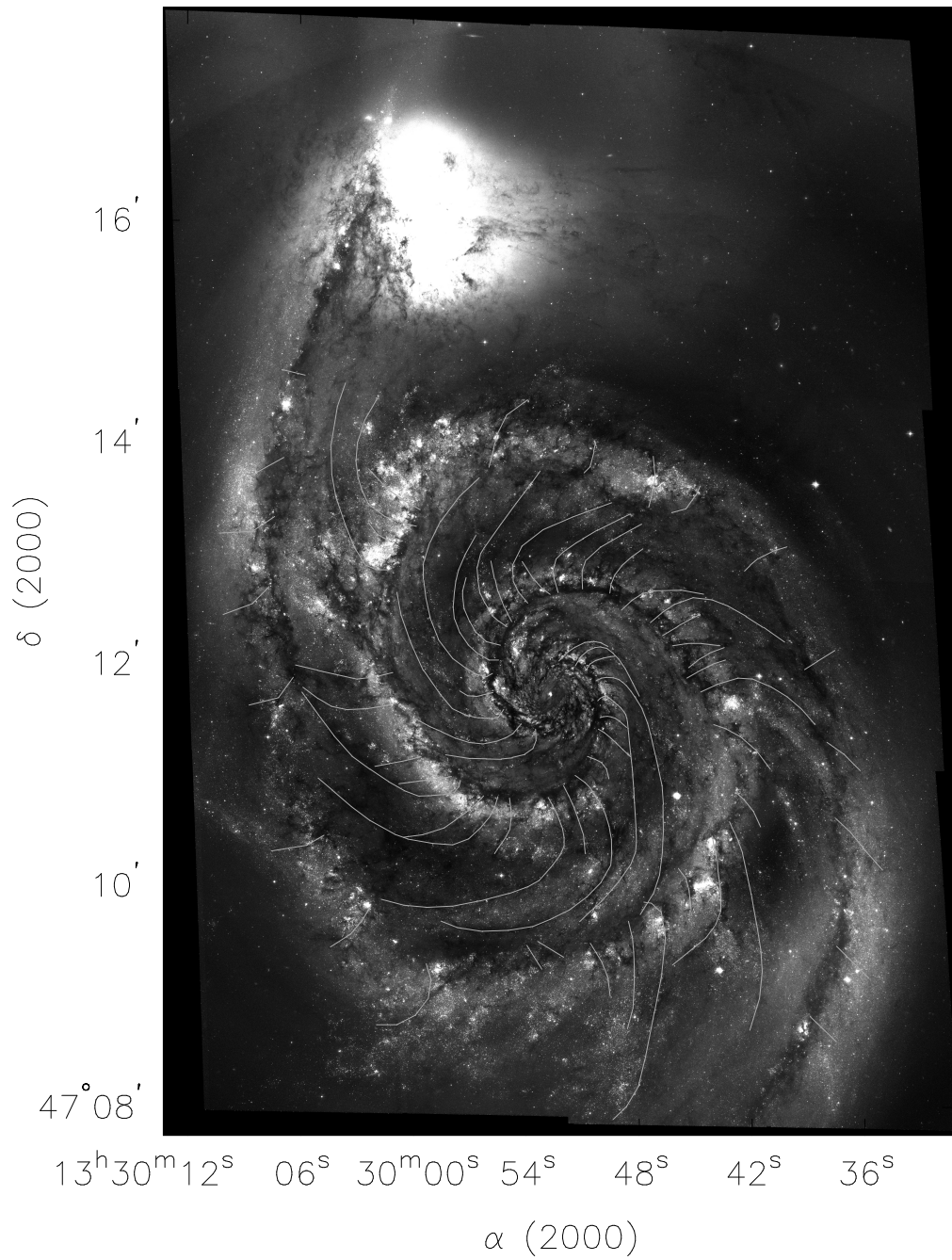
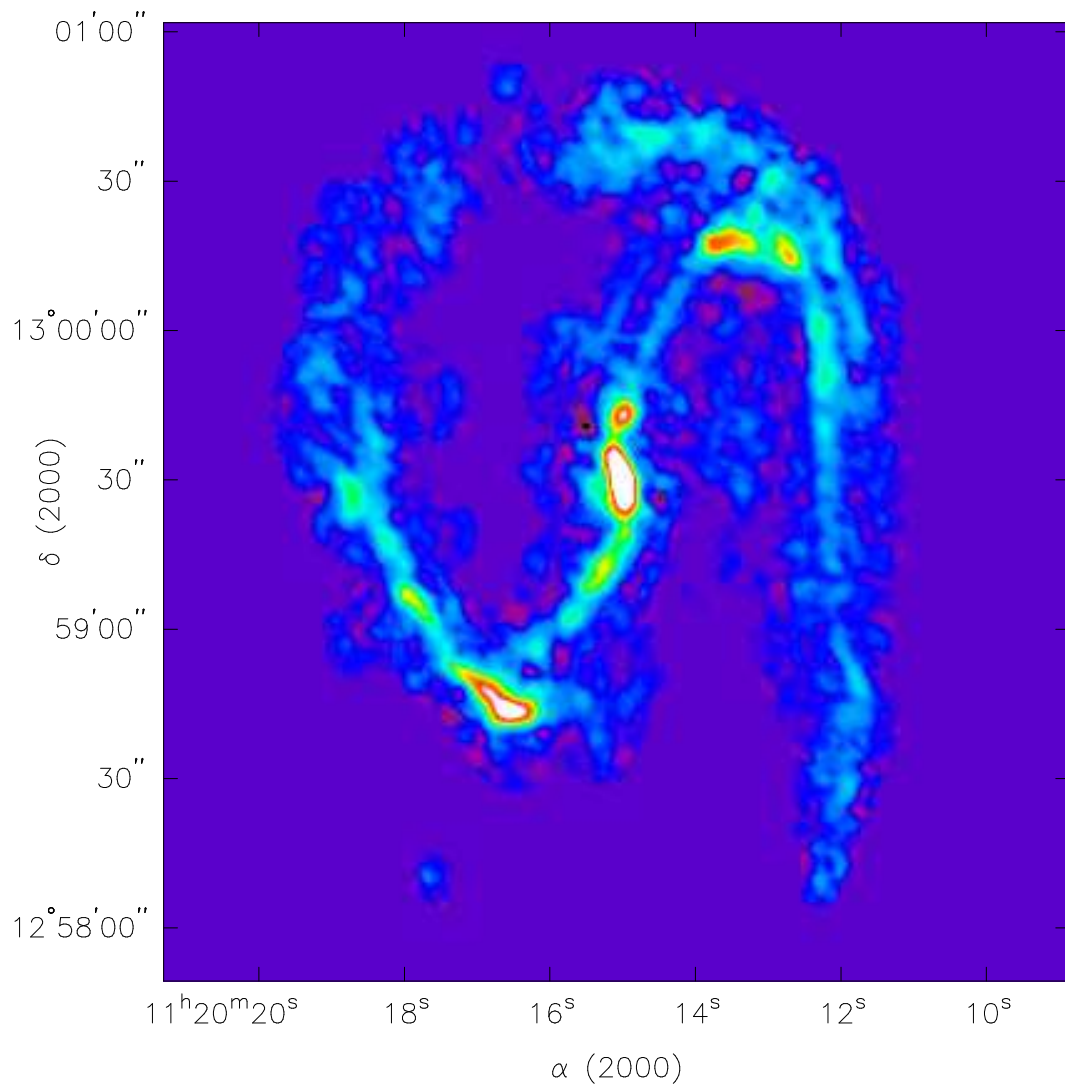Figure 5.27 Feather markings for NGC 5194 overlaid on the HST broadband image.
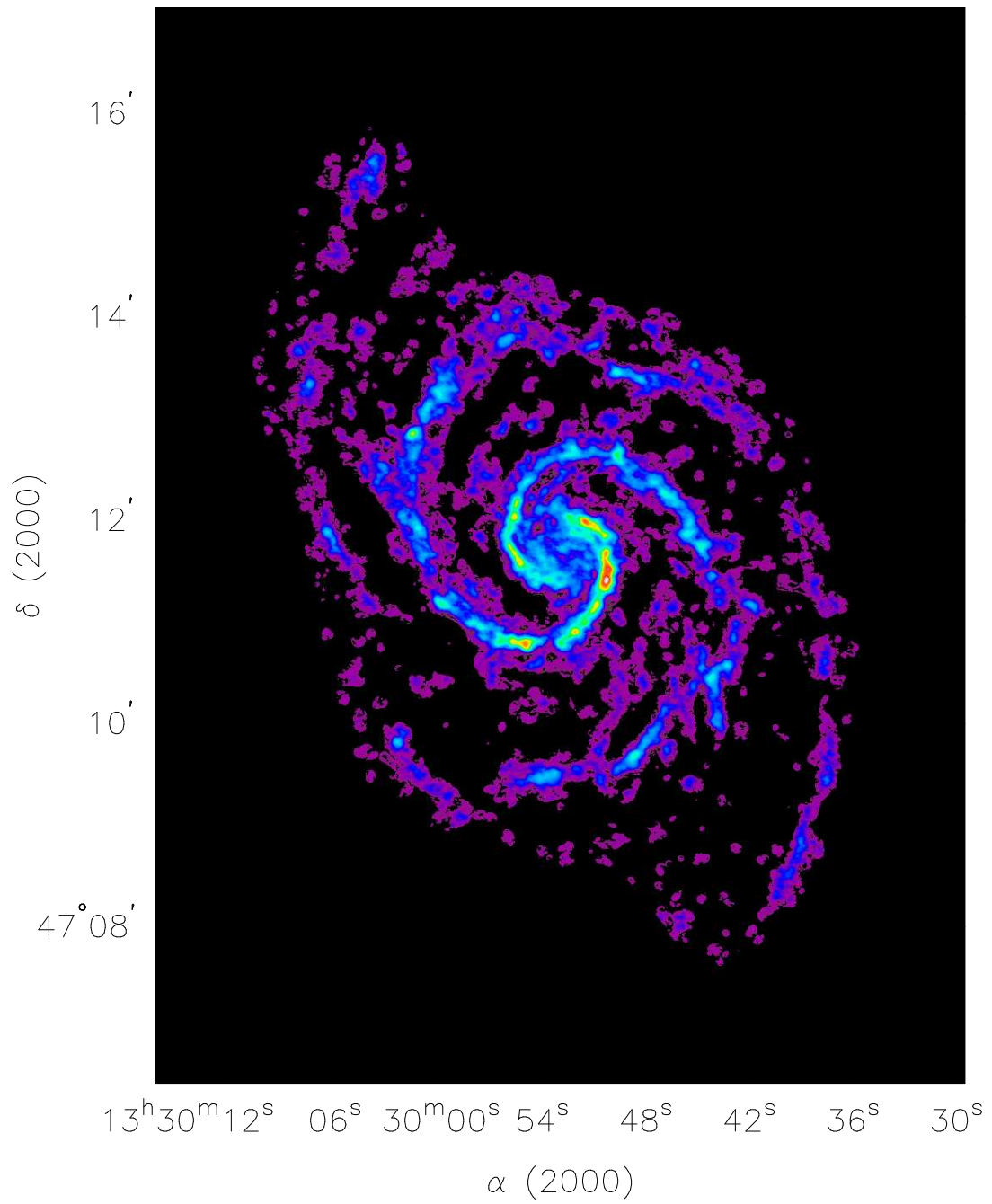
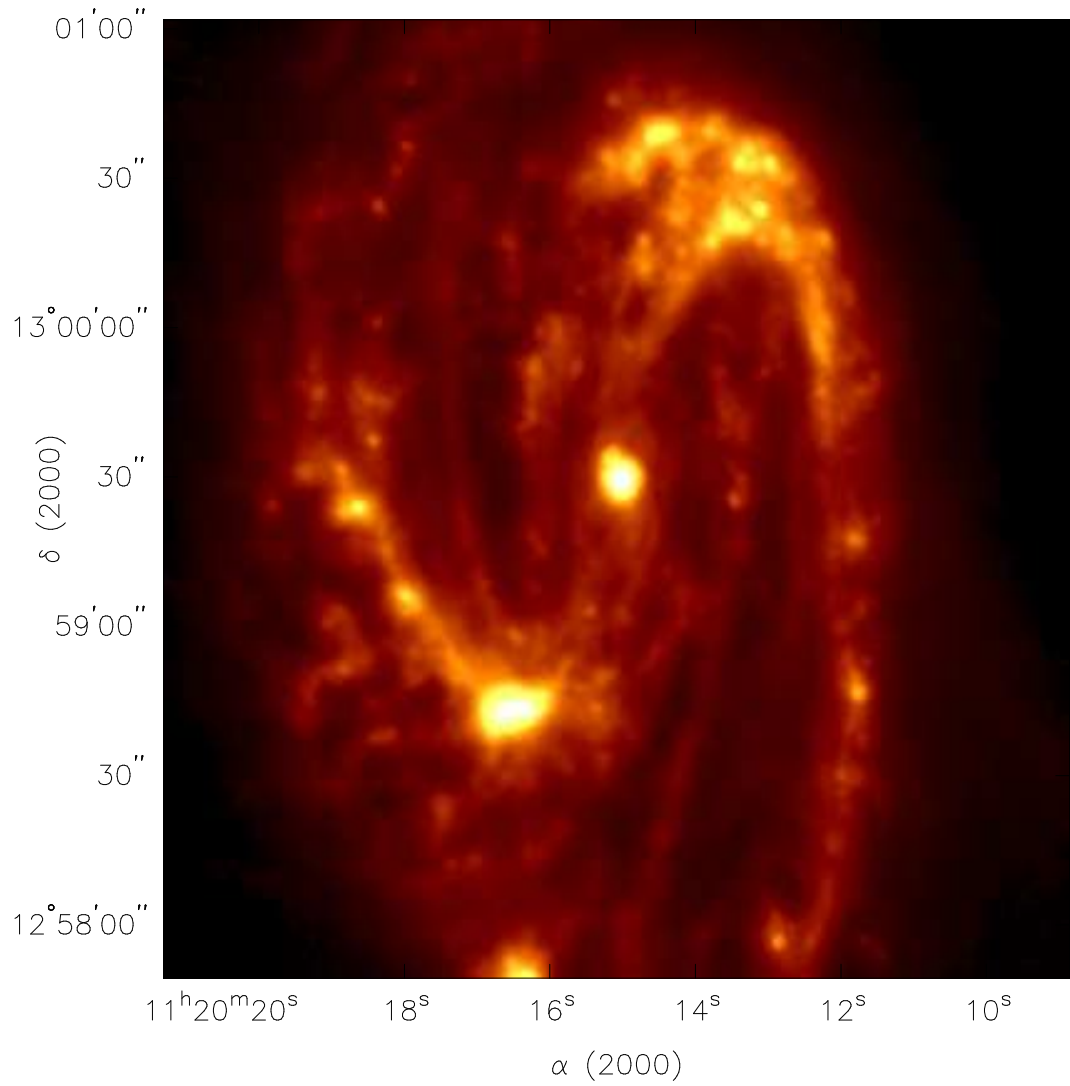Figure 5.28 NGC 5194 CARMA CO(1-0) velocity-integrated map without feather markings.
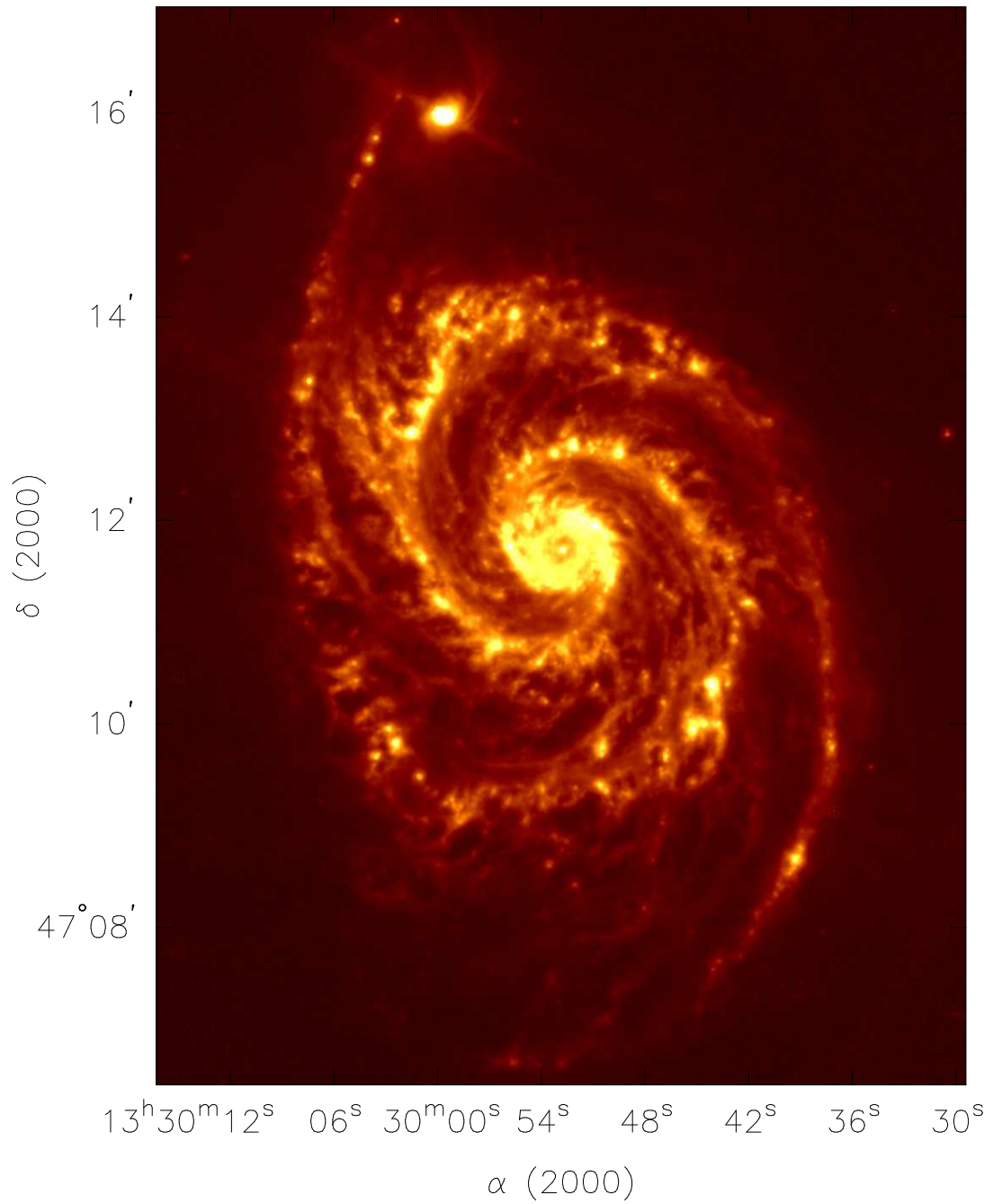
Figure 5.29 NGC 5194 Spitzer 8 μm map without feather markings.
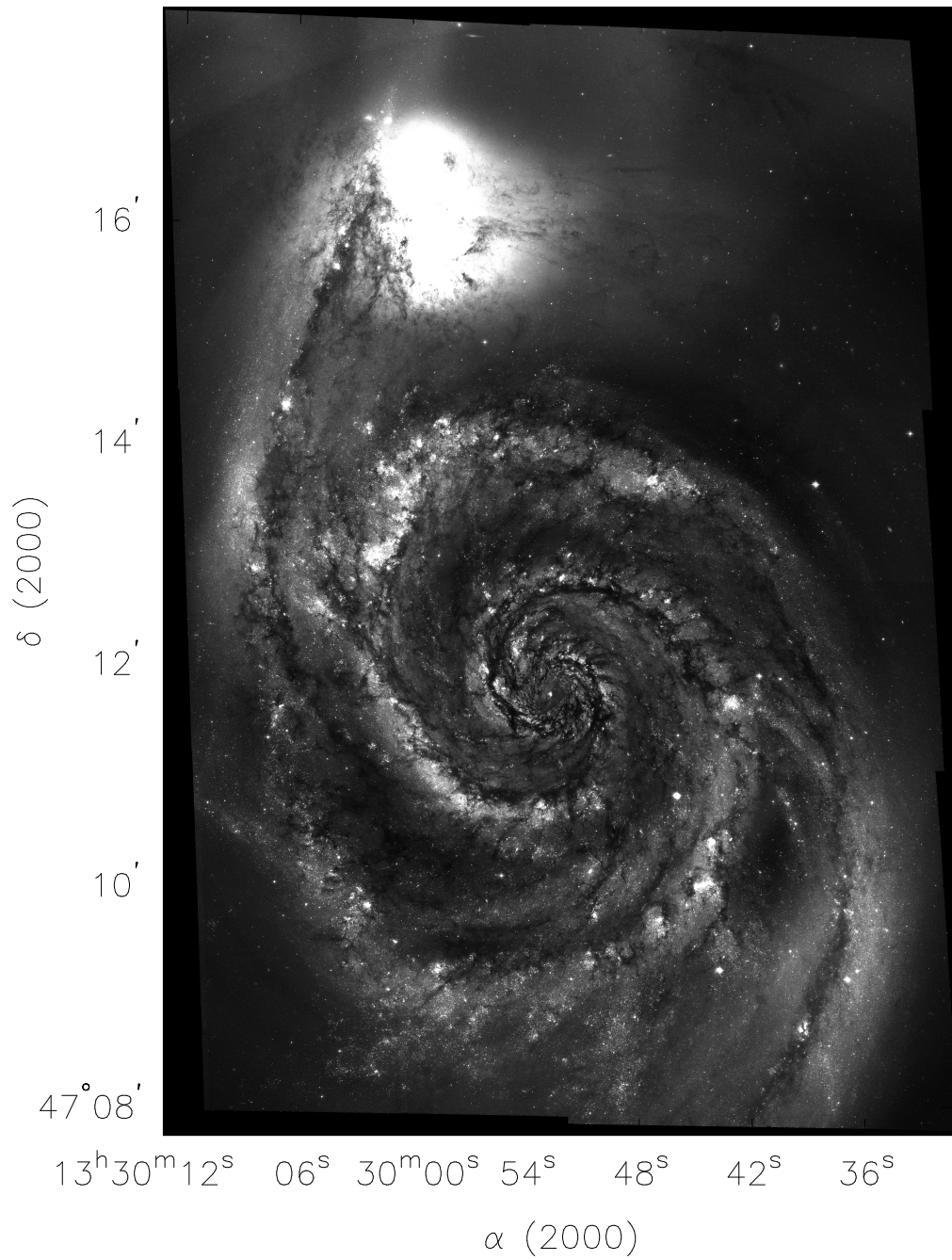
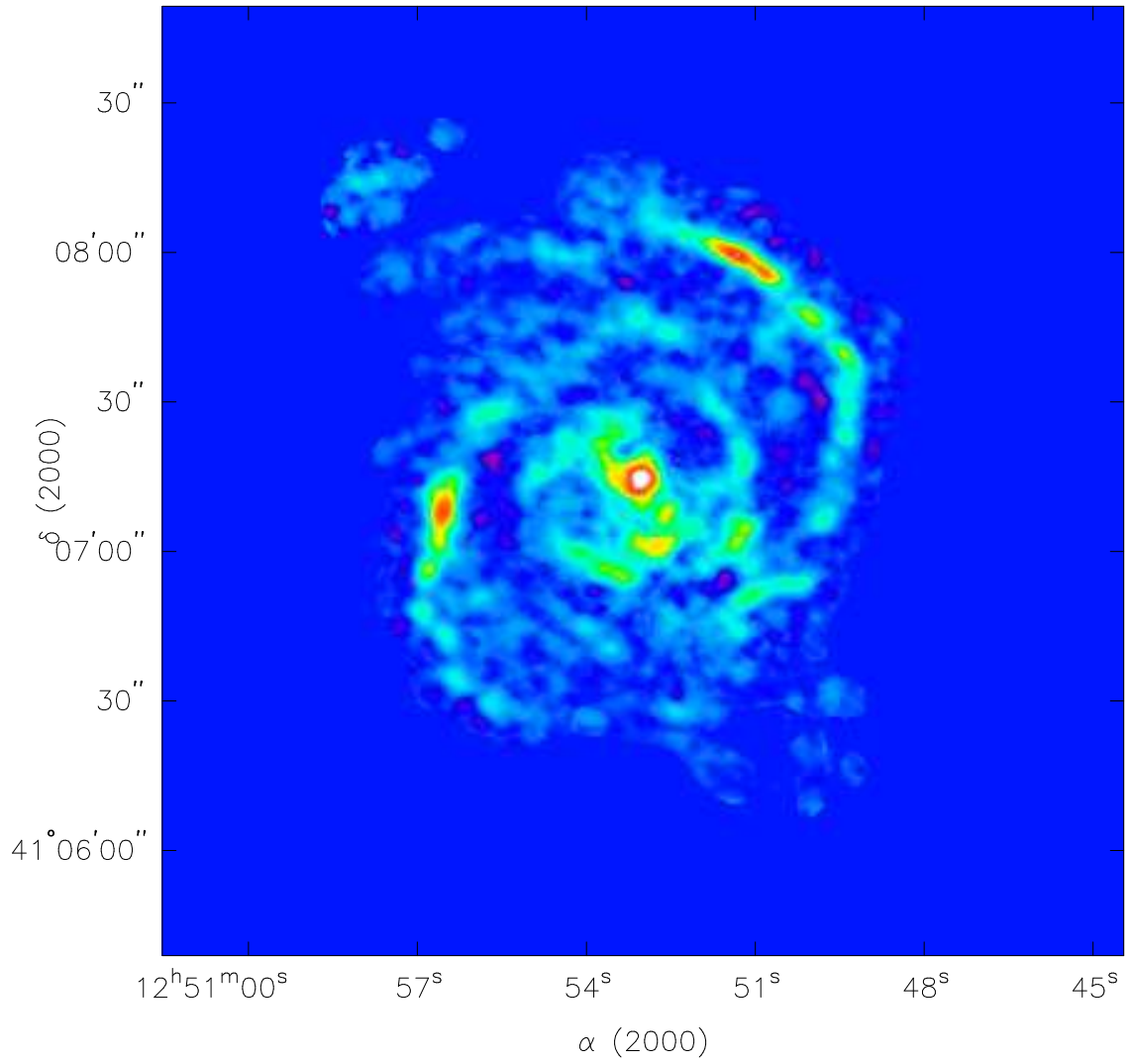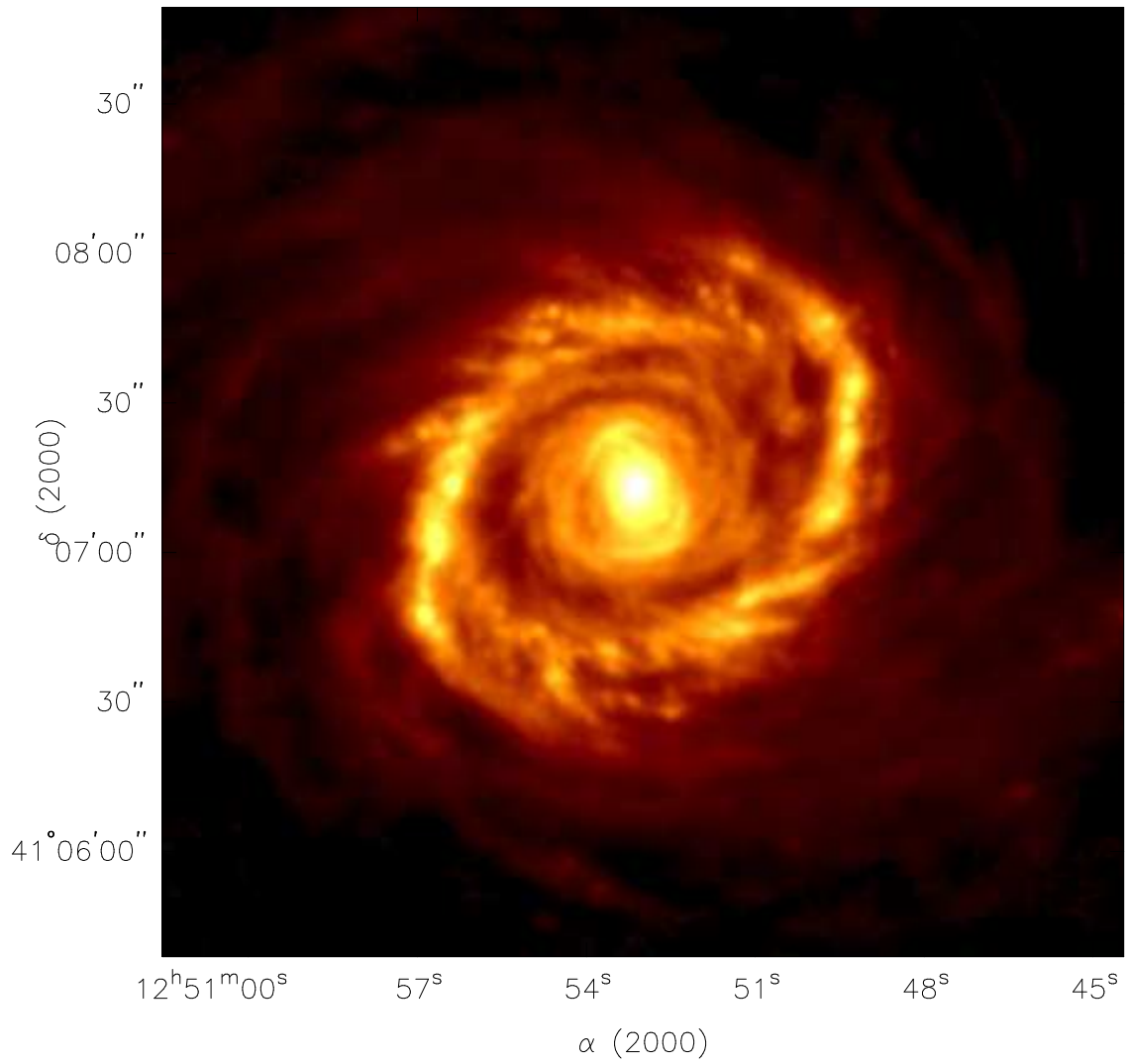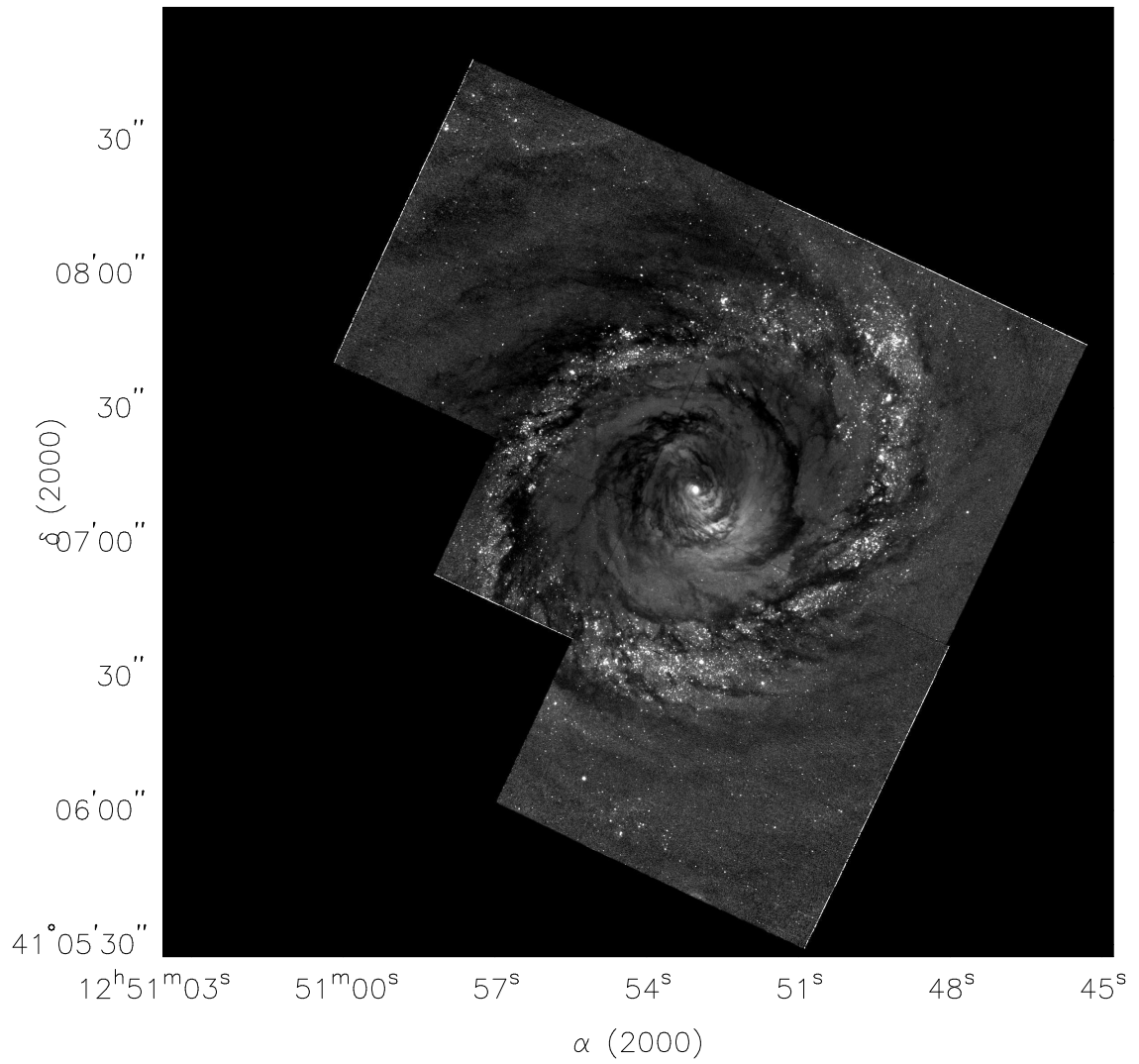Figure 5.30 NGC 5194 HST broadband image without feather markings.

5.3   Gas Mass in Feathers

As discussed in §2.3.6, although the feathers in M51 have been previously associated with GMAs (La Vigne et al. 2006), it is still not yet clear whether feathers in galaxies of other morphological types trace significant gas mass concentrations. To determine if the feathers identified in §5.2 are associated with significant gas mass, we used the IDL version of Clumpfind (Williams et al. 1994) to analyze the 3D (position-position-velocity) CO(1-0) datacubes to identify molecular cloud structures within. To perform the analysis, the data cubes first needed to be normalized by the data rms, which is not uniform across the field due to the interferometric mosaic pattern. Clumpfind works by contouring the data, searching for local peaks of emission, and following he peaks down to lower intensity levels (Williams et al. 1994). It works most effectively by allowing the increment between contours to be $2\sigma_{rms}$, with the suggested lowest contour to be $2\sigma_{rms}$ as well. The limits for detecting a clump require that it be resolved in velocity, over at least one velocity channel, and that its radius be larger than the beam size. While these limits typically weeded out most false detections, a handful were also rejected for each galaxy by inspection with the plotting package for Clumpfind, CLPLOT. Termed "runaway" clumps, they result from poorly defined clumps with parameters falling just above the set limits.

Next the mass and location of each clump were determined. Mass M of a clump is proportional to the CO(1-0) integrated intensity and is given by,

$$M \propto \Sigma T \Delta x \Delta y \Delta v D^2,$$

where T is the brightness temperature and the summation is over all the pixels in

a clump, Δx and Δy are the pixel size or grid spacing of the map, Δv is velocity channel width, and D is the distance to the galaxy (Williams et al. 1994). The position and mass distribution of the identified clumps is shown in Figures 5.31-5.35. While the most massive clumps are concentrated along the spiral arms in each of the galaxies, there are clumps of significant mass detected in the interarm region of each galaxy. Furthermore, these interarm clumps coincide with previously identified feathers (see §5.2). The most massive molecular structures, GMAs, with masses ranging from $10^7 - 10^8$ M$_\odot$ only occur along the spiral arms or in the central regions of a galaxy. For NGC 5194 and NGC 3627, most of the peaks along the PDLs are GMAs, from which feathers originate; for the other three galaxies, most of the peaks are GMCs with M $> 10^6$ M$_\odot$, and these are also the source of the feathers. The association of feathers with massive concentrations of gas is not limited to the spiral arms. The interarm clumps observed lining the feathers range in mass from small GMCs (10^4 M$_\odot$) to massive GMCs (10^6 M$_\odot$). In all of our galaxies, the feathers are associated with significant amounts of molecular gas. In particular, the gas concentrations have the mass of GMAs and GMCs, the primary sites of massive star formation. Since our sample covers a wide range of spiral galaxy Hubble types and arm morphology, this suggests that this conclusion can be applied more generally to spirals as a class.

To determine the total fraction of gas in feathers compared to that concentrated in the PDLs, we summed the mass of the clumps in each galaxy. The percentage of total feather mass to total spiral arm mass is presented in Table 5.1 and varies from galaxy to galaxy. For NGC 3627, NGC 4736, and NGC 5194 the percentages
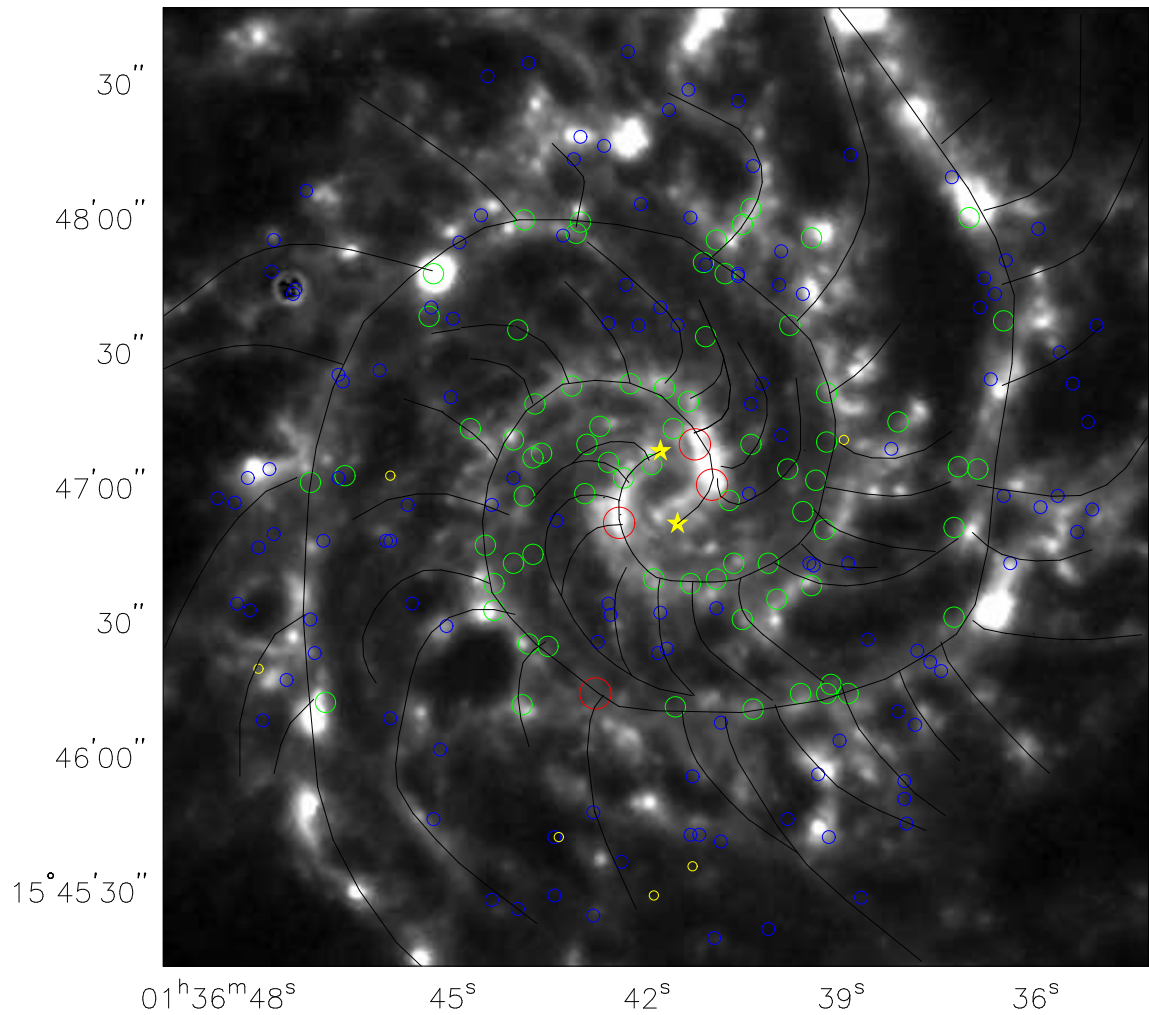
Figure 5.31 Distribution of molecular gas clumps in NGC 0628, overlaid on the Spitzer 8 μm map. The size and color of a circle indicates the mass of the clumps; black $> 10^7 M_\odot$, red $> 10^7 M_\odot$, green $> 10^6 M_\odot$, blue $> 10^5 M_\odot$, and yellow $> 10^4 M_\odot$. The black lines indicate the location of the PDL and the stars indicate where the PDLs begin.

Figure 5.32 Distribution of molecular gas clumps in NGC 3627, overlaid on the Spitzer 8 μm map. See Fig. 5.31 for details.

are most similar, ranging from 12-14%. For both NGC 3627 and NGC 4736, most of the gas mass is concentrated along the PDLs, with few interarm clumps. This is primarily due to the "stubby" nature of the feathers in these galaxies. The emission along the feathers peaks at the PDLs and extends briefly into the interarm region. For these types of feathers, Clumpfind identifies the entire feather as a part of the clump along the PDL. Thus the ratio of the independent interarm clumps to the clumps along the PDLs is low for these two galaxies. For NGC 5194 the ratio of
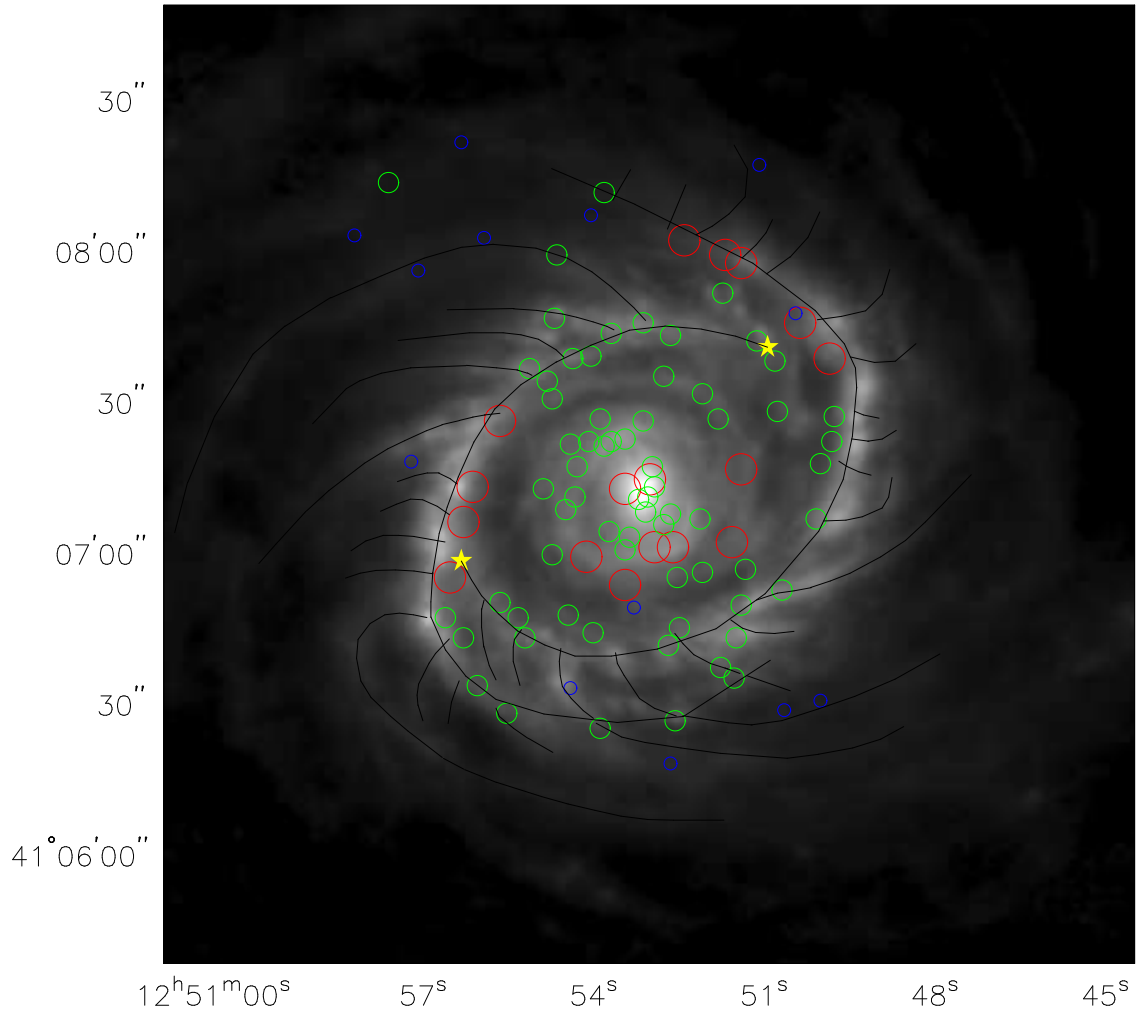
Figure 5.33 Distribution of molecular gas clumps in NGC 4736, overlaid on the Spitzer 8 μm map. See Fig. 5.31 for details.

total feather mass to total spiral arm mass is low for a different reason. Unlike the rest of the sample, the sensitivity map for NGC 5194 was not available for use in the analysis. Therefore, in order to limit the number of "runaway" detections due to attenuation at the edge of the mosaic field, the lower contour level of NGC 5194 was set to $4\sigma_{rms}$ in the data cube. This set a lower limit to the mass of the molecular clouds Clumpfind detected, resulting in a lower ratio.

Both NGC 0628 and NGC 5055 have significantly higher feather mass to spiral
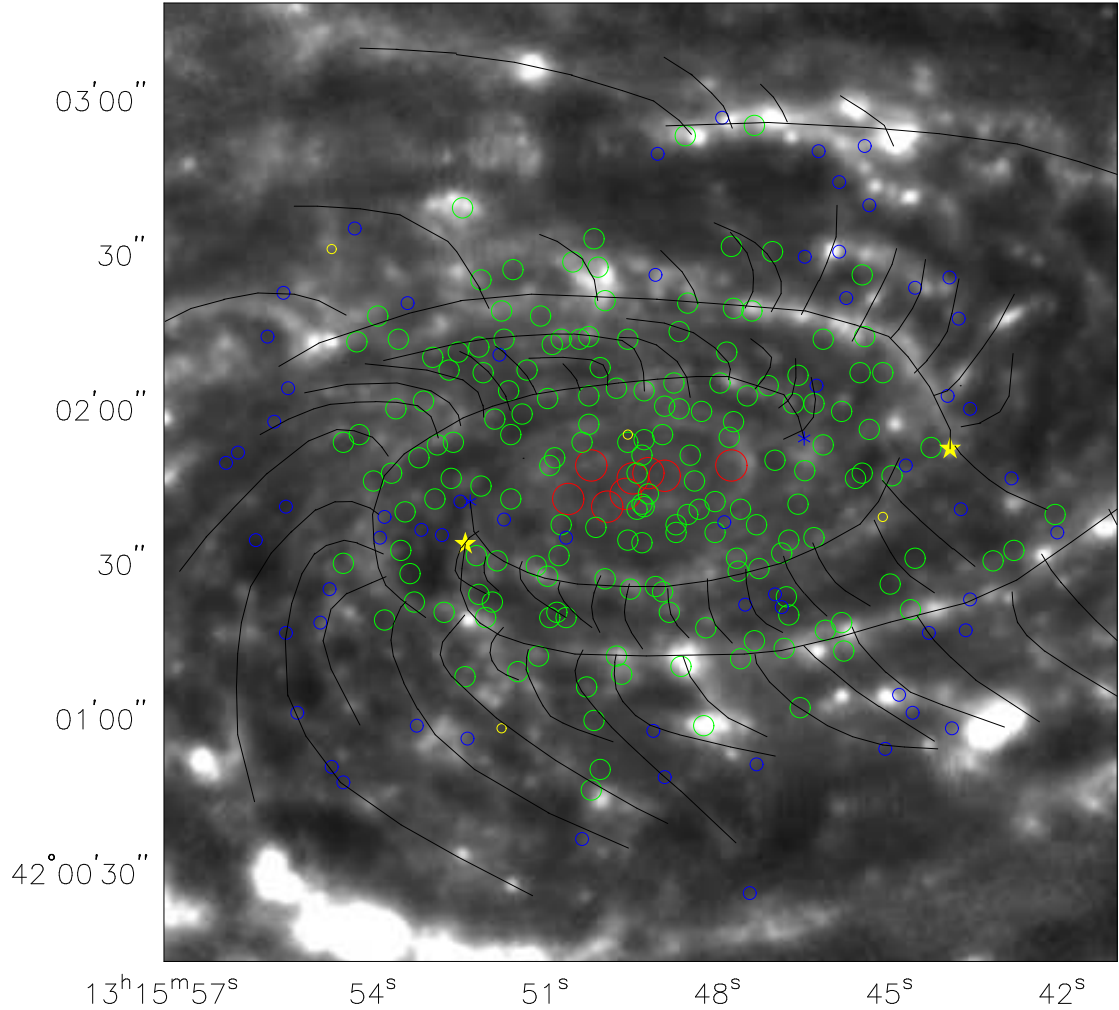
Figure 5.34 Distribution of molecular gas clumps in NGC 5055, overlaid on the Spitzer 8 μm map. See Fig. 5.31 for details.

arm mass ratios than the other galaxies. Within both galaxies, the feathers are more extended than NGC 3627 and NGC 4736, and there is a significant amount of gas associated with these extended feathers. However, the concentration of gas in the spiral arms of NGC 5055 is quite low compared to the rest of the sample; the spiral arms only have ~1.7 times the mass in the interarm region, which is mostly likely an indication of the weakness of the spiral density wave.
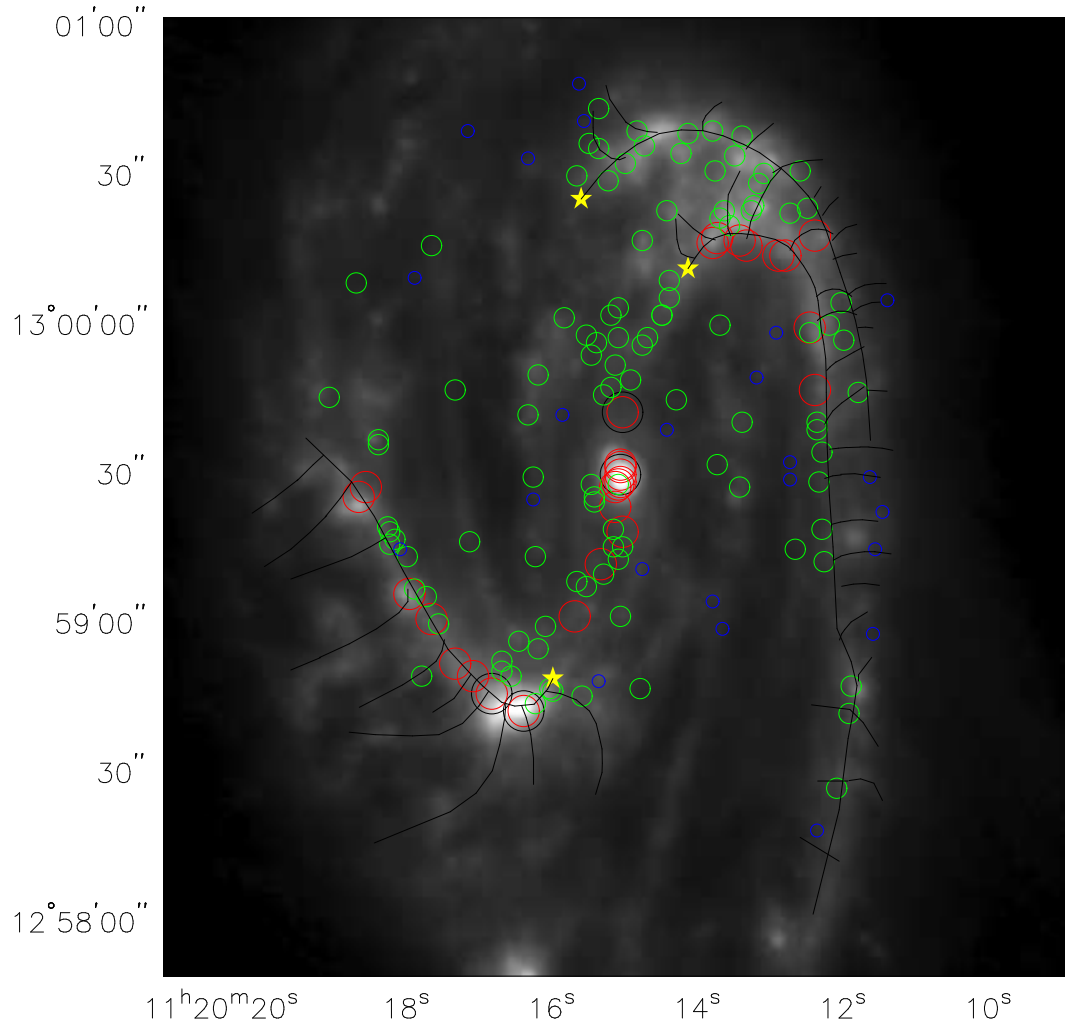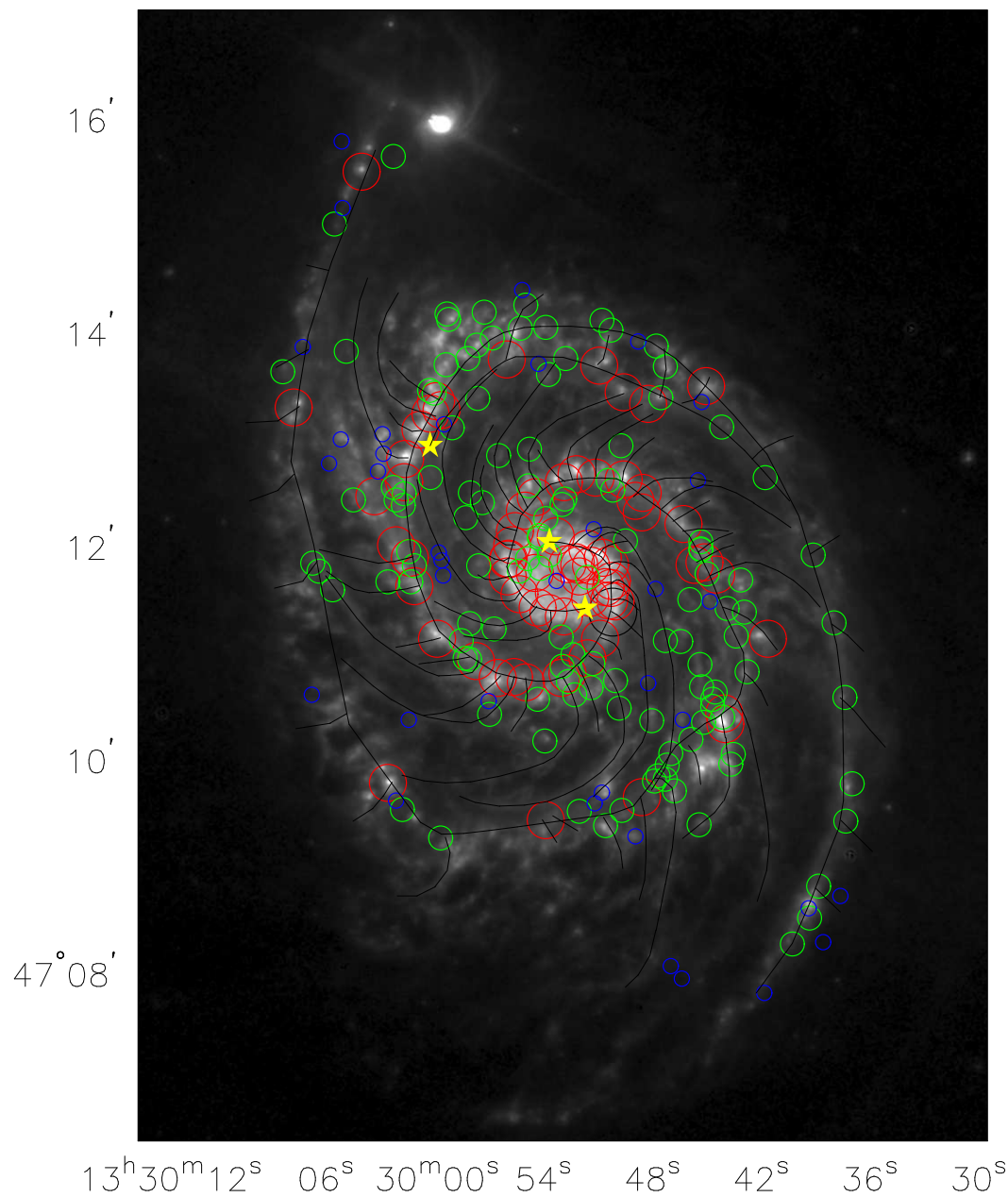
Figure 5.35 Distribution of molecular gas clumps in NGC 5194, overlaid on the Spitzer 8 μm map. See Fig. 5.31 for details.

Table 5.1.   Mass of Interarm and PDL Clumps

Galaxy	Total Mass of Clumps $M_\odot$	PDL Clump Mass $M_\odot$	Interarm Clump Mass $M_\odot$	Interarm Mass to PDL Mass %
NGC 0628	3.3×10^8	2.8×10^8	6.3×10^7	23.5
NGC 3627	2.5×10^9	1.3×10^9	1.6×10^8	12.2
NGC 4736	2.9×10^8	1.4×10^8	2.0×10^7	14.3
NGC 5055	1.2×10^9	4.9×10^8	2.9×10^8	59
NGC 5194	2.5×10^9	2.2×10^9	3.1×10^8	14.4

5.4   Feather Spacing

Analysis of $6''$ resolution data previously indicated a relationship between feather spacing and the local gas column density in M51 (La Vigne et al. 2006). Furthermore, in the previous section, §5.3, we showed that feathers are associated with a significant amount of gas mass in each of the galaxies in the sample. Therefore, we further develop the analysis first conducted by La Vigne et al. (2006) by comparing the azimuthal spacing of the feathers to the local gaseous surface density along the spiral arms in each galaxy of our sample using the higher resolution, velocity-integrated CARMA CO(1-0) maps.

To measure the gaseous surface density along the spiral arms, we followed the prescription described in §2.3.7. We sampled the CO(1-0) maps along the PDLs of each arm at $\sim 0.5''$ (the pixel size) spacing. We then estimated the H_2 column densities and corresponding deprojected molecular hydrogen surface density, Σ_{H_2}, using the relations previously assumed in §2.3.7.

We plot Σ_{H_2} versus the distance along the PDLs for each galaxy in Figures 5.36-

5.40. Below each surface density profile, the location of feathers along the PDL is indicated by tick marks.

We compare the molecular surface density profiles for the sample of galaxies. The profiles of NGC 5194 and NGC 3627 are similar: Σ_{H_2} rises from the beginning of the PDL, peaks, and then generally declines, although there are fluctuations. In NGC 5194, the peak Σ_{H_2} occurs at $\sim 50''$ from the beginning of the PDL in both arms and in NGC 3627 the peaks occur at $\sim 10''$; both galaxies have one arm that has a peak Σ_{H_2} significantly higher than the other.

NGC 0628 and NGC 5055 both have similar surface density profiles; the peaks in surface density are relatively constant along the PDLs. The PDLs in NGC 0628 are traced for $\sim 350''$ in the new CARMA images, much further than the 100–150$''$ traced in the BIMA images (See §2.3.7). These peaks, as well as those observed in the rest of the sample galaxies, have surface densities of typical GMCs. This indicates that a gravitational collapse has already occurred.

The gas surface density profile for NGC 4736 is different from the other four galaxies. It does not exhibit the "peak, then decline" profile seen in NGC 3627 and NGC 5194, nor does it have constant peaks in surface density as in NGC 0628 and NGC 5055. The peak in gas surface density for NGC 4736 occurs much further out along both arms, and in Arm 2 the peak actually occurs close to the end of the CO(1-0) arm.

We then compared the azimuthal positions of the feathers to the molecular surface density profiles for each arm in each galaxy. The feathers are associated with peaks in the gaseous surface density along the spiral arms, as noted in §5.3.
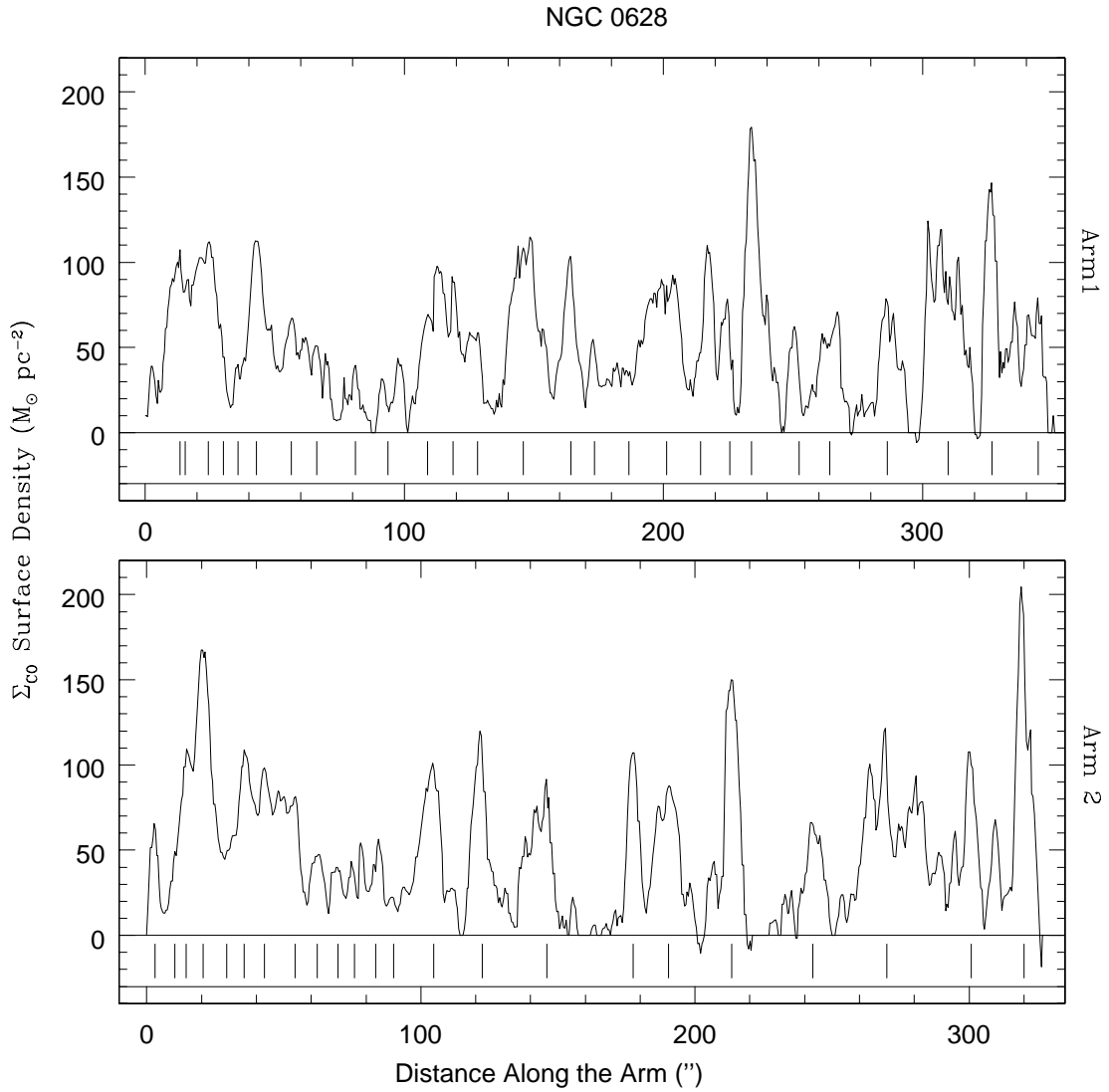
Figure 5.36 Variation in deprojected H$_2$ surface density, Σ_{H_2}, along the spiral arms of NGC 0628. The short vertical lines indicate the location of a feather along an arm.

Generally, the feathers are spaced closer together at the beginning of the PDLs and further apart towards the end.
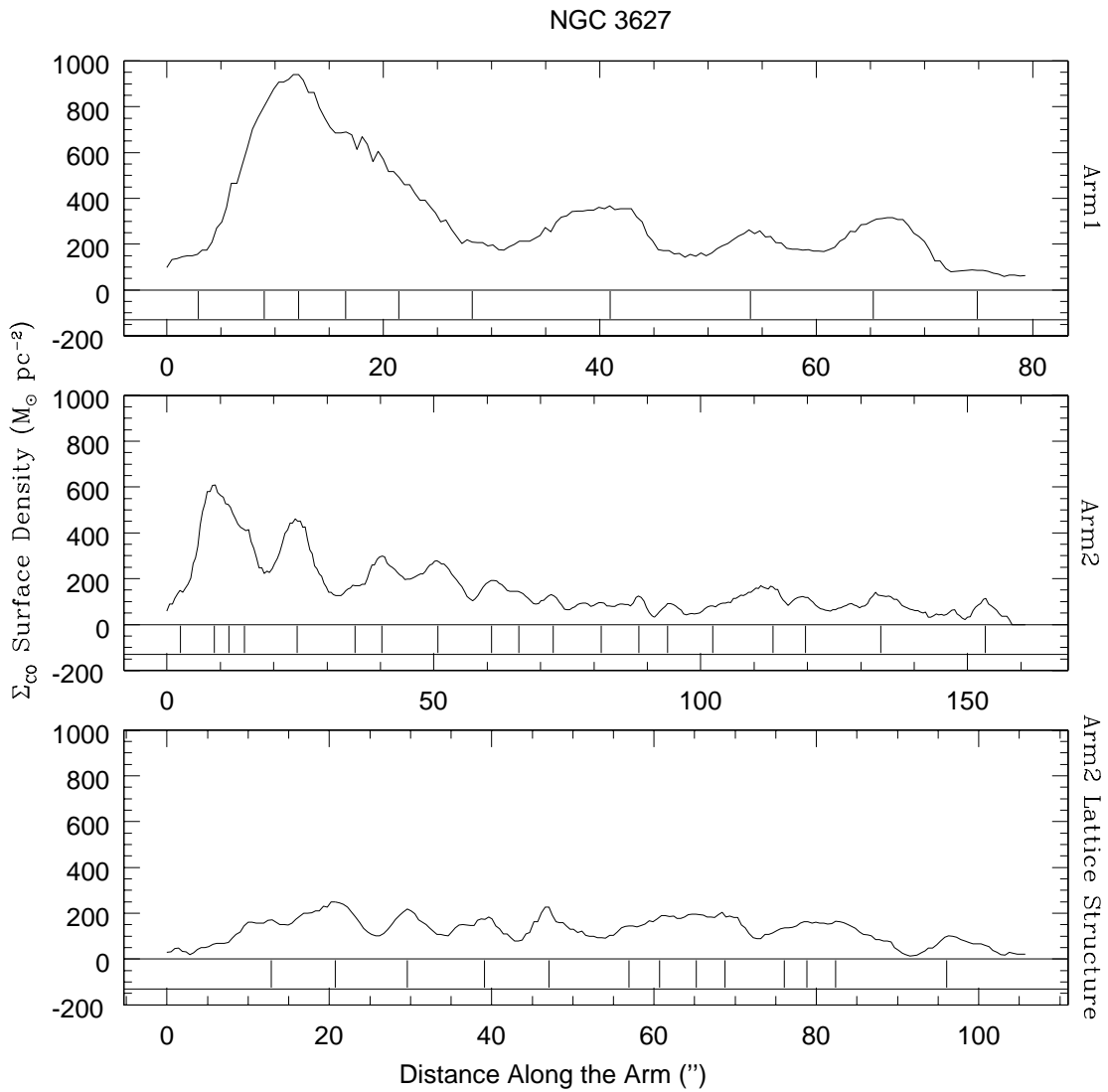
Figure 5.37 Variation in deprojected H$_2$ surface density, Σ_{H_2}, along the spiral arms of NGC 3627. The short vertical lines indicate the location of a feather along an arm.
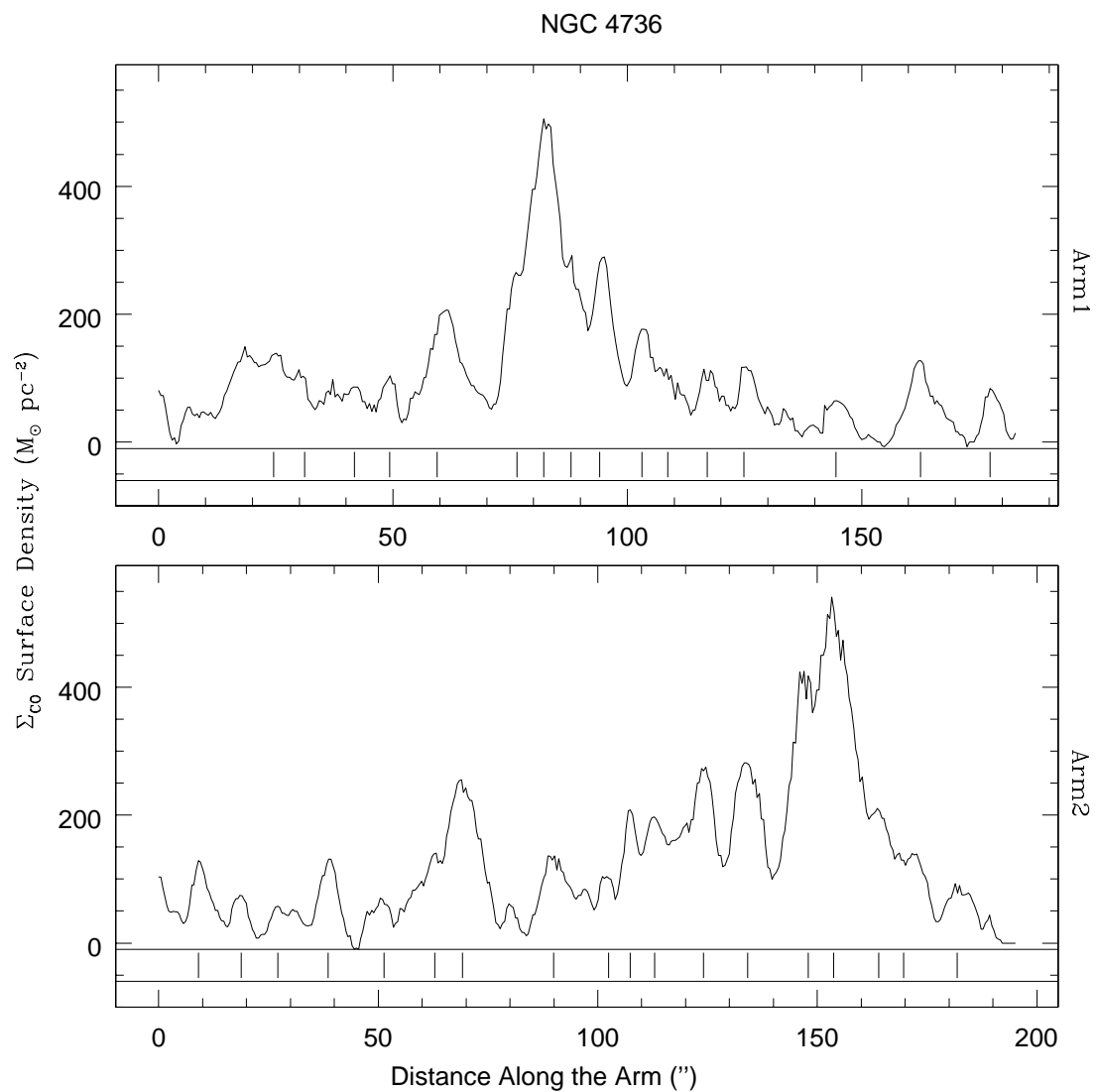
Figure 5.38 Variation in deprojected H_2 surface density, Σ_{H_2}, along the spiral arms of NGC 4736. The short vertical lines indicate the location of a feather along an arm.
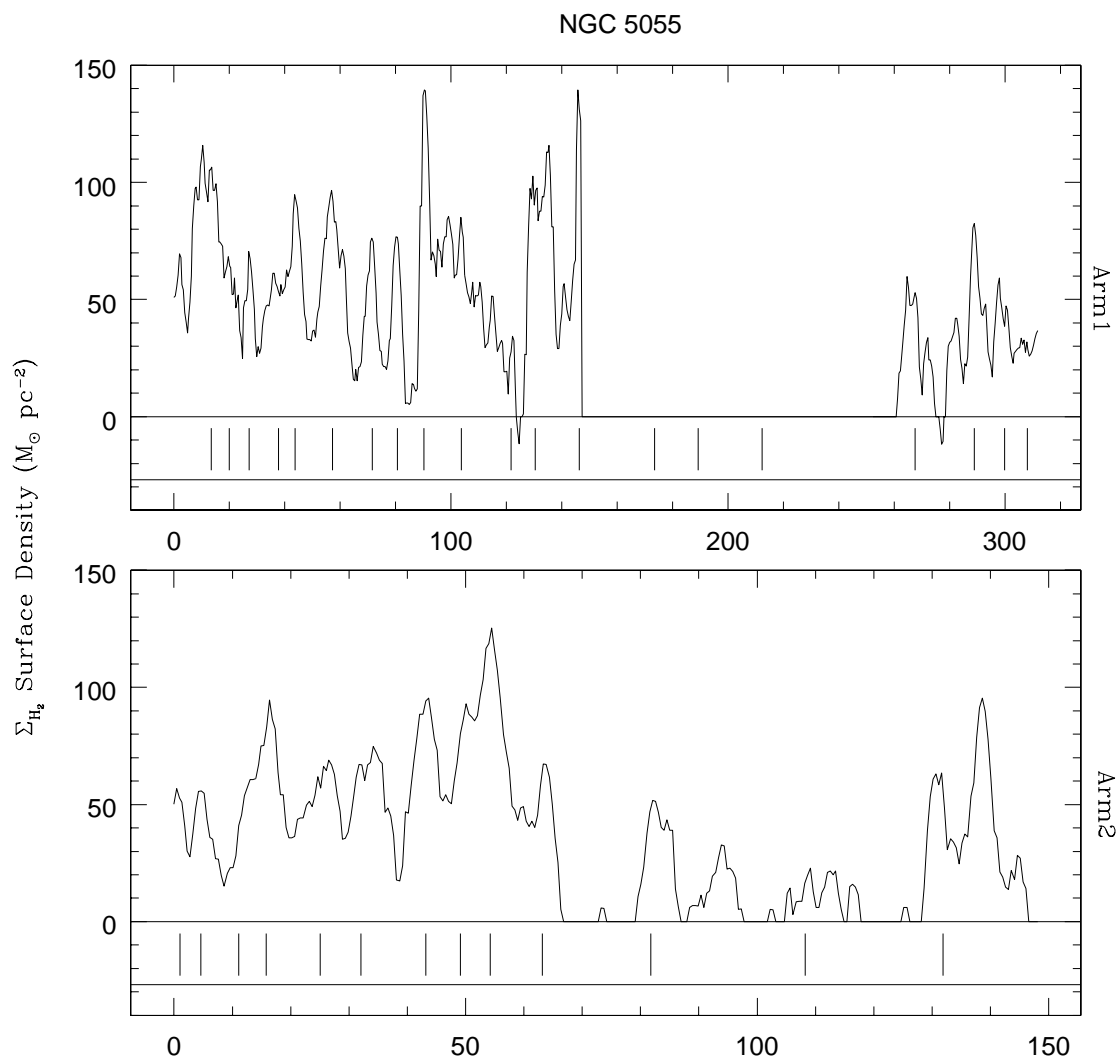
Figure 5.39 Variation in deprojected H$_2$ surface density, Σ_{H_2}, along the spiral arms of NGC 5055. The short vertical lines indicate the location of a feather along an arm.
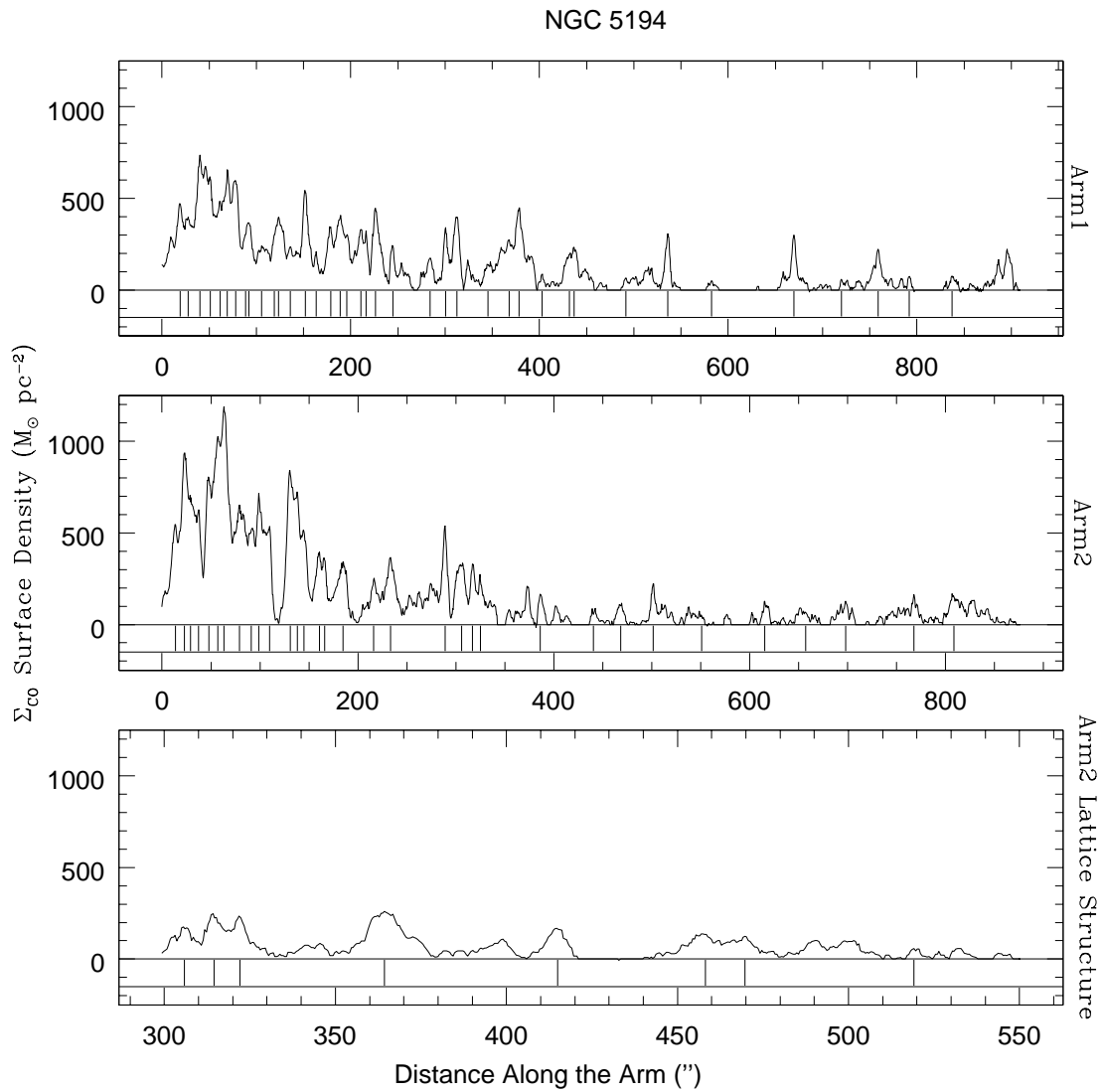
Figure 5.40 Variation in deprojected H_2 surface density, Σ_{H_2}, along the spiral arms of NGC 5194. The short vertical lines indicate the location of a feather along an arm.

5.5 Testing Models for Feather Origin

5.5.1 Relation between Spacing and Jeans Length

In the previous section, we found that feathers are associated with significant gas mass, both along the PDLs and in the interarm region. We also found a correlation between feather spacing and gas surface density along the spiral arms. This suggests that feathers may form via a gravitational instability, such as the Jeans instability. To investigate further, we compared the linear or deprojected feather spacing (see Appendix A for method of calculation) along the arm to the spacing for gravitational collapse estimated by the Jeans length. As in §2.3.7, we estimate the Jeans length as

$$\lambda_{Jeans} = c_s^2/(G\Sigma).$$

where c_s is the effective sound speed, which we adopt to be 7 km s^{-1} for the entire sample. In our previous analysis (La Vigne et al. 2006), the value for Σ was simply selected as the local maximum in the gaseous surface density at the site of feathers along the spiral arms. However, the molecular gas peaks we see now are the *result* of gravitational collapse; depending on the size of the region that collapsed, the original surface density could vary widely. Therefore, for this analysis we have averaged the molecular gaseous surface density within an elliptical aperture, circular when deprojected, centered on the location of the feathers along the spiral arms. The aperture size was determined by averaging the deprojected spacing between the neighboring feathers on both sides of a feather, and then corrected for the inclination

of the galaxy. This method more accurately measures the total amount of gas that contributed to the gravitational instability in the past when it originally condensed along the spiral arm.

Figures 5.41-5.45 show the feather spacing, Jeans length, and their ratio as a function of the distance along each spiral arm for the galaxies in the sample. Overall, the feather spacings increase with distance along the arms, from the inner galaxy to the outer as discussed in §5.4. This trend is most noticeable in NGC 0628 and NGC 5194 where the feather spacings increase from ∼200 pc in the inner galaxy for both out to 1100-1500 pc and 2000-3000 pc, respectively in the outer galaxy. Both NGC 3627 and NGC 5055 also exhibit the same trend in feather spacing versus distance along the arm, though the change in feather spacing from the inner galaxy to that in the outer is not as large as in NGC 0628 and NGC 5194. For NGC 4736, Arm1 also shows an increase in feather spacing, ranging from 200 pc in the inner galaxy to 400 pc in the outer galaxy. However, Arm2 shows an overall decline in feather spacing with distance along the arm.

For each spiral arm in the sample, the Jeans length typically follows the same trend as the feather spacing for that arm (see left column of Figs. 5.41-5.45). We therefore find a linear relationship between the deprojected feather spacing and the corresponding spacing predicted by the Jeans length in each galaxy within the sample (see Figs. 5.41-5.45). This includes Arm2 of NGC 4736, which exhibits a decline in feather spacing with distance along the arm, which can now be understood as the Jeans length declining in a similar fashion. Furthermore, we find that the ratio of feather spacing to the Jeans length varies considerably, ranging from 1.4 to

10.2 for the sample (Table 5.2). It is interesting to note that the prototypical grand design spiral galaxy NGC 5194 and the strongly barred galaxy NGC 3627 have the largest $\lambda_{feather}/\lambda_{Jeans}$. Both are strongly interacting galaxies; NGC 5194 with NGC 5195 and NGC 3627 is apart of the Leo Triplet. Though the spiral arms of NGC 0628 have a grand design nature similar to NGC 5194, its $\lambda_{feather}/\lambda_{Jeans}$ ratio is quite low, almost unity in Arm 2, and is an isolated galaxy compared to NGC 5194. It is also important to note that NGC 5055, a visibly flocculent galaxy, clearly displays the same linear relationship between feather spacing and Jeans length.

The feather spacings found in the sample are typically larger than the range of 100–200 pc predicted by Wada & Koda (2004; here after WK04), only occurring in the inner regions of a few galaxies in the sample. Dobbs & Bonnell (2006; here after DB06) predicted a constant feather spacing of $\sim$700 pc; such large spacings are seen in the majority of the galaxies towards the outer regions. However, both hydrodynamical models predict constant feather spacing along spiral arms, which is contrary to what we observe.

Kim & Ostriker (2002, 2006), and Shetty & Ostriker (2006) predicted the characteristic spacing of feathers to be 7-10 times the local Jeans length for their magnetized models, which include self-gravity and are stable to quasi-axisymmetric modes. In those models which are unstable to quasi-axisymmetric modes, the arms do not have well defined surface densities prior to the formation of feathers or "pre-fragmentation", but the feather spacings are in general smaller. For the observed range in ratios of feather spacing to Jeans length, NGC 5194 and NGC 3627, the two strongly interacting galaxies of the sample, fit the values predicted by Kim

Table 5.2.   Average Ratio of $\lambda_{feathers}$ to λ_{Jeans}

Galaxy	Arm1	Arm2	Lattice Structure
NGC 0628	1.4	1.2	
NGC 3627	9.5	4.7	4.1
NGC 4736	1.4	1.5	
NGC 5055	1.4	1.4	
NGC 5194	7.5	10.2	8.1

& Ostriker (2002, 2006) and Shetty & Ostriker (2006). Moreover, the increase in feather spacing with decreasing molecular gaseous surface density in conjunction with the correlation between the location of feathers with gaseous surface density peaks along spiral arms is consistent with the view that feathers form via a gravitational instability for the entire sample of galaxies.

5.5.2   Feathers in Tightly Wrapped Spirals

While in §5.5.1 we presented evidence that feathers are formed via a gravitational instability, it is important to test the observable model parameters of other formation mechanisms for feathers. In the WK04 hydrodynamical models, the formation of feathers depends on the pitch angle of the spiral arms. WK04 find that spiral shocks tend to be more unstable to a 'wiggle' instability if their pitch angles are larger ($i \gtrsim 10$-$15°$) and for a higher Mach number ($M \gtrsim 3$). More importantly, WK04 find that the 'wiggle' instability is not likely to occur in galaxies with tightly wound spiral arms and a flat rotation curve.

To test the WK04 theory, we determined the pitch angles of the spiral arms
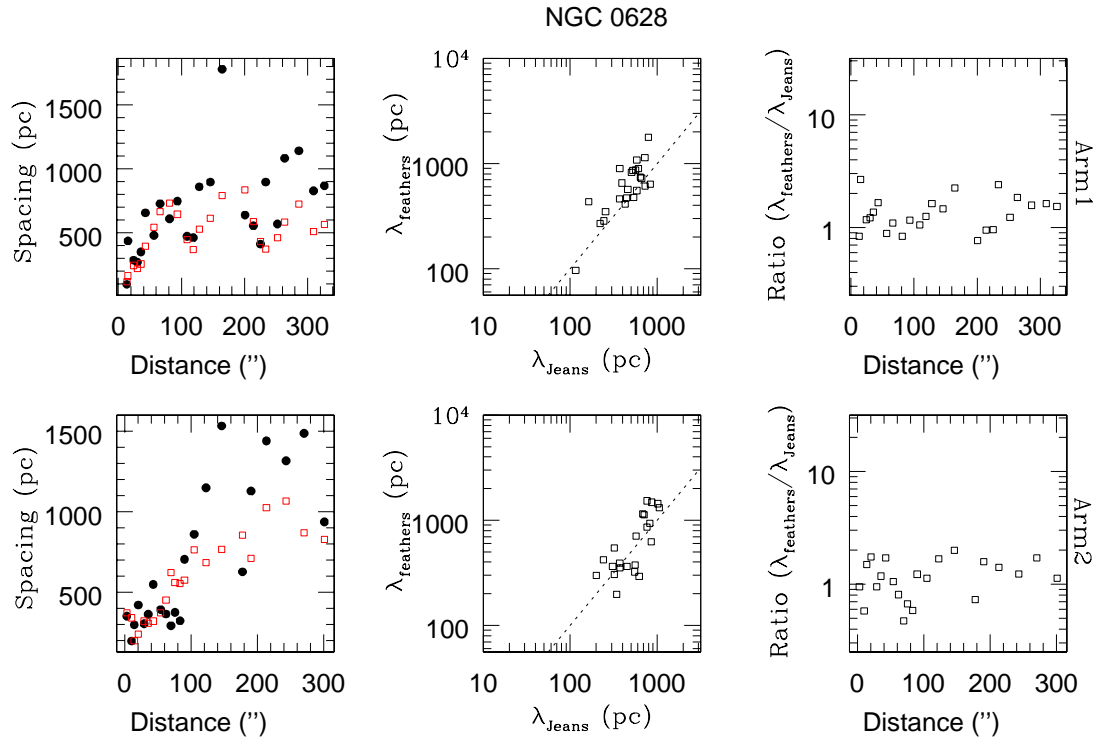
Figure 5.41 Comparison of feather separation to the local Jeans length in NGC 0628. *Left column:* Deprojected feather spacing (solid circles) and Jeans length (open squares) as a function of distance along an arm. *Middle column:* Deprojected feather separation versus local Jeans length. The dashed line shows the relationship $\lambda_{feather} = \lambda_{Jeans}$. *Right column:* Ratio of deprojected feather spacing to the local Jeans length.
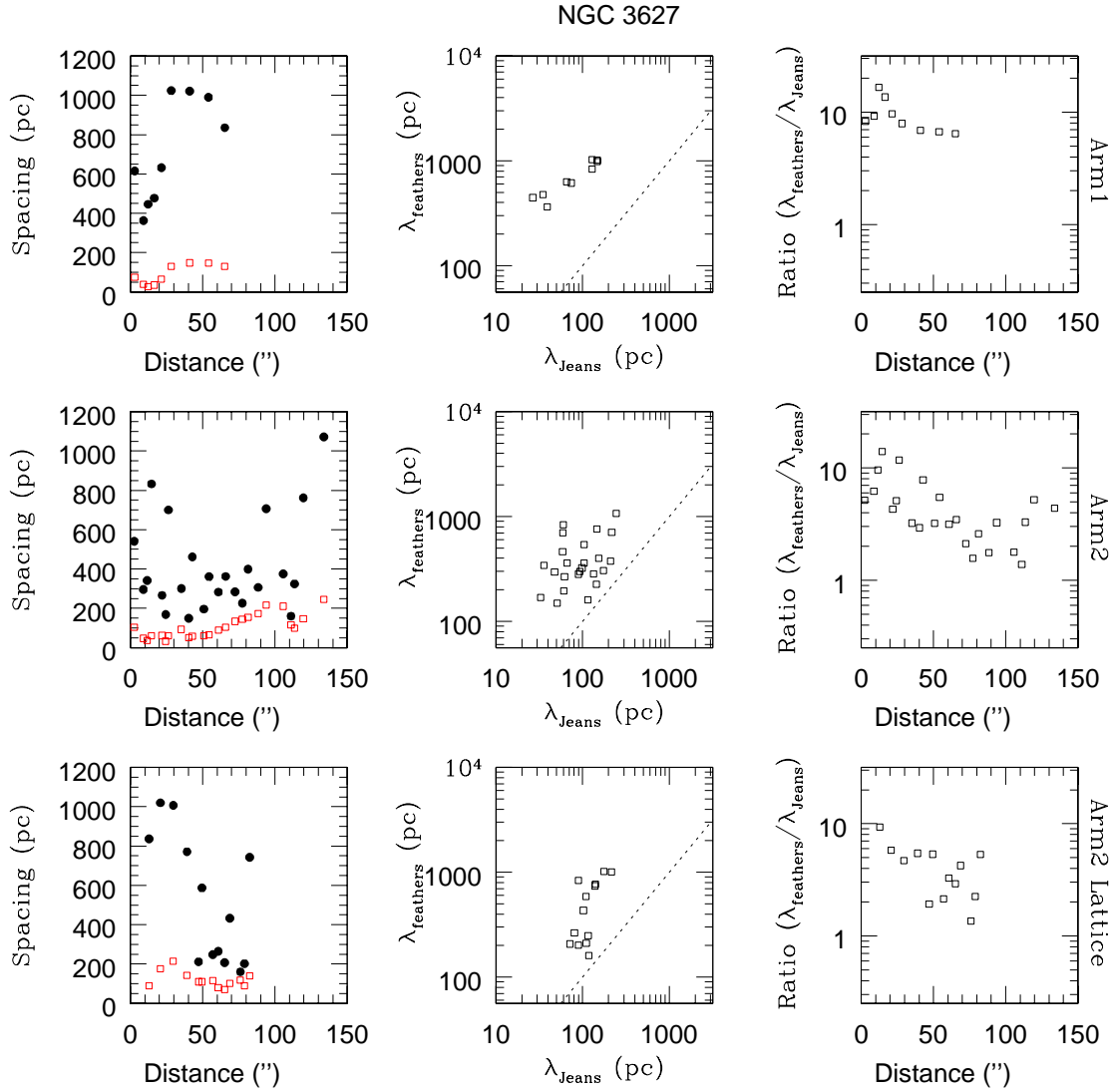
Figure 5.42 Comparison of feather separation to the local Jeans length in NGC 3627. See Fig. 5.41 for details.

for galaxy in the sample. NGC 4736 is of particular interest since it is an early-type galaxy and is classified as having tightly wound spiral arms. If the pitch angle of the spiral arms is found to be $i \lesssim$ 10-15° for NGC 4736 or any of the galaxies in the sample, this would indicate that the feathers found along the arms are most likely not produced by the WK04 wiggle instability.
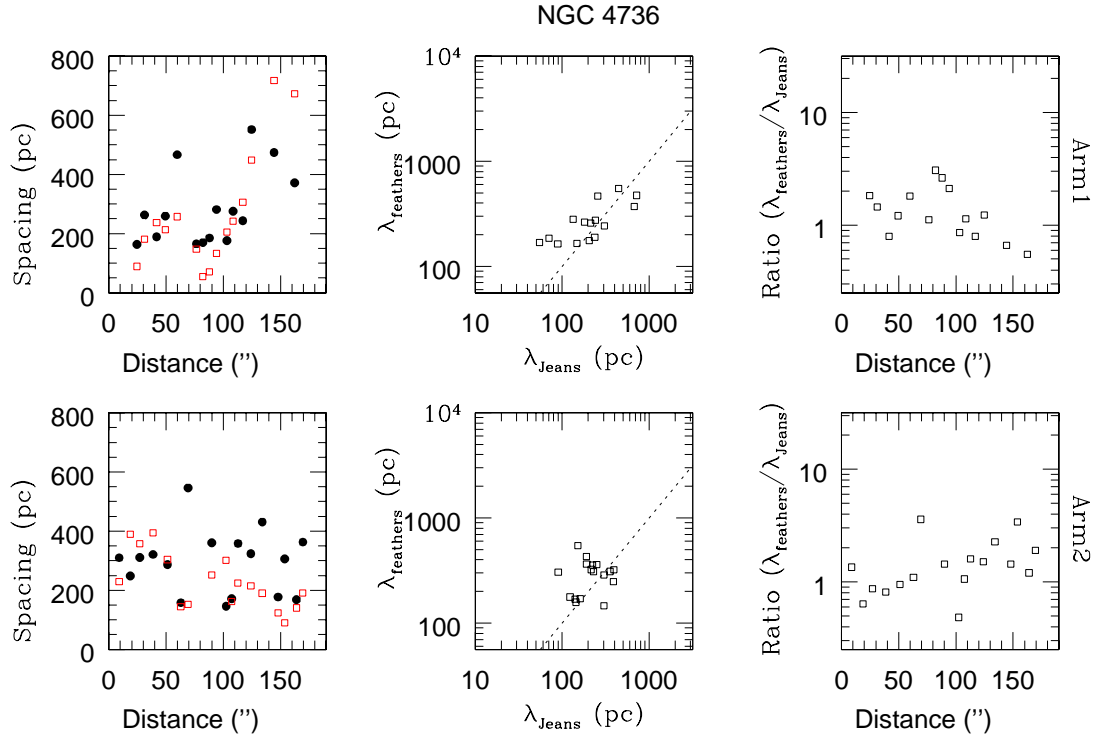
Figure 5.43 Comparison of feather separation to the local Jeans length in NGC 4736. See Fig. 5.41 for details.

To measure the pitch angle of the arms, we first deprojected the velocity-integrated CO(1-0) CARMA maps (see Fig. 5.46-5.48) as well as the Spitzer 8 μm images. The resultant deprojected images of the face-on galaxies in the sample, such as NGC 0628, appear almost unaltered when compared to their projected view. However, galaxies with higher inclinations, such as NGC 5055, appear very different;
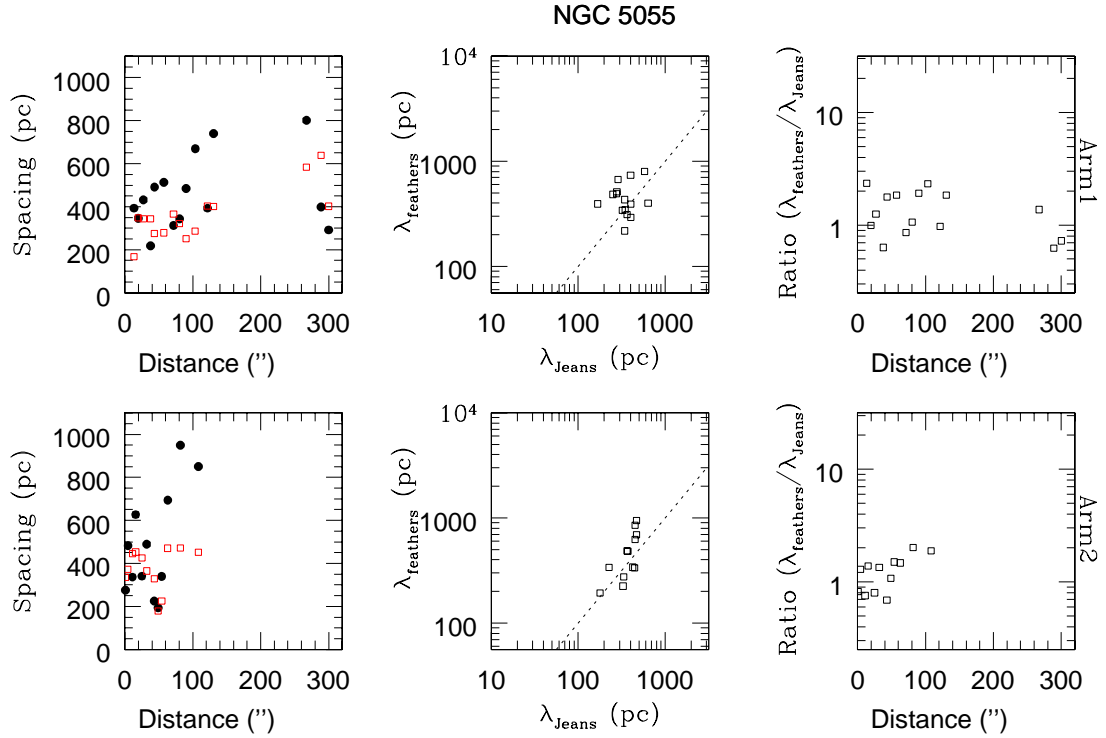
Figure 5.44 Comparison of feather separation to the local Jeans length in NGC 5055. See Fig. 5.41 for details.

after deprojection NGC 5055 appears more like a grand design spiral galaxy, similar to NGC 0628, than a flocculent galaxy.

Next the deprojected images were regridded to form polar coordinate images with the y-axis being log(R) and the x-axis the azimuthal coordinate, Θ. In log(R)-Θ space, logarithmic spiral arms appear straight and the slope s of the arms is related

189
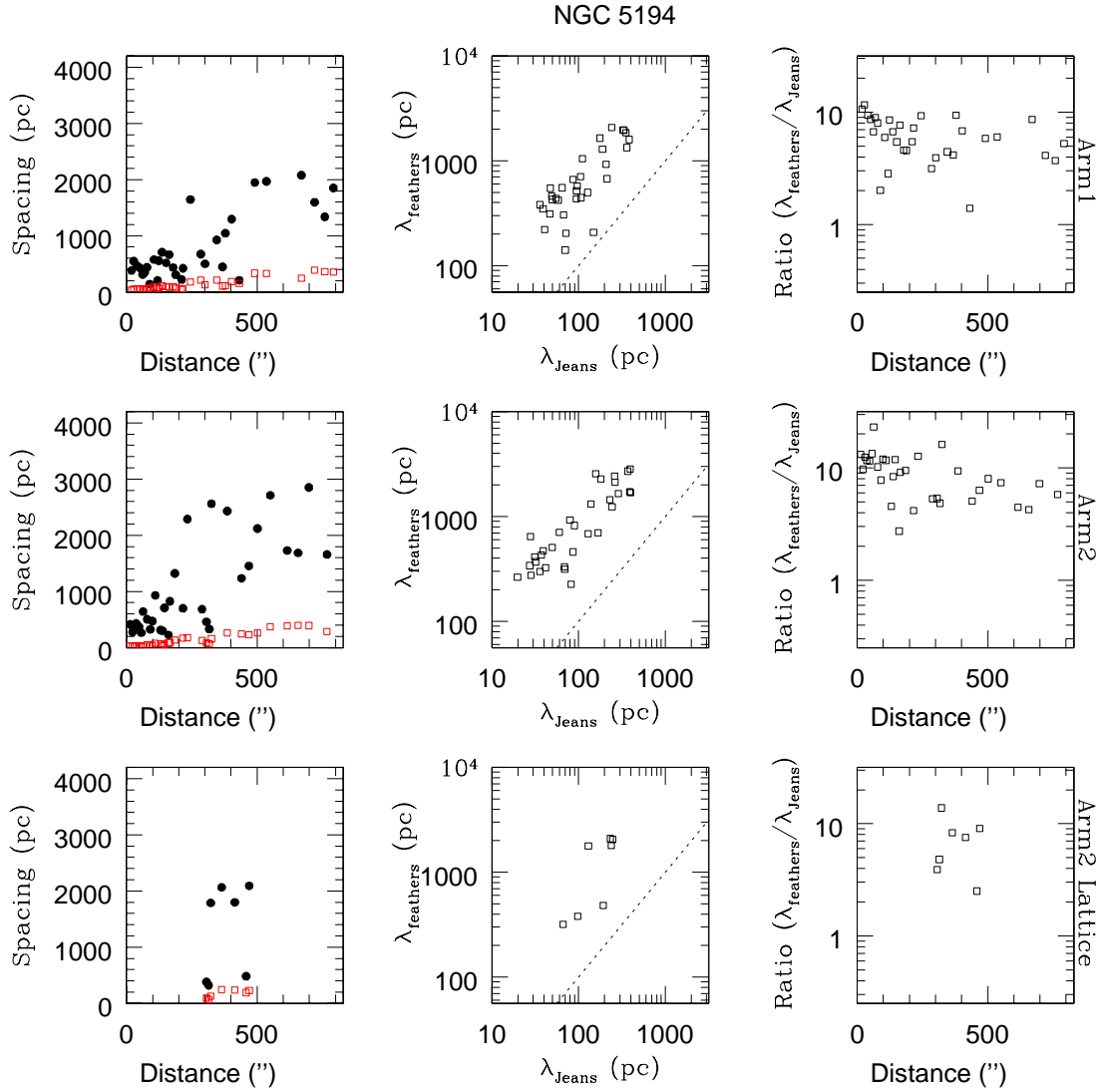
Figure 5.45 Comparison of feather separation to the local Jeans length in NGC 5194. See Fig. 5.41 for details.

to the pitch angle by $i = \arctan(s)$. We then fit the slope of the spiral arms using both the CO(1-0) and 8 μm observations (see Fig. 5.49-5.53). For the majority of the sample, we fit the most regular spiral arm in the galaxy and then plotted the fit exactly 180° distance in azimuth. After determining the best fits, we calculated the corresponding pitch angles from the slopes (see Table 5.3).
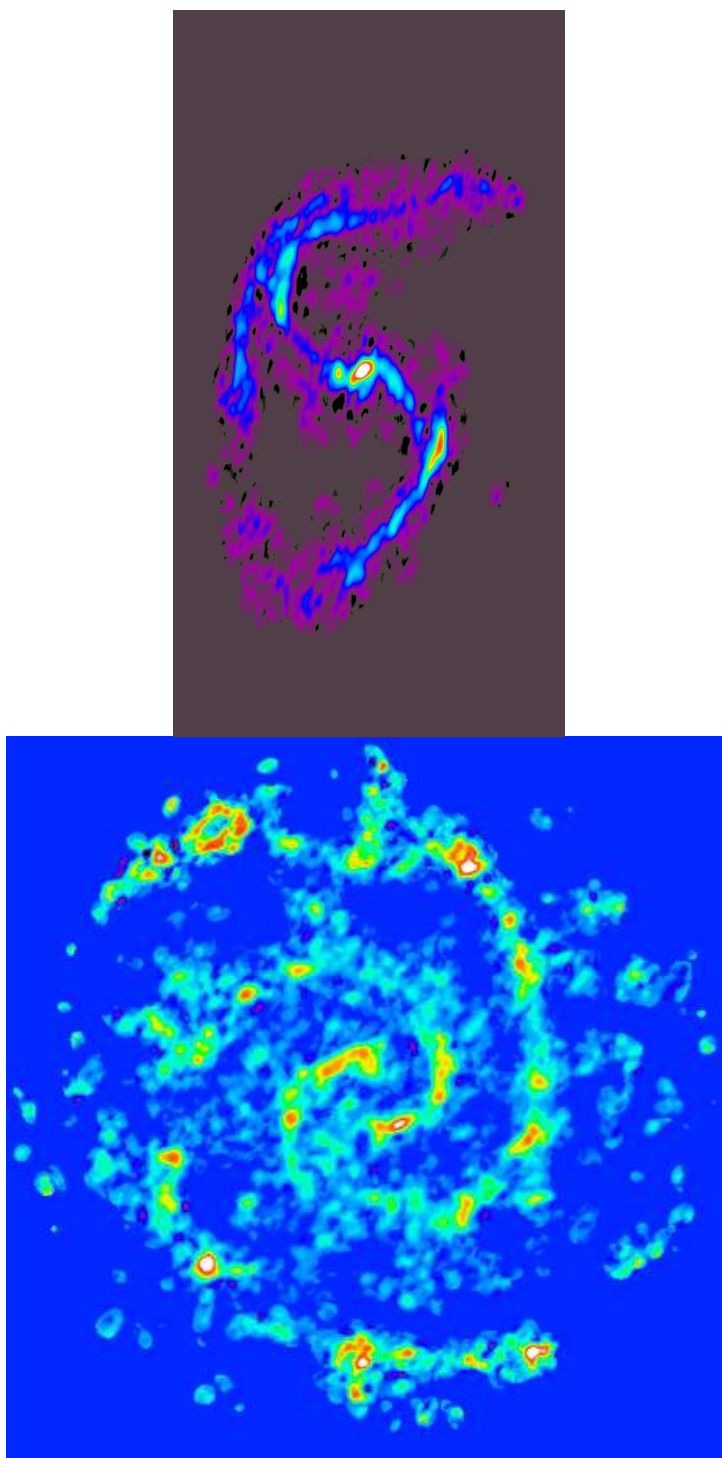
Figure 5.46 Deprojected velocity-integrated CO(1-0) CARMA maps. *Top:* NGC 3627, *Bottom:* NGC 0628.
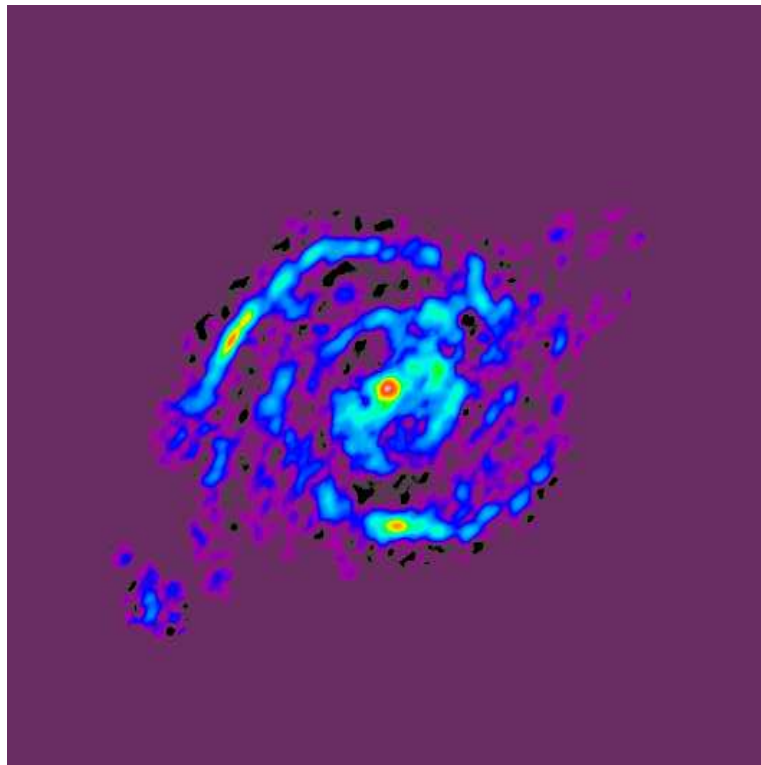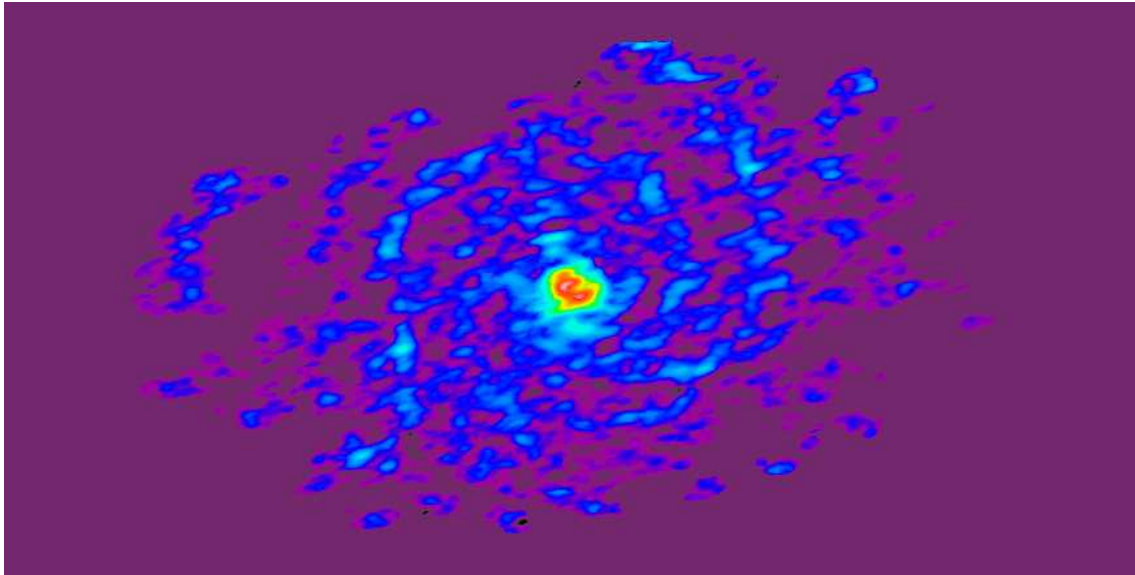
Figure 5.47 Deprojected velocity-integrated CO(1-0) CARMA maps. *Top:* NGC 5055, *Bottom:* NGC 4736.
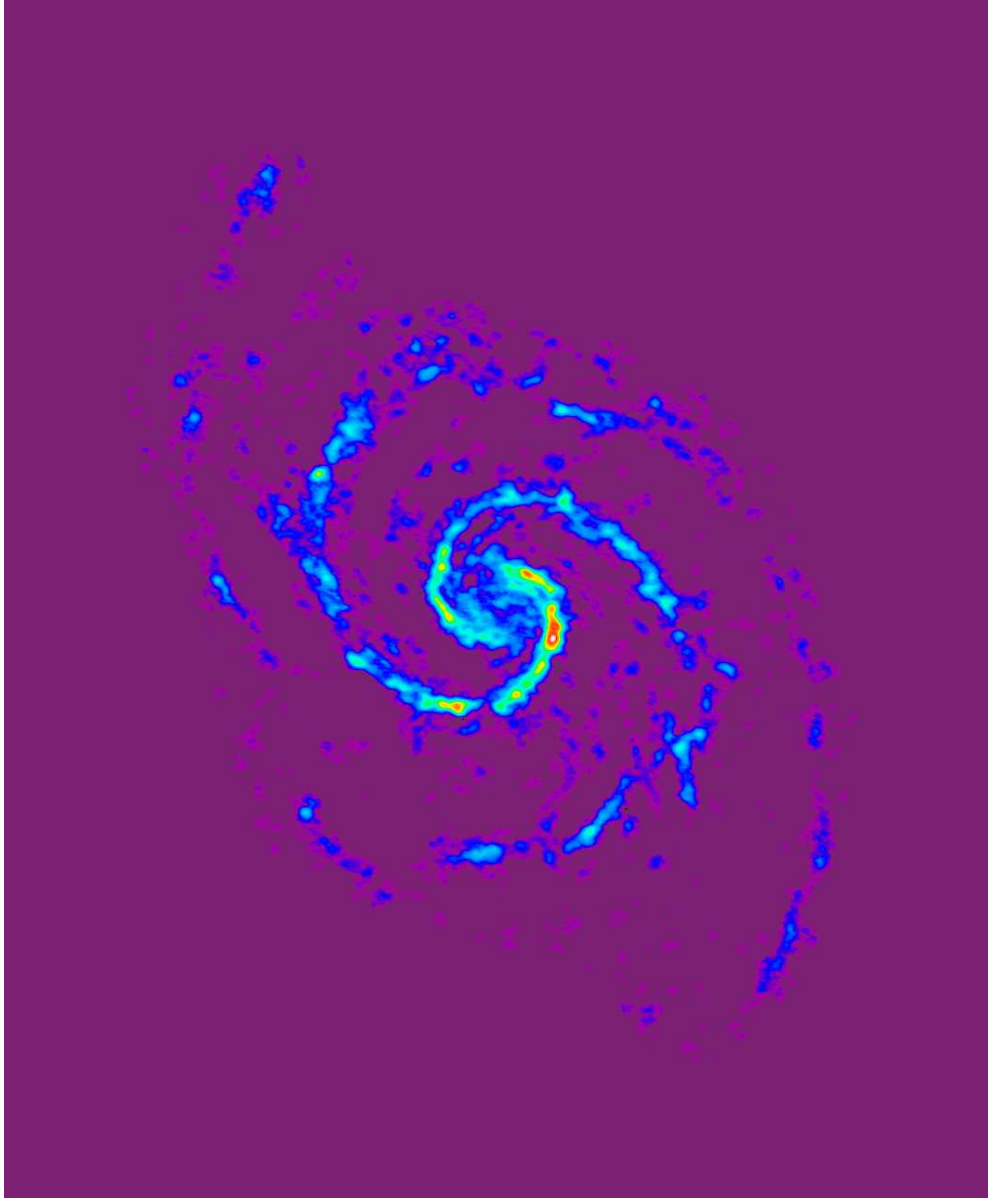
Figure 5.48 Deprojected velocity-integrated CO(1-0) CARMA map for NGC 5194.

Table 5.3. Spiral Arm Pitch Angles

Galaxy	Pitch Angle
NGC 0628	24.1
NGC 3627	34.3
NGC 4736	13.7
NGC 5055	13.1, 5.8
NGC 5194	19.7

For both NGC 4736 and NGC 5055 the pitch angle of the spiral arms is $\sim 13°$; this angle is less than the minimum angle specified by WK04 as required for a 'wiggle' instability to be present. Furthermore, Kim & Ostriker (2006) have shown in their "thick disk" simulations that the Kelvin-Helmholtz instability, which forms the feathers in the 2D WK04 simulations, is stabilized in three-dimensional disks. Therefore, the observed feathers in NGC 4736 and NGC 5055 are not adequately explained by the WK04 model for the formation of feathers.

5.6 Conclusions

We find that the spacing of feathers is related to the molecular surface density along the spiral arms in a range of galaxy types. Previously in §2.3.7 we showed that typically the distance between feathers increases as the molecular surface density decreases and the majority of feathers originated in regions of higher gas surface density in two grand design spiral galaxies. Now, we have shown that these trends can be generalized to include molecular-dominated flocculent, ringed, and strongly barred galaxies that range from early to late type. We further showed a linear
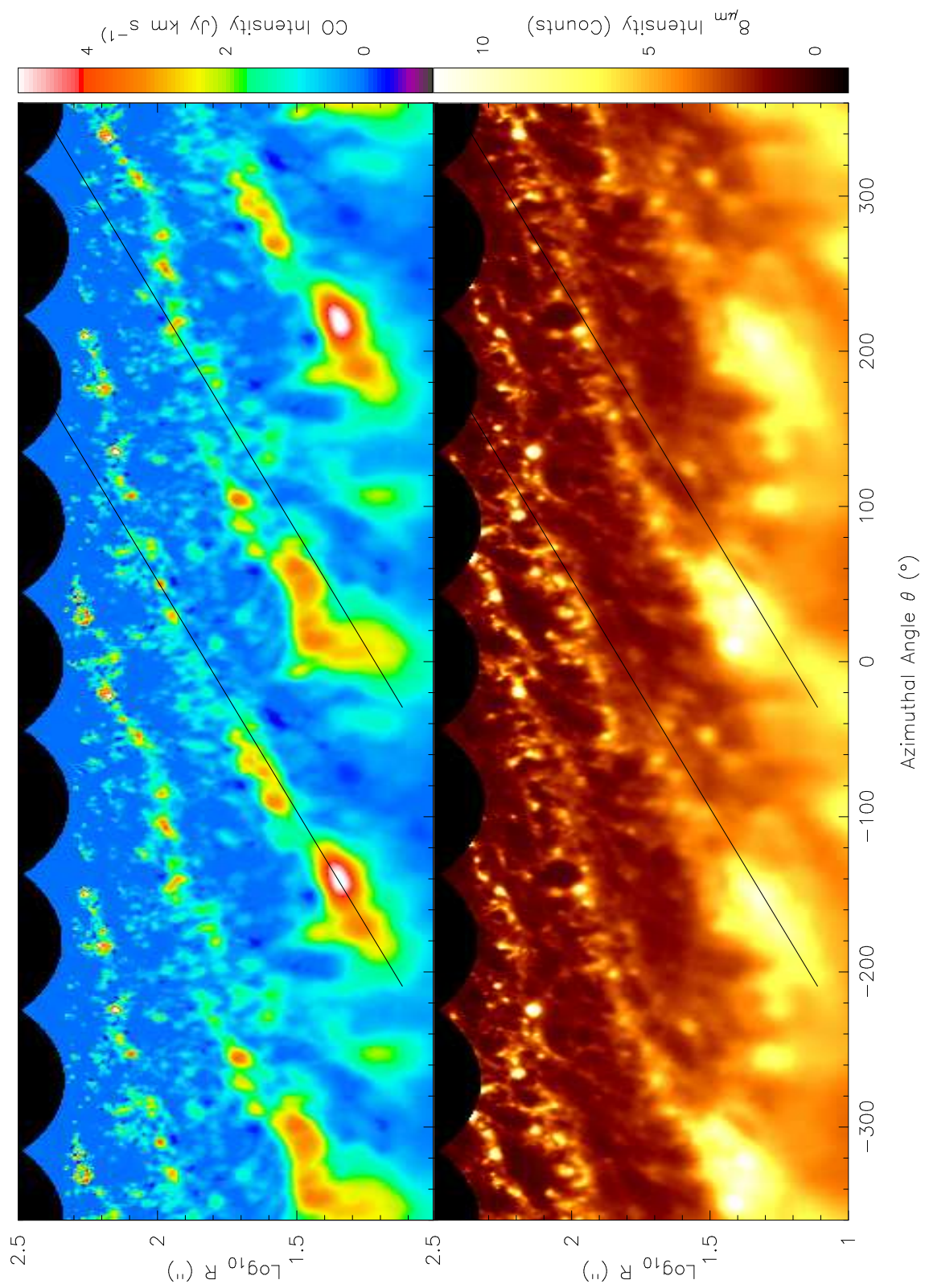
Figure 5.49 Polar coordinate image of NGC 0628. The y-axis is log(R) and the x-axis is Θ. The black lines indicate the linear fit to the spiral arms.
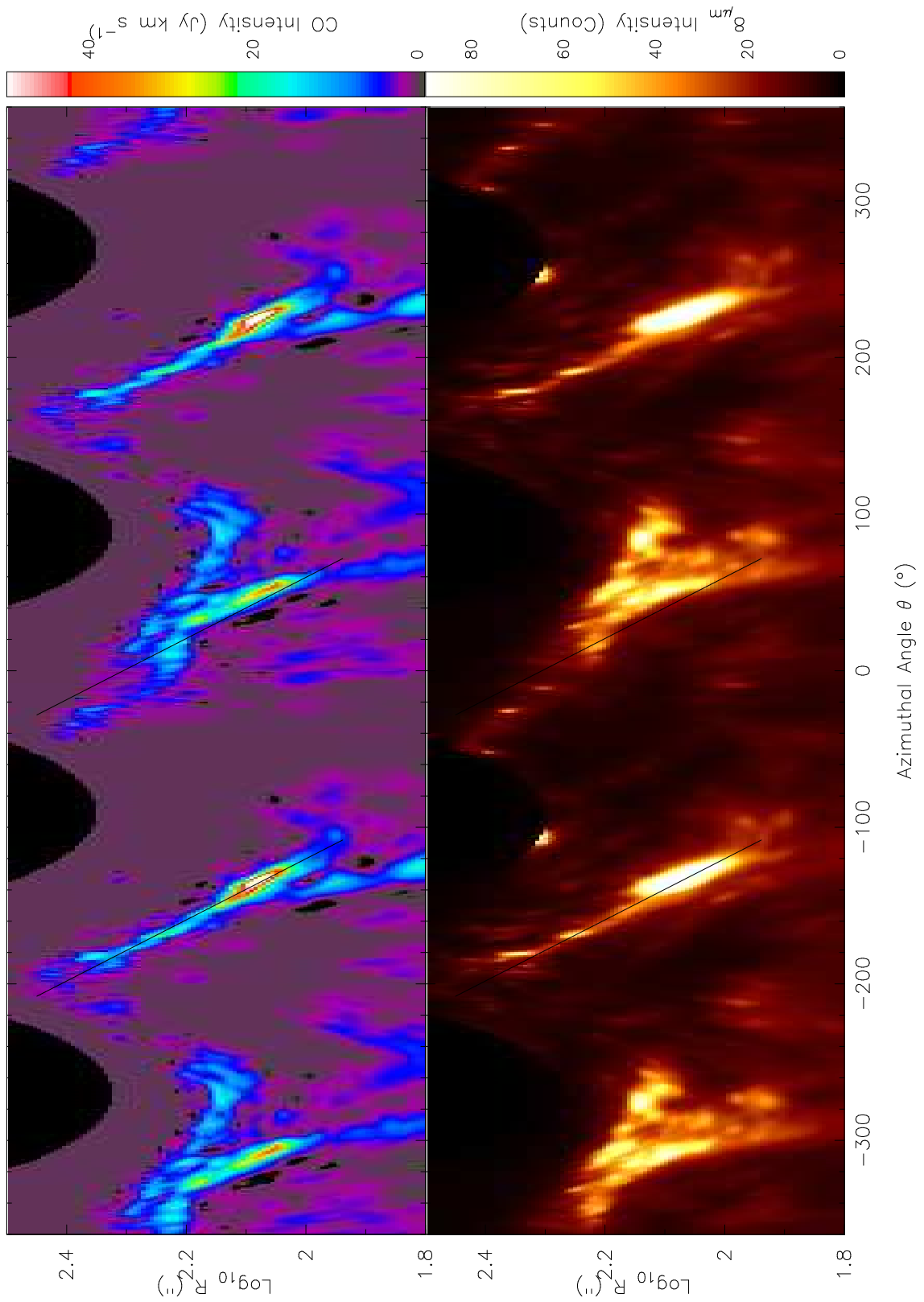
Figure 5.50 Polar coordinate image of NGC 3627. See Fig. 5.49 for details.
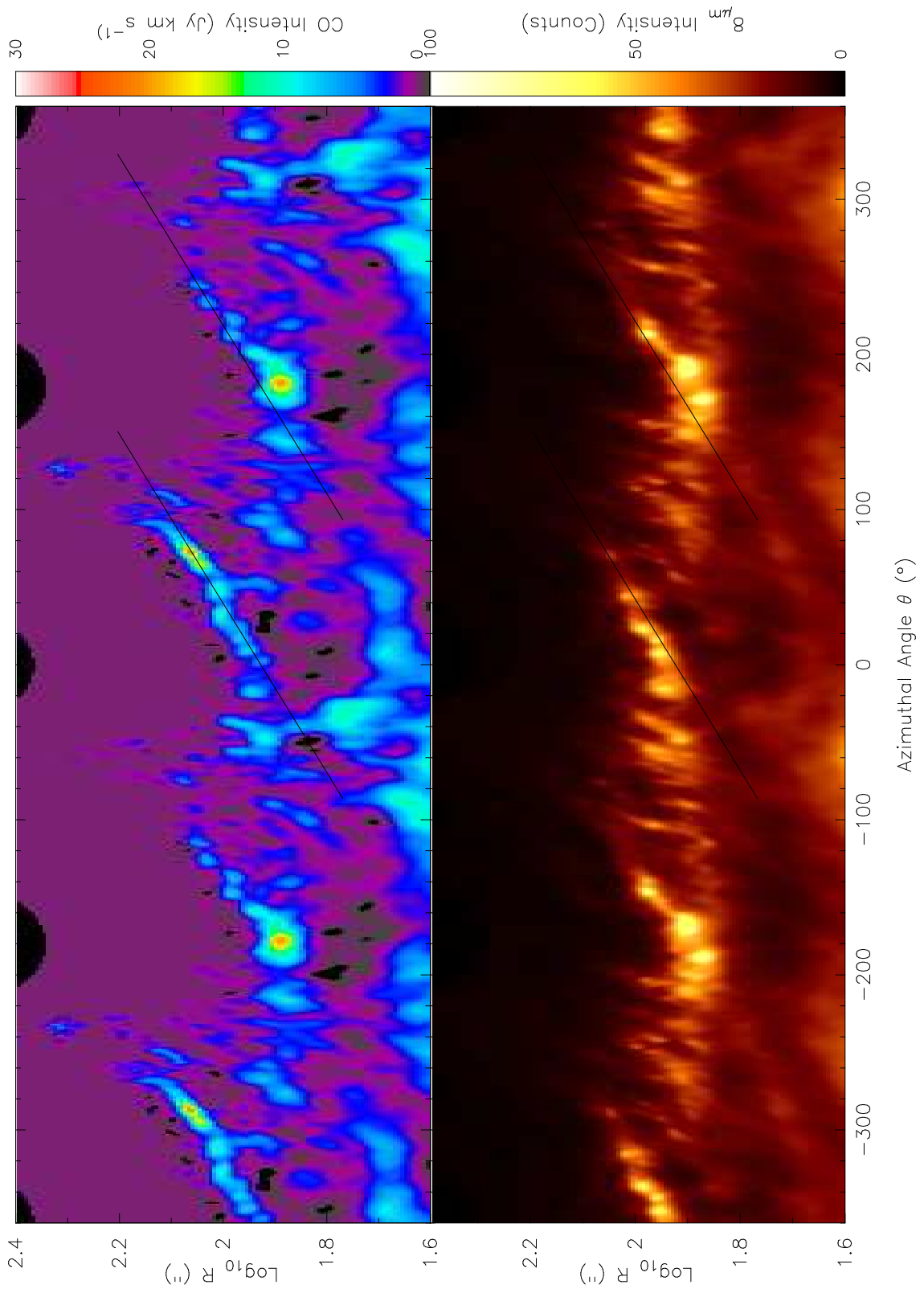
Figure 5.51 Polar coordinate image of NGC 4736. See Fig. 5.49 for details.
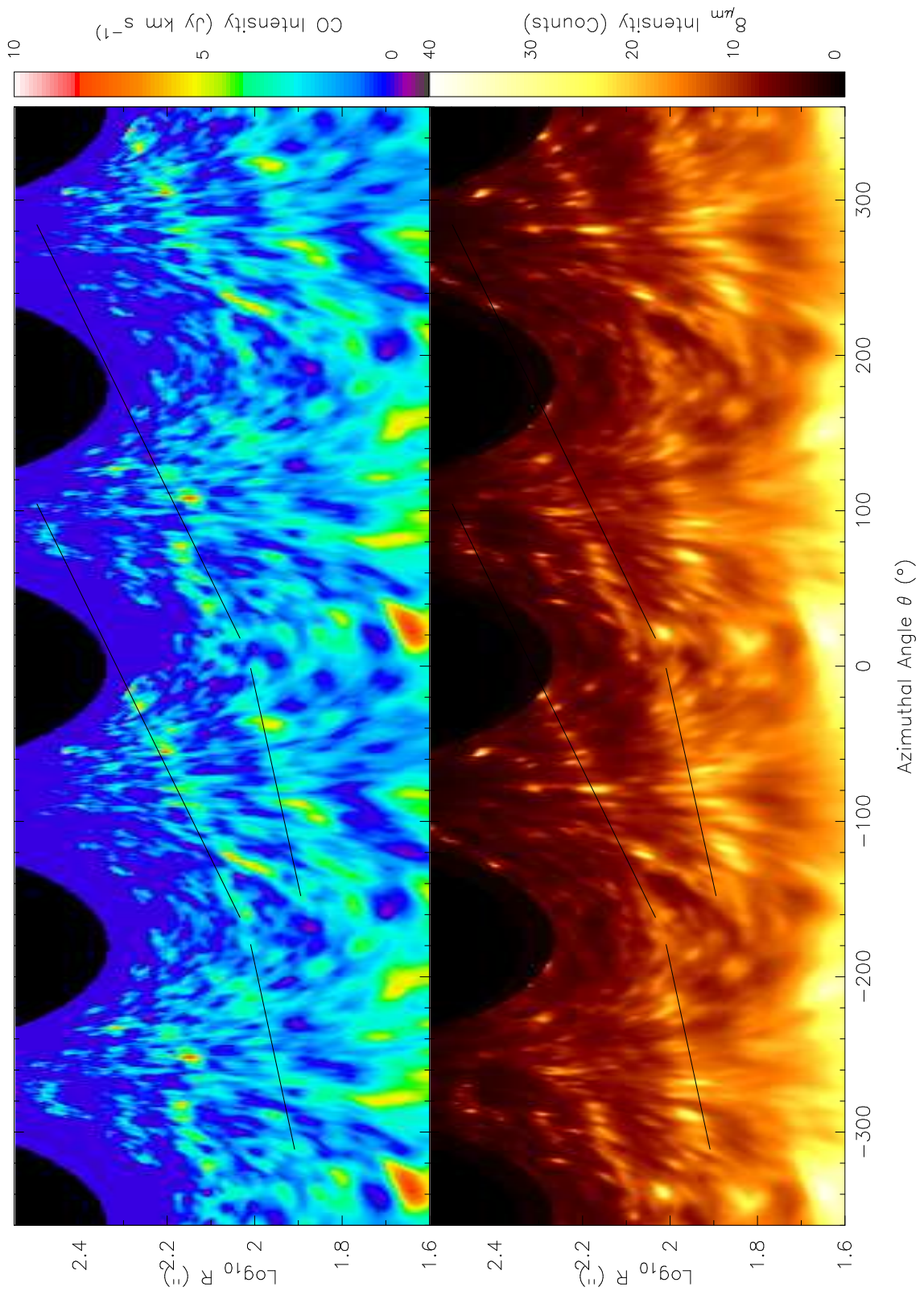
Figure 5.52 Polar coordinate image of NGC 5055. The inner ring is also fit in addition to the spiral arms. See Fig. 5.49 for details.
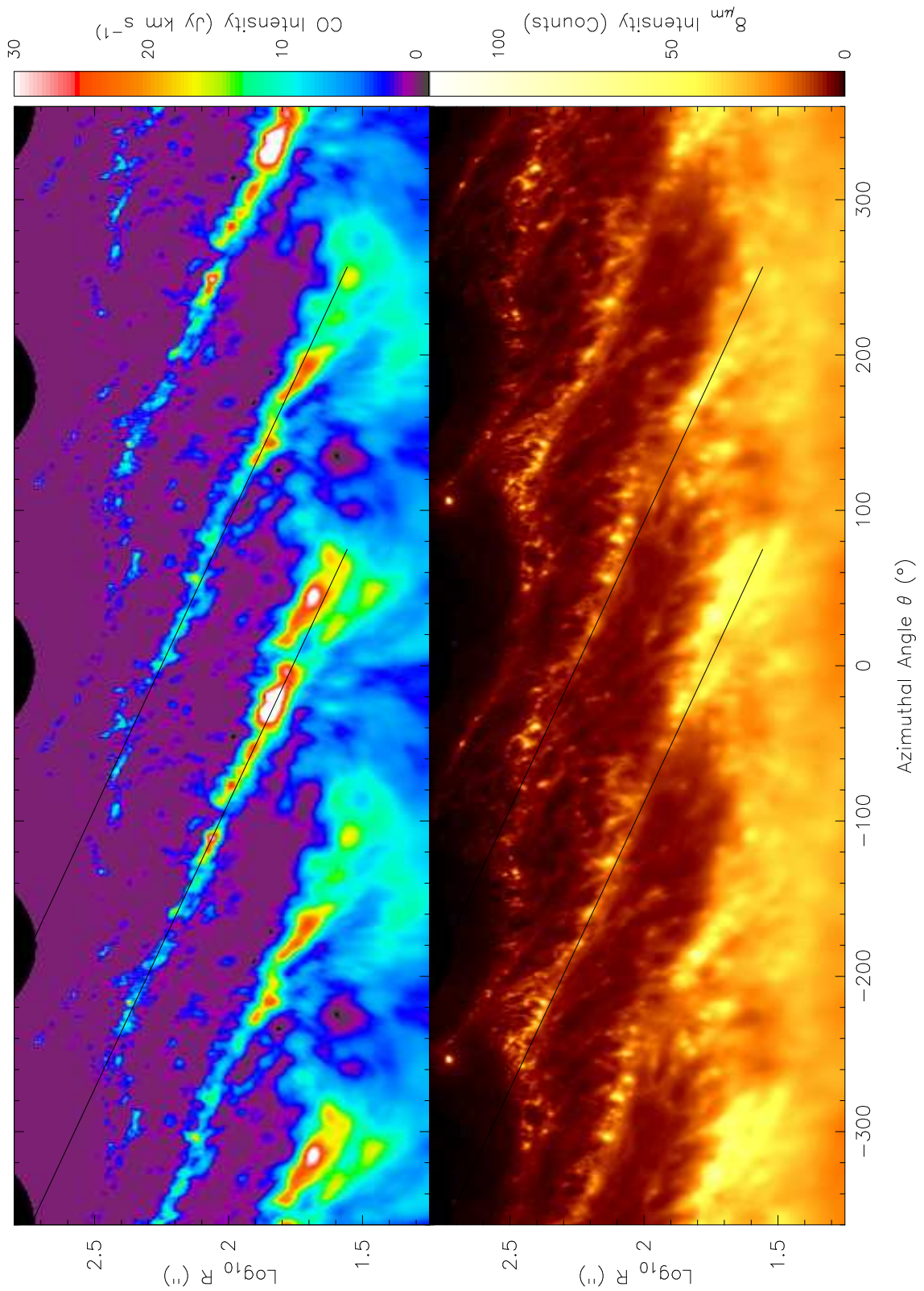
Figure 5.53 Polar coordinate image of NGC 5194. See Fig. 5.49 for details.

correlation between feather spacing and Jeans length for all of the galaxies in the sample, with the mean separation of feathers ranging from 1.4-10.2λ_{Jeans}. These observable characteristics are consistent with models in which feathers are produced via local gravitational instabilities in the gas.

Chapter 6

Summary and Future Work

6.1 Summary

The dynamics of spiral galaxies yield a plethora of structure at various scales within the disks of galaxies. On large scales, spiral density waves impede the rotation of material in the disk, such as the stars, gas, and dust, building spiral arms. As the slowed material compresses, it condenses, forming a ridge of extinction that marks the inner edge of spiral arms, and subsequently forms new stars. On smaller scales, spiral arms do not appear smooth and continuous but rather they are composed of smaller substructure. Within a spiral arm, extinction material originating in the dust lane is "brushed-out" from the inner edge to the faint outer edge. These thin lanes of extinction crossing the arm are termed feathers. Associated with the new star formation in spiral arms are bright chains of OB associations and HII regions that appear like "beads on a string" and are termed spurs. In this thesis, we present the results of our investigation into the frequency and characteristics of such spiral arm substructure in a sample of 233 spiral galaxies. We also discuss newly acquired high-resolution ($\sim 4''$) CARMA CO(1-0) velocity-integrated maps of five target spiral galaxies used to compare the distribution of star formation tracers along spiral arms, and test formation theories for spiral arm substructure.

Using broadband archival HST WFPC2 observations, we surveyed a sample of 233 bright, nearby, low-inclination spiral galaxies ranging from early to late type (Sa–Sd) for spiral arm substructure. We considered a galaxy to have well-defined, extinction substructure if it exhibited multiple dust lanes with approximately regular spacing that emerged from a PDL at roughly similar large angles. Using this criteria, we identified extinction feathers in 45 of the 223 spiral galaxies, or nearly 20% of the sample. The galaxies identified with feathers ranged in type from Sa to Sc, and most commonly occurred in Sb–Sc galaxies. We further found that the presence of feathers was closely tied to the existence of a primary dust lane (PDL) and that the probability of detecting feathers increased with the delineation of the PDL. We determined that the highest detection rate of feathers was 83% for spirals with well-delineated PDLs. We thus concluded that feathers are ubiquitous in spiral galaxies with well defined PDLs.

In Chapter 4, we presented the new high resolution, $\sim 4''$, CARMA CO(1-0) velocity-integrated maps of five target spiral galaxies that range in type (Sab–Sc) and spiral arm morphology. We compared the distribution of the CO(1-0) emission to the distribution of atomic gas using the THINGS H I dataset. We found that the sample of galaxies is H I deficient in the inner $3'$ of the galaxies. Furthermore, using the CO(1-0) to estimate the molecular surface density along the arms and the THINGS H I to estimate the atomic surface density, we found the spiral arms are molecule-dominated in regions where we detect strong CO(1-0). Along the arms, $\Sigma_{\text{H I}}$ was at most $\sim 20\%$ of the total gaseous surface density within surface density peaks along the arms. We found contrary to previous observations that the H I is not

offset azimuthally along the spiral arms from the CO(1-0). While we did not find a 1:1 correlation between CO(1-0) and HI peaks, the HI peaks do lie along the location of the spiral arms as traced by CO(1-0) and 8 μm emission. We also performed a multi-wavelength comparison of star formation tracers (Hα, 8 μm, CO(1-0), HI) along the spiral arms at the resolution of the THINGS HI observations. We found that the CO(1-0) and 8 μm are well aligned, tracing the PDLs of the spiral arms. The Hα emission however, was offset from both the CO(1-0) and 8 μm emission, further downstream in the spiral arms.

We furthered our analysis of feathers and tested the theories for feather formation in Chapter 5. Utilizing the target sample from Chapter 4, we determined if feathers were more than merely extinction features by measuring the mass of "clumps" in the CARMA CO(1-0) observations using Clumpfind. We found that feathers are associated with a significant amount of star forming gas within spiral galaxies. Within the sample, the feathers were found to emerge from either GMAs or massive GMCs along the spiral arms. Furthermore, within the interarm region we found those interarm GMCs identified by Clumpfind were also associated with feathers as well. We found that the spacing of feathers is related to the molecular surface density along the spiral arms for all galaxy types in the sample. We showed that the distance between feathers increased as the molecular surface density decreased, which yielded a linear correlation between feather spacing and Jeans length for all of the galaxies in the sample. We found the mean separation of feathers ranged from 1.4-10.2λ_{Jeans}, which is consistent with models in which feathers are produced via local gravitational instabilities in the gas.

6.2 Future Work

An outstanding issue pertaining to the understanding of feather formation is a detailed, multi-wavelength comparison of feathers. It is important to characterize the properties of feathers at all wavelengths to (1) further test formation theories for spiral arm substructure and (2) determine the amount of star formation and characteristic SFR associated with feathers. We plan to investigate the location of feathers identified by CO(1-0) peaks along the spiral arms and extended 8 μm emission in the interarm region relative to other high resolution images from Spitzer SINGS (Kennicutt et al. 2003) and GALEX NGS (Bianchi et al. 2003). We will convolve all images to the lowest resolution map and measure the spacing between feathers at each new wavelength. We will determine if there are any systematic offsets and compare our findings with predictions from different formation theories.

We also plan to extend this multi-wavelength comparison to along feathers. Even at first glance, it is obvious that CO(1-0) emission does not extend out radially from spiral arms into the interarm region as far as 8 μm. However, it is important to fully characterize this radial "fall-off" from the arm not only for CO(1-0) and 8 μm, but for all star formation tracers. We plan to use the the CARMA CO(1-0) maps, in addition to the high resolution Spitzer SINGS (Kennicutt et al. 2003) and GALEX NGS (Bianchi et al. 2003) to characterize this "fall-off" along feathers. We will convolve the images to the Spitzer 24 μm PSF ($\sim 6''$) and measure the intensities of each wavelength along the feather. Additionally, we plan to determine the SFR associated with the feathers using the GALEX NGS FUV images and the

Spitzer Ancillary Hα+ 24 μm images to correct for extinction (Calzetti et al. 2007,

Kennicutt et al. 2007).

Appendix A

Method for Deprojection

To deproject the spacings between feathers in §5.5.1, we followed the Elmegreen &
Elmegreen (1983) method. First we calculate the galactocentric distance to each
feather, F_i, in a galaxy.

$$F_i = \sqrt{((RA_C - RA_{F_i})\cos(DEC_{F_i}))^2 + (DEC_C - DEC_{F_i})^2} \qquad \text{(A.1)}$$

where RA_C and DEC_C are the galactic center. Next, using the galactocentric
distances of consecutive feathers, F_i, F_{i+1}, and L_o, the measured distance between
the feathers, we calculate α

$$\alpha = \cos^{-1}\left(\frac{F_i^2 + L_o^2 - F_{i+1}^2}{2F_iL_o}\right). \qquad \text{(A.2)}$$

Then, the deprojected length L is

$$L = L_o \left(1 + \frac{\tan^2(\alpha - \theta)}{\cos^2 i}\right)^{1/2} (1 + \tan^2(\alpha - \theta))^{-1/2} \qquad \text{(A.3)}$$

where θ is measured counterclockwise from the major axis of the galaxy to each
feather.

Bibliography

Afanasiev, V. L., & Sil'chenko, O. K. 2005, A&A, 429, 825

Allen, R. J., Atherton, P. D., & Tilanus, R. P. J. 1985, The Milky Way Galaxy, 106, 275

Balbus, S. A. 1988, ApJ, 324, 60 (B88)

Ballesteros-Paredes, J., & Hartmann, L. 2007, Revista Mexicana de Astronomia y Astrofisica, 43, 123

Battaglia, G., Fraternali, F., Oosterloo, T., & Sancisi, R. 2006, A&A, 447, 49

Beckwith, S., NASA, ESA, and The Hubble Heritage Team (STScI/AURA) 2005, Hubble Heritage image of M51 (Baltimore, STScI), http://heritage.stsci.edu/2005/12a/index.html

Bianchi, L., Madore, B., Thilker, D., Gil de Paz, A., & GALEX Science Team 2003, Bulletin of the American Astronomical Society, 35, 1354

Bigiel, F., Leroy, A., Walter, F., Brinks, E., de Blok, W. J. G., Madore, B., & Thornley, M. D. 2008, AJ, 136, 2846

Binney, J. & Tremaine, S. 1987, Galaxy Dynamics, Princeton, NJ, Princeton University Press, 1987, 747

Bock, D. C.-J. 2006, Revealing the Molecular Universe: One Antenna is Never Enough, 356, 17

Briggs, F. H. 1982, ApJ, 259, 544

Briggs, D. S. 1995, Bulletin of the American Astronomical Society, 27, 1444

Brinks, E. 1994, Tracing violent star formation: HI observations of nearby galaxies., ed. Tenorio-Tagle, G. (Violent Star Formation), from 30 Doradus to QSOs, 145-155

Calzetti, D., et al. 2005, ApJ, 633, 871

Calzetti, D., et al. 2007, ApJ, 666, 870

Chakrabarti, S., Laughlin, G., & Shu, F. H. 2003, ApJ, 596, 220 (CLS)

Chemin, L., Cayatte, V., Balkowski, C., Marcelin, M., Amram, P., van Driel, W., & Flores, H. 2003, A&A, 405, 89

Chen, P. C., et al. 1992, ApJ, 395, L41

Cornett, R. H., et al. 1994, ApJ, 426, 553

de Blok, W. J. G., Walter, F., Brinks, E., Trachternach, C., Oh, S.-H., & Kennicutt, R. C. 2008, AJ, 136, 2648

de Vaucouleurs, G. 1959, Handbuch der Physik, 53, 275

de Vaucouleurs, G. 1975, Nearby Groups of Galaxies, ed. Sandage, A., Sandage, M., & Kristian, J. (the University of Chicago Press), 557

de Vaucouleurs, G., de Vaucouleurs, A., Corwin, H. G., Buta, R. J., Paturel, G., & Fouque, P. 1995, VizieR Online Data Catalog, 7155, 0

Dobbs, C. L., & Bonnell, I. A. 2006, MNRAS, 367, 873

Elmegreen, D. M. 1980a, ApJS, 43, 37

Elmegreen, D. M. 1980b, ApJ, 242, 528

Elmegreen, B. G., & Elmegreen, D. M. 1983, MNRAS, 203, 31

Elmegreen, D. M. & Elmegreen, B. G. 1987, ApJ, 314, 3

Elmegreen, D. M., Elmegreen, B. G., Frogel, J. A., Eskridge, P. B., Pogge, R. W., Gallagher, A., & Iams, J. 2002, AJ, 124, 777

Elmegreen, B. G., Elmegreen, D. M., Chandar, R., Whitmore, B., & Regan, M. 2006, ApJ, 644, 879

Ferrière, K. M. 2001, Reviews of Modern Physics, 73, 1031

Giovanelli, R., & Haynes, M. P. 1988, Galactic and Extragalactic Radio Astronomy, 522

Haynes, M. P., Giovanelli, R., & Chincarini, G. L. 1984, ARA&A, 22, 445

Helfer, T. T., Vogel, S. N., Lugten, J. B., & Teuben, P. J. 2002, PASP, 114, 350

Helfer, T. T., Thornley, M. D., Regan, M. W., Wong, T., Sheth, K., Vogel, S. N., Blitz, L., & Bock, D. C.-J. 2003, ApJS, 145, 259

Helou, G. 1999, in ESA Special Publication, Vol. 427, The Universe as Seen by ISO, ed. P.Cox & M. Kessler, 797

Hubble, E. P. 1926, ApJ, 64, 321

Irwin, J. A. 1995, PASP, 107, 715

Jałocha, J., Bratek, Ł., & Kutschera, M. 2008, ApJ, 679, 373

Jarrett, T. H., Chester, T., Cutri, R., Schneider, S. E., & Huchra, J. P. 2003, AJ, 125, 525

Kennicutt, R. C., Jr., & Kent, S. M. 1983, AJ, 88, 1094

Kennicutt, R. C., Jr. 1989, ApJ, 344, 685

Kennicutt, R. C., Jr. 1998a, ARA&A, 36, 189

Kennicutt, R. C., Jr. 1998b, ApJ, 498, 541

Kennicutt, R. C., et al. 2003, PASP, 115, 928

Kennicutt, R. C., Jr. 2004, First Peek at Spitzer's Legacy: Mysterious Whirlpool Galaxy, Spitzer Space Telescope Newsroom, http://www.spitzer.caltech.edu/Media/releases/ssc2004-19/index.shtml

Kennicutt, R. C., et al. 2005, Delivery of Data from the Spitzer Legacy Project: IRAC, IRS, & MIPS (Pasadena, SSC), http://ssc.spitzer.caltech.edu/legacy/original.html

Kennicutt, R. C., Jr., et al. 2007, ApJ, 671, 333

Kim, W. & Ostriker, E. C. 2002, ApJ, 570, 132 (KO)

Kim, W.-T., & Ostriker, E. C. 2006, ApJ, 646, 213

Koda, J., et al. 2009 ApJ, 700, L132

Larsen, S. S., & Richtler, T. 1999, A&A, 345, 59

La Vigne, M. A., Vogel, S. N., & Ostriker, E. C. 2006, ApJ, 650, 818

Lin, C. C. & Shu, F. H. 1964, ApJ, 140, 646

Lindblad, B. 1964, Astrophysica Norvegica, 9, 103

Lo, K. Y., Ball, R., Masson, C. R., Phillips, T. G., Scott, S., & Woody, D. P. 1987, ApJ, 317, L63

Lynds, B. T. 1970, in IAU Symp. 38, The Spiral Structure of Our Galaxy, ed. W. Becker & G. Contopouplos (Dordrecht:Reidel), 26

Marcum, P. M., et al. 2001, ApJS, 132, 129

Martin, D. C., et al. 2005, ApJ, 619, L1

Moellenhoff, C., Matthias, M., & Gerhard, O. E. 1995, A&A, 301, 359

Mouschovias, T. C., Tassis, K., & Kunz, M. W. 2006, ApJ, 646, 1043

Oort, J. H. 1962, The Distribution and Motion of Interstellar Matter in Galaxies, 234

Pahre, M. A., Ashby, M. L. N., Fazio, G. G., & Willner, S. P. 2004, ApJS, 154, 229

Peeters, E., Spoon, H. W. W., & Tielens, A. G. G. M. 2004, ApJ, 613, 986

Piddington, J. H. 1973, ApJ, 179, 755

Prendergast, K. H., & Burbidge, G. R. 1960, ApJ, 131, 243

Rand, R. J., & Kulkarni, S. R. 1990, ApJ, 349, L43

Rand, R. J., & Tilanus, R. P. J. 1990, The Interstellar Medium in Galaxies, 161, 525

Rand, R. J., & Wallin, J. F. 2004, ApJ, 614, 142

Regan, M. W., Thornley, M. D., Helfer, T. T., Sheth, K., Wong, T., Vogel, S. N., Blitz, L., & Bock, D. C.-J. 2001, ApJ, 561, 218

Regan, M. W., Sheth, K., Teuben, P. J., & Vogel, S. N. 2002, ApJ, 574, 126

Rickard, L. J., Palmer, P., Morris, M., Zuckerman, B., & Turner, B. E. 1975, ApJ, 199, L75

Roberts, W. W. 1969, ApJ, 158, 123

Roberts, M. S., & Haynes, M. P. 1994, ARA&A, 32, 115

Rots, A. H. 1978, AJ, 83, 219

Rubin, V. C., Thonnard, N., & Ford, W. K. 1978, ApJL, 225, L107

Saha, A., Sandage, A., Tammann, G. A., Labhardt, L., Macchetto, F. D., & Panagia, N. 1999, ApJ, 522, 802

Sakamoto, K., Okumura, S. K., Ishizuki, S., & Scoville, N. Z. 1999, ApJS, 124, 403

Sandage, A. 1961, The Hubble Atlas of Galaxies, ed. Sandage, A. (Washington: Carnegie Institution, 1961)

Sault, R. J., Teuben, P. J., & Wright, M. C. H. 1995, Astronomical Data Analysis

Software and Systems IV, 77, 433

Scoville, N. Z., Polletta, M., Ewald, S., Stolovy, S. R., Thompson, R., & Rieke, M. 2001, AJ, 122, 3017

Sellgren, K. 1984, ApJ, 277, 623

Shetty, R., & Ostriker, E. C. 2006, ApJ, 647, 997

Shetty, R., Vogel, S. N., Ostriker, E. C., & Teuben, P. J. 2007, ApJ, 665, 1138

Shostak, G. S., & van der Kruit, P. C. 1984, A&A, 132, 20

Shu, F. H. 1985, The Milky Way Galaxy, 106, 561

Smith, B. J., Struck, C., Hancock, M., Appleton, P. N., Charmandaris, V., & Reach, W. T. 2007, AJ, 133, 791

Steer, D. G., Dewdney, P. E., & Ito, M. R. 1984, A&A, 137, 159

Strong, A. W., et al. 1988, A&A, 207, 1

Thornley, M. D. 1996, ApJL, 469, L45

Thornley, M. D., & Mundy, L. G. 1997, ApJ, 484, 202

Toomre, A. 1978, Structure and Properties of Nearby Galaxies, 77, 267

Tosaki, T., Shioya, Y., Kuno, N., Nakanishi, K., & Hasegawa, T. 2002, 8th Asian-Pacific Regional Meeting, Volume II, 221

Tully, R. B. 1988, Nearby Galaxies Catalog, ed. Tully, R. B. (Cambridge and New York, Cambridge University Press), 221

van der Kruit, P. C. & de Bruyn, A. G. 1976, A&A, 48, 373

van Dishoeck, E. F. 2004, ARA&A, 42, 119

Vogel, S. N., Kulkarni, S. R., & Scoville, N. Z. 1988, Nature, 334, 402

Wada, K. & Koda, J. 2004, MNRAS, 349, 270 (WK)

Walter, F., Brinks, E., de Blok, W. J. G., Bigiel, F., Kennicutt, R. C., Thornley, M. D., & Leroy, A. 2008, AJ, 136, 2563

Weaver, H. 1970, in IAU Symp. 39, Interstellar Gas Dynamics, ed. H Habing (Dordrecht: Kluwer), 22

Welch, W. J., et al. 1996, PASP, 108, 93

Williams, J. P., de Geus, E. J., & Blitz, L. 1994, ApJ, 428, 693

Wong, T., & Blitz, L. 2000, ApJ, 540, 771

Wong, T., & Blitz, L. 2002, ApJ, 569, 157

Young, J. S., & Scoville, N. Z. 1991, ARA&A, 29, 581

Young, J. S., Allen, L., Kenney, J. D. P., Lesser, A., & Rownd, B. 1996, AJ, 112, 1903

Zwicky, F. 1956, Ergebnisse der exakten Naturwissenschaften, 29, 344